



**HAL**  
open science

# Hybrid III-V on silicon lasers for optical communications

Antonin Gallet

► **To cite this version:**

Antonin Gallet. Hybrid III-V on silicon lasers for optical communications. Optics / Photonics. Université Paris Saclay (COMUE), 2019. English. NNT : 2019SACL019 . tel-02203554

**HAL Id: tel-02203554**

**<https://pastel.hal.science/tel-02203554>**

Submitted on 31 Jul 2019

**HAL** is a multi-disciplinary open access archive for the deposit and dissemination of scientific research documents, whether they are published or not. The documents may come from teaching and research institutions in France or abroad, or from public or private research centers.

L'archive ouverte pluridisciplinaire **HAL**, est destinée au dépôt et à la diffusion de documents scientifiques de niveau recherche, publiés ou non, émanant des établissements d'enseignement et de recherche français ou étrangers, des laboratoires publics ou privés.

# Hybrid III-V/Si lasers for optical communications

Thèse de doctorat de l'Université Paris-Saclay  
préparée à Télécom ParisTech

Ecole doctorale n°575 Electrical, Optical, Bio-physics and  
Engineering (EOBE)  
Spécialité de doctorat: Electronique et Optoélectronique, Nano- et  
Microtechnologies

Thèse présentée et soutenue à Palaiseau, le 4 Avril 2019, par

**Antonin Gallet**

Composition du Jury :

Xavier Letartre Directeur de recherche, INL	Rapporteur
Geert Morthier Professeur, Ghent University	Rapporteur
Ségolène Olivier Ingénieur de recherche, CEA Leti	Examineur
Delphine Marris-Morini Professeur, C2N	Président
Alfredo de Rossi Ingénieur de recherche, TRT	Examineur
Mohand Achouche Ingénieur de recherche, III-V Lab	Examineur
Frédéric Grillot Professeur, Télécom ParisTech	Directeur de thèse
Guanghua Duan Ingénieur de recherche, 3S Photonics	Invité

*Une cuisinière ne peut rien faire  
sans riz.*

PROVERBE CHINOIS

# Remerciements

**A** PRÈS presque 3 ans et demi à III-V lab et Télécom ParisTech, il est temps de remercier ceux qui m'ont permis de réaliser ce travail.

- Je remercie les sociétés Nokia, Thales et CEA Leti d'avoir créé et de soutenir le III-V Lab.
- Un grand merci à Guanghua Duan, qui m'a fait confiance et m'a permis de réaliser ma thèse dans son équipe. Je le remercie pour la transmission de ses connaissances, son implication ainsi que pour sa bienveillance à mon égard.
- Merci à mon directeur de thèse Frédéric Grillo, qui m'a grandement aidé dans ce travail. Je le remercie spécialement pour son soutien pour le manuscrit et pour la préparation de la soutenance.
- Je remercie les rapporteurs pour leurs commentaires et éloges. Je remercie les examinateurs du jury pour leurs questions et commentaires, dont j'ai apprécié la pertinence.
- Je remercie Hélène Debrégeas, qui a repris mon encadrement au départ de Duan. J'ai beaucoup appris à son contact. Je lui suis aussi redevable pour son aide sur le manuscrit.
- Je remercie Romain Brenot et Jean-Guy Provost pour tout ce qu'ils m'ont apporté dans tous les domaines.
- J'aimerais remercier Alfredo de Rossi pour sa générosité, sa disponibilité et sa patience.
- J'aimerais remercier Frédéric Van Dijk pour sa bonne humeur, ainsi que sa "team 11h 30" : Peppino, Andrzej, Cecil, Sylvain, Gil, Barbara et François D.
- Je remercie Christophe Jany, Ségolène Olivier et Karim Hassan du Leti pour la réalisation des composants et leur bienveillance.

- Je remercie Dalila, Harry, Catherine et Michel pour la préparation des composants et des bancs ainsi que les membres de l'équipe photonique sur Silicium David C., Alexandre S. Delphine N. et Mohand. A. J'aimerais remercier mon professeur Henri Benisty qui m'a conseillé au moment de rejoindre cette super équipe.
- Je remercie Guillaume, Xavier, Lina et Inès qui m'ont accueilli et intégré à l'équipe dès mon arrivée. Je remercie tout spécialement Guillaume pour m'avoir inculqué la science des mesures et un certain sens du travail d'équipe. J'ai été ravi de passer du temps en mesure avec Inès et de travailler sur les passifs avec Xavier. Je remercie Lina pour son aide sur le manuscrit, 2 ans après avoir quitté l'équipe Silicium.
- Bien sûr, je remercie Hajar et Théo sans qui la deuxième partie de ma thèse n'aurait pas eu la même saveur. J'aimerais aussi remercier Raouia et Claire ici. Je vous souhaite une bonne chance pour la suite.
- Je remercie Anaëlle, avec qui j'ai pu découvrir Dusseldorf, Goteborg et Rome. Je remercie aussi mes camarades doctorants Marja, Valeria, Florian, Guillaume B. et S, Agnès, Nicolas, Gregory, Romain, Nadia, Kebede et Stefano.
- Je remercie Delphine L., Karim M., Estelle, Geneviève, Alexandre G., Fabrice, Christophe C., Mathilde, Giancarlo, Jean, Axel, Jean-Luc, Filipe, JF, Carmen, Clément, Michel K., Philippe, Pascale, Maryline, Aline, Myriam, Olivier T., Nathalie et François C. ainsi que tous les membres de III-V Lab que je ne peux citer ici.
- Je remercie ma famille qui a été d'un grand support. Sans eux, ce manuscrit n'existerait pas, et les derniers mois de rédaction et de préparation de soutenance n'aurait tout simplement pas pu se faire. J'aimerais aussi remercier mes amis.  
Enfin, ma dernière pensée va à Marie-Anaïs. Avec son amour et son dévouement, elle m'a épaulé sans jamais faillir. Merci de partager ma vie.  
A tous, je vous remercie du fond du coeur.

# Contents

<b>1</b>	<b>Introduction</b>	<b>6</b>
1.1	Optical communications . . . . .	6
1.2	Photonic components . . . . .	8
1.3	Photonic links and WDM Technology . . . . .	11
1.4	Photonic integration platforms . . . . .	14
1.5	III-V/Si heterogeneous integration technology . . . . .	17
1.6	Introduction to III-V/Si lasers . . . . .	21
1.7	Aim of the thesis . . . . .	22
<b>2</b>	<b>Tunable laser diodes</b>	<b>29</b>
2.1	Hybrid III-V on silicon tunable laser . . . . .	30
2.1.1	Tunable laser introduction . . . . .	30
2.1.2	Silicon ring resonator filter . . . . .	31
2.1.3	Ring resonator based laser . . . . .	34
2.1.4	Laser output power optimization . . . . .	41
2.1.5	Integration of semiconductor optical amplifiers . . . . .	44
2.2	Advanced double ring resonator designs . . . . .	46
2.2.1	Low linewidth tunable lasers . . . . .	46
2.2.2	Fast tunable laser . . . . .	47
2.3	Tunable lasers in optical access network . . . . .	52
2.3.1	Introduction to passive optical networks. . . . .	52
2.3.2	NG-PON2 Standard . . . . .	54
2.3.3	Tunable laser DML . . . . .	57
2.3.4	Integration with an SOA . . . . .	59
2.4	Chapter conclusion . . . . .	65

<b>3</b>	<b>High Speed Hybrid Distributed Feedback Lasers</b>	<b>71</b>
3.1	Introduction to DFB lasers . . . . .	71
3.1.1	DFB laser theoretical description . . . . .	71
3.1.2	III-V/Si DFB laser . . . . .	75
3.2	Distributed feedback Directly Modulated Lasers . . . . .	79
3.2.1	High speed DFB lasers . . . . .	79
3.2.2	DML chirp . . . . .	83
3.2.3	Pros and cons of DML sources . . . . .	86
3.2.4	Filtered DMLs and CML . . . . .	87
3.2.5	Add-drop ring resonator filters . . . . .	88
3.3	Directly modulated III-V/Si DFB Laser integrated with extinction ratio en- hancement filter . . . . .	90
3.3.1	Basic characteristics of extinction ratio enhanced DFB laser . . . . .	90
3.3.2	Fabricated RR filter . . . . .	91
3.3.3	RR impact on laser dynamics . . . . .	92
3.4	Transmission experiments . . . . .	94
3.4.1	Modulation at 10 Gb/s . . . . .	94
3.4.2	Modulation at 25 Gb/s and beyond . . . . .	96
3.4.3	Comparison with state of the art . . . . .	99
3.5	Design improvements . . . . .	100
3.6	DFB laser with tapered grating . . . . .	104
3.6.1	Direct modulation at 25 Gb/s . . . . .	109
3.7	Chapter conclusion . . . . .	110
<b>4</b>	<b>High Q hybrid lasers</b>	<b>116</b>
4.1	Introduction to narrow linewidth DFB lasers . . . . .	117
4.2	High Q hybrid laser design . . . . .	119
4.2.1	Introduction to Q factors . . . . .	119
4.2.2	Design introduction . . . . .	120
4.2.3	Grating parameters . . . . .	124
4.2.4	Actual design . . . . .	129
4.2.5	Threshold gain calculations . . . . .	132
4.3	Laser static characteristics . . . . .	133
4.3.1	Light-Intensity characteristics . . . . .	133
4.3.2	Spectra . . . . .	136

4.3.3	Linewidth enhancement factor . . . . .	136
4.4	High Q laser dynamics and noise properties . . . . .	138
4.4.1	Small signal bandwidth . . . . .	138
4.4.2	Relative intensity noise measurements . . . . .	140
4.4.3	Linewidth measurements . . . . .	143
4.5	Chapter conclusion . . . . .	149
<b>5</b>	<b>General Conclusion</b>	<b>155</b>
<b>6</b>	<b>Résumé en Francais</b>	<b>165</b>
	<b>Appendices</b>	<b>176</b>
<b>A</b>	<b><math>Q_{ext}</math> calculations for phase shifted lasers</b>	<b>177</b>
	<b>List of Acronyms</b>	<b>179</b>

# Chapter 1

## Introduction

### 1.1 Optical communications

**T**ELECOMMUNICATION is the use of technical devices to transmit data. Optical communication is a very efficient telecommunication technology: the signal propagates at the speed of light on a very low loss optical fibre. As sketched in fig. 1.1, fiber losses are minimal around  $1.55 \mu\text{m}$ , where fiber Rayleigh scattering and infrared absorption curves cross. With losses of  $0.2 \text{ dB/km}$  in this wavelength window, the signal needs to be amplified only every 50-100 km. This wavelength window is thus the preferred choice for fiber optic communications. Apart from fiber, an optical link is composed of an emitter, amplifiers and a receiver. Optical links are deployed all over the world to make a global telecom network. As sketched

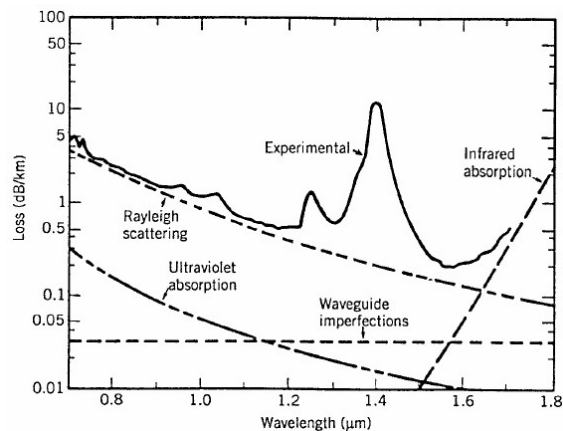


Figure 1.1: Experimental loss measurement of single mode fiber versus wavelength from [1] realized in 1979. Nowadays, fiber losses are below  $0.2 \text{ dB/km}$  at  $1.55 \mu\text{m}$ .

in fig. 1.2a the network is structured in three main scales. The long haul network connects

continents with transpacific cables (around 11 000 km long) and transatlantic cables (around 6000 km). Those links need components with extreme reliability as repairing cables have a huge cost.

The regional and metropolitan networks (several hundreds kilometers) connects countries and cities. Metropolitan network have a ring topology to efficiently connect regional, access and data center interconnects (DCI) networks. DCI link two datacenters that are 50 - 100 km away. DCI are important as datacenters are more and more widespread.

The last scale is access networks, which connect the end user to internet with a broadband connection. Access standardized distances between the user and the central office are 20 or 40 km. Optical access is a large market with more than 50 million subscribers in Europe in 2017 [2]. As long haul and Metro aggregate the access data traffic, their data rate operation are one or two order of magnitude greater than in access network.

Over the years, data rate increases at each scale. After a period of rapid growth in the 1990s, total data traffic growth rate is x10 every 8 years (fig. 1.2b). Recently, data traffic increases

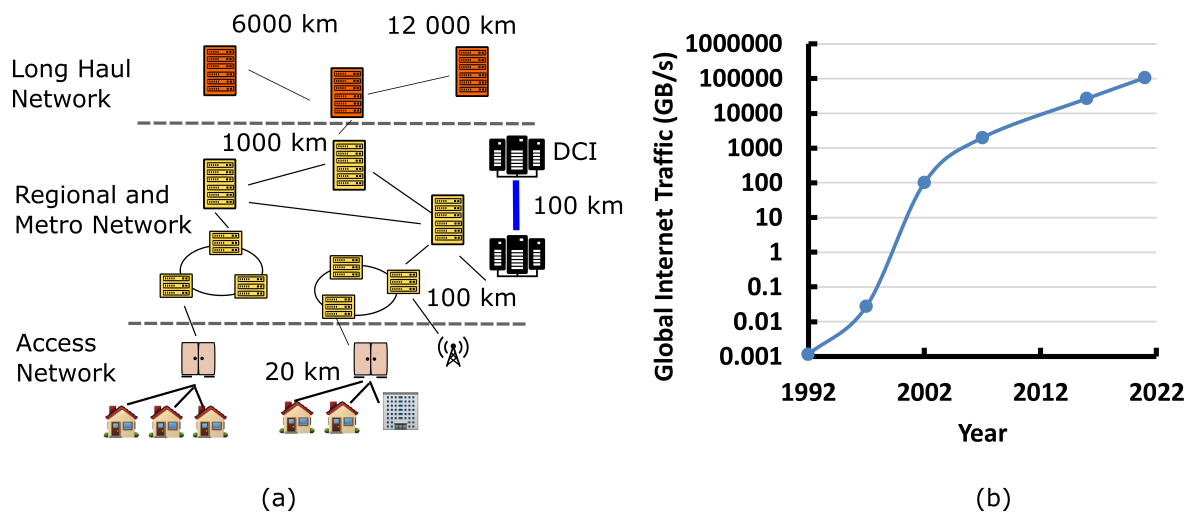


Figure 1.2: (a) Topology of the telecom network, featuring the long haul, regional and access networks. (b) Global internet evolution since 1992, clearly demonstrating the exponential data traffic growth [3].

as smartphones generate a large amount of data. Bandwidth demand also comes from 4K videos and related services.

The exponential data traffic increase is known as "photonic Moore's law" in reference with the performance increase of electronic microprocessors. As in the microelectronics industry, photonic Moore's law means that although datarates increase, power consumption and price of optical systems should remain stable over time. This is possible only if a high R&D invest-

ment is done to introduce new technologies. New fibers, amplifiers, emitters and receivers are investigated by the optical communication community. In the following section I will shortly introduce photonics components, with a focus on lasers.

## 1.2 Photonic components

A photonic emitter is a packaged module with a laser, a modulator and its electronic driver and an isolator. The receiver is a packaged module with a photodetector and a trans-impedance amplifier. As this thesis is centered on laser development, I will briefly introduce semiconductor laser here, following [4] and [5]. Modulator and photodetector technology overview can be found in [6] and [7] respectively.

Schawlow and Townes first described a laser as a gain region in an optical resonator in 1958 [8]. Telecommunication lasers are made with semiconductor materials as they are reliable sources that can be manufactured in large volumes. They have been invented in 1962 soon after the first laser demonstration [9]. Alloys of materials from column III and V of Mendeleev table are used as they have direct bandgap and large optical gain in the C band. For those devices, amplification in semiconductor comes from interband electron-hole recombinations, as indicated by fig. 1.3a. To have amplification, we need to inject electrons in the conduction

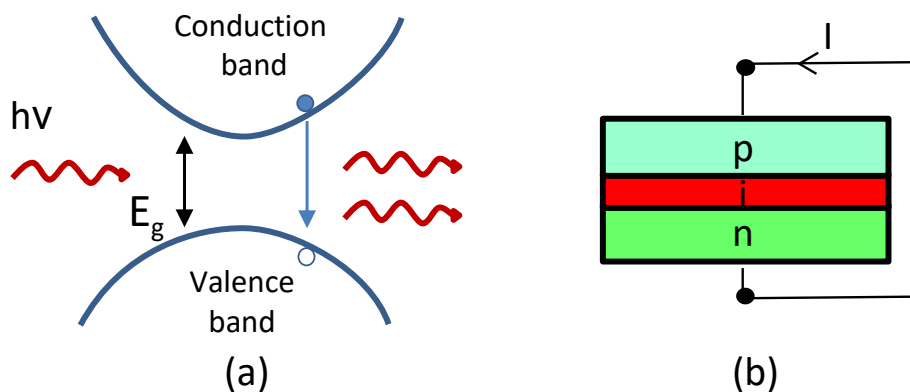


Figure 1.3: (a) Interband transitions in semiconductor leading to stimulated amplifications.(b) Electrons and holes are injected with a forward biased P-I-N junction .

band and holes in the valence band. As their population is described by fermi distributions with quasi fermi level  $E_{Fc}$  and  $E_{Fv}$ , the amplification condition is [5]:

$$E_{Fc} - E_{Fv} > h\nu > E_g \quad (\text{Bernard-Duraffourg}) \quad (1.1)$$

$h\nu$  is the photon energy and  $E_g$  is the energy band gap. To satisfy this condition, carriers are injected in the semiconductor. As sketched in fig. 1.3, this is done by a forward biased P-I-N junction. Several band structures engineering have been proposed, from the heterostructure laser [10], to the quantum well [11] and quantum dot [12] laser diodes. Modal gain for a carrier density  $N$  is given by :

$$G(N) = \Gamma_{act} a \times (N - N_{tr})$$

where  $\Gamma_{act}$  is the optical mode confinement in the active region,  $a$  is the differential gain,  $N$  and  $N_{tr}$  are the carrier density and carrier density at transparency respectively. As we will see in the next section, a laser is a gain region inside an optical resonator.

### Fabry-Perot Lasers and oscillation condition

The simplest laser is based on a Fabry-Perot (FP) cavity. It is a gain region of length  $L$  between two broad band mirrors. Laser threshold is obtained when gain  $G(N_{th})$  equals losses [5]:

$$G(N_{th}) = g = \alpha_i + \alpha_m \tag{1.2}$$

$\alpha_i$  and  $\alpha_m$  are the the internal and mirror loss respectively. Carrier density at threshold  $N_{th}$  gives the threshold current  $I_{th}$ . Above threshold, output power is proportional to bias current with slope  $\eta_d$ , as described in fig.1.4.

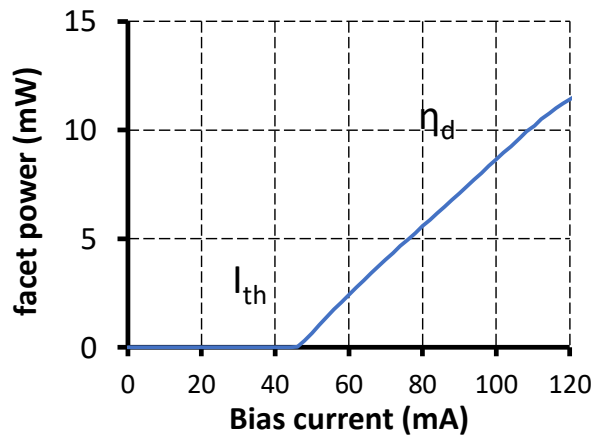


Figure 1.4: L-I characteristics of a III-V/SOI laser

In a laser, the round trip phase is a multiple of  $2\pi$ :

$$2\beta L = 2\pi p \Leftrightarrow \lambda_p = \frac{2n_{eff}(\lambda_p)L}{p} \quad (1.3)$$

Where  $\beta$  is the propagation constant,  $L$  the cavity length,  $n_{eff}$  the waveguide effective index and  $\lambda_p$  the allowed wavelengths. Equation 1.3 indicates that several modes can propagate in the cavity. If  $n_g$  is the waveguide group index, the longitudinal mode spacing is  $\Delta\lambda = \frac{\lambda^2}{2n_g L}$ , several 10 GHz for typical cavity lengths and index of in-plane lasers. As the mode spacing is small compared to the 3 dB gain bandwidth of semiconductor lasers (several 1000 GHz for typical  $N_{th}$  and at  $1.55 \mu m$ ), FP lasers are multimode.

### Low noise single wavelength lasers

A single mode laser has a spectral filter inside the FP cavity which introduces a wavelength dependence of internal losses. With tunable filters, full C band lasers can be realised. Spectral purity of single mode laser is characterised by side-mode suppression ratio (SMSR). For optical communications, required SMSR are usually better than 40 dB.

Laser noise properties are important for optical systems performances as modern communication are based on phase and amplitude modulation formats. As we will see in chapter 2, a narrow spectral linewidth is required. A formula for laser linewidth has been derived by Schawlow and Townes [8], and modified by Lax [13]. Spectral broadening is due to spontaneous emission in the lasing mode. In semiconductor lasers, there is an extra term due to phase-amplitude coupling factor  $\alpha_H$ . As explained in [14], spontaneous emission induces a transient gain change, resulting in a variation of both imaginary and real part of refractive index leading to a linewidth increase. So-called Schawlow-Townes-Henry formula is

$$\Delta\nu = \frac{R_{sp}}{4\pi I} \times (1 + \alpha_H^2) \quad (1.4)$$

Where  $R_{sp}$  is the spontaneous emission rate and  $I$  is the average intensity in the cavity.  $\alpha_H$  is the linewidth enhancement factor defined as [14]:

$$\alpha_H = -\frac{4\pi}{\lambda} \times \frac{\frac{dn}{dN}}{\frac{d\mathcal{G}}{dN}} \quad (1.5)$$

$n$  is the effective index,  $N$  the carrier density and  $\mathcal{G}$  the material gain. As they have high  $R_{sp}$  and as usually  $2 < \alpha_H < 5$  semiconductor lasers were not the preferred choice for low

linewidth applications. As  $R_{sp}$  and  $\alpha_H$  can be lowered, semiconductor lasers with linewidth below 70 kHz are now available [15].

### 1.3 Photonic links and WDM Technology

With a 1.3  $\mu\text{m}$  Fabry-Perot laser modulated at 280 Mb/s, AT&T, British telecom and France Telecom layed the first transatlantic optical cable in 1988. But due to fiber chromatic dispersion, the different modes don't propagate at the same speed. The signal is distorted after a certain distance thus single mode laser are preferable solutions.

Moreover, as engineering works to lay fibre are expensive, propagating multiple signals in the same fibre is cost effective. This technology is called "wavelength division multiplexing" (WDM) and is possible as multiple lasers can be simultaneously amplified in an Erbium Doped Fiber Amplifier (EDFA). Its amplified spontaneous emission spectrum is represented on fig. 1.5a. EDFA gain bandwidth defines the conventional (C) band used in telecommunications

As presented in fig. 1.5b, each modulated wavelength is multiplexed by a passive multiplexer. Multiplexers can be arrayed waveguide grating, echelle grating or free space gratings. Up to 96 channels with 50 GHz channel spacing can be transmitted and amplified in the same fibre in the C band. At the receiver side, wavelengths are demultiplexed and each wavelength is detected independently. From 1990 to 2010, systems used simple two level amplitude

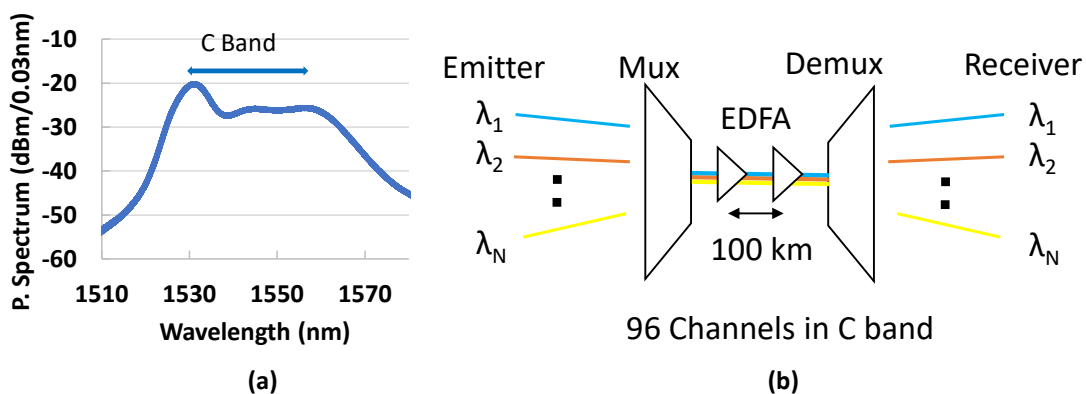


Figure 1.5: (a) EDFA Amplified spontaneous spectrum. (b) Schematic representation of a WDM system, with multiple wavelength channels. As EDFA amplifier and single mode lasers become available, telecom system bandwidths were multiplied by 100 in few years.

modulation known as on-off keying (OOK). Data rates evolved regularly from 2.5 Gb/s to 40 Gb/s, as described in fig. 1.6 (blue triangle in red curve). In those systems, dispersion compensation modules are placed regularly in the network.

After 2010, long haul, metro and DCI systems use coherent modulation formats as dispersion compensation can be done with a digital signal processor (DSP) at the receiver side. In coherent technology the bit rate increases with Phase and amplitude modulation formats. It is also possible to use polarisation multiplexing (PDM) to double the bit rate. Hence 100 or 200 Gb/s signals per wavelength can be generated (purple triangles in red curve). As several bit per symbol are transmitted, the symbol rate ranges only from 30 to 60 Gbaud (blue curve). It is thus possible to have 200 Gb/s or more with similar optical component as 40 Gb/s OOK systems.

As single wavelength bit rate increase, total fiber capacity blows up, with several 10 Tb/s already demonstrated (green curve). Total fiber capacity depends on the number of channel used. This value is linked with the signal spectrum width and the amplifier bandwidth.

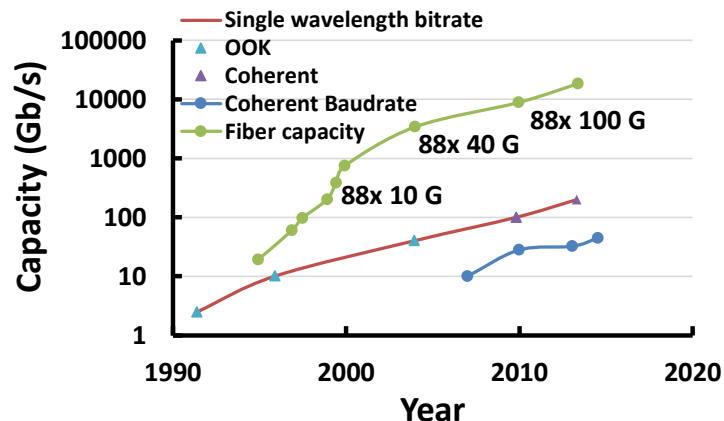


Figure 1.6: Evolution of telecom long haul products. Evolution of single wavelength bitrate (red), with OOK (blue triangles) and coherent (purple triangles) systems. Coherent systems baudrate (blue curve) is the modulation speed of a Mach Zehnder Modulator in a coherent modulator. Aggregated fiber capacity is presented in green. Data come from [16].

A coherent module includes a widely tunable laser, a dual polarization I-Q modulator with four Mach-Zehnder modulators, a coherent receiver and a digital signal processor (DSP). The corresponding number of discrete components per module is about 10. As multiple lasers, modulators and filters are used in the same WDM system, photonic integrated circuits (PIC) where all components are on the same chip became commercially available [17]. As coherent

transceivers are more complex than previous OOK technology, photonic integration is even more appealing.

### Need for photonics integration

As bandwidth demands exponentially increases, optical component power consumption and size need to be reduced. As described in [18], in a coherent module power consumption is driven by the DSP chip and its size by optical components. DSP power consumption reduces with every new CMOS node. The size of optical components decreases with optical integration and/or packaging progress. As pictured in fig. 1.7, there are four standardized packages for coherent modules. Size and power consumption is approximately divided by two at each new generation, introduced every two years. To decrease package footprint and power consumption, there are two solutions:

- closely package discrete components.
- integrate laser, modulator, receiver on the same photonic integrated circuit (PIC).

First choice have a high yield as components are tested before packaging and a fast time to market as individual components are optimized separately and have simple fabrication processes. The latter can bring a high reduction in size, power consumption and packaging costs as all optical components are on the same chip. As technology process is complex for PIC, it may take time to have high performance components with a reliable process. As the chip is large, it is more difficult to have a high yield. A high time to market is a problem for

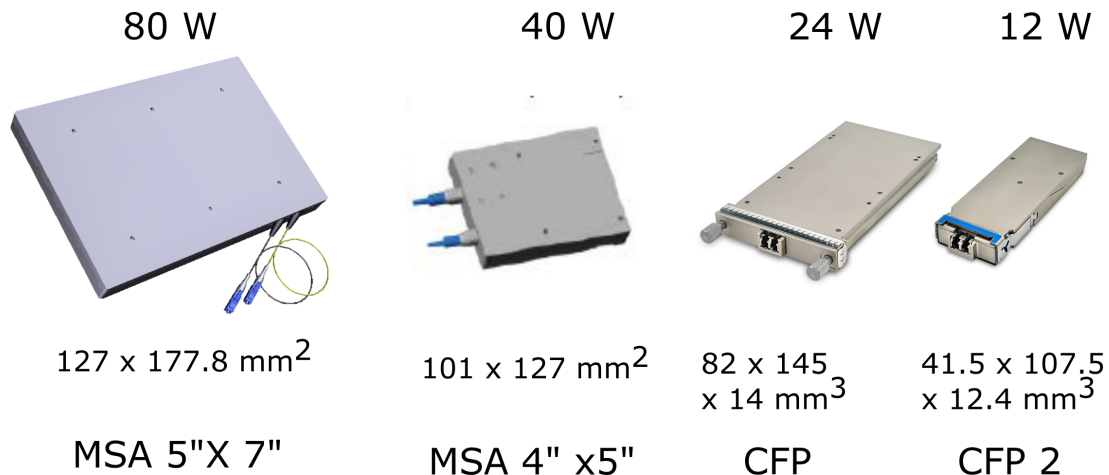


Figure 1.7: Evolution of coherent modules, featuring a 1/2 power consumption and size reduction at each generation. A new generation is introduced every two years.

PIC commercialisation as industry technology cycles take 5-10 years and as prices for the same component drop year after year. It is possible to mix integrated and non integrated approaches. A PIC company uses one chip for emitter and one chip for receiver [17]. Another vendor chose one chip for laser and one for emitter/receiver [19]. As optics need to follow DSP power consumption which decline according to Moore's law, optical integration may be unavoidable in the future.

## 1.4 Photonic integration platforms

The idea of photonic integration was initially proposed in the end of the 1960s' [20]. It matured for 40 years in research labs and is a well established technology since the 2000s. Infinera corporation first demonstrated WDM PICs in 2004 and coherent PICs in 2010. III-V PICs are now sold by other major component vendors.

Silicon started to be considered as an optical compound when Soref and Bennett demonstrated that it could be used as an optical modulator [21] and after Reed and Rickman showed that extremely low loss waveguide can be realized [22]. In silicon photonics, waveguide core is made of silicon and cladding of silica. As there is a high index contrast between both, light can propagate along sharp bends.

After the pioneering work, silicon photonics became a "hot topic" when silicon foundries developed photonics devices [23]. Their wafers have 200 or 300 mm diameter, 2.5 - 4 times their III-V counterparts. Silicon photonics processing uses the same wafer and patterning processes developed in the SOI microelectronics industry. As silicon processes are mature and highly automated, yield and cost per mm square is improved compared to III-V PICs. A high performance uniformity and low failure rate is critical for opto-electronics components as they need to operate for years without maintenance.

Since the beginning of the 2010', silicon photonics components are accessible through multi project wafers runs, like integrated circuits in the microelectronics industry. Fabless companies such as Luxtera [24] or Acacia [25] fabricated high performances components in foundries and commercially demonstrated the benefit of silicon photonics. Their success is based on their Mach-Zehnder modulators with state of the art performances in terms of insertion losses, efficiency (small length  $L$ ) and drive voltage. They also demonstrated high temperature operation and wavelength/temperature insensitivity. A review of silicon modulators can be found in [26].

Another key component is the high speed and high absorption bandwidth Germanium pho-

modulator available in the silicon platform. With the unique features of the silicon platform, innovative components have been introduced, as the ring resonator modulator [27], the Silicon Insulator Silicon Capacitor (SISCAP) modulator and the III-V on silicon capacitor modulator [28]. As silicon photonics components are made in a CMOS fab, it is possible to integrate modulator electronic drivers with silicon photonics components. [29].

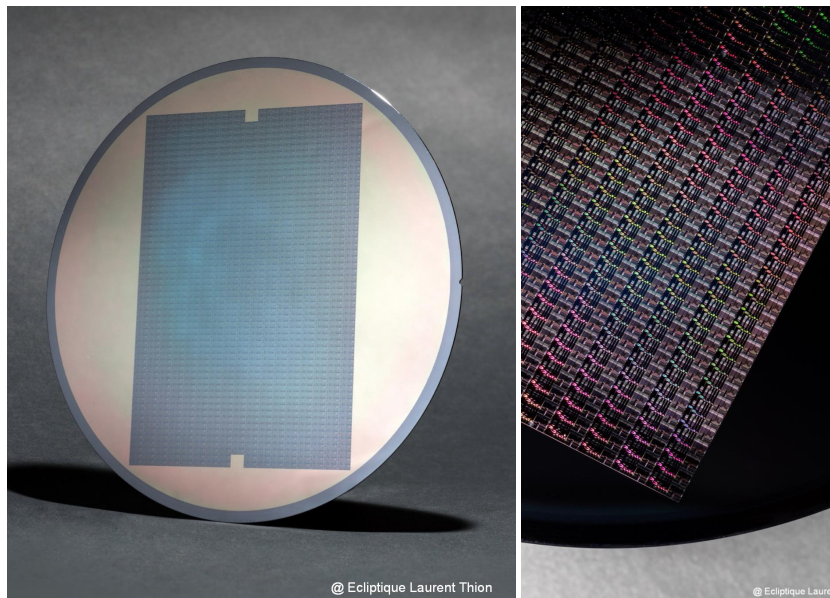


Figure 1.8: Silicon wafers from III-V lab (photo credit: Laurent Thion)

### Light source in Silicon photonics platforms

As silicon has an indirect bandgap, there is no native light source in the silicon photonics platform. Component makers developed several strategies to couple light to silicon PICs [19]. The simpler solution is to package separately laser and silicon PIC and connect them with a fiber. To avoid fiber coupling we can also "butt couple" laser and silicon PIC approaching the two waveguide facets. But these techniques are not always cost-effective.

Integrate III-V semiconductor material directly on top of silicon is more satisfying and is a long term evolution of the silicon photonics platform. Two approaches gave significant results: direct growth of quantum dot structure on Si substrate [30][31][32] and heterogeneous integration by wafer bonding [33] [34]. Direct growth is not straightforward as silicon and III-V have large lattice mismatch that create dislocations and defects in the material. Quantum dots are used as they are known to be less sensitive to dislocations and offer a high thermal

stability. In this approach, no group demonstrated the coupling to silicon waveguides as a  $2\ \mu\text{m}$  III-V buffer between silicon and active region is generally used to reduce dislocations in the active region. Hence this platform only offers the same components as the pure III-V one for the moment.

In the heterogeneous integration scheme, an unprocessed III-V die or wafer is bonded on a processed silicon wafer. As in the III-V platform, lasers are processed in a 2, 3 or 4 inch wafer clean room. As bonding layers are thin (5-100 nm), it is possible to couple light from III-V to silicon waveguides.

As III-V wafer growth is an established technology, we may expect to have high performance components with III-V on silicon technologies. Both heterogeneous integration and direct growth have reached a certain maturity. There are already two commercial products based on heterogeneous bonding at Intel for intra datacenter communication. Intel products use four  $1.3\ \mu\text{m}$  III-V/Si DFB lasers with Silicon Mach-Zehnder modulators to have a 100 Gb/s emitter. Startup Aurion also developed a 100 Gb/s solution with heterogeneous integration scheme. They use four tunable laser together with four electro-absorption modulators [35]. Aurion reported a laser threshold current of 18 mA and output power greater than 35 mW [36] for an O band Fabry Perot laser. Direct growth lasers have already passed long term reliability tests [31].

Table 1.1 summarizes the comparative advantages of PIC platforms: monolithic integration on InP, pure silicon photonics, III-V/Si by heterogeneous bonding, and III-V/Si by direct growth. As those four platforms are more and more mature, other applications of PIC than WDM communications arise. We can cite for example microwave photonics [37], chip to chip communications [38] or LIDAR [39].

Platform	Laser	feat. size	Maturity	Wafer size (mm)	Yield	Fabless
InP	yes	++	+++	76	++	Yes
Silicon Photonics	no	+++	+++	200-300	+++	Yes
III-V/Si bonding	yes	+++	++	200-300	/	No
III-V/Si dir. growth	yes	++	+	200-300	/	No

Table 1.1: Photonic integration platforms pros and cons. No representative yield data is available for III-V/Si lasers. InP platforms currently develop a fabless model [40].

## 1.5 III-V/Si heterogeneous integration technology

### Silicon waveguides

Silicon fabrication starts with a silicon on Isolator (SOI) wafer. In our platform silicon is 500 nm thick and buried silicon dioxide (BOX) is usually 2  $\mu\text{m}$  thick.

Then, three types of silicon waveguides are patterned: laser rib waveguide, strip waveguide or passive rib waveguide. Their dimensions are sketched in fig. 1.9. Rib width  $W_{Si}$  is defined by 193 nm deep UV lithography as its size needs to be very precisely controlled. Slab width  $W_{slab}$  is usually large compared to the mode size. As  $W_{slab}$  value has very little impact on mode properties, it is defined with a less precise 248 nm deep UV lithography. Silicon waveguides are etched with a 180 nm HBr dry etching process [41].

After patterning, waveguides are encapsulated in  $\text{SiO}_2$ . Finally  $\text{SiO}_2$  thickness is reduced to 80 nm and planarised by chemical-mechanical planarisation (CMP).

As described in [42], waveguide single mode operation depends on the rib width  $W_{Si}$ . If  $W_{Si}$  is larger than a cut-off value  $W_{Si_c}$ , both  $TE^0$  and  $TE^1$  modes are guided in the structure. Fortunately, as deep UV lithography and silicon etching processes are very accurate, it is possible to fabricate waveguides with  $W_{Si} < W_{Si_c}$ .

Rib waveguide has losses around 1.5 dB/cm and strip waveguide around 4 dB/cm [42]. As pointed out by [43], losses depend on sidewall roughness and mode leakage in the substrate. As we will see in the next section, III-V on silicon lasers are made by bonding a III-V wafer on top of a processed silicon wafer.

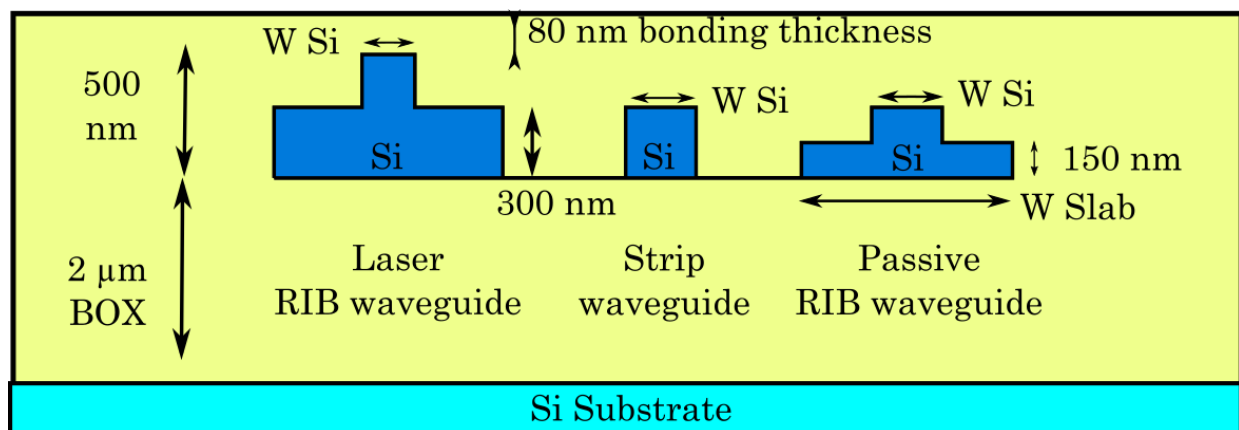


Figure 1.9: Silicon waveguides in III-V lab-Leti technology.

### III-V wafers and bonding

III-V wafers are grown by metal organic vapor phase epitaxy (MOVPE) or molecular beam epitaxy (MBE) in III-V lab epitaxy clean room. From the III-V material point of view, III-V on silicon lasers are very similar to their pure III-V counterpart.

In this thesis, we use an active region with eight AlInGaAs quantum wells that are 8 nm thick. They are sandwiched between two separate confinement heterostructures and n- and p-doped Indium Phosphide.

Usually, III-V lasers are grown from an n-type substrate to a p-doped layer. As we need to remove the III-V wafer substrate, we grow an inverse structure. We first grow p-doped InP, active region and n-doped InP (fig. 1.10). We then bond the n-doped side to SOI wafer and remove the substrate, as described in details in [44].

The University of Santa Barbara (UCSB) and Intel Lab first developed III-V/SOI laser

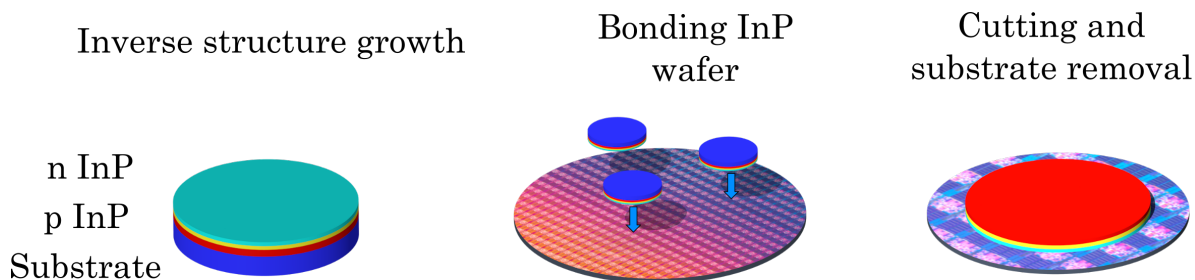


Figure 1.10: III-V on silicon epitaxy and bonding.

[45]. In their platform the silicon and III-V wafers are only oxidized before bonding. This technique results in a very thin spacer of 5 nm between III-V and silicon. As sketched in fig. 1.11a, the silicon waveguide is not encapsulated: there are air trenches at each side of it. They use a wide III-V mesa, greater than  $7 \mu\text{m}$ . Proton implantation limits the current injection on a small surface to efficiently inject carriers in the gain region and prevents the coupling to III-V higher order mode (gain guided structure). The mode is also index-guided by the silicon waveguide.

Another approach is developed by Ghent university, represented in fig. 1.11b. In this process, silicon waveguides are encapsulated in  $\text{SiO}_2$ .  $\text{SiO}_2$  thickness is reduced down to 5 to 60 nm. Then, DVS-BCB is deposited by spin coating, resulting in a spacer thickness lower than 110 nm. III-V wafer is bonded by DVS-BCB as it sticks to both wafers. DVS-BCB bonding is more tolerant to III-V wafers defects than molecular bonding used in this thesis [46].

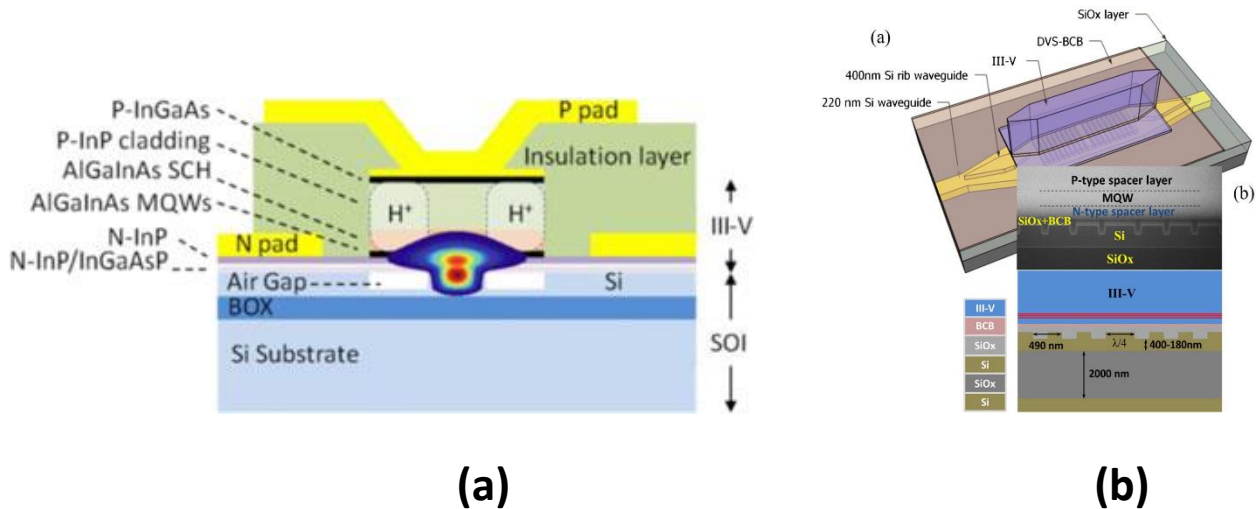


Figure 1.11: 2 other III-V/Si heterogeneous integration platforms: (a) UCSB/Intel platform with low bonding thickness and non encapsulated silicon waveguides, picture from [34](b) Gent-Imec platform uses BCB bonding, picture from [46]

### III-V Processing at III-V lab

The III-V process is done on 2, 3 or 4 inch wafers bonded on silicon. III-V processing steps are displayed on fig. 1.12. In (1), Contact lithography is used to define the different III-V active sections. Then both dry and wet etching processes are used. In (2) a NiCr heater is plated on top of an alumina layer. Alumina protects the optical mode from the highly absorbing metal. In (3) heater contacts, laser contacts and modulator electrodes are made. The component is then encapsulated in BCB. In (4) vias are made in BCB and there is a second metallisation. The process is done either in Palaiseau or Grenoble and takes several months. One of the main difficulty of III-V on silicon processing is the fact that etching methods were developed for III-V wafers with n-doped substrates. Those recipes have to be changed as SOI wafers have an isolating substrate (see [41], p91). A schematics cross section and a scanning electron image of the structure are displayed in fig. 1.13.

### III-V process steps

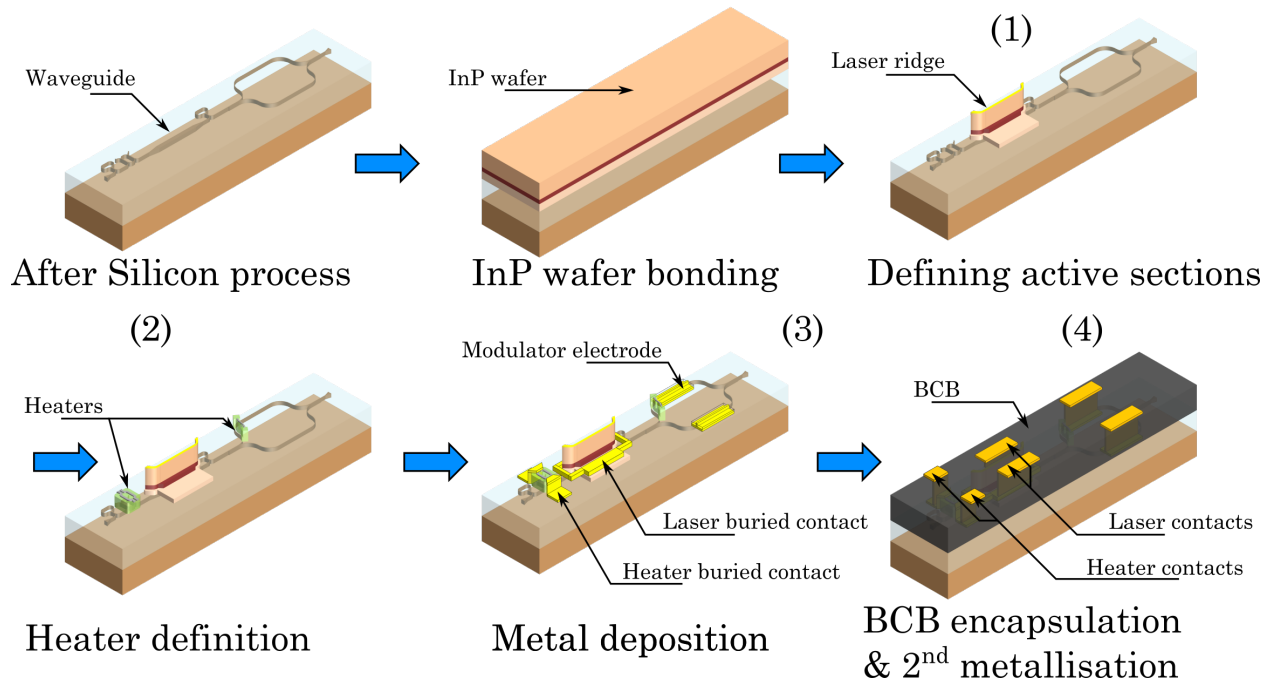


Figure 1.12: (a) III-V/SOI laser process, from [42]

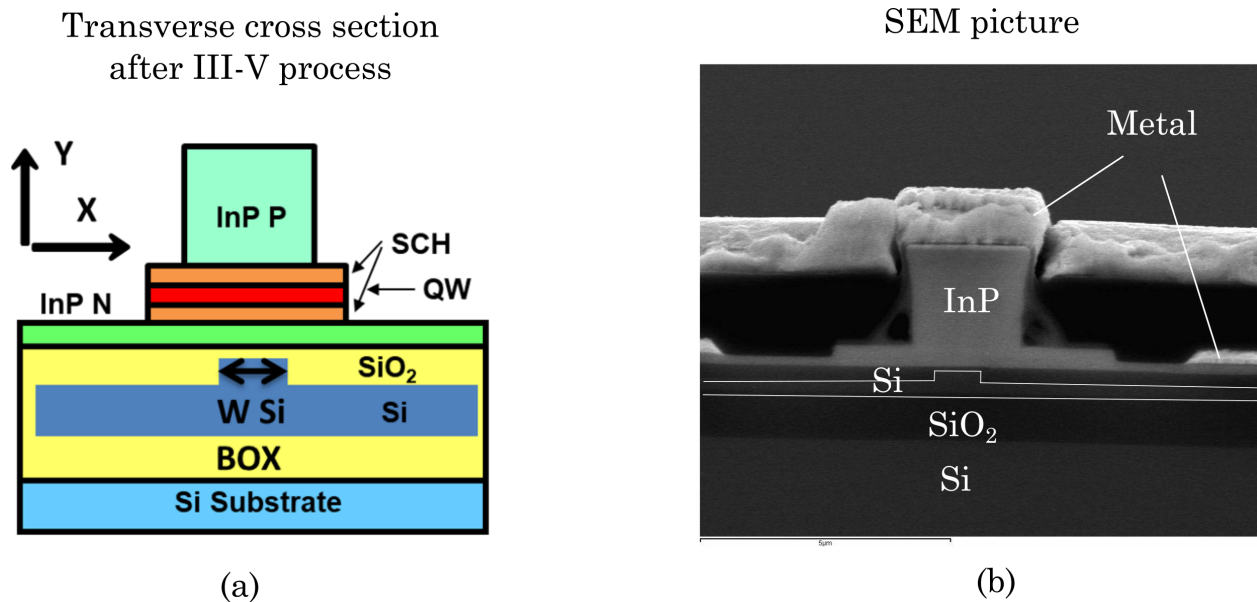


Figure 1.13: (a) Schematic cross section of the III-V/SOI structure. (b) Scanning electron microscope (SEM) image of the structure.

## 1.6 Introduction to III-V/Si lasers

To obtain a III-V on silicon gain section, light is transferred from the silicon to the III-V waveguide and vice versa. As they have similar refractive index and are close enough, the two waveguides eigenmodes are coupled and can be described as an unique supermode [47]. When we change the rib width of the silicon waveguide  $W_{Si}$ , we change the effective index of the silicon waveguide. As the effective index changes, the repartition between silicon and III-V varies. Simulated field intensity for three different silicon rib widths is presented in fig. 1.14, showing that the mode repartition is finely controllable. An adiabatic taper structure is designed to transfer the mode from the silicon to the III-V region [48].

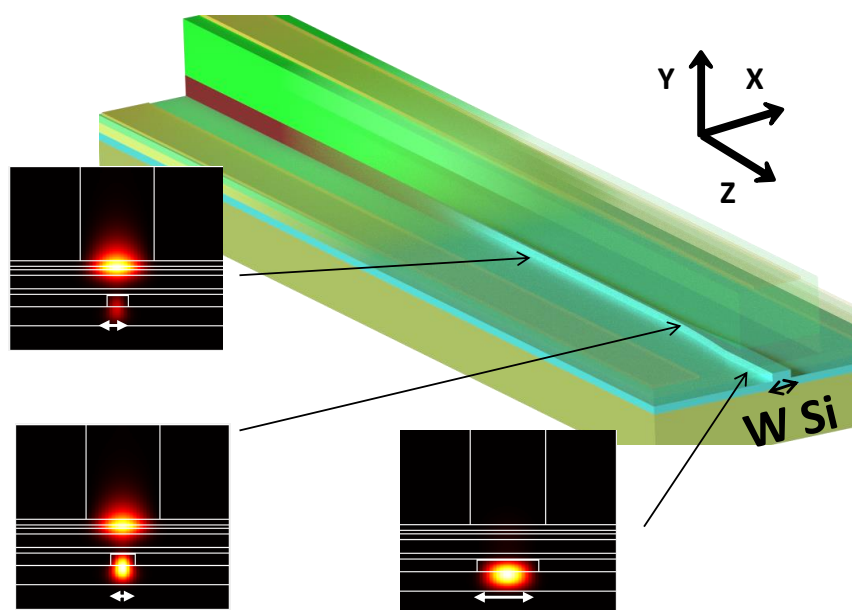


Figure 1.14: III-V on silicon waveguide 3D view. The width  $W_{Si}$  of the silicon waveguide controls the confinement in the III-V region. The picture is adapted from [42].

The gain region is inserted inside a III-V on silicon optical resonator to make a laser. For III-V on silicon Fabry Perot lasers, we use silicon Bragg gratings or Sagnac loop mirrors. Bragg grating is made by etching regularly the passive silicon waveguide, as pictured in fig. 1.15a. After the mirror, we collect the output power vertically with a fibre grating coupler (fig. 1.15b). We can also cleave the amplification region at each side to make Fresnel mirrors and collect the light horizontally.

In 2012, III-V lab demonstrated a low threshold FP laser in M. Lamponi et al. [49]. Laser had a 30 mA threshold and an output power better than 4 mW.

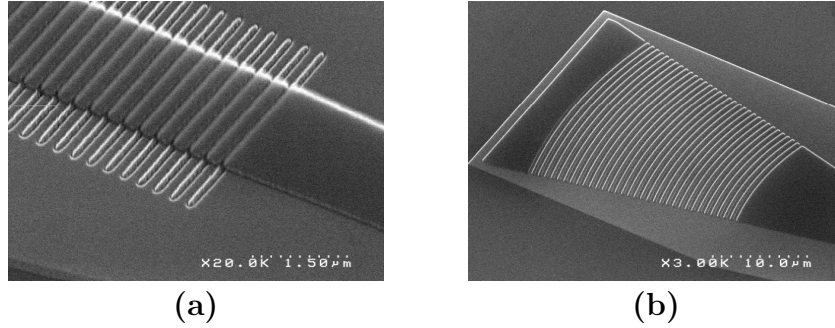


Figure 1.15: Scanning electron microscope images of (a) a Bragg grating and (b) a focusing grating coupler.

### III-V on silicon tunable and DFB lasers

Soon after the FP laser, A. Le Liepvre *et al* [50] demonstrated a hybrid tunable laser with two ring resonators (RR) filters and 45 nm tuning range, covering the C-band.

In 2016, a distributed feedback laser was also demonstrated [48]. It uses a grating etched in the silicon waveguide.

As fiber grating couplers couples the light vertically, lasers characteristics can be measured on wafer. Throughout this thesis, I used the manual wafer prober pictured in fig. 1.16a. However, cleaving the lasers reduce the coupling losses. After wafer thinning laser bars are cleaved and measured with a lensed fibre as presented in fig. 1.16b.

## 1.7 Aim of the thesis

The objective of this thesis is to design and demonstrate new laser designs for integrated photonics: widely tunable lasers, high speed distributed feedback (DFB) lasers and narrow linewidth high Q hybrid lasers.

During my thesis, I focused on modelling, design, mask layout and measurements of III-V on silicon devices. Fabrication was realised in both Leti and III-V lab clean rooms.

In chapter 2, I show performances of ring resonator based tunable lasers. After an introduction, I will discuss their basic properties such as tuning range and output power, and compare my results with state of the art lasers. I will also describe how to reduce their linewidth and wavelength tuning speed (section 2.2). To finish I will describe their direct modulation properties on section 2.3 for access network, focusing on burst mode operation. In chapter 3, I show the modulation dynamics of phase shifted distributed feedback lasers

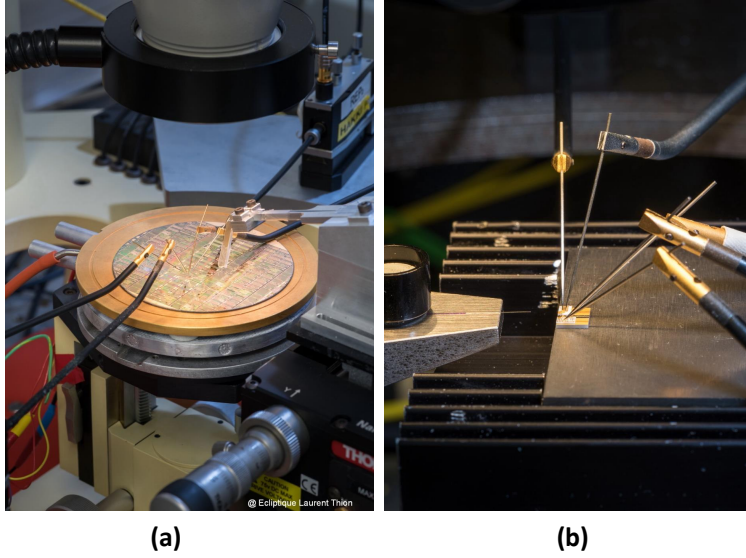


Figure 1.16: (a) Vertical coupling bench (b) Horizontal coupling bench. Laser is on an alumina sub-mount. Photo credit: Laurent Thion

which integrate a grating in the silicon waveguide. I first evaluate their chirp and modulation dynamics, then show a device which integrate an external ring resonator filter to enhance their modulation properties in transmission.

In chapter 4, I describe the dynamics and noise properties of high Q hybrid lasers recently introduced by A. researchers from Caltech. I will first introduce the concept and describe how to adapt the design in our platform. I will then show their interesting dynamic and noise properties. I will confirm that such lasers have a narrow linewidth, as indicated by [51] and measure their relative intensity noise.

In each section, I will emphasise on laser dynamic characteristics of III-V/Si lasers. I will also try to highlight the benefits of hybrid III-V on silicon platform for the targeted application. The last part of the thesis ends by a conclusion where the main results of this work are summarized. I will position my results with respect to state of the art, summarized in table 1.2.

	wg P (mW)	$\Delta\nu$ (kHz)	Tun. speed	Mod.	Reach
RR Tun. laser	15 [52]	18 [52]	$\mu$ s [53]	10 Gb/s [54]	25 km [54]
DFB laser	25 [55]	1000 [46]	ns [56]	28 Gb/s [57]	2 km [57]
High Q DFB	8 [51]	18 [51] 1 [58]	/	/	/

Table 1.2: III-V/Si lasers state of the art

## References

- [1] T. Miya et al. “Ultimate low-loss single-mode fibre at 1.55  $\mu\text{m}$ ”. In: *Electronics Letters* 15.4 (Feb. 1979), pp. 106–108.
- [2] *New Market Panorama data at the FTTH Conference 2018*. URL: <https://www.ftthcouncil.eu/documents/PressReleases/2018/PR%20Market%20Panorama%20-%2015-02-2018-%20FINAL.pdf>.
- [3] *The Zettabyte Era, Trends and Analysis*. URL: <https://webobjects.cdw.com/webobjects/media/pdf/Solutions/Networking/White-Paper-Cisco-The-Zettabyte-Era-Trends-and-Analysis.pdf>.
- [4] Coldren, Corzine, and Masanovic. *Diode Lasers and Photonic Integrated Circuits*. John Wiley & Sons, 2012.
- [5] J. Buus, M.-C. Amann, and D. J. Blumenthal. “Fundamental Laser Diode Characteristics”. In: *Tunable Laser Diodes and Related Optical Sources*. IEEE, 2005.
- [6] H. Yasaka and Y. Shibata. “Semiconductor-Based Modulators.” In: *Fibre Optic Comms: key devices. Springer Series in Optical Science*. 2017.
- [7] A. Beling and J. C. Campbell. “Photodetectors.” In: *Fibre Optic Communication: key devices. Springer Series in Optical Science*. 2017.
- [8] A. L. Schawlow and C. H. Townes. “Infrared and Optical Masers”. In: *Phys. Rev.* 112 (6 Dec. 1958), pp. 1940–1949.
- [9] R. N. Hall et al. “Coherent Light Emission From GaAs Junctions”. In: *Phys. Rev. Lett.* 9 (9 Nov. 1962), pp. 366–368.
- [10] H. Kroemer. “A proposed class of hetero-junction injection lasers”. In: *Proceedings of the IEEE* 51.12 (Dec. 1963), pp. 1782–1783.
- [11] R. Dingle and C. H. Henry. “Quantum effects in heterostructure lasers”. US3982207A. 1976.
- [12] Y. Arakawa and H. Sakaki. “Multidimensional quantum well laser and temperature dependence of its threshold current”. In: *Applied Physics Letters* 40.11 (1982), pp. 939–941. eprint: <https://doi.org/10.1063/1.92959>.
- [13] M. Lax. “Classical Noise. V. Noise in Self-Sustained Oscillators”. In: *Phys. Rev.* 160 (2 Aug. 1967), pp. 290–307.

- [14] C. Henry. “Theory of the linewidth of semiconductor lasers”. In: *IEEE Journal of Quantum Electronics* 18.2 (Feb. 1982), pp. 259–264.
- [15] M. C. Larson. “Narrow linewidth tunable DBR lasers”. In: *2016 International Semiconductor Laser Conference (ISLC)*. Sept. 2016, pp. 1–2.
- [16] I. W. and B. F. “Higher-Order Modulation Formats – Concepts and Enabling Devices.” In: *Fibre Optic Communication: key devices. Springer Series in Optical Science*. 2017.
- [17] R. Nagarajan et al. “Large-scale photonic integrated circuits”. In: *IEEE Journal of Selected Topics in Quantum Electronics* 11.1 (Jan. 2005), pp. 50–65.
- [18] A.Srivastava. “Optical Integration and the Role of DSP in Coherent Optics Modules”. In: *OFC Market Focus 2014* ().
- [19] C. Doerr. “Silicon photonic integration in telecommunications”. In: *Frontiers in Physics* 3 (2015), p. 37.
- [20] S. E. Miller. “Integrated optics: An introduction”. In: *The Bell System Technical Journal* 48.7 (Sept. 1969), pp. 2059–2069.
- [21] R. Soref and B. Bennett. “Electrooptical effects in silicon”. In: *IEEE Journal of Quantum Electronics* 23.1 (Jan. 1987), pp. 123–129.
- [22] A. G. Rickman and G. T. Reed. “Silicon-on-insulator optical rib waveguides: loss, mode characteristics, bends and y-junctions”. In: *IEE Proceedings - Optoelectronics* 141.6 (Dec. 1994), pp. 391–393.
- [23] A. E. Lim et al. “Review of Silicon Photonics Foundry Efforts”. In: *IEEE Journal of Selected Topics in Quantum Electronics* 20.4 (July 2014), pp. 405–416.
- [24] A. Narasimha et al. “A Fully Integrated 4×10-Gb/s DWDM Optoelectronic Transceiver Implemented in a Standard 0.13μm CMOS SOI Technology”. In: *IEEE Journal of Solid-State Circuits* 42.12 (Dec. 2007), pp. 2736–2744.
- [25] C. Doerr et al. “O, E, S, C, and L Band Silicon Photonics Coherent Modulator/Receiver”. In: *Optical Fiber Communication Conference Postdeadline Papers*. Optical Society of America, 2016, Th5C.4.
- [26] D. Marris-Morini et al. “Recent Progress in High-Speed Silicon-Based Optical Modulators”. In: *Proceedings of the IEEE* 97.7 (July 2009), pp. 1199–1215.
- [27] F. Gardes et al. “High-speed modulation of a compact silicon ring resonator based on a reverse-biased pn diode”. In: *Opt. Express* 17.24 (Nov. 2009), pp. 21986–21991.

- [28] T. Hiraki et al. “Heterogeneously integrated III–V/Si MOS capacitor Mach–Zehnder modulator”. In: *Nature Photonics* (2017).
- [29] S. Meister et al. *Silicon photonics for 100 Gbit/s intra-data center optical interconnects*. 2016.
- [30] M. Liao et al. “Monolithically Integrated Electrically Pumped Continuous-Wave III–V Quantum Dot Light Sources on Silicon”. In: *IEEE Journal of Selected Topics in Quantum Electronics* 23.6 (Nov. 2017), pp. 1–10.
- [31] A. Y. Liu and J. Bowers. “Photonic Integration With Epitaxial III–V on Silicon”. In: *IEEE Journal of Selected Topics in Quantum Electronics* 24.6 (Nov. 2018), pp. 1–12.
- [32] J. Kwoen et al. “All MBE grown InAs/GaAs quantum dot lasers on on-axis Si (001)”. In: *Opt. Express* 26.9 (Apr. 2018), pp. 11568–11576.
- [33] G.-H. Duan et al. “Hybrid III–V on Silicon Lasers for Photonic Integrated Circuits on Silicon”. In: *IEEE Journal of Selected Topics in Quantum Electronics* 20.4 (July 2014), pp. 158–170.
- [34] M. J. R. Heck et al. “Hybrid Silicon Photonic Integrated Circuit Technology”. In: *IEEE Journal of Selected Topics in Quantum Electronics* 19.4 (July 2013), pp. 6100117–6100117.
- [35] G. A. Fish and D. K. Sparacin. “Optical Transceivers Using Heterogeneous Integration on Silicon”. In: *Silicon Photonics III: Systems and Applications*. Ed. by L. Pavesi and D. J. Lockwood. Berlin, Heidelberg: Springer Berlin Heidelberg, 2016, pp. 375–395.
- [36] B. R. Koch et al. “Integrated Silicon Photonic Laser Sources for Telecom and Datacom”. In: *2013 Optical Fiber Communication Conference and Exposition and the National Fiber Optic Engineers Conference (OFC/NFOEC)*. Mar. 2013, pp. 1–3.
- [37] G. Carpintero et al. “Microwave Photonic Integrated Circuits for Millimeter-Wave Wireless Communications”. In: *Journal of Lightwave Technology* 32.20 (Oct. 2014), pp. 3495–3501.
- [38] C. Sun et al. “Single-chip microprocessor that communicates directly using light”. In: *Nature* 528 (Dec. 2015), pp. 534–538.
- [39] A. Martin et al. “Photonic Integrated Circuit-Based FMCW Coherent LiDAR”. In: *J. Lightwave Technol.* 36.19 (Oct. 2018), pp. 4640–4645.
- [40] M. Smit et al. “Generic foundry model for InP-based photonics”. In: *IET Optoelectronics* 5.5 (Oct. 2011), pp. 187–194.

- [41] M. Lamponi. “Hybrid III-V on silicon lasers for telecommunication applications”. Theses. Université Paris Sud - Paris XI, Mar. 2012.
- [42] X. Pommarede. “Hybrid III-V/Si photonics integrated circuits for optical communication applications”. PhD thesis.
- [43] F. Grillot et al. “Propagation Loss in Single-Mode Ultrasmall Square Silicon-on-Insulator Optical Waveguides”. In: *J. Lightwave Technol.* 24.2 (Feb. 2006), p. 891.
- [44] D. Bordel et al. “Direct and polymer bonding of III-V to processed silicon-on-insulator for hybrid silicon evanescent lasers fabrication”. In: *ECS Transactions* 33.4 (2010), pp. 403–410.
- [45] A. W. Fang et al. “Electrically pumped hybrid AlGaInAs-silicon evanescent laser”. In: *Opt. Express* 14.20 (Oct. 2006), pp. 9203–9210.
- [46] S. Keyvaninia et al. “Heterogeneously integrated III-V/silicon distributed feedback lasers”. In: *Opt. Lett.* 38.24 (Dec. 2013), pp. 5434–5437.
- [47] X. Sun and A. Yariv. “Engineering supermode silicon/III-V hybrid waveguides for laser oscillation”. In: *J. Opt. Soc. Am. B* 25.6 (June 2008), pp. 923–926.
- [48] N. Girard. “Lasers à faible bruit d’intensité en InP sur circuit Silicium pour l’optique hyperfréquence”. 2016SACLS113. PhD thesis. 2016.
- [49] M. Lamponi et al. “Low-Threshold Heterogeneously Integrated InP/SOI Lasers With a Double Adiabatic Taper Coupler”. In: *IEEE Photonics Technology Letters* 24.1 (Jan. 2012), pp. 76–78.
- [50] A. L. Liepvre et al. “Widely wavelength tunable hybrid III-V/silicon laser with 45 nm tuning range fabricated using a wafer bonding technique”. In: *The 9th International Conference on Group IV Photonics (GFP)*. Aug. 2012, pp. 54–56.
- [51] C. T. Santis et al. “High-coherence semiconductor lasers based on integral high-Q resonators in hybrid Si/III-V platforms”. In: *Proceedings of the National Academy of Sciences* 111.8 (2014), pp. 2879–2884. eprint: <http://www.pnas.org/content/111/8/2879.full.pdf>.
- [52] M. Tran Anh et al. “Multi-Ring Mirror-Based Narrow-Linewidth Widely-Tunable Lasers in Heterogeneous Silicon Photonics”. In: *2018 European Conference on Optical Communication (ECOC)*. Sept. 2018, pp. 1–3.

- [53] G. Duan et al. “Hybrid III-V Silicon Photonic Integrated Circuits for Optical Communication Applications”. In: *IEEE Journal of Selected Topics in Quantum Electronics* 22.6 (Nov. 2016), pp. 379–389.
- [54] G. Levaufre. “Circuits photoniques intégrés incluant des lasers hybrides III-V sur silicium pour applications en télécommunication très haut débit”. PhD thesis. 2016.
- [55] R. Blum. “Scaling the compute and high speed networking needs of the datacenter with silicon photonics”. In: *2017 European Conference on Optical Communication (ECOC) Market Focus*. Sept. 2017, pp. 1–2. eprint: <https://www.intel.com/content/www/us/en/architecture-and-technology/silicon-photonics/market-focus-article.html>.
- [56] S. Dhoore et al. “Electronically Tunable DFB Laser on Silicon”. In: *2018 International Semiconductor Laser Conference*. Sept. 2018, pp. 1–2.
- [57] A. Abbasi et al. “28 Gb/s direct modulation heterogeneously integrated C-band InP/SOI DFB laser”. In: *Opt. Express* 23.20 (Oct. 2015), pp. 26479–26485.
- [58] C. T. Santis et al. “Quantum control of phase fluctuations in semiconductor lasers”. In: *Proceedings of the National Academy of Sciences* 115.34 (2018), E7896–E7904. eprint: <https://www.pnas.org/content/115/34/E7896.full.pdf>.

# Chapter 2

## Tunable laser diodes

**T**UNABLE laser diodes are central optical components in modern communication systems. This chapter will discuss the design and measurements of hybrid III-V/Si tunable lasers based on ring resonator filters.

The first section is an introduction to ring resonator based tunable lasers. I describe its operating principle and basic characteristics and I compare three types of selective filter. I will also show how to improve their output power working on the cavity design or using a semiconductor optical amplifier.

In the second section I introduce two new tunable laser designs. The first one is designed to have a narrower linewidth. The second is a fast tunable laser which can switch wavelength in less than 1.5 ns thanks to the ring PIN junctions.

In the third section I will discuss the use of hybrid III-V/SOI lasers for access network NG-PON2. In time division multiple access (TDMA) operation, we need to switch on and off the laser as each client has to emit data in a specific time slot. This process may produce a detrimental wavelength drift. We introduce a method to mitigate this drift using a semiconductor optical amplifier (SOA) as a burst switch. Results presented here have been published in [1] and [2].

## 2.1 Hybrid III-V on silicon tunable laser

### 2.1.1 Tunable laser introduction

For the metro and long-haul network, system vendors use preferentially the C-band (1530-1565 nm) as Erbium-Doped-Fiber-Amplifier (EDFA) are available. To maximise the per fiber capacity, industry adopted the wavelength division multiplexing (WDM) scheme: several wavelengths are modulated and multiplexed into one fiber. Fixed wavelength sources are not the preferred choice as they have supplementary managing costs and are not flexible ([3], p124). As depicted in [4], several tunable laser configurations have been proposed. They share a similar operation principle: a spectral filter inserted in a Fabry-Perot cavity selects an unique mode on the gain window, as presented in fig. 2.1a. As pictured in fig. 2.1b, a booster SOA after the laser may be used to enhance the output power.

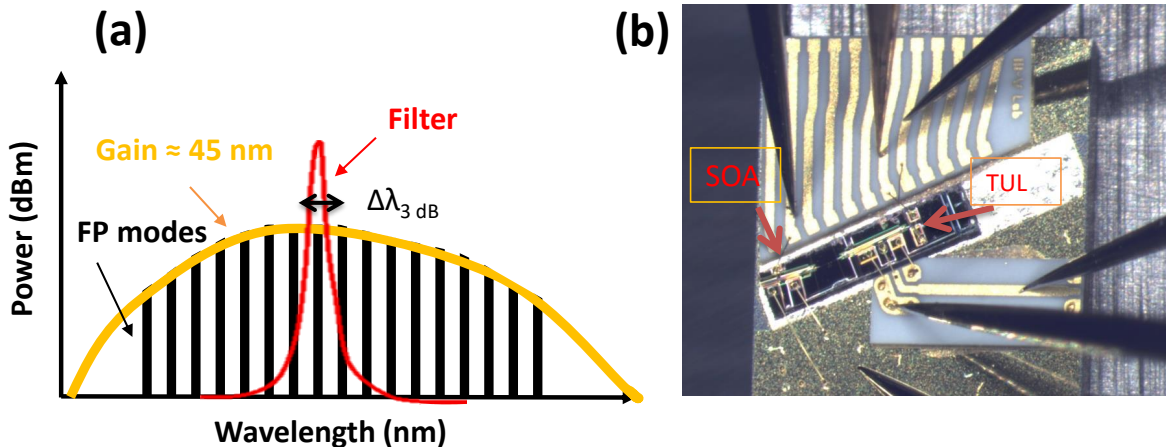


Figure 2.1: (a) The FP comb is filtered by the material gain window and by the intra-cavity filter. (b) Photograph of a hybrid III-V/SOI laser integrated with an SOA on an alumina submount.

A simple solution is the distributed Bragg reflector (DBR) laser. In this configuration, the grating mirror has a narrow spectral reflectivity centered on the Bragg wavelength. A 16 nm tuning range has been obtained with such device [4].

To obtain a widely tunable laser, people introduced a laser based on two sampled gratings distributed Bragg reflector (SG-DBR) in a Vernier configuration [5]. Sampling the grating produces a periodic reflectivity spectrum, as sketched in fig. 2.2. The Vernier reflectivity spectrum is the product of two SG-DBRs spectra. The bell shape of the SG-DBR reflectivity envelope is not very favourable for a wide tunability due to Vernier side mode competition. To overcome this problem, the superstructure grating distributed Bragg reflector (SSG-DBR)

concept has been proposed. Grating is carefully designed with several phase shifts to obtain a square reflectivity envelope, at the price of a complex design.

Ring resonators (RR) have been introduced in tunable lasers in [6] in the InP platform. This first device had a 40 nm tuning range with low tuning power consumption. Its side mode suppression ratio was however limited to 30 dB. RR based lasers have the filtering properties of SSG with a simpler and more versatile design: as explained in the next section both its free spectral range and 3 dB bandwidth are easy to control. Silicon on insulator RR are low loss and can be made very small: minimal radii are lower than 10  $\mu\text{m}$  [7].

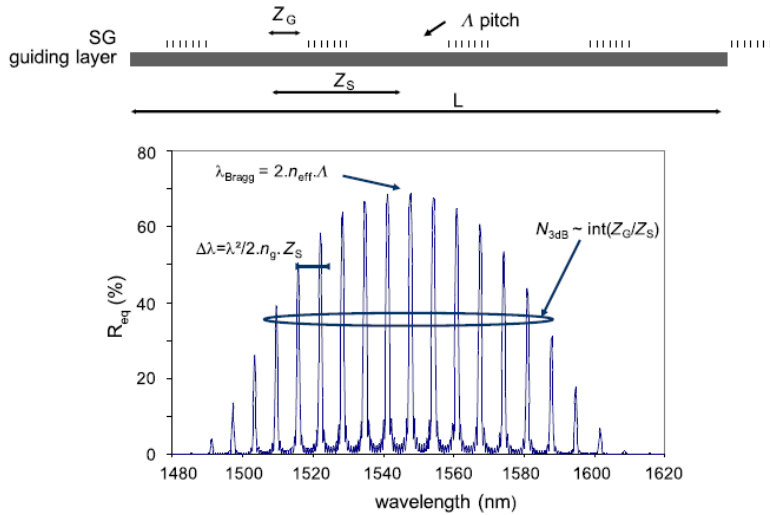


Figure 2.2: Schematic and transmission of a SG-DBR laser, from [4].

### 2.1.2 Silicon ring resonator filter

To obtain a narrow bandwidth filter, we will use a ring resonator (RR). Details about this device can be found in [8]. To make a RR, we first need to design a directional coupler.

A directional coupler (DC) is made by approaching two waveguides such that optical fields propagating in both of them are coupled. The field in a DC can be represented as two supermodes with different propagation constants. The beating between those modes leads to a power exchange between the two waveguides [9]. A DC is sketched in fig.2.3a, where we define its intensity transmission coefficient  $T = t^2$ . Depending on the length  $L$  of the coupling region, it is possible to arbitrarily choose  $T$ . A simulated directional coupler with  $T = 0.5$  is displayed in fig. 2.3b.

Ring resonators are made by connecting two directional couplers, as sketched in fig. 2.4a.

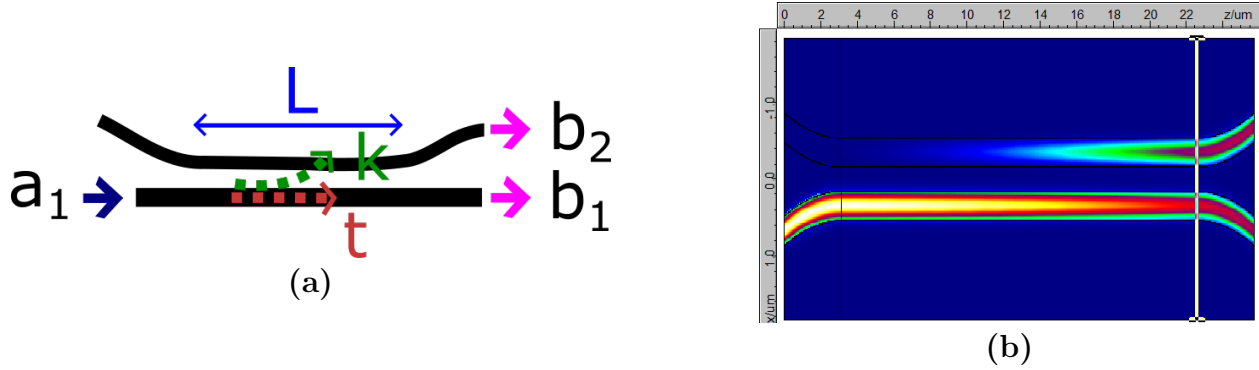


Figure 2.3: (a) Schematic of the directional coupler. Depending on the interaction length  $L$ , the intensity is more coupled to  $b_1$  or  $b_2$ , resulting in a different transmission coefficient  $T$ . (b): simulation of a 50-50 directional coupler using the commercial software Fimmwave.

The silicon waveguide is either a rib or strip (see fig. 1.9). The rib offers lower losses than strip in the straight region. However, as higher bend loss of rib [7] imposes to work with high radius rings we preferably use strip waveguides in RR designed for tunable laser.

For the sake of clarity I only reproduce here the useful formulae without calculation.  $L$  is the ring resonator perimeter and  $n_{eff}$  the effective index of the waveguide.  $\alpha_0$  is the power losses per unit length, in  $cm^{-1}$  and  $\alpha_l = \exp(-\alpha_0 L/2)$  is the amplitude round trip losses. We also define the round trip phase  $\theta = \frac{2\pi}{\lambda} \times n_{eff} L$ . The free spectral range (FSR) of the ring is the wavelength spacing  $\Delta\lambda$  between two resonances. It is given by  $\Delta\lambda = \frac{\lambda^2}{n_g L}$ , with  $n_g$  the group index. With notation defined in fig. 2.4a, the intensity transfer function  $\mathfrak{T}_d(\theta)$

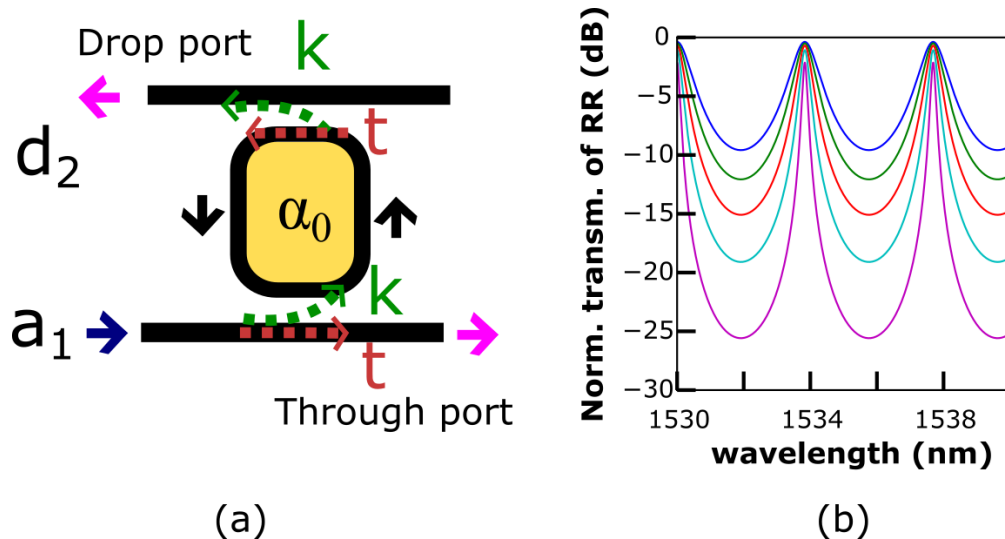


Figure 2.4: (a) Schematic of an add-drop ring resonator filter. (b) Transmission of the ring resonator filter for  $T$  varying from 0.5 (blue) to 0.9 (purple) by 0.1. The round trip loss  $\alpha_l$  is set to 0.97.

is given by:

$$\mathfrak{T}_d(\theta) = \left| \frac{d_2}{a_1} \right|^2 = \frac{(1-T)^2 \alpha_l}{1 + (T\alpha_l)^2 - 2T\alpha_l \cos \theta} \quad (2.1)$$

$\mathfrak{T}_d$  versus wavelength is plotted for different transmission coefficient  $T$  in fig. 2.4b. As  $T$  increases, the filter has a narrower transmission and higher contrast. At resonance we have  $\theta = 2\pi m$  where  $m$  is an integer. It means  $\cos \theta = 1$  in equation 2.1. From this expression we can deduce the transmission at resonance  $\mathfrak{T}_{max}$ :

$$\mathfrak{T}_{max} = \left| \frac{d_2}{a_1} \right|_{max}^2 = \frac{(1-T)^2 \alpha_l}{(1-T\alpha_l)^2} \quad (2.2)$$

In presence of losses  $\alpha_l$ , the transmission at resonance of an add-drop ring resonator filter  $\mathfrak{T}_{max}$  will decrease with  $T$ , leading to insertion losses.  $\mathfrak{T}_{max}$  versus transmission coefficient  $T$  is reported in fig. 2.5a in orange. Insertion losses increases rapidly for  $T \approx \alpha_l$ . It is thus very important to have low loss waveguides, bends and directional coupler for ring resonators. Fortunately, it is the case in the SOI platform. If  $Q_r$  is  $\frac{4T\alpha_l}{(1-T\alpha_l)^2}$  and if the Finesse  $F$  is defined as the FSR divided by the 3 dB bandwidth, we have:

$$\Delta\lambda_{3dB} = \frac{\lambda^2}{2\pi n_g L} \times \frac{4}{\sqrt{Q_R}} = \frac{FSR}{F} \quad (2.3)$$

$$F = \frac{\pi\sqrt{Q_R}}{2} = \frac{\pi\sqrt{T\alpha_l}}{1-T\alpha_l} \quad (2.4)$$

Finesse versus transmission coefficient  $T$  is displayed in fig. 2.5a in blue. The contrast  $C$  is defined by  $\frac{\mathfrak{T}_{max}}{\mathfrak{T}_{min}}$ . We have:

$$T\alpha_l = \frac{\sqrt{C} - 1}{\sqrt{C} + 1} \quad (2.5)$$

$T\alpha_l$  versus contrast is plotted on fig. 2.5b. This abacus helps to retrieve  $T\alpha_l$  from straightforward contrast measurements.

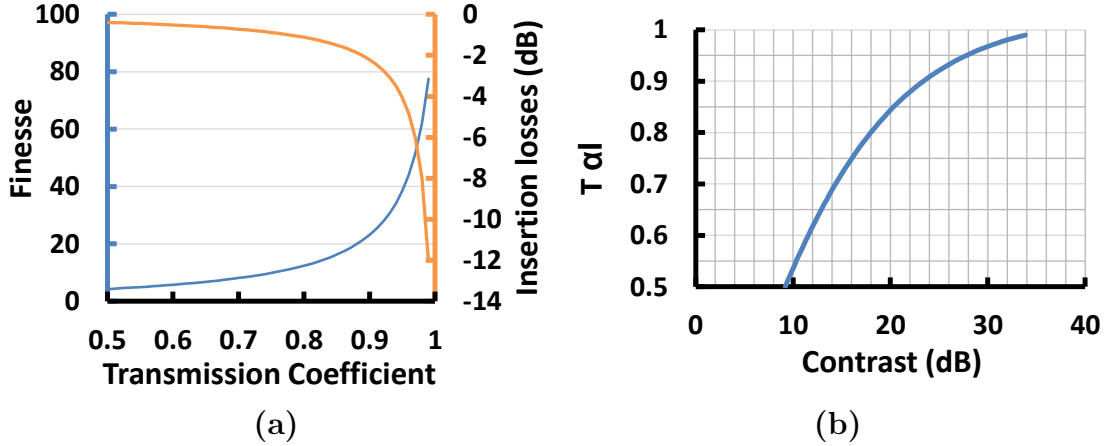


Figure 2.5: (a) Finesse versus transmission Coefficient (blue) and insertion loss versus transmission coefficient (orange). Calculated round trip loss  $\alpha_l$  is 0.97. (b) Transmission coefficient times round trip losses as a function of contrast.

### 2.1.3 Ring resonator based laser

#### Laser description

As described in fig. 2.6a, the laser cavity is shared between III-V and silicon. It is composed of a Bragg mirror in the back, the filter system, a III-V/Si transition, a 400  $\mu\text{m}$  long gain section, another III-V/Si transition and an output Bragg mirror. In the gain region, which stack structure is recalled in fig. 2.7, the confinement in the quantum wells is 10% (excluding barriers). After the front mirror, light is out-coupled by a focusing grating coupler (FGC) at the vertical of the chip. The laser can also be cleaved in the III-V region to minimize coupling losses. Light is then edge coupled with a lensed fibre. To obtain a single mode laser with a RR filter system, there are two design rules:

- The filter selects a single Fabry-Perot (FP) mode. This means that the 3 dB bandwidth of the filter must be around the FP cavity spacing  $\Delta\lambda_{FP} = \frac{\lambda^2}{2n_g L}$  where  $L$  is the cavity length and  $n_g$  the group index.
- The filter selects one FP mode on the 3 dB bandwidth of the gain medium ( $\approx 30$  nm), thus the filter free spectral range  $FSR_F$  must be greater than this value.

Those two rules are summarised in fig. 2.6b. In the following, I will show three different filter systems: the single RR, the RR and Mach Zehnder interferometer (MZI) and the double RR. The three filter systems are sketched in fig. 2.6cde. Those results complete the work of N. Girard [10].

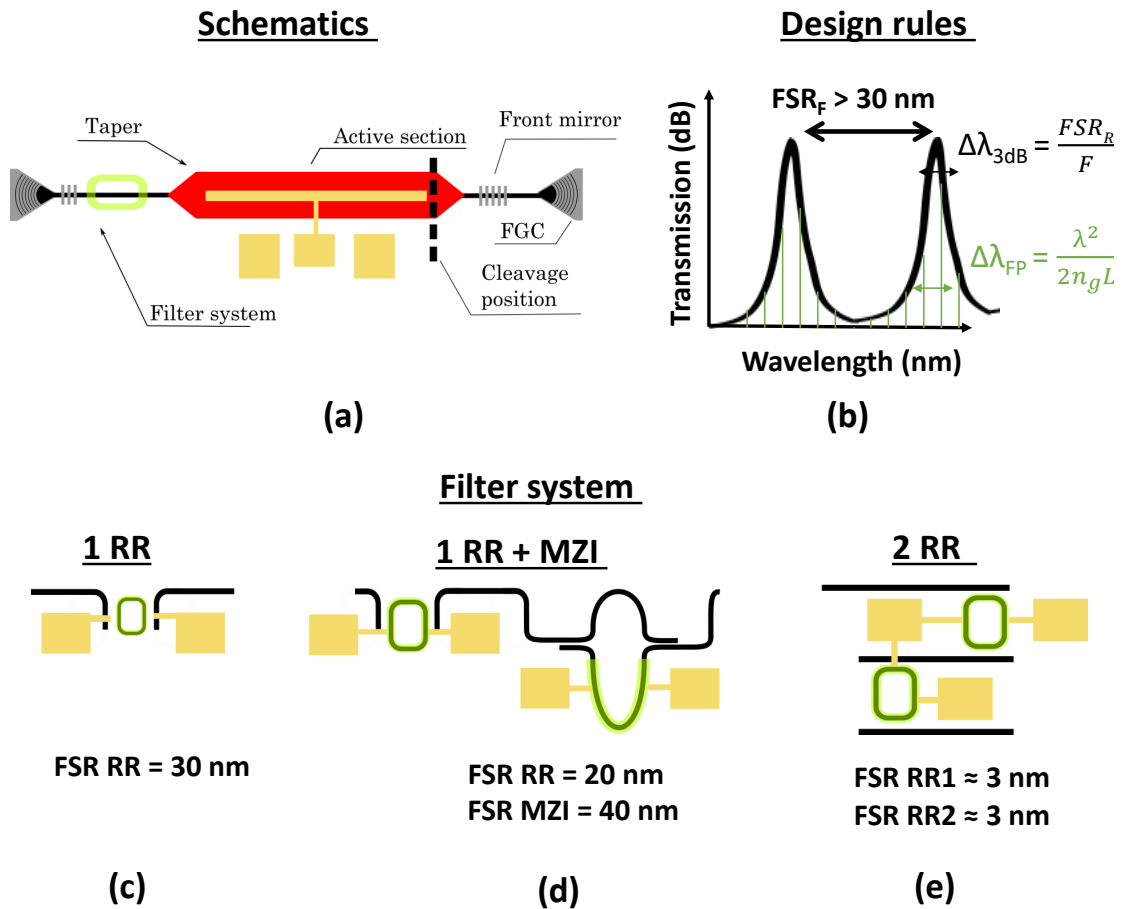


Figure 2.6: (a) Schematic of the hybrid III-V/Si tunable filter. (b) Tunable filter system design rules: its 3 dB bandwidth is at least equal to the Fabry Perot mode spacing. Filter FSR is equal to the material gain 3 dB bandwidth. (c) Single ring resonator filter. (d) Ring and Mach Zehnder interferometer. (e) dual ring resonator system.

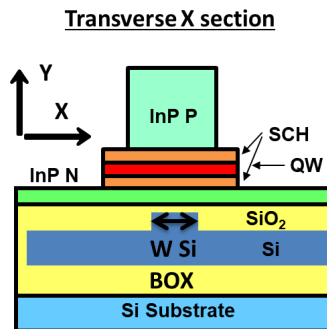


Figure 2.7: III-V on silicon gain region structure

## Single ring resonator laser

Using a single ring resonator provides a simple tuning mechanism: we only tune the heater on top of the RR to tune the wavelength. This filter is sketched on fig. 2.6c. As indicated by fig. 2.6b a single RR is not very favourable: its high  $FSR_F$  leads to high  $\Delta\lambda_{3dB}$ .

On our fabricated designs, we have a directional coupler transmission coefficient of 0.9 and a free spectral range of 30 nm, leading to a RR 3 dB bandwidth of 1.5 nm. The measured FP spacing is 0.25 nm, which is narrower than the filter 3 dB bandwidth.

The spectrum of such a laser is presented in fig. 2.8a and b. It shows side mode suppression ratio of 30-35 dB, limited by the Fabry-Perot mode competition. As calculated, the second RR peak is 30 nm away from the first peak and is well attenuated.

The tuning range is 8 nm, limited by the RR heater size: as it is small it is fragile and can't handle high current densities. When we try to modulate the current of such a laser, side mode suppression ratio decreases. Higher RR finesse could improve the RR SMSR. However, as indicated in fig. 2.5, a higher finesse means higher insertion losses which can prevent lasing at a reasonable bias current threshold.

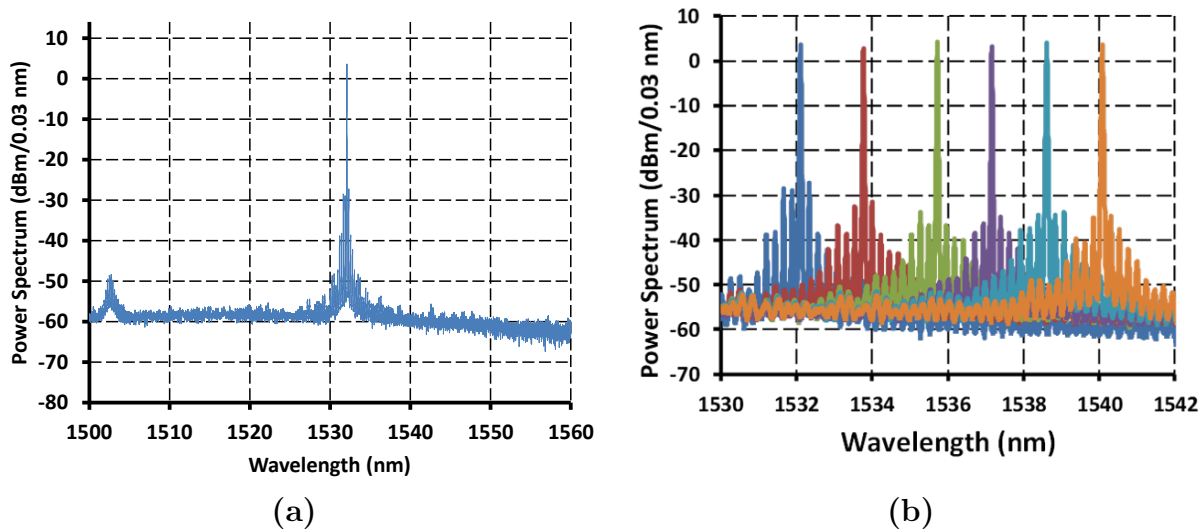


Figure 2.8: (a) Spectrum of a single RR tunable laser featuring a 30 dB SMSR. (b) Close up spectrum showing the FP mode competition and a 8 nm tuning range.

## Ring and Mach Zehnder interferometer laser

In this paragraph, I introduce a laser with the tuning simplicity of single ring resonator with better SMSR and tuning range. The filter is made of a ring resonator with 20 nm FSR

and a 40 nm FSR Mach-Zehnder interferometer, as sketched in fig. 2.6d. Since the ring resonator FSR is reduced by a factor 2/3 compared to single ring resonator, a better SMSR is expected. The MZI transmission can be tuned such that every other peak of the ring transmission spectrum is suppressed.

The effective free spectral range of the device is then 40 nm, leading to single mode operation of the device. Fig. 2.9 explains the tuning principle of such a device: first the MZI is adjusted to select one of the two ring resonances on the gain window (fig. 2.9a). Then a current  $I_{RR}$  is injected into the resistance above the RR to tune the device. As the MZI transmission has a smooth shape, only a coarse MZI tuning is needed. After a 20 nm tuning,  $I_{RR}$  is reset to zero and the MZI is switched to the second RR resonance (right peak in fig. 2.9b). Another 10 nm tuning range is achievable injecting current on the RR resistance. It is interesting to note that the tuning range covers the extended band of NG-PON2 access networks specified for upstream signals. This band ranges from 1524 to 1544 nm (see section 2.3). The total

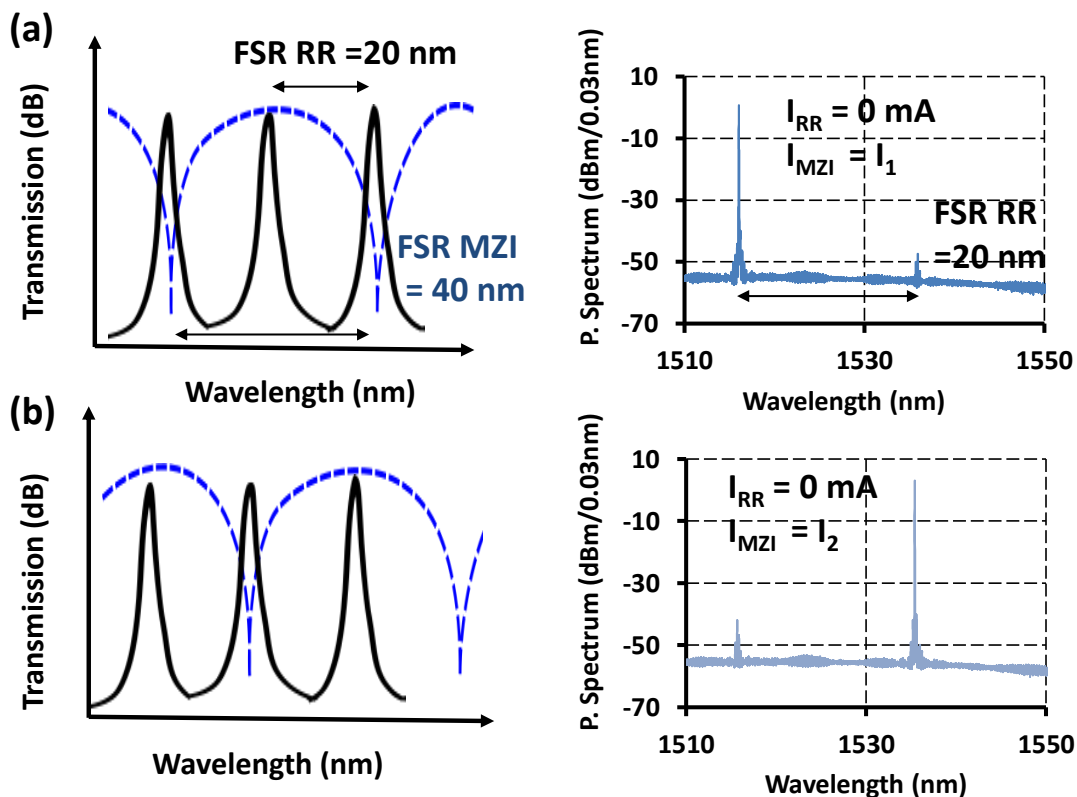


Figure 2.9: Operation principle of the RMZI laser (a): the MZI is set to select one wavelength on the gain spectrum. (b) The MZI is switched to select another RR peak separated by the RR FSR (20 nm).

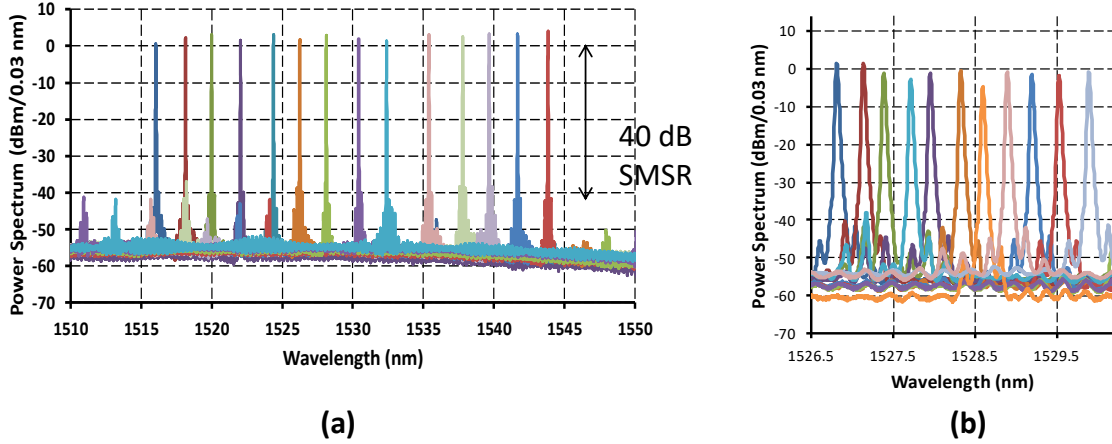


Figure 2.10: Spectrum of the RMZI laser featuring (a) wide tunability and (b) Fine tuning curves. The SMSR is equally limited by the FP competition and the second RR peak.

spectrum showing 30 nm tuning range is displayed on fig. 2.10.a, featuring a  $\text{SMSR} \geq 40$  dB, a 10 dB increase compared to the single ring resonator design.

Fig. 2.10b shows spectra for small changes in the RR heater. We can see a  $\approx 40$  GHz granularity corresponding to the cavity FSR. With such a device, quasi-continuous tuning can be achieved with a phase tuning control.

Advantages of this configuration are on the one hand the increase in filter finesse due to FSR reduction, and on the other hand a broader tunability with no increase in the control complexity. Other values of RR and MZI FSR will be investigated in a near future to increase SMSR and tuning range.

## Double Ring resonator laser

Lelievre et al. proposed in [11] a laser with two ring resonators in a Vernier configuration. The FSR of each RR is slightly different such that the two ring combs have only one coincidence in the gain window of the material. The filter is sketched in fig. 2.6e and operation principle of such a laser is presented in fig. 2.11. When we inject current on a resistor on top of the ring, we change the refractive index by thermo-optic effect. Its comb is shifted in the longer wavelength as  $\frac{dn_{Si}}{dT} > 0$ . If we tune the ring with the small FSR the coincidence wavelength is shifted in the longer wavelength, as in fig. 2.11b. The opposite yields for the ring with large FSR.

The joint FSR is given by:

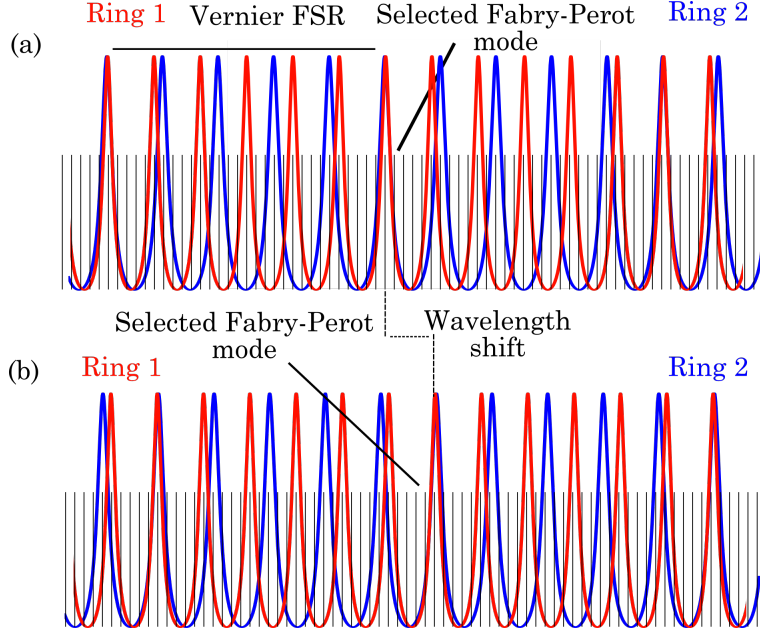


Figure 2.11: Operation principle of a double RR filter. Schematic (b) is after tuning the ring with the smaller FSR, thus having a new coincidence with a longer wavelength. Adapted from [7]

$$FSR_{\text{Vernier}} = \frac{FSR_{R1} \times FSR_{R2}}{FSR_{R1} - FSR_{R2}} \quad (2.6)$$

In the standard design, the two rings FSR are 3.2 and 3.44 nm (400 and 430 GHz) hence  $FSR_{\text{Vernier}}$  is 45 nm. The transmission coefficient  $T$  of directional couplers in the ring are 0.9. The corresponding resonator finesse is around 20. As described in equation 2.3,  $\Delta\lambda_{3dB} = \frac{FSR}{F} = \frac{400}{20} = 20$  GHz. As  $\Delta\lambda_{FP} = 30$  GHz the adjacent Fabry Perot modes are highly suppressed.

As we may cleave the laser in the III-V region, the filters are placed near the rear mirror, as sketched in fig. 2.6. Here, resonators are in a serial configuration. Parallel ring configurations were also tested and gave similar results.

Passive measurements of a single ring resonator is presented in fig. 2.12a. Maxima and minimum are extracted (red and green dots) to measure the transmission coefficient using equation 2.5. The value of  $T\alpha_l$ , (blue cross) is very close to the design value (green dashed line). The directional coupler has been optimized to have a very low wavelength dependence. Passive double ring measurements is presented in fig. 2.12b, featuring a Vernier FSR of 43 nm and a Vernier mode suppression of 5.8 dB. The spectrum of a double ring laser cavity is presented in fig. 2.13a for various currents injected in the heater. Laser side mode suppression ratio is better than 45 dB, with a very regular switching between the modes. With a RR

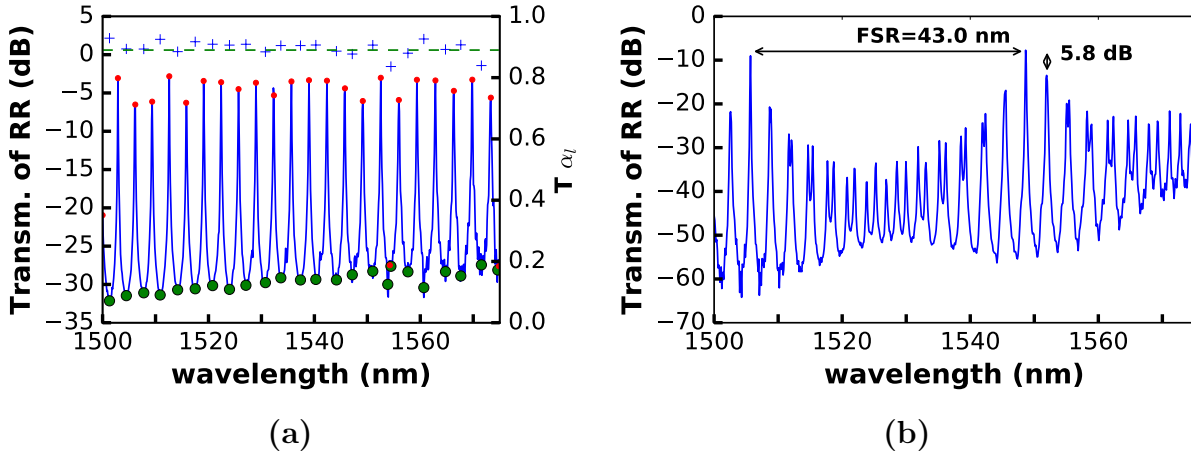


Figure 2.12: (a) Passive measurement of a single RR used in a double RR cavity. (b) measured spectrum of a double ring resonator laser. Measurements were performed on an automated wafer prober at Leti.

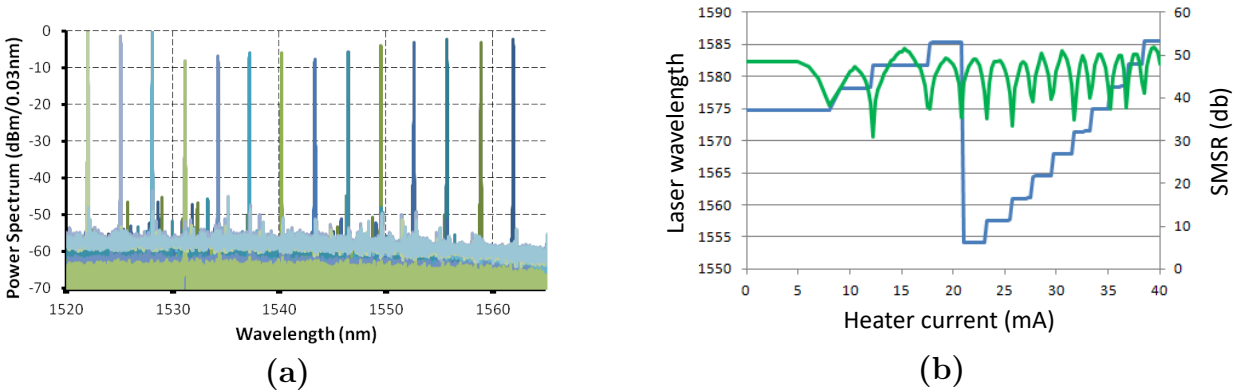


Figure 2.13: (a) Double RR laser spectrum for different current injected in one RR heater. (b) Double RR laser wavelength and SMSR for different current injected in the low FSR RR heater. SMSR is greater than 45 dB for all channels. (a) and (b) are for two different lasers.

based design, it is possible to go beyond a 45 nm tunability. In equation 2.6, if the FSRs of the two rings are increased and their spectral difference decreased, a 120 nm Vernier FSR can be obtained. Experimentally the tuning range is limited by the gain material: a record 95 nm tuning range has been recently obtained [12].

### Filter system comparison

To conclude, single RR lasers performances are limited due to FSR and filter 3 dB bandwidth trade-off. RR+MZI is a convenient solution as it offers simple fine tuning mechanism, a

good tuning range of 30 nm and a SMSR of 40 dB. However, double RR lasers have better performances, especially when full C band laser is required. To obtain the wavelength allocation table, several controls are needed: temperature, gain section bias current, RR/MZI heaters and phase heater. Those considerations are summed up in table 2.1.

Filter config.	SMSR (dB)	Tun. range	N. control	Tun. complexity
1R	30	8	4	+
1R + MZI	40	30	5	++
2 RR	40-50	45-95[12]	5	+++

Table 2.1: Comparison of filter systems for III-V/Si tunable lasers

### 2.1.4 Laser output power optimization

The Optical Internetworking Forum (OIF) has defined a standard for tunable lasers, the integrated-tunable-laser-assembly (ITLA) multi-source agreement. The power specifications are 10 or 20 mW coupled in the fiber over product lifetime. III-V on silicon lasers have demonstrated a reasonable output power of more than 4 mW with a reasonable current threshold since their demonstration [13].

However, the III-V technology process in the III-V on silicon platform is not as mature as the pure III-V one. At III-V lab in 2015, the CW output power was 16 mW for hybrid Fabry-Pérot lasers and around 12 mW for tunable lasers [14], measured in a large area photodiode. To reach this power level, lasers are cleaved in the III-V region: indeed, it is not yet possible to get optimized fiber grating coupler or edge coupler in the technology process for the moment. If the component is cleaved, the facet acts as a Fresnel mirror with a  $\approx 30\%$

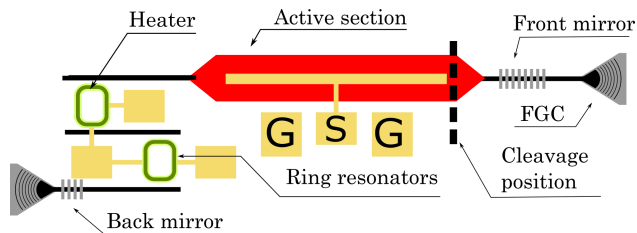


Figure 2.14: Schematic of the double RR laser design. Output is either a Fiber grating coupler or the cleaved gain section.

reflectivity. In the following paragraph, I will show how an AR coating can increase the collected power. First the external quantum efficiency is proportional to  $\frac{\alpha_m}{\alpha_0 + \alpha_m}$ , where  $\alpha_0$  is the internal loss and  $\alpha_m = \frac{1}{2L} \ln\left(\frac{1}{R_1 R_2}\right)$  is the mirror losses. Increasing mirror losses will

increase the external efficiency. Secondly as the two mirrors coefficients are different the power distribution in the cavity is asymmetric.

### Power distribution in the cavity

In this section, I will make a qualitative analysis with a simple Fabry Perot laser and assume that similar results would be obtained for tunable lasers.

In a laser, the photon density is the sum of a propagating wave  $S^+(z) = S^+(0) \exp(g_{net}z)$  and a contra-propagating wave  $S^-(z) = S^-(0) \exp(-g_{net}z)$ . If both facets have equal reflectivity  $R$ , the field is maximum at the facet and minimum in the centre, as shown in fig. 2.15. We use the value just before the right mirror to normalize the power. The output power is  $\frac{1-R}{1+R}$  times the value just before the mirror.

An asymmetry of the mirror reflectivity creates an asymmetry in the power distribution in the cavity. If there is a 100 % reflectivity in the back mirror then there is a power minimum near this interface. It can be understood as a folding of the symmetric cavity. If we reduce the front mirror reflectivity  $g_{net}$  increases. The asymmetry increases accordingly and more power is collected at the front facet. The efficiency increase is at the cost of a threshold current increase. The L-I curve of a RR+MZI based laser is plotted in fig. 2.16 for a cleaved front facet laser and a laser with a 2% anti reflection (AR) coating on its front facet. Up to 21 mW of power from the facet is obtained for the 2% AR laser, to be compared with the 14 mW obtained for the cleaved laser. Slope efficiency evolves from 0.06 to 0.12, a 2x improvement. As expected, the AR laser has a higher threshold of 40 mA, compared to the 25 mA for the cleaved case.

As described in fig. 2.16, the fiber coupling losses is around 3 dB. It can be reduced to 2 dB using coupling lenses. Fibre coupling depends on the mode size and shape. As it depends on the cleavage position it may not be highly reproducible. Implementation of low loss edge couplers will decrease fiber coupling loss in the future [15].

A series resistor of nearly  $9 \Omega$  is extracted from fig.2.16, a significantly higher value than buried heterostructure lasers which is as low as  $2 \Omega$  [16]. The series resistor leads to self heating which degrades the output power at high bias current.

To obtain 20 mW in the fiber over laser lifetime, the power collected in a large photodiode should be over 50 mW. This value could be obtained by further improving the cavity design, especially optimizing the gain length and the confinement in the III-V region. A semiconductor optical amplifier is also a simple solution to enhance output power.

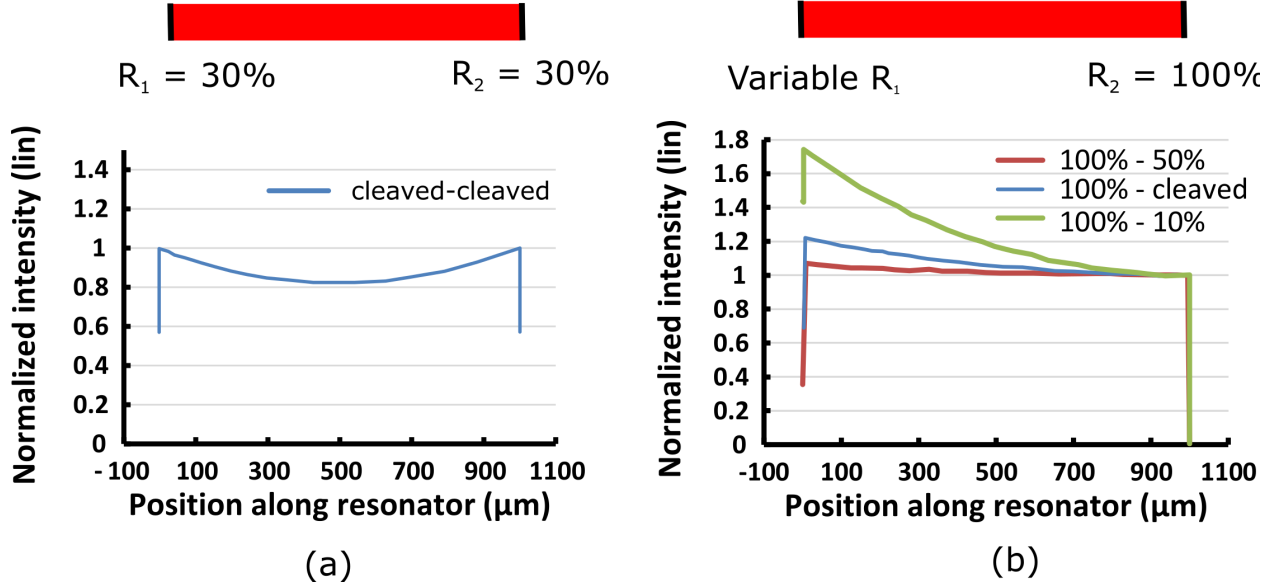


Figure 2.15: Power distribution in the cavity for (a) a Fabry-Perot laser cleaved at both sides. (b) a laser with a 100 % coating on the right side and a 50%, 33% (cleaved) and 10% on the other side. The power is normalized at the right side (100% mirror), inside the laser cavity. The left facet output power is  $\frac{1-R}{1+R}$  times the value inside the laser.

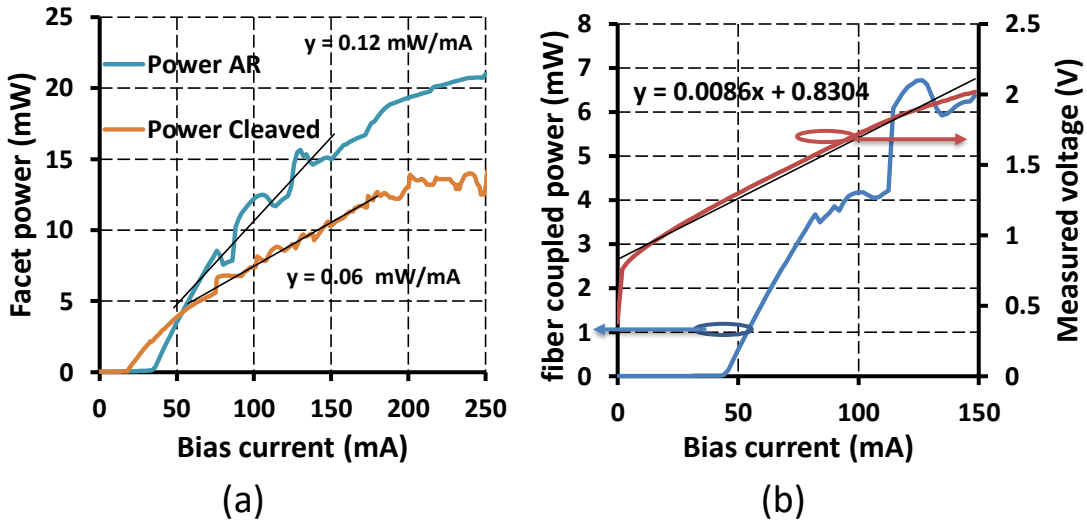


Figure 2.16: (a) L-I curve for the cleaved and AR facet case. A 1.5x output power improvement at 200 mA is obtained. (b) Fiber coupled output power, with more than 6 mW at 120 mA. Efficiency are near the values of pure III-V DBR lasers fabricated at 3-5 lab [4], p218.

### 2.1.5 Integration of semiconductor optical amplifiers

To increase the output power, semiconductor optical amplifiers (SOA) are a simple and robust solution as both a high gain and a high output power are possible [17]. A SOA is a gain section of length  $L$  and gain per unit length  $g_0$  placed outside the laser cavity.

Its integration with laser doesn't add any complexity in the technology process as it uses the same gain material. If too many photons enter the SOA, there is not enough electron recombination to provide gain. Hence the gain  $g_0$  is divided by  $1 + \frac{P(z)}{P_s}$ , where  $P_s$  is the input saturation power. Neglecting internal losses, the amplification equation on an infinitesimal length  $dz$  is:

$$P(z + dz) = P(z) + \frac{g_0 dz}{1 + \frac{P(z)}{P_s}} \times P(z) \quad (2.7)$$

The amplification equation is thus:

$$\frac{dP(z)}{dz} = \frac{g_0}{1 + \frac{P(z)}{P_s}} \times P(z) \quad (2.8)$$

If  $P(z) \ll P_s$  for all  $z$ , we can write

$$\frac{dP(z)}{dz} = g_0 \times P(z) \quad (2.9)$$

and  $P(z) = P(0) \exp(g_0 z)$  The unsaturated gain  $G_L = \exp(g_0 L)$  is the gain for an SOA of length  $L$  in this regime. For the saturated regime I integrated equation 2.8 over length  $L$  and solved it using a simple numerical root finding procedure.

The gain versus  $P_{in}/P_s$  is presented in figure 2.18 for unsaturated gain of 10, 20 and 30 dB. To design a SOA, both small signal gain and saturation power are of great importance. The small signal gain increase with a higher confinement in the active region but the saturation power decreases. There is thus a trade off relation between those two quantities.

### Experimental results and outlook

The schematic of the integrated tunable laser and SOA is presented in fig. 2.18a. To avoid spurious reflections from the facet, the SOA waveguide is tilted. After the cleavage, an anti-reflection coating is applied on the front facet. The L-I for different SOA bias currents  $I_{SOA}$  is presented on fig. 2.18b. When  $I_{SOA}$  increases from 20 to 120 mA power increases as both gain and saturation power increase with current.

When the laser bias current evolves from 100 to 200 mA, the power doesn't increase very

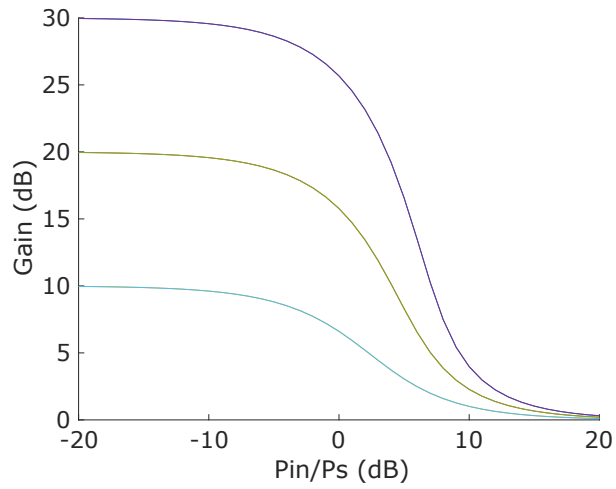


Figure 2.17: Calculated gain versus  $P_{in}$  over  $P_s$  for unsaturated gain of 10 (blue), 20 (green) and 30 dB (purple).

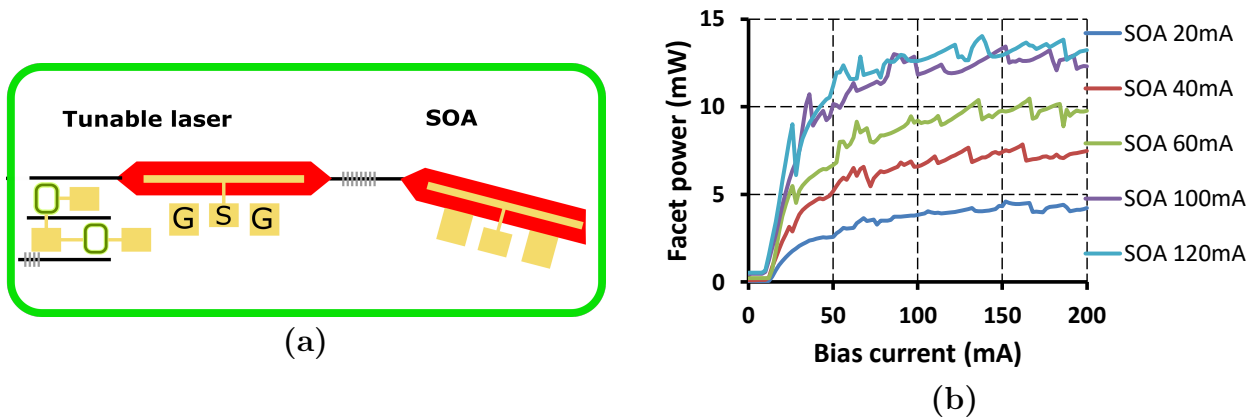


Figure 2.18: (a) Schematic of a tunable laser integrated with SOA. (b) L-I curve for different bias current in the SOA. As the transparency current is around 25 mA, we can assume that the laser emits 5 mW. As the the maximum output power at 100 mA is 14 mW, we can estimate a gain of 4.5 dB.

much : the SOA is saturated. We can extract a limited gain of 4.5 dB at a SOA bias current of 100 mA. If this current increases over 100 mA, undesirable lasing effect occurs in the SOA section due to imperfect coating on the facet.

In the design presented here, the mode quantum well overlap  $\Gamma$  is similar in the laser and in the SOA (10%). As described in [17],  $P_s \simeq \frac{A}{\Gamma}$  with  $A$  the quantum well cross section that overlaps the optical mode. Designs with increased  $A$  and lower  $\Gamma$  may have higher output power and should be implemented in future fabrication runs. They are only preliminary published results on III-V on silicon SOAs. At III-V lab, we reported a III-V/SOI SOA with an unsaturated gain of 28 dB and output saturation power of 9 dBm [18]. A more complete study announced a saturation power around 16 dBm in the C band [19]. However, this value is extrapolated from the two facet power of a Fabry-Perot laser and not directly measured. A more recent demonstration shows waveguide output power of 16 dBm with 10 dB of gain in the O band by Intel [20].

## 2.2 Advanced double ring resonator designs

Based on the double ring resonator laser, I will investigate two new designs. A first one aims at reducing linewidth for coherent transmissions, and a second one targets high speed tuning. Linewidth of tunable laser is of great importance for coherent communications. A way to reduce tunable laser linewidth is presented in the first part of this section. As explained in [21], the tuning speed of heater based RR are around 10  $\mu$ s. This value needs to be lowered to the 50 ns range to be used in wavelength packet switching networks. In the second part of this section, I present a component with a high tuning speed of 1.5 ns.

### 2.2.1 Low linewidth tunable lasers

#### Linewidth requirements

As explained in the first chapter, long haul and metropolitan systems use coherent modulation schemes, where phase noise degrades performances. Linewidth requirements are described in [22]. They depend on the symbol rate, modulation format and forward error correction threshold. For transcontinental communications, large chromatic dispersion compensation also introduces non negligible phase to amplitude noise conversion [23]. Laser linewidth requirements for this application are thus lower. In commercial products, linewidth below 100 kHz are used [24]. Those values are well below the requirements of [22] to have a

negligible impact on performances. To obtain such a linewidth, external cavity lasers with free space grating are generally used [25]. Linewidth of integrated lasers have dropped very recently up to 70 kHz [5] and can now compete with external cavity lasers.

The first generation of III-V/Si double RR lasers had linewidths of 2.3 MHz ([26], p133). In the following section, I will explain one way to design a low linewidth tunable laser.

## Low noise designs

To reduce the spectral linewidth, we may introduce an optical feedback to reduce the linewidth [27]. However, decreasing the intrinsic linewidth of the laser is more desirable. According to Henry's formula [28], laser linewidth is proportional to  $\frac{g\alpha_m}{P_0}$ , where  $\alpha_m$  is the mirror loss,  $P_0$  is the facet output power and  $g = \alpha_{int} + \alpha_m$  is the total loss.

In a hybrid cavity, if  $R_1$  and  $R_2$  are the mirror reflectivity coefficients the loss coefficients are:

$$\begin{cases} \alpha_{int} = \frac{\alpha_{passive}L_{passive} + \alpha_{active}L_{active}}{L_{passive} + L_{active}} \\ \alpha_m = \frac{1}{2(L_{passive} + L_{active})} \log\left(\frac{1}{R_1 R_2}\right) \end{cases} \quad (2.10)$$

$\alpha_{active}$  is dominated by inter-valence band absorption in the p doped region. Induced loss coefficient is  $\alpha_{InPp} = \Gamma_{InPp} \times 88$  dB/cm [29]. As  $\Gamma_{InPp} \approx 30\%$ ,  $\alpha_{active} \approx 26$  dB/cm. As  $\alpha_{passive} \approx 2$  dB/cm, loss coefficient of the passive section is well below the active one. It is thus possible to reduce the internal and mirror losses by increasing the passive cavity length. As the loss per unit length of silicon waveguide is low, threshold current won't degrade much. However, as the cavity length increases, Fabry-Perot spacing gets tighter. We thus need to reduce the 3 dB width of the RR transmission. This might increase the RR insertion losses due to a higher finesse (see equ. 2.2).

This means that there is an optimal design that trade off RR and cavity losses. As presented in fig. 2.19, cavity length is increased with a waveguide coil. Different ring resonator finesse and waveguide coil length will be implemented in a fabrication run.

This "long cavity" design has been already demonstrated using assembled reflective SOA and planar lightwave circuit in [30], achieving a linewidth of 2 kHz.

## 2.2.2 Fast tunable laser

New metropolitan networks use the wavelength dimension to switch and route packets [31]. A wavelength tunable laser that switches its output frequency in the nanosecond time-scale is needed, as wavelength needs to be switched in the 100 ns guard band of optical packets.

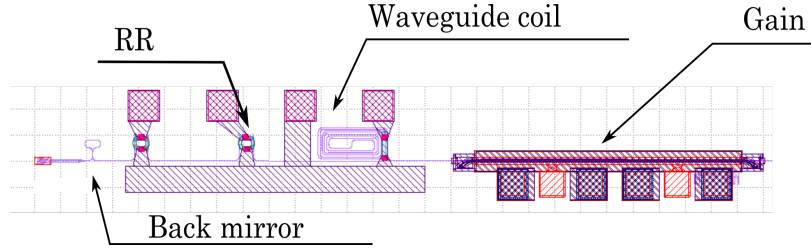


Figure 2.19: Mask layout of a long cavity laser.

Now, thermal tuning has switching times in the  $\mu\text{s}$  time scale. Fast tuning can be achieved by replacing passive RR with heater with carrier injection in ring PIN junctions. Details about this mechanism can be found in [4].

Such components are already available in the monolithic InP platform. For example, a sampled grating distributed Bragg reflector laser [32] with PIN junction with switching time around 6 ns has been reported. RR based tunable laser are also interesting architectures. We introduce here a III-V/Si hybrid laser with 45 nm tuning range and fast tunability.

### Ring P-I-N junctions filters

As in the previous sections, two rings resonators in a Vernier configuration are used (fig. 2.20a). As carriers are injected in the PIN junction, both free carrier absorption and plasma dispersion effect (PDE) [33] reduce the waveguide refractive index. The 3D view and the cross section of the RR PIN are sketched in fig. 2.20b and c.

In this design, the ring is made of rib waveguides as it is highly preferable for biasing the PIN structure. The PIN junction provides a refractive index change  $\Delta n \approx -n_f \Delta N$  with a  $n_f$  value of  $2. \times 10^{-21} \text{ cm}^3$  for an injection of  $\Delta N$  carrier density in the range of  $10^{18} \text{ cm}^{-3}$  [34].

The electrical bandwidth of a forward biased silicon PIN junction is in the GHz range, leading to ns tuning speed. The RR transmission spectrum is plotted in fig. 2.20d. We measured a finesse of both RRs greater than 9.

This value is half the value for ring resonator made with strip waveguide because presented in the first section. Finesse depends on the directional coupler transmission coefficient  $T$ . Here it is well below the targeted value of 0.9 due to fabrication/conception errors.

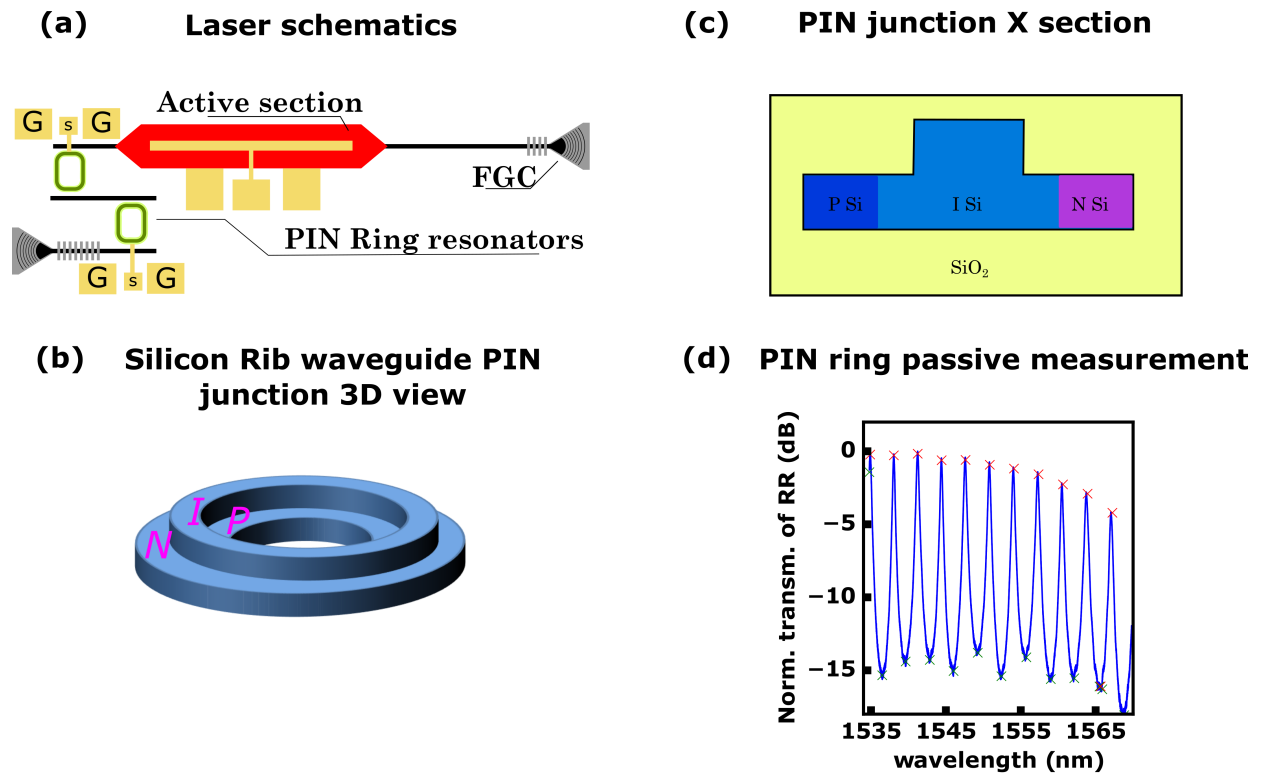


Figure 2.20: (a) Top view schematics of the laser. (b) 3D view of the P-I-N ring resonator junction. (c) Cross section. (d) Passive measurement of a RR, showing a finesse of 9.

## Optical characteristics

Laser optical characteristics at 20°C are shown on fig. 2.21. The L-I curve shows a threshold of 52mA, and a fiber coupled power greater than 1.7 mW for a 160 mA bias current. Spectra for different voltages applied on one RR PIN junction are displayed in fig. 2.21b, for a 100 mA bias applied on the gain medium.

In this device the tuning mechanism is the change of refractive index as carriers are injected in the junction. The effective index change lead to a RR transmission shift, exactly as in thermally tunable RR based laser. The tuning range is 45 nm, limited by the Vernier filter comb. For every operating point we measure a SMSR greater than 40 dB. Output power is lowered for higher wavelength because the vertical grating coupler transmission is centered around 1540 nm and has additional losses for wavelength in the 1570-1590 nm range. I

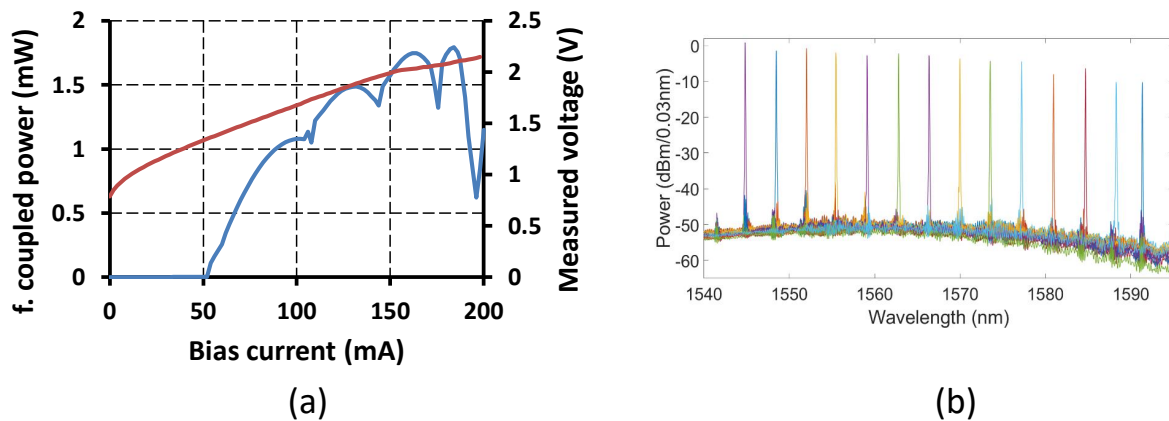


Figure 2.21: (a) L-I-V curve of the device. The device shows 1.8 mW fiber coupled power. (b) Spectrum of the device for different injected currents in the junction showing 45 nm tunability.

characterized the laser linewidth by measuring the power spectral density (PSD) of laser frequency noise, as presented in chapter 4. A linewidth under 400 kHz for a 110 mA current is obtained, below the requirements for coherent applications [22].

## Fast switching demonstration

Switching dynamics is characterised with the setup presented in fig. 2.22. When a square signal at 200 MHz is applied with a 1 V peak to peak voltage on one RR, the laser spectrum hops between two wavelengths of the vernier comb. For this design they are 400 GHz apart as it is the FSR of the considered RR.

We used an external narrow band pass optical filter to convert the frequency switching to an amplitude modulation. The OSA spectrum is displayed on fig. 2.23a for a filter centered on  $\lambda_1$  (1551.9 nm) in red and the blue curve when the filter is centered on  $\lambda_2$  (1548.5 nm). When the filtered is centered on  $\lambda_1$ ,  $\lambda_2$  is attenuated by 20 dB as sketched in fig. 2.23. After the band pass filter, the signal is detected by a fast photodiode. We observe the output signal on a sampling oscilloscope. The recorded signal is plotted in fig. 2.23b. As in fig. 2.23a the red (blue) curve is obtained when the optical filter is centered on  $\lambda_1$  ( $\lambda_2$ ). With those two curves, we can conclude on a fast switching dynamics. Rise and fall time are below 1.5 ns. This represents a great improvement as thermal tuning only offer  $\mu s$  tuning speed [21]. As thermal effects may disturb the fast switching dynamics, a closer look on long term wavelength stability is needed. System experiments are planned with those devices.

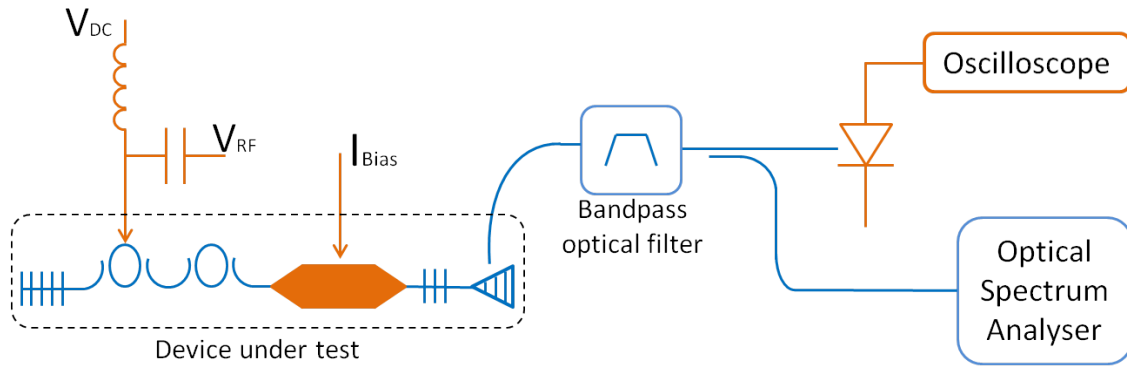


Figure 2.22: Schematic of the switching experiment. After the fiber coupling a band pass filter is inserted. The signal is then detected and measured on a sampling scope or displayed on an OSA.

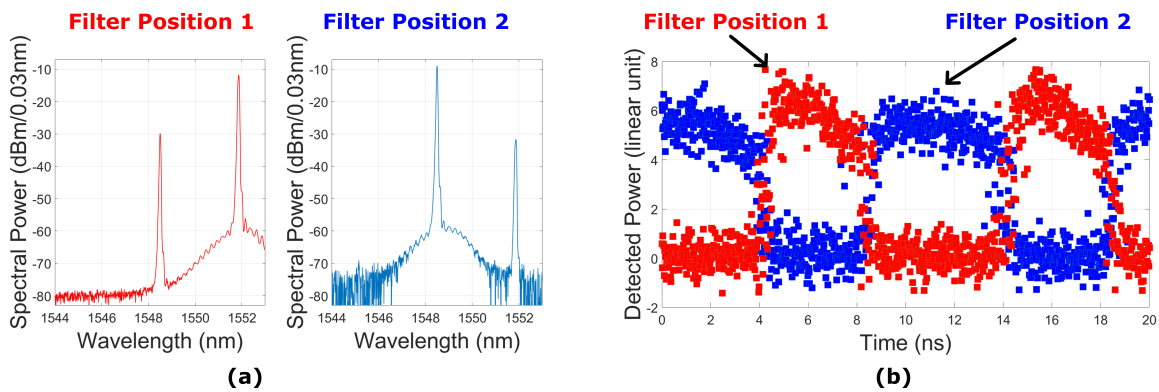


Figure 2.23: (a) Spectrum of the device for the filter centered on  $\lambda_1$  (red curve) and for the filter centered on  $\lambda_2$  (blue curve). (b) Superimposed traces recorded on the sampling scope. The red curve corresponds to the filter centered on  $\lambda_1$  and the blue one on  $\lambda_2$

## 2.3 Tunable lasers in optical access network

### 2.3.1 Introduction to passive optical networks.

Access network provides the end user with a fixed internet connection. Nowadays, fiber to the home (FTTH) is the preferred broadband technology in most countries. The French government set up a 20 billion Euro plan to have 80% of French houses connected to FTTH by 2022. In access, operators use a point to multi-point technology.

In this scheme, illustrated in fig. 2.24, the optical line terminal (OLT) is the emitter/receiver at the central office and the Optical Network Unit (ONU) is the emitter/receiver in the subscriber's premises. The optical distribution network (ODN) is the fiber distribution tree between both. Its splitting ratio, ie the number of ONU per OLT, is usually 1:32 (15 dB loss) or 1:64 (18 dB loss). The standardized distance between ONU and OLT is 20 or 40 km. The technology is called passive optical network (PON) because there is usually no amplification nor dispersion compensation between ONU and OLT. The high PON therefore requires a high power budget of 20-40 dB.

To meet the budget requirements access systems use relatively high power emitters and very sensitive receivers such as avalanche photodiodes. The receiver sensitivity is enhanced by a forward error correction code (FEC). With the FEC code used in access, a pre-FEC bit error rate (BER) of  $10^{-3}$  is sufficient to obtain error free operation.

Pre-FEC back to back (b2b) sensitivity is defined as the power on the receiver for BER =  $10^{-3}$  when the emitter is directly connected to the receiver. Transmission penalty is the difference between sensitivity back to back and after transmission. The power budget PB is defined as:

$$PB = \text{Modulated fiber coupled power} - \text{Pre-FEC b2b sensitivity} - \text{transmission penalty}$$

The client to network direction is named upstream (US) while the network to client direction is named downstream (DS). Depending on direction and standard, 1.3 or 1.5  $\mu\text{m}$  components are used, as sketched in fig. 2.24b. Directly modulated lasers (DML) have the lowest cost and higher power. However, they have limited extinction ratio and are sensitive to dispersion for DML around 1.5  $\mu\text{m}$ . For this reason electro absorption modulated lasers are used when DML performances are not sufficient.

As we will see in the next section, NG-PON 2 introduces C and L band wavelength division multiplexing in access networks.

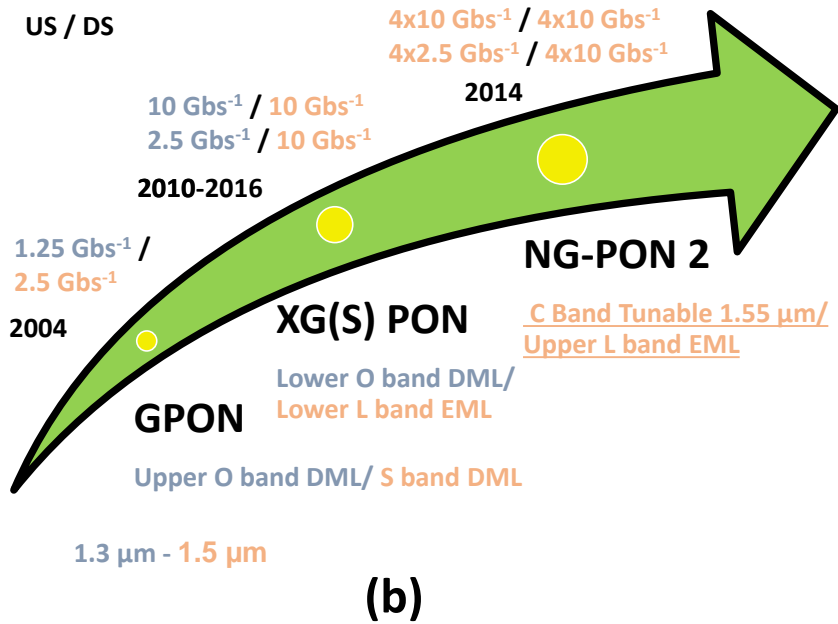
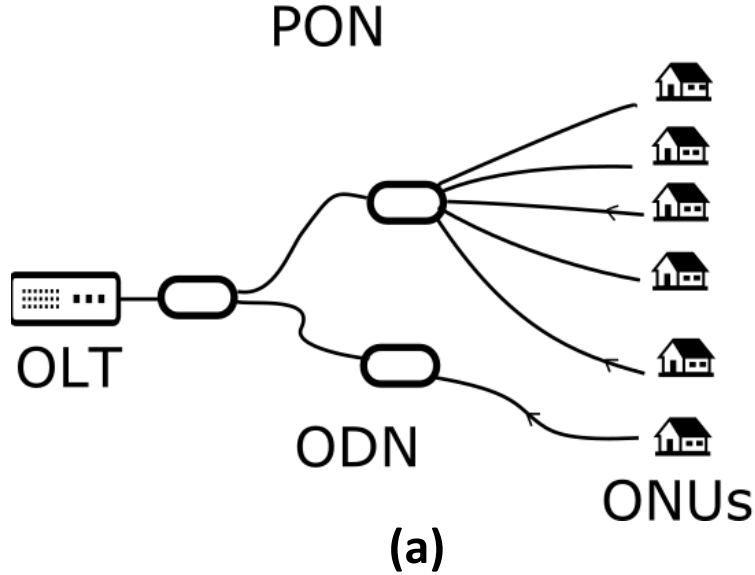


Figure 2.24: (a) Schematic of a PON network featuring the Optical line terminal (OLT) at the central office, the optical distribution network (ODN) and the Optical Network Units (ONUs) in the subscriber premises. (b) Evolution of the last three ITU-T access networks. The upper part features the upstream/downstream data rates. The lower part features the emitter used at the ONU/OLT : directly modulated lasers (DML) or Electro-absorption modulated laser (EML) and their wavelength band.

### 2.3.2 NG-PON2 Standard

In 2014, ITU-T standardized the time and wavelength division multiplexing (TWDM) technology NG-PON 2. It uses four or eight wavelengths around 1530 nm for upstream and four or eight channels wavelength for downstream. Upstream channels can be chosen in the narrow (1532-1540 nm), extended (1528-1540 nm) or large (1524-1544 nm) bands. The channel spacing is 50, 100 or 200 GHz, as in dense WDM metropolitan systems. C and L band multiplexers manufactured in volume for those systems are used. NGPON2 may serve different clients: home, offices and antennas on the same ODN.

In the standard, there is also a point to point scenario (PtP WDM), where each client is linked to a single OLT. A schematic of a NG-PON2 system is described in fig. 2.25.

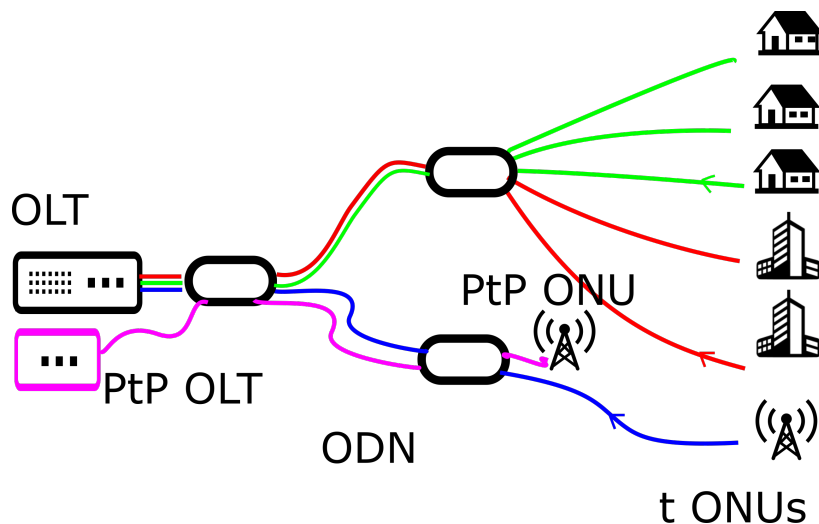


Figure 2.25: NG-PON2 TWDM-PON and PtP WDM technologies. Only three upstream channel and 1 upstream PtP WDM wavelengths have been represented.

#### ONU emitter specifications and available solutions

The specifications for NG-PON 2 are presented on table 2.2. In NG-PON2, the FEC allows to have a bit error rate of  $10^{-3}$  for 9.95 Gb/s and  $10^{-4}$  for 2.48 Gb/s.

The standardized power budget is 29, 31, 33 and 35 dB. This high value is needed to compensate for the 20 km fibre span, the dispersion penalty, the splitting ratio and filter losses. Due to fibre chromatic dispersion in C band, distributed feedback DMLs can hardly reach distances beyond 10 km. Indeed, adiabatic and transient chirp of distributed feedback DML limit the reach. We will analyse this phenomenon in more details in chapter 3.

Available solutions are electro-absorption modulated laser (EML) with thermally tuned distributed feedback lasers [35] or directly modulated distributed Bragg reflector (DBR) laser [36]. DBR lasers have a wider tuning range than EML. However, the high cost of DBR may prevent their use in access networks. III-V on silicon tunable lasers may also be attractive for such application.

As we will see in the following a specific problem arise in TWDM-PON: the frequency drift in burst mode operation.

Optical Budget class name	N1	N2	E1	E2	Units
Optical Budget	29	31	33	35	dB
Downstream/Upstream datarate (per channel)		9.95/2.48 or 9.95/9.95 or 2.48/2.48			Gb/s
Downstream Channel wavelengths		1596-1603			nm
Upstream Channel wavelength	1524-1544 or 1528-1540 or 1532-1540				nm
Channel spacing		50 or 100 or 200			GHz
OLT Power (min-max)-2.5 Gb/s ONU	0-4	2-6	4-8	6-10	dBm
OLT Power (min-max)-10 Gb/s ONU	3-7	5-9	7-11	9-11	
ONU emission power		4-9			dBm
Splitting ratio		1 : 64			S.U.
Reach		20 or 40			km
Number of channel		4 to 8			S.U.

Table 2.2: NG-PON2 standard requirements, table from [37]

## Introduction to burst mode

In time and wavelength division multiplexing PON (TWDM-PON), each ONU emitter only send data during a specific time slot, a fraction of a 125  $\mu$ s long packet, as sketched in fig. 2.26a. This fraction is adjusted every 125  $\mu$ s depending on the client need (fig. 2.26b). The TDM scheme is well suited for access networks as users may not use their connection at the same time.

When one ONU sends data, the emitted power of other ONUs needs to be efficiently suppressed to avoid crosstalk in the receiver. In a semiconductor laser, the simplest way to decrease the power is to switch off the bias current.

But when the laser is switched on again, there is a temperature increase in the chip due to the finite series resistor of the laser. This temperature increase depends on the burst length  $\Delta t$ , as sketched in fig. 2.26c. When the laser thermalizes, its wavelength shifts to longer wavelengths as III-V materials have a positive thermo-optic coefficient. Thermalisation has



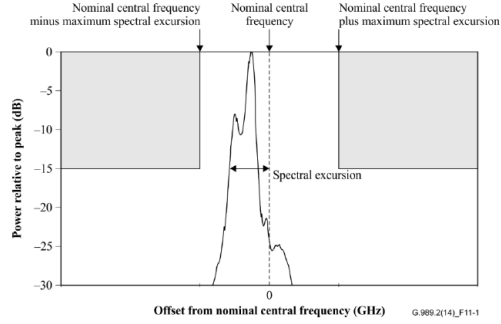


Figure 2.27: NGPON2 Wavelength drift specification, from [38]. The total window size is  $2\Delta f_{max} = 40$  GHz for 100 GHz spacing or  $2\Delta f_{max} = 25$  GHz for 50 GHz

### 2.3.3 Tunable laser DML

Hybrid III-V/SOI lasers are attractive solutions for NG-PON2 standard. With a widely tunable laser, any of the desired wavelengths of the narrow, wide or extended band of the standard, with any of the different channel spacing can be obtained. As it may have long passive sections, their chirp is reduced, as explained in Coldren et al. [40]. The chirp may also be reduced due to the ring resonator transfer function, as described by Duan et al. [41]. As explained in section 2.1.3, the tunable laser developed here uses 400 and 430 GHz FSR ring resonators. To finely tune the laser on the 100 GHz spaced grid, we need to adjust the two RR heaters and the phase section. The following section will show the direct modulation results of this laser.

#### Direct modulation of Tunable laser

After carefully selecting the chip, the laser has been mounted on a butterfly package. BER and eye diagrams are measured with the bench described in fig. 2.28. A pseudo random bit sequence (PRBS) generator creates a determined sequence of bits. This electrical signal is mixed with the laser bias current with a bias tee. A switch selects either the eye diagram or bit error rate measurements. For eye diagram measurement, the signal is detected by a photodiode and the electrical signal is displayed on a sampling scope. The signal has an "eye" shape defined by '1'  $\rightarrow$  '0' and '0'  $\rightarrow$  '1' bit transitions. The extinction ratio (ER) is the ratio of power of '1'bits over power of '0' bit. A minimal ER of 6 dB is required for NGPON2 upstream transmissions at 10 Gb/s [38]. BER measurements are done with an Anritsu error counter which compares the detected signal with the PRBS sequence. BER is measured as a function of the received signal, set by a variable attenuator before the receiver,

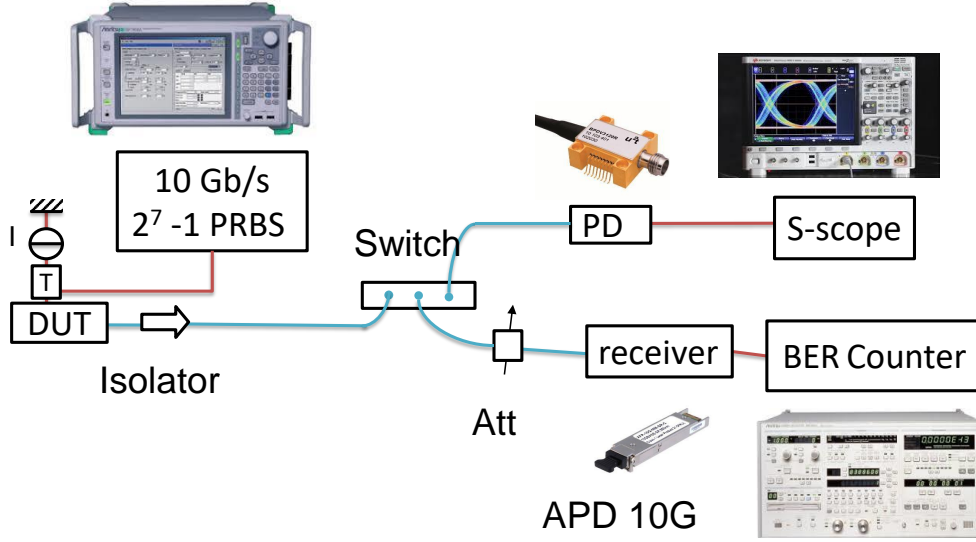


Figure 2.28: Bit error rate measurement setup.

a high sensitivity avalanche photodiode.

First direct modulation results were obtained in [14] and are reproduced in fig. 2.29. The BER at 10 Gb/s for 10 channels with a 100 GHz spacing is presented on fig. 2.29 for back to back (red) and after 25 km (blue). In those measurements a  $2^7 - 1$  PRBS length is used. Higher PRBS sequence lengths introduce error floors around  $\text{BER} = 1\text{E-}5$  but no degradation of the  $\text{BER} = 1\text{E-}3$  sensitivity. As III-V/Si laser has a 20 km reach with very limited penalty, it may be used for NG-PON2 access.

However, this module was not compliant with burst mode operation due to mode hops. This phenomenon is analysed in the following section.

### Wavelength drift analysis of III-V/SOI lasers

When we switch on and off the laser, the chip temperature varies  $\Delta T$ , leading to a waveguide effective index  $n_{eff}$  increase  $n_{eff} + \frac{dn_{eff}}{dT} \Delta T$ , generating a shift of the Fabry-Perot (FP) comb. The temperature variation is important in the gain section, where we inject the carriers. In the silicon waveguide, there is a negligible induced effect: silicon is located beneath the III-V, isolated by silica and BCB. The RR filter transmission curve is not affected by the temperature change. As the FP comb moves but the filter doesn't, mode hop may occur, as sketched in fig. 2.30. To avoid those mode hops risks, we propose to keep laser always on, and use instead an external SOA integrated in the same chipset to switch off the output power between bursts.

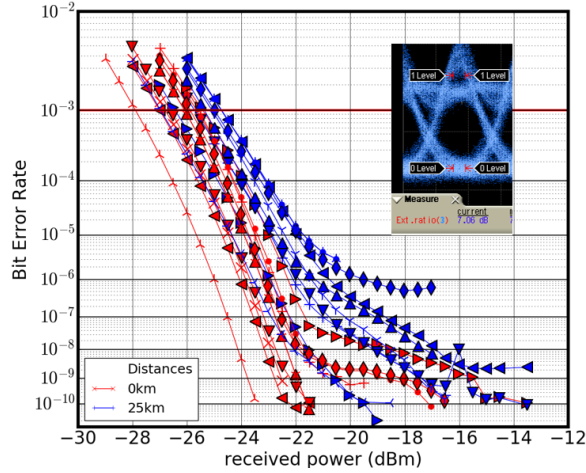


Figure 2.29: BER measurements of the double RR DML module back to back (red curve) and after 25 km (blue curve) for 10 channels with 100 GHz spacing. The inset shows a typical eye diagram with 7 dB extinction ratio. The PRBS sequence length is  $2^7 - 1$ . Those results were obtained in [14].

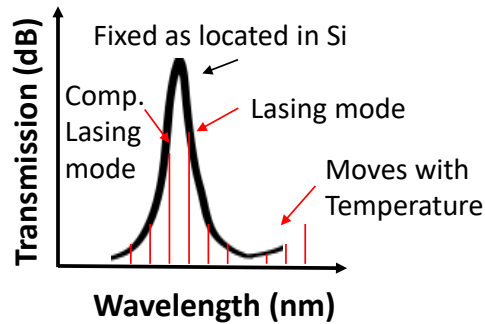


Figure 2.30: Temperature changes lead to mode hops

### 2.3.4 Integration with an SOA

III-V on silicon offers a convenient active-passive integration platform. It is thus possible to integrate an SOA that is not too close to the laser as it is separated by a silicon waveguide. Here, the SOA is  $550 \mu\text{m}$  long (including two  $125 \mu\text{m}$  long III-V/Si tapers) with quantum well overlap of 10%. If such SOA is reversed bias, the signal is greatly reduced. As the SOA electrical bandwidth is in the GHz range, it is possible to use it as a 8 kHz burst switch.

As the laser is isolated from the SOA its induced frequency drift will be low. We first investigate the direct modulation of the III-V/Si laser and SOA in continuous mode with a test structure comprising after the laser a 3 dB coupler that leads to a fiber grating coupler or to the SOA.

Direct modulation BER and eye diagrams are presented in fig. 2.31, for a 6 dB extinction ratio and PRBS length of  $2^7-1$ . The results are presented for the laser output (x sign) and for the laser + SOA output (+ sign) back to back and after 15 km. The penalty at BER=1E-3 after 15 km is less than 1.5 dB.

The SOA doesn't perturb the eye diagram nor introduce penalty on the BER curve. A performance increase is even found after 15 km. This is consistent with the eye diagram slightly more open with the SOA. This experiment indicates that the designed SOA doesn't negatively impact on the laser modulation performances. However, the reach is slightly degraded compared to the chip without SOA presented in the previous section. If we compare the eye diagrams we can see that it is more open in the second case. In DML, reach is limited by adiabatic chirp.

As pointed out in [40] and [41] it depends on carrier density at threshold, cavity length, and ring resonator finesse. A more complete study is required to analyse the adiabatic chirp of hybrid III-V on silicon tunable lasers.

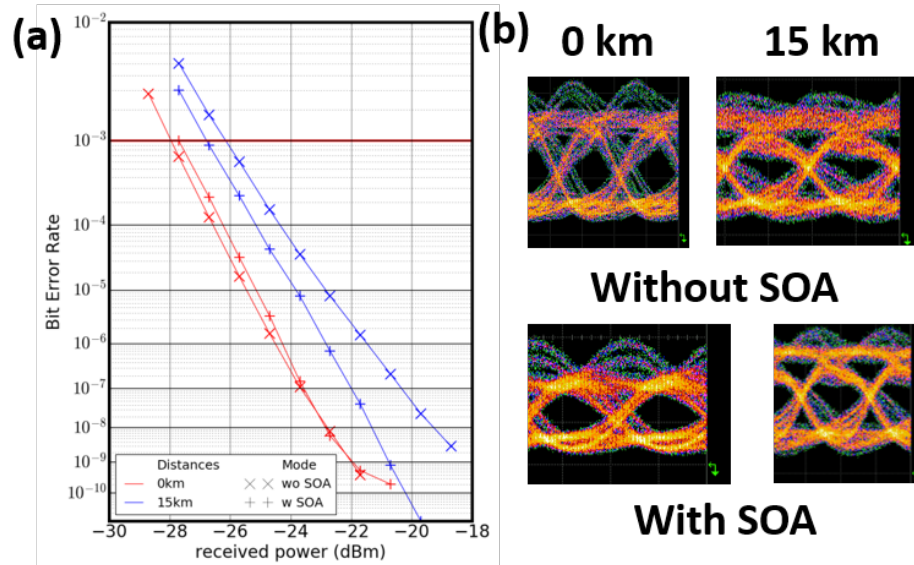


Figure 2.31: Direct modulation results of Tul SOA with (a) BER measurements after 0 km (in red) and 15 km (in blue) for the laser output (cross) and SOA output (plus). (b) corresponding eye diagrams.

### Static thermal characterisation

To analyse the thermal behaviour of the device, we firstly investigate the device in a DC configuration. Laser is biased at 100 mA and SOA is set at -1.3 V, 0 V, 1 V (15 mA), 1.2 V

(33 mA) and 1.4 V (51 mA).

Spectra are displayed on fig. 2.32. The SOA switches the laser off with an extinction of 50 dB. This value is consistent with the absorption of the 300  $\mu\text{m}$  length SOA. In the NG-PON2 standard, the specified power when the signal is switched off is  $-68.5$  dBm. A longer SOA could be used to meet the requirements. When the SOA is biased from 15 to 50 mA there is a wavelength shift  $\delta\lambda = 42$  pm due to the global temperature increase of the chipset.  $\delta\lambda = 42$  pm corresponds to a frequency shift of 5 GHz.

As this value is low, we can expect the device to work well in burst mode operation. In the NG-PON2 standard, the drift is specified as the -15 dB spectrum width, for all burst length. We will perform this characterisation in the next section.

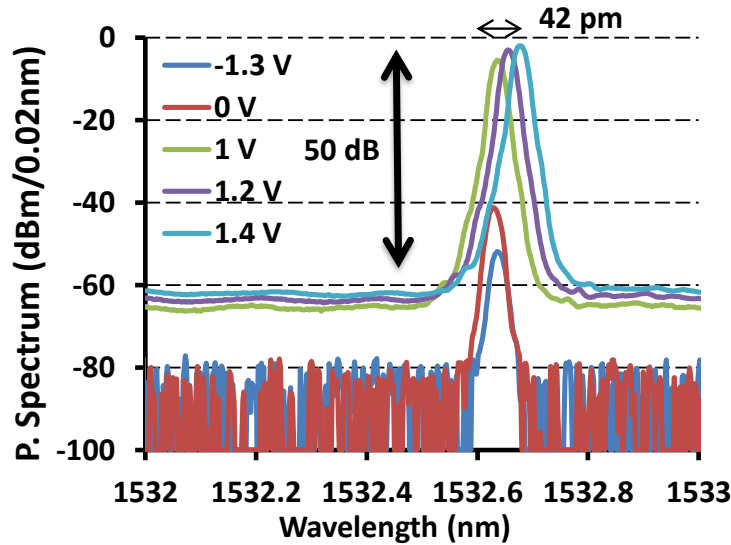


Figure 2.32: Attenuation and wavelength shift induced by the SOA for different polarization conditions. When the SOA is reverse biased, the power is 50 dB less than with forward bias. The induced wavelength shift is only 42 pm.

### SOA performances as a burst switch

The experiment schematic is presented in fig. 2.33. A square signal between 0 and 1.4 V is applied to the SOA at 8 kHz, corresponding to 125  $\mu\text{s}$  long packets used in access networks, with variable burst length from 6 to 125  $\mu\text{s}$ . Optical signal is sent to a photodiode and acquired by a sampling oscilloscope. Signal is displayed on fig. 2.34 for duty cycles of 95% (118.5  $\mu\text{s}$  long packet), 50% (62.5  $\mu\text{s}$ ) and 5% (6.25  $\mu\text{s}$ ) without data signal applied to the laser (2.34 a) or with data signal (2.34 b). We can see that power variation during the packet

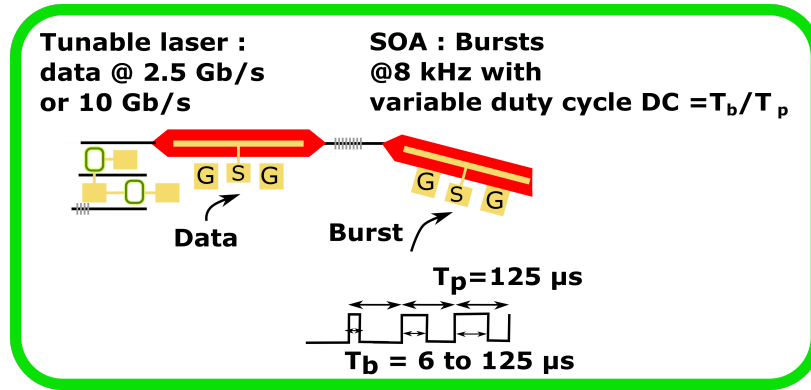


Figure 2.33: Schematic of the integrated tunable laser and SOA. In this configuration, the data signal is applied on the laser and the burst signal to the SOA.

is negligible as a very limited transient effect in the beginning of a packet is observed, in particular for packets with 95% duty cycle.

The power difference between two different packet sizes is also negligible. If we compare the non-modulated curves in fig. 2.34a and the modulated curves in fig. 2.34b we can conclude that the modulation doesn't affect the SOA switching dynamics.

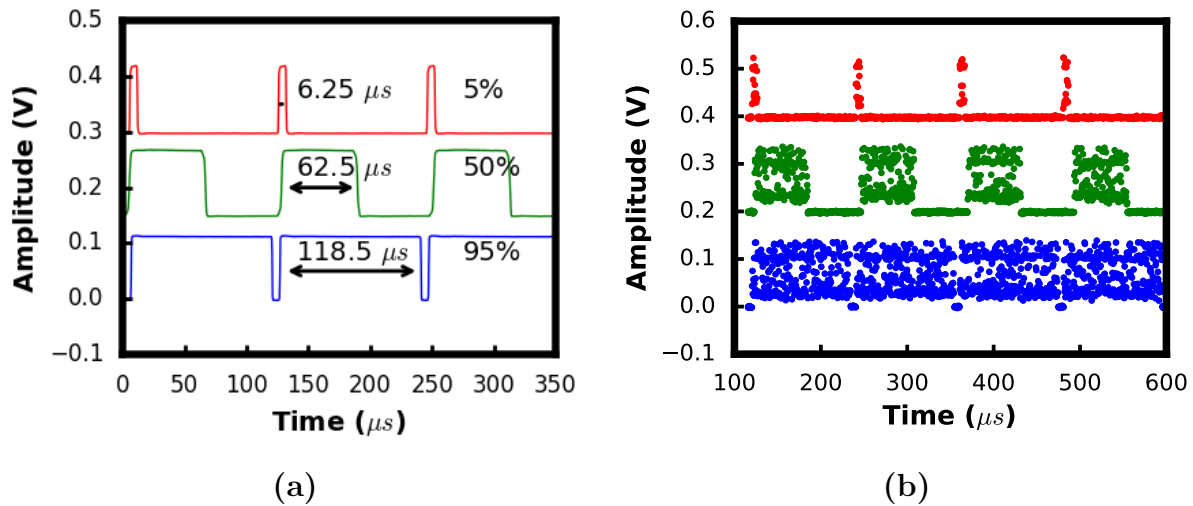


Figure 2.34: Experimental signal recorded on sampling scope for 95% duty cycle (blue), 50% (green), and 5% red for (a) without data on the laser (b) with data.

Spectra are recorded and displayed on fig. 2.35a for different packet length. The extracted parameters are presented on fig. 2.35b. The size of the spectrum is constant for the different

packet lengths, with a mean value of 15.8 GHz and a maximum deviation of 0.5 GHz. The wavelength peak increases linearly with the size of the packets due to the linear temperature increase. The wavelength drift between short and long packets is only 3.5 GHz. As the sampling quantization limit of the OSA is 0.5 GHz, a fit is used to record the wavelength peak with greater accuracy. In [42], the peak increase was slightly higher, around 10 GHz. Standardized spectral excursion, defined in fig. 2.25 is  $15.5 + 3.5 = 19$  GHz. The values are well below the specifications of NG-PON2 of 40 GHz for 100 GHz spacing or 25 GHz for 50 GHz spacing.

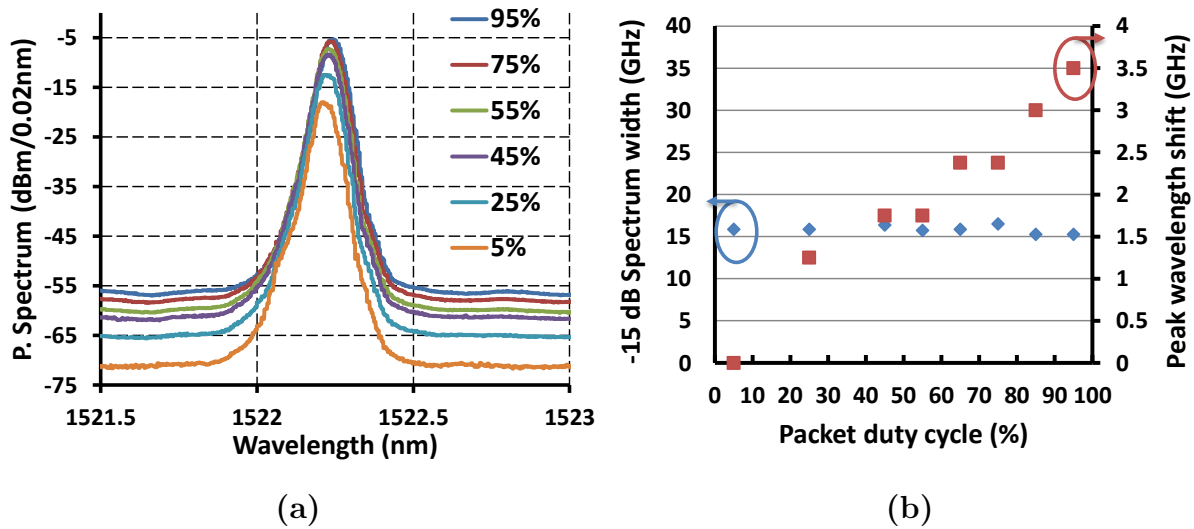


Figure 2.35: (a) Recorded spectrum for packet length duty cycles varying from 95 (blue) to 5% (orange). (b) The extracted -15 dB spectrum width is represented in blue, featuring a 15.8 GHz mean value. The maximum derivation from the mean is 0.5 GHz. The wavelength peak shift is represented in red. The maximum shift for the different packet length is 3.5 GHz.

## Time resolved measurements

A filter is then inserted after the device to investigate the wavelength drift with time resolved measurements and to validate the results obtained in fig. 2.35. The filter can be set to diminish more the shorter (position (1) in fig. 3.29a) or longer wavelength (position (2)). In fig. 3.29b, the laser wavelength is placed at the center of the filter. As marked in green in the figure, the filter suppresses the laser spontaneous emission with a slope of 26 dB/nm.

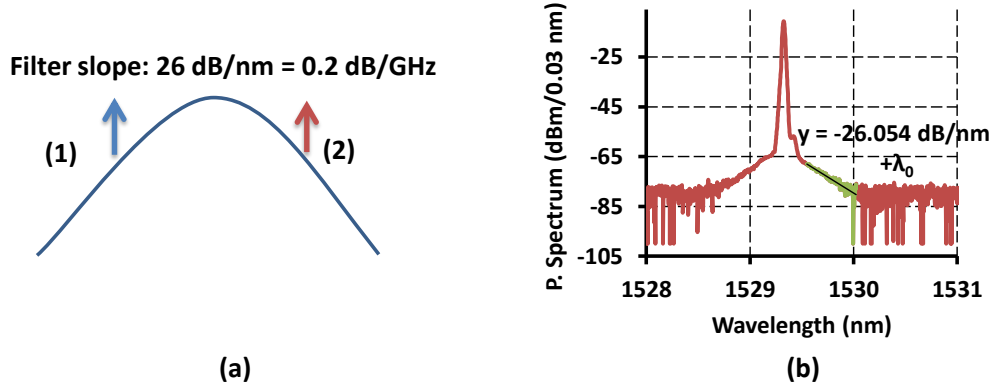


Figure 2.36: (a) Schematic of the spectral filter. In the experiment, the filter is tuned either to position (1), where the lower wavelengths are more attenuated or in position (2) where the higher wavelengths are more attenuated. (b) laser placed at the filter center.

The recorded traces for different packet lengths are shown in fig 3.29a, for filter position (1) and (2). The results are consistent with spectrum analysis: long packets have longer wavelength than short packets as they have higher transmission in position (1) and lower in position (2). The same ratio between long (blue curve) and short (purple curve) is observed for the two sides:

$$\frac{P_{5\%}}{P_{95\%}}|_{(a)} = \frac{P_{95\%}}{P_{5\%}}|_{(b)} = 0.9 = -0.5 \text{ dB} \rightarrow \Delta\nu_{ext} = \frac{0.5 \text{ dB}}{0.2 \text{ dB/GHz}} = 2.5 \text{ GHz} \quad (2.11)$$

The extracted value is very close to the observed spectrum shift of 3.5 GHz presented in fig. 2.35. A very small blue shift ( $< 0.5$  GHz) during packets is observed as the curves are slightly tilted. This experiment clearly demonstrates the interest of integrated tunable laser-SOA for burst mode operation. Further work will focus on the measurement of BER under burst mode operation and new SOA design to increase its extinction.

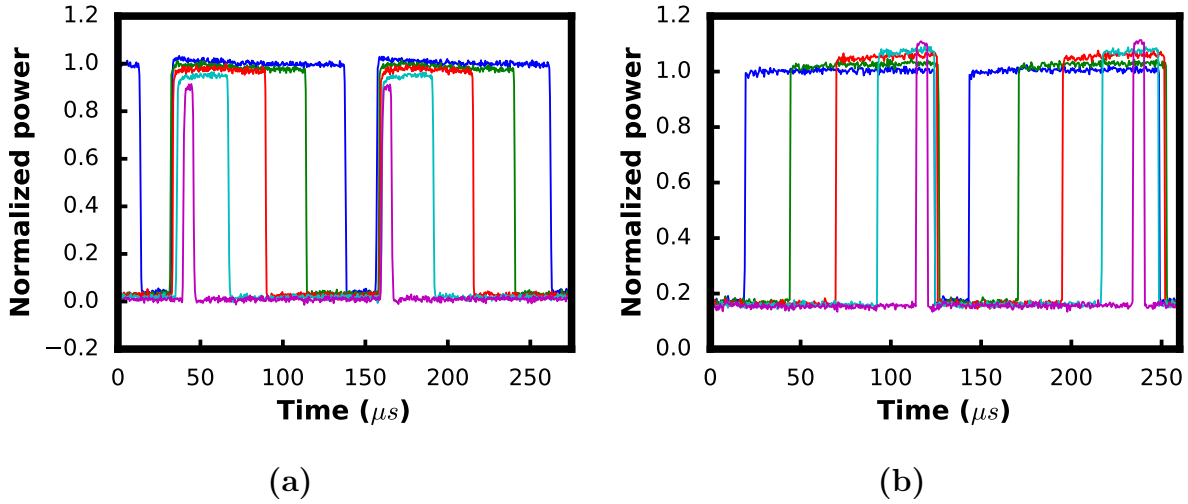


Figure 2.37: Signal recorded on sampling scope for (a) a filter that attenuates more the shorter wavelength (b) the longer wavelength. We normalized the data by the values of long packets. The two graphs are consistent with the symmetry of the filter (same slope in both cases). The extracted drift is 2.5 GHz and negligible drift is seen during packets.

## 2.4 Chapter conclusion

In this chapter, the properties of hybrid III-V on silicon tunable lasers are investigated. In the introduction, I showed that low loss silicon ring resonators are particularly suited for tunable lasers as they have low minimal radius and low insertion loss. For this reason and because tapers efficiently couple the mode to the gain region, hybrid III-V on silicon platform is particularly suited for tunable lasers.

With optimal front mirror reflectivity, output power is improved to 21 mW at 250 mA [1] and the differential efficiency is 0.12 mW/mA, a two times improvement compared to cleaved lasers.

In a second section, a novel design to reduce the linewidth inspired by [30] is studied. I also investigated the wavelength switching dynamics of a design with ring P-I-N junctions, demonstrating a switching time below 1.5 ns [2]. Further work is needed to demonstrate fast switching in any channel of the C band.

In a third section I studied directly modulated tunable lasers for NG-PON2 TWDM-PON access networks. I characterised the wavelength dynamics in burst mode operation with an integrated semiconductor optical amplifier used as a burst switch. BER in burst mode should be performed in a near future.

The following table sums up my work done in this chapter:

RR Tun. laser	wg P	Tun. speed	Mod.	Reach	B. mode
State of the art	15 mW [43]	$\mu$ s [21]	10 Gb/s [14]	25 km [14]	No
This work	<b>21 mW</b> [1]	<b>1.5 ns</b> [2]	10 Gb/s	25 km	<b>Yes</b>

Table 2.3: III-V on silicon tunable lasers compared with state of the art results.

## Outook

To be part of a coherent transceiver product, III-V/SOI tunable laser performance should meet the integrated tunable laser assembly (ITLA) multi source agreement specifications [44]. In this standard, power is defined as fibre coupled power over the product lifetime for all working condition. I compare the results presented here with ITLA specifications in table 2.4.

Tunable laser linewidth should be investigated in more details in the future as an other group reported a linewidth of 160 kHz [45] and 18 kHz [43] with similar devices. Relative intensity noise is to be considered as only preliminary results have been reported [10].

To reach fiber coupled power greater than 13.5 dBm, integration of a high saturation power SOA is a key. As relatively high power tunable lasers are now demonstrated and as the fabrication process is more and more mature, we will be able to integrate those lasers in complex circuits. A laser integrated with a coherent modulator has been recently demonstrated in [46].

	P (dBm) A	P (dBm) B	SMSR
ITLA spec.	13.5	10.5	43
This work		8.75	45

Table 2.4: ITLA Specifications for ultra long haul compared with the obtained results.

## References

- [1] A. Gallet et al. “Nouveaux lasers hybrides iii/v sur silicium Largement accordables pour les reseaux d’accès NG-PON2.” In: *JNOG 2018*. Aug. 2018, pp. 1–3.
- [2] T. Verolet et al. “Hybrid III-V on Silicon Fast and Widely Tunable Laser Based on Rings Resonators with PIN Junctions”. In: *2018 Asia Communications and Photonics Conference (ACP)*. Oct. 2018, pp. 1–3.

- [3] M. M. Norbert Grote and M. Ortsiefer. *Laser components, in Fibre Optic Communication: Key Devices Springer Series in Optical Science*.
- [4] H. Debrégeas. *Widely Tunable Laser Diodes, in Fibre Optic Communication: Key Devices Springer Series in Optical Science*.
- [5] M. C. Larson. “Narrow linewidth tunable DBR lasers”. In: *2016 International Semiconductor Laser Conference (ISLC)*. Sept. 2016, pp. 1–2.
- [6] S. Matsuo and T. Segawa. “Microring-Resonator-Based Widely Tunable Lasers”. In: *IEEE Journal of Selected Topics in Quantum Electronics* 15.3 (May 2009), pp. 545–554.
- [7] X. Pommarede. “Hybrid III-V/Si photonics integrated circuits for optical communication applications”. PhD thesis.
- [8] W. Bogaerts et al. “Silicon microring resonators”. In: *Laser & Photonics Reviews* 6.1 (2012), pp. 47–73.
- [9] A. Yariv. “Coupled-mode theory for guided-wave optics”. In: *IEEE Journal of Quantum Electronics* 9.9 (1973), pp. 919–933.
- [10] N. Girard. “Lasers à faible bruit d’intensité en InP sur circuit Silicium pour l’optique hyperfréquence”. 2016SACLS113. PhD thesis. 2016.
- [11] A. L. Liepvre et al. “Widely wavelength tunable hybrid III-V/silicon laser with 45 nm tuning range fabricated using a wafer bonding technique”. In: *The 9th International Conference on Group IV Photonics (GFP)*. Aug. 2012, pp. 54–56.
- [12] H. Elfaiki et al. “Ultra Wide Hybrid III-V On Silicon Tunable Laser”. In: *2018 ECOC Conference*. Sept. 2018, pp. 50–51.
- [13] M. Lamponi et al. “Low-Threshold Heterogeneously Integrated InP/SOI Lasers With a Double Adiabatic Taper Coupler”. In: *IEEE Photonics Technology Letters* 24.1 (Jan. 2012), pp. 76–78.
- [14] G. Levaufre. “Circuits photoniques intégrés incluant des lasers hybrides III-V sur silicium pour applications en télécommunication très haut débit”. PhD thesis. 2016.
- [15] A. Dewanjee et al. “A low-loss, compact, broadband, polarization insensitive edge coupler for silicon photonics”. In: *2014 IEEE Photonics Conference*. Oct. 2014, pp. 560–561.

- [16] S. Joshi. “Quantum dash based photonic integrated circuits for optical telecommunications”. 2014TELE0031. PhD thesis. 2014.
- [17] M. J. Connelly. *Semiconductor optical amplifiers*. 2002.
- [18] P. Kaspar et al. “Packaged hybrid III-V/silicon SOA”. In: *2014 The European Conference on Optical Communication (ECOC)*. Sept. 2014, pp. 1–3.
- [19] M. L. Davenport et al. “Heterogeneous Silicon/III–V Semiconductor Optical Amplifiers”. In: *IEEE Journal of Selected Topics in Quantum Electronics* 22.6 (Nov. 2016), pp. 78–88.
- [20] R. Kumar et al. “Demonstration of an On-Chip III-V/Si Hybrid Semiconductor Optical amplifier for Photonics Integration”. In: *2018 Group Four Photonics*. Sept. 2014, pp. 50–51.
- [21] G. Duan et al. “Hybrid III-V Silicon Photonic Integrated Circuits for Optical Communication Applications”. In: *IEEE Journal of Selected Topics in Quantum Electronics* 22.6 (Nov. 2016), pp. 379–389.
- [22] M. Sales, M. S. Faruk, and S. J. Savory. “Improved linewidth tolerant carrier phase recovery based on polar MAP metric estimate”. In: *2017 Optical Fiber Communications Conference and Exhibition (OFC)*. Mar. 2017, pp. 1–3.
- [23] C. Xie. “Local Oscillator Phase Noise Induced Penalties in Optical Coherent Detection Systems Using Electronic Chromatic Dispersion Compensation”. In: *2009 Conference on Optical Fiber Communication - includes post deadline papers*. Mar. 2009, pp. 1–3.
- [24] *Advantages of Ultra Narrow Linewidth Lasers For Coherent Communications*. URL: <https://www.neophotonics.com/advantages-ultra-narrow-linewidth-lasers-coherent-communications/>.
- [25] *FTBx-2850 -  $\mu$ ITLA tunable light source*. URL: <https://www.exfo.com/fr/produits/tests-laboratoire-fabrication/tunable-laser-sources/ftbx-2850/>.
- [26] A. L. Liepvre. “Silicon Photonics Hybrid Lasers”. PhD thesis.
- [27] T. Komljenovic et al. “Widely Tunable Narrow-Linewidth Monolithically Integrated External-Cavity Semiconductor Lasers”. In: *IEEE Journal of Selected Topics in Quantum Electronics* 21.6 (Nov. 2015), pp. 214–222.
- [28] C. Henry. “Theory of the linewidth of semiconductor lasers”. In: *IEEE Journal of Quantum Electronics* 18.2 (Feb. 1982), pp. 259–264.

- [29] H. C. Casey and P. L. Carter. “Variation of intervalence band absorption with hole concentration in p-type InP”. In: *Applied Physics Letters* 44.1 (1984), pp. 82–83. eprint: <https://doi.org/10.1063/1.94561>.
- [30] H. Debregeas et al. “2kHz Linewidth C-Band Tunable Laser by Hybrid Integration of Reflective SOA and SiO<sub>2</sub> PLC External Cavity”. In: *2014 International Semiconductor Laser Conference*. Sept. 2014, pp. 50–51.
- [31] H. Brahmi et al. “On the fly all-optical packet switching based on hybrid WDM/OCDMA labeling scheme”. In: *Optics Communications* 312 (2014), pp. 175–184.
- [32] R. O’Dowd et al. “Frequency plan and wavelength switching limits for widely tunable semiconductor transmitters”. In: *IEEE Journal of Selected Topics in Quantum Electronics* 7.2 (Mar. 2001), pp. 259–269.
- [33] R. Soref and B. Bennett. “Electrooptical effects in silicon”. In: *IEEE Journal of Quantum Electronics* 23.1 (Jan. 1987), pp. 123–129.
- [34] R. Wu et al. “Compact models for carrier-injection silicon microring modulators”. In: *Opt. Express* 23.12 (June 2015), pp. 15545–15554.
- [35] H. Debrégeas et al. “Quasi frequency drift suppression for burst mode operation in low-cost thermally-tuned TWDM-PON”. In: *2017 Optical Fiber Communications Conference and Exhibition (OFC)*. Mar. 2017, pp. 1–3.
- [36] Y. Matsui et al. “Transceiver for NG-PON2: Wavelength tunability for burst mode TWDM and point-to-point WDM”. In: *2016 Optical Fiber Communications Conference and Exhibition (OFC)*. Mar. 2016, pp. 1–3.
- [37] G. Simon. “Introduction des technologies de multiplexage en longueur d’onde dense dans les futures générations de réseaux d’accès optique”. 2016ENST0076. PhD thesis. 2016.
- [38] *G.989.2 : 40-Gigabit-capable passive optical networks 2 (NG-PON2): Physical media dependent (PMD) layer specification*. URL: <https://www.itu.int/rec/T-REC-G.989.2-201412-I/en>.
- [39] R. Bonk et al. “The underestimated challenges of burst-mode WDM transmission in TWDM-PON”. English. In: *Optical Fiber Technology* 26.Part A (2015), pp. 59–70.
- [40] Coldren, Corzine, and Masanovic. *Diode Lasers and Photonic Integrated Circuits*. John Wiley & Sons, 2012.

- [41] G. Duan, P. Gallion, and G. Debarge. “Analysis of the phase-amplitude coupling factor and spectral linewidth of distributed feedback and composite-cavity semiconductor lasers”. In: *IEEE Journal of Quantum Electronics* 26.1 (Jan. 1990), pp. 32–44.
- [42] H. Debrégeas et al. “TWDM-PON Burst Mode Lasers With Reduced Thermal Frequency Shift”. In: *Journal of Lightwave Technology* 36.1 (Jan. 2018), pp. 128–134.
- [43] M. Tran Anh et al. “Multi-Ring Mirror-Based Narrow-Linewidth Widely-Tunable Lasers in Heterogeneous Silicon Photonics”. In: *2018 European Conference on Optical Communication (ECOC)*. Sept. 2018, pp. 1–3.
- [44] *ITLA MSA specifications*. URL: [www.oiforum.com/wp-content/uploads/OIF-ITLA-MSA-01.3.pdf](http://www.oiforum.com/wp-content/uploads/OIF-ITLA-MSA-01.3.pdf).
- [45] S. Srinivasan et al. “Coupled-Ring-Resonator-Mirror-Based Heterogeneous III–V Silicon Tunable Laser”. In: *IEEE Photonics Journal* 7.3 (June 2015), pp. 1–8.
- [46] A. Shen et al. “A Packaged Silicon Photonic Circuit Integrating a Hybrid Tunable Laser, a Modulator and an amplifier,” in: *2018 Group Four Photonics*. Sept. 2018, pp. 50–51.

# Chapter 3

## High Speed Hybrid Distributed Feedback Lasers

**I**N this chapter, I will describe III-V on silicon distributed feedback lasers (DFB) and their direct modulation properties. After a short theoretical introduction to DFB lasers I will introduce their design in the hybrid III-V on silicon platform.

I will then describe their direct modulation properties, both theoretically and experimentally. To overcome chirp limitations, a spectral filter is integrated after the laser. I will present transmission results at 10 and 25 Gb/s.

To finish I will introduce a novel DFB design with axially varying parameters, based on theoretical work described in [1]. This device is designed to enhance the per-facet efficiency as power is concentrated on one side of the cavity. Results presented in this chapter have been published in [2], [3], [4] and [5].

### 3.1 Introduction to DFB lasers

#### 3.1.1 DFB laser theoretical description

In 1972, people from Bell Labs introduced theoretically a laser based on distributed feedback (DFB)[6]. A DFB grating is an index or gain periodic perturbation on an active waveguide. The corrugation with pitch  $\Lambda$  acts as a distributed reflector for light with wavelength around  $\lambda_B = 2n_{eff}\Lambda$ . Two years after their theoretical description, Nakamura *et al.* [7] fabricated the first DFB structure. They used holographic lithography to define a grating in p-GaAs, as sketched in fig. 3.1. A very complete and useful description of DFB lasers can be found

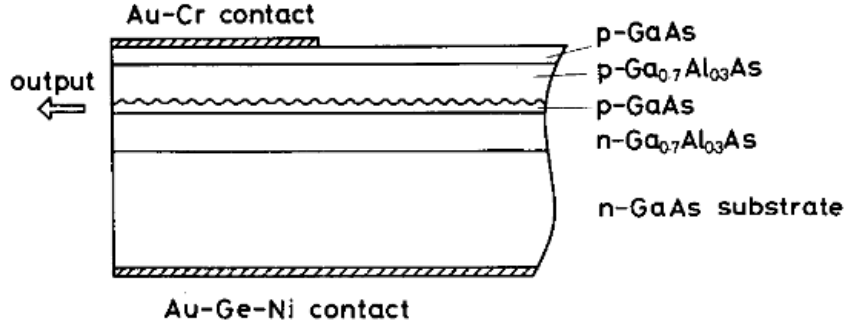


Figure 3.1: Schematic of first fabricated DFB laser, from [7].

in [8]. There are two main ways to represent the field in a DFB, described in details in [9]:

- Coupled mode theory (CMT) equations. If  $\beta_0 = \frac{2\pi}{\lambda_B}$  is the Bragg wavenumber, the field is the sum of a propagating wave  $R$  and contra-propagating wave  $S$ :

$$E(z) = R(z) \exp(-j\beta_0 z) + S(z) \exp(j\beta_0 z) \quad (3.1)$$

For a uniform structure with no phase shift  $R$  and  $S$  are linked by the following complex coupled first order differential equations [6]:

$$\begin{cases} \frac{-dR}{dz} + (\alpha_{th} - j\Delta\beta)R = j\kappa S \\ \frac{dS}{dz} + (\alpha_{th} - j\Delta\beta)S = j\kappa R \end{cases} \quad (3.2)$$

- Transfer matrix method (TMM) formulation of CMT equation [10]. Propagating and contra-propagating waves amplitudes  $u_N$  and  $v_N$  at the end of the structure are the product of the device matrix  $\bar{\bar{A}}$  times the initial amplitudes  $u_1$  and  $v_1$ :

$$\begin{pmatrix} u_N \\ v_N \end{pmatrix} = \bar{\bar{A}} \begin{pmatrix} u_1 \\ v_1 \end{pmatrix} \quad (3.3)$$

DFB lasers properties depend on the grating strength  $\kappa$ , proportional to the index variation. For a given  $\kappa L$  product, solutions of those equations are the allowed wavelengths and the corresponding threshold gain  $\alpha_{th}$ . Although  $\alpha_{th}$  is a mirror loss coefficient, it is usually named "threshold gain" as it is the gain to achieve threshold if we neglect internal losses. As  $\alpha_{th}$  is an amplitude coefficient and as the threshold condition is given by power coefficients, we have  $\alpha_m = 2\alpha_{th}$ . With internal losses  $\alpha_0$ , the gain  $G(N_{th})$  to achieve threshold is  $G(N_{th}) =$

$\alpha_m + \alpha_0 = 2\alpha_{th} + \alpha_0$ . In coupled mode theory, the effective index variation is supposed to be weak. This assumption corresponds to  $\kappa \ll \beta_0$ . As there is usually a ratio of more than 100 between both, coupled mode theory can be applied to DFB lasers.

I first investigated a uniform structure with no reflective facets. The transfer matrix for such a structure is ([9] p 48):

$$\bar{A} = \begin{pmatrix} \left[ \cosh(\gamma L) - \frac{j\Delta\beta}{\gamma} \sinh(\gamma L) \right] & \frac{-jK}{\gamma} \sinh(\gamma L) \\ \frac{jK}{\gamma} \sinh(\gamma L) & \left[ \cosh(\gamma L) + \frac{j\Delta\beta}{\gamma} \sinh(\gamma L) \right] \end{pmatrix} \quad (3.4)$$

In those equations  $\gamma^2 = \kappa^2 + (\Delta\beta - j\alpha_{th})^2$ . The oscillation condition is given by [10]:

$$\bar{A}_{22} = 0 \quad (3.5)$$

To solve this equation, I used the software LaserMatrix developed by R. Schatz at KTH royal institute of technology. A plot of  $2\alpha_{th}L$  for the different modes is represented in fig. 3.2. Modes at each side of the stop band have the same threshold gain, leading to a two frequency laser spectrum (fig. 3.2b).

There are several ways to realize a single mode DFB laser. The most common is to make

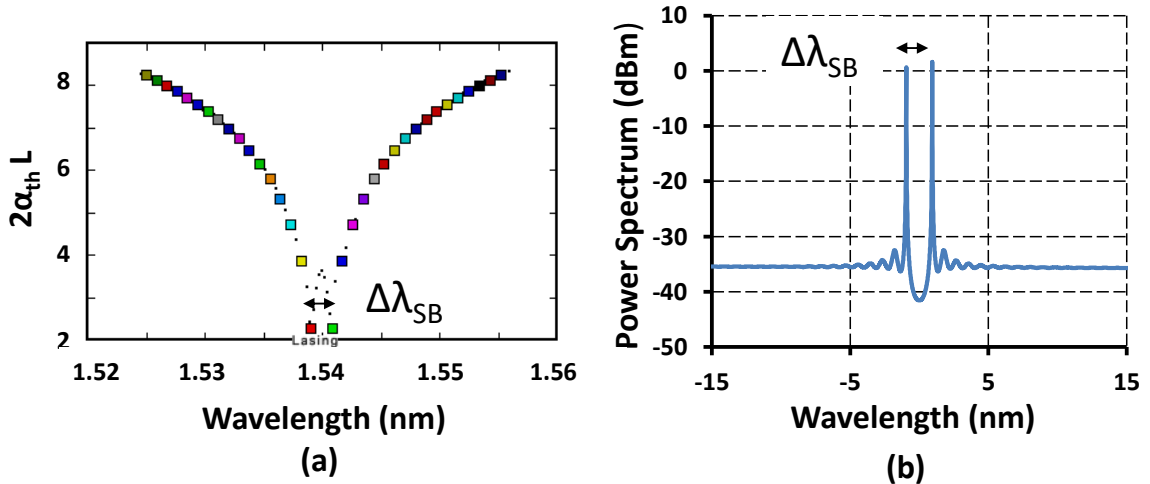


Figure 3.2: (a)  $2\alpha_{th}L$  versus wavelength. (b) Simulated spectrum of a uniform DFB laser with stop band  $\Delta\lambda_{SB}$ .

a high reflection (HR) coating on one facet and an anti reflection (AR) coating on the other one. As described theoretically by [11], it leads to single mode operation of the device with sufficient side mode suppression ratio (SMSR).

The threshold gain margin is the difference  $\alpha_{th_2} - \alpha_{th_1}$  where  $\alpha_{th_1}$  is the mode with lowest threshold gain and  $\alpha_{th_2}$  the second mode with lower threshold gain. All else being equal, SMSR increases with increasing threshold gain margin. The threshold gain margin depends on the cleavage position in the grating [9]. As it can't be controlled, threshold gain margin (and SMSR) of HR-AR lasers may vary from laser to laser.

Moreover, it is not very practical to cleave and make coatings on integrated lasers. In this context the most simple way to make a single mode laser is to introduce a  $\lambda/4$  phase shift in the middle of the DFB cavity [8] and ensure that there are no reflections in the chipset. In the III-V on silicon platform, power is extracted by fiber grating couplers with low reflection coefficients hence  $\lambda/4$  phase shifted lasers can be used.

With a phase shifted grating, the mode with the lowest threshold gain is at the center of the stop band, as sketched in fig. 3.3. The corresponding spectrum at threshold is sketched in fig. 3.3b. High threshold gain margin of phase shifted lasers is sufficient to have SMSR greater than 50 dB. As sketched in fig. 3.4a,  $2\alpha_{th}L$  rapidly decays with  $\kappa L$  for all modes. The normalised threshold gain margin is presented in fig. 3.4b. It is optimum for  $\kappa L = 2$ . In this section I introduced coupled mode theory and transfer matrix method. In the next section, I will present how to design DFB lasers in the III-V on silicon platform.

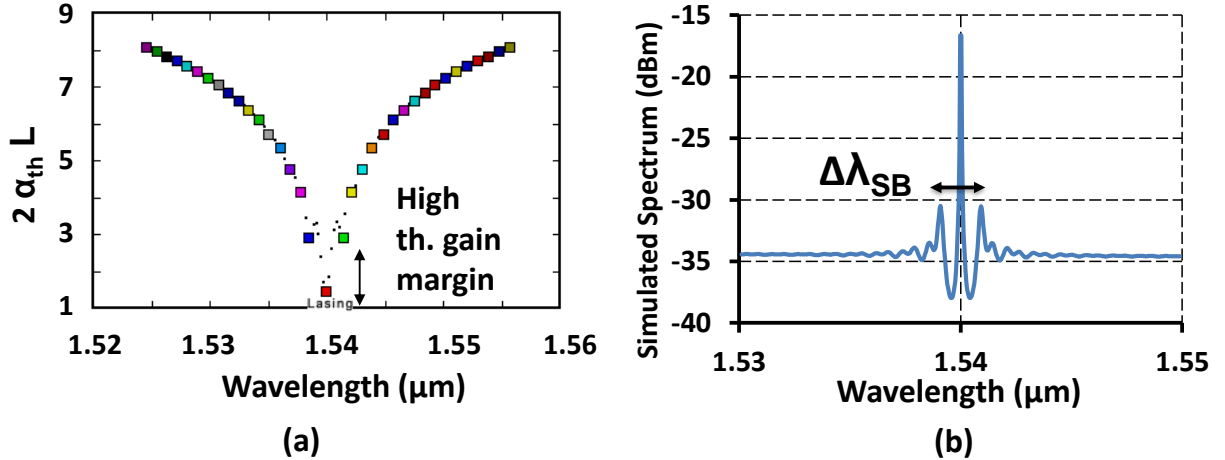


Figure 3.3: (a)  $2\alpha_{th}L$  versus wavelength for a typical DFB laser. Phase shifted laser have high threshold gain margin. (b) Simulated spectrum at threshold of a phase shifted DFB laser with stop band  $\Delta\lambda_{SB}$ .

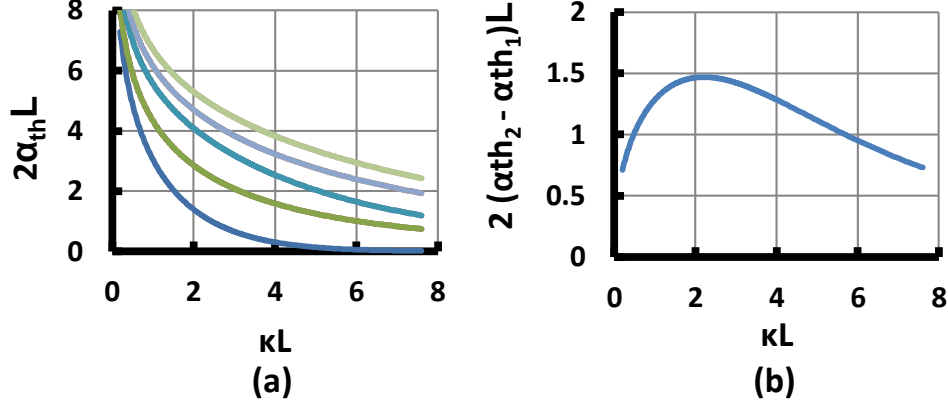


Figure 3.4: (a) Normalised threshold gain evolution with  $\kappa L$  for the 5 first modes of a phase shifted DFB. (b) Evolution of threshold gain margin with  $\kappa L$ , maximum at  $\kappa L = 2$ .

### 3.1.2 III-V/Si DFB laser

The grating of III-V on silicon DFB laser is made by etching teeth in the upper part of the laser silicon waveguide, as sketched in fig. 3.5a. The 30 nm deep etched DFB grating is defined by e-beam lithography and etched with reactive ion etching.

Transverse cross section is shown in fig. 3.5b. As in tunable lasers, the cavity is shared between III-V and silicon. A 80 nm bonding oxide separates both waveguide. Top view is shown in fig. 3.5c, with the etched region in yellow. In the center of the cavity, two teeth are etched to form a  $\lambda/4$  phase shift. Silicon waveguide width  $W_{Si}$  defined in fig. 3.5b controls the mode properties.

Calculated effective index variation with  $W_{Si}$  for the main mode is presented in fig. 3.6a in blue, with mode profiles shown as insets. When  $W_{Si}$  is narrow, the mode is highly confined in the III-V material. Conversely, for a large silicon waveguide the mode is confined in silicon. As the effective index of the III-V/Si supermode is 3.2, we chose a grating period  $\Lambda = 242$  nm to obtain a Bragg wavelength  $\lambda_B \approx 1550$  nm. Quantum well confinement evolves smoothly with  $W_{Si}$ , from 14% for narrow waveguide width to less than 1% when  $W_{Si}$  is large (fig. 3.6b). In a III-V/Si DFB laser, grating strength  $\kappa$  also strongly depends on  $W_{Si}$  as it is proportional to the grating confinement. An estimation of  $\kappa$  is [9]:

$$\kappa \approx \frac{\pi(n_u - n_e)}{2\lambda} \approx \frac{\pi\Gamma\Delta n_{mat}}{2\lambda} \quad (3.6)$$

I simulated the effective index in the un-etched ( $n_u$ ) and etched region ( $n_e$ ) with the commercial mode solver Fimmwave. This method provides only an estimate of grating strength

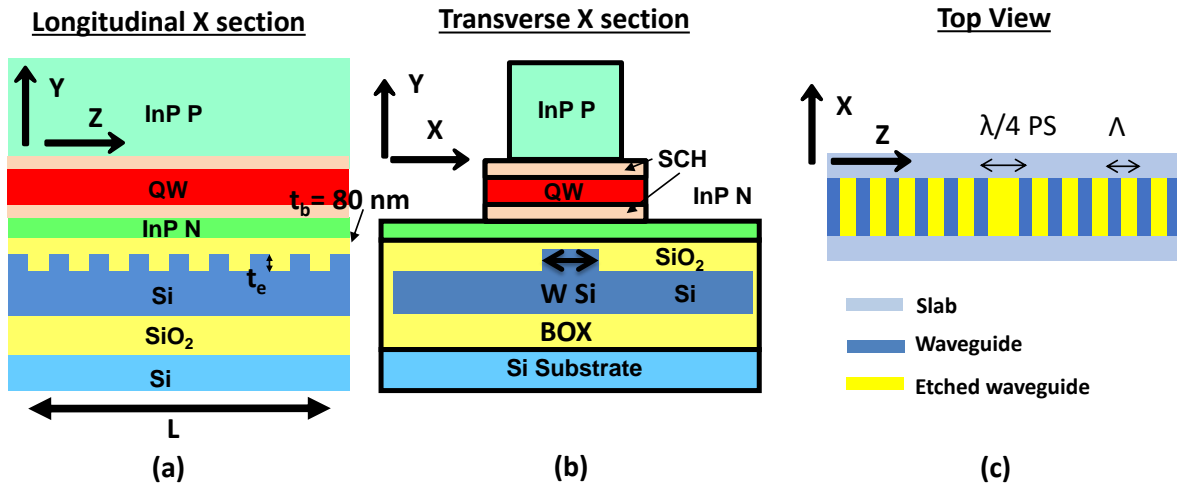


Figure 3.5: III-V on silicon DFB structure. (a) Longitudinal cross section. Grating is made on top of the silicon waveguide. (b) Transverse cross section. DFB parameters depends on the rib width  $wSi$ . (c) Top view featuring the slab (light blue), the waveguide (blue) and the etched region (yellow). A  $\frac{\lambda}{4}$  phase shift is inserted in the centre of the cavity.

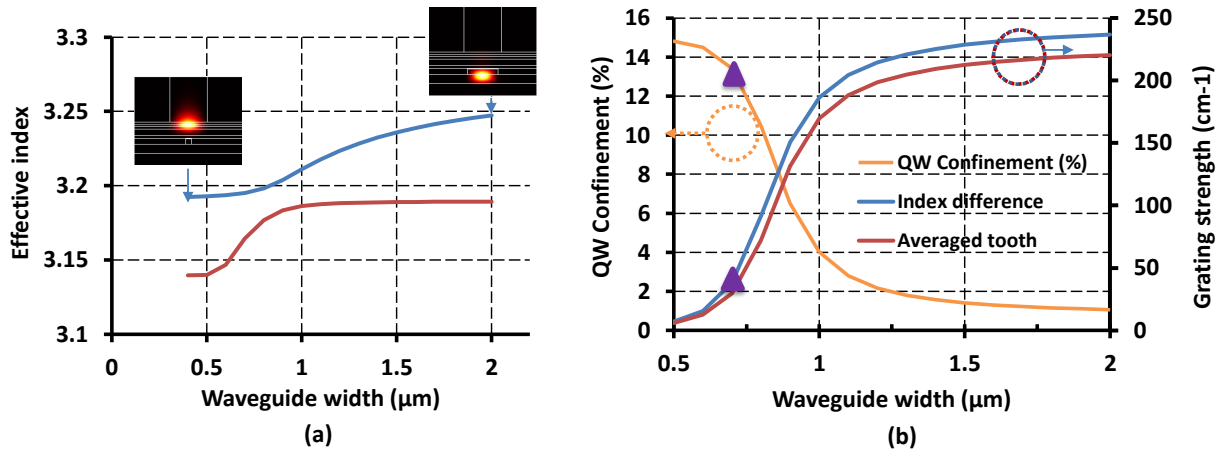


Figure 3.6: (a) Effective index versus waveguide width for the two first guided modes. (b) Variations of grating strength and quantum well confinement with waveguide width. Purple triangle indicates a high speed design.

as the mode shape doesn't change abruptly at the tooth interface. Another method is to simulate the mode in an effective structure. In this structure the tooth has a refractive index which is the mean of silicon and silica.

Then I calculate the confinement  $\Gamma$  in the tooth and multiply it by the material refractive index difference  $\Delta n_{mat} = n_{Si} - n_{SiO_2}$ . Grating strength versus  $W Si$  for both calculation methods is presented in fig. 3.6. As  $W Si$  increases, the mode is more and more confined in silicon. Hence, QW overlap decreases and grating strength increases. The two methods give similar results, with grating strength around  $50 \text{ cm}^{-1}$  for  $W Si = 0.75 \text{ }\mu\text{m}$  to above  $200 \text{ cm}^{-1}$  for  $W Si = 2 \text{ }\mu\text{m}$ .

With the same technology process we have a low grating strength with a high QW overlap laser or a low overlap with high grating strength laser. The first type of laser is a high speed optimization and is described in this chapter. As we will see in the next section, for those lasers lengths between 200 and 400  $\mu\text{m}$  and  $\kappa L$  between 1.5 and 2.5 are typical, corresponding to  $\kappa$  of a few  $10 \text{ cm}^{-1}$ . A purple triangle in fig. 3.6b indicates the selected parameters. The second type is a low linewidth optimization and will be presented in the fourth chapter. As presented in red in fig. 3.6, another supermode is guided in the structure. Contrary to the main mode, the confinement in the III-V is high when  $W Si$  is large and low when it is narrow. The grating strength is affected accordingly: it is low when  $W Si$  is large and high when it is narrow. As we will see, such mode can compete with the main mode. As its effective index is lower, the Bragg wavelength is shifted to lower wavelengths. This mode may have a lower material gain if the gain is peaked at the main mode wavelength.

### Fabricated DFB designs

A first generation of III-V on silicon DFB had been fabricated in 2015 at III-V lab. As sketched in fig. 3.7a, the DFB cavity length is 600  $\mu\text{m}$ . An adiabatic taper couples light from the active region to the silicon waveguide which leads to a fiber grating coupler. After wafer thinning, laser bars are mounted on alumina sub-mounts and measured with a vertical fibre. Lasers are single mode with SMSR  $> 40 \text{ dB}$ . To measure the grating strength, we simulate the group index  $n_g$  to obtain the Fabry-Perot spacing  $\Delta\lambda_{FP} = \frac{\lambda^2}{2n_g L}$ . Then we measure the stop band width  $\Delta\lambda_{SB}$  and use abacus calculated with TMM of fig. 3.7 to retrieve  $\kappa L$  from the normalized stop-band  $\frac{\Delta\lambda_{SB}}{\Delta\lambda_{FP}}$ . In fig. 3.8 we measure  $\kappa L = 1.3$ . In this section, I introduced DFB designs in the III-V on silicon platform. In the next section, I will present the modulation properties of such lasers.

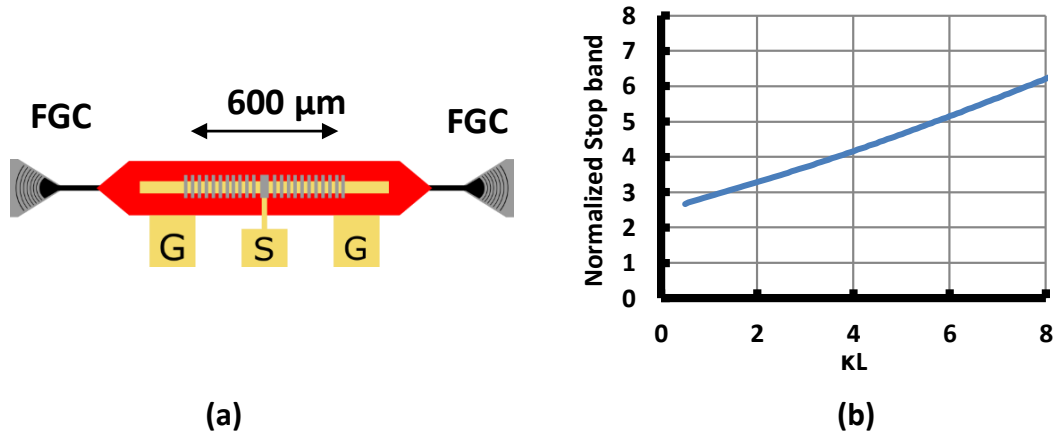


Figure 3.7: (a) Sketch of the DFB laser. (b) Evolution of normalized stopband  $NSB = \frac{\Delta\lambda_{SB}}{\Delta\lambda_{FP}}$  with  $\kappa L$  product calculated with transfer matrix method.

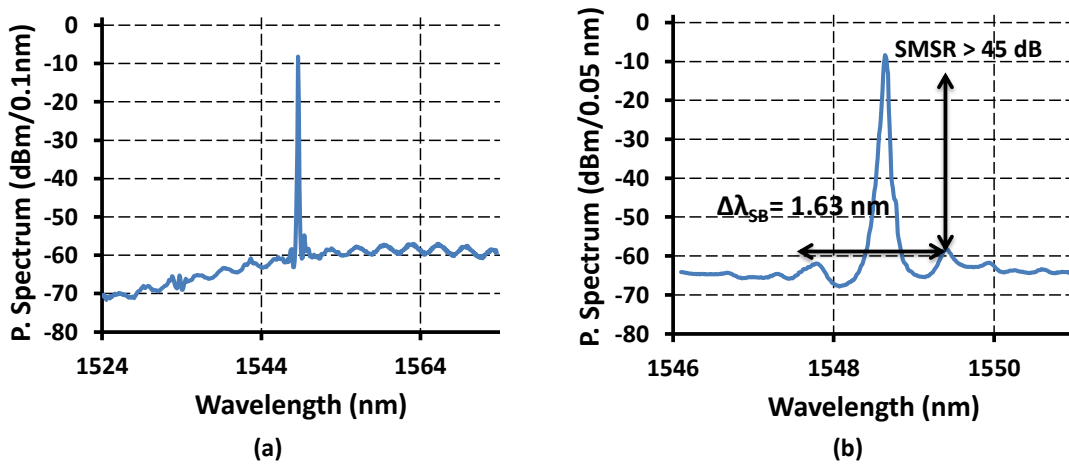


Figure 3.8: Spectrum of a  $600 \mu\text{m}$  long DFB laser. As  $n_g = 3.6$ ,  $\Delta\lambda_{FP} = 0.55 \text{ nm}$ . With  $\Delta\lambda_{SB} = 1.63 \text{ nm}$  we obtain  $NSB = 2.98$  and can extract  $\kappa L = 1.3$

## 3.2 Distributed feedback Directly Modulated Lasers

Directly modulated lasers are useful optical components for short reach and access networks. Improving their bandwidth is an active field of research, in particular for 100-400 Gb/s Ethernet data communications at 1.3  $\mu\text{m}$  [12] [13][14]. Record bandwidth of 55 GHz has recently been obtained [15]. In this thesis, I investigate III-V on silicon DML around 1.5  $\mu\text{m}$ . At 10 Gb/s, it may be interesting for XGSPON OLT and NGPON2 OLT and ONU. A cost-effective transmitter achieving a transmission distance of 20 km at 25 Gb/s is still challenging in the C band as chirp limits the reach. Such component could be used in future PONs as the international telecommunication union is considering 25 Gb/s C band ONU for future PON standards. Development of 25 Gb/s C band DML was one of the goal of the FP7 Sequoia project [16]. In the following section I introduce high speed DFB lasers.

### 3.2.1 High speed DFB lasers

Laser optoelectronic modulation response has a second order transfer function  $H(\omega)$ , with a relaxation oscillation pulsation/frequency  $\omega_r = 2\pi f_r$  and damping coefficient  $\gamma$ . Its expression is derived by a differential analysis of rate equations [17].

The transfer function is:

$$H(\omega) = \frac{\omega_r^2}{\omega_r^2 - \omega^2 + j\omega\gamma} \quad (3.7)$$

$H$  is peaked around  $f_r$  and decreases with a 40 dB/decade slope after  $f_r$ . As derived in [17], the relaxation oscillation pulsation is:

$$\omega_r^2 = (2\pi f_r)^2 \approx \frac{v_g a N_p}{\tau_p} \quad (3.8)$$

$v_g$  is the group velocity,  $a$  is the differential gain,  $N_p$  is the photon density in the cavity and  $\tau_p$  is the photon lifetime. We can write the photon lifetime as

$$\frac{1}{\tau_p} = v_g(\alpha_m + \alpha_0) \quad (3.9)$$

As described in fig. 3.4,  $\alpha_m \times L$  quickly decays with  $\kappa L$ . Although not really accurate, the approximation  $\alpha_m \approx \frac{1}{L(\kappa L)^2}$  indicates that decreasing  $L$  and the  $\kappa L$  product increases  $\alpha_m$  thus decreases photon lifetime.

However,  $\alpha_m$  must stay relatively low to keep low threshold. DFB targeting 25 Gb/s applications are usually between 200 and 400  $\mu\text{m}$  long and have  $\kappa L$  between 1 and 2. Use of

strained quantum well is an efficient way to increase  $a$  ([18],p110). Using 20 compressive strain quantum wells, more than 30 GHz bandwidth laser have been demonstrated [19]. The damping coefficient is given by:

$$\gamma = K f_r^2 + \frac{1}{\tau_{\Delta N}} \quad (3.10)$$

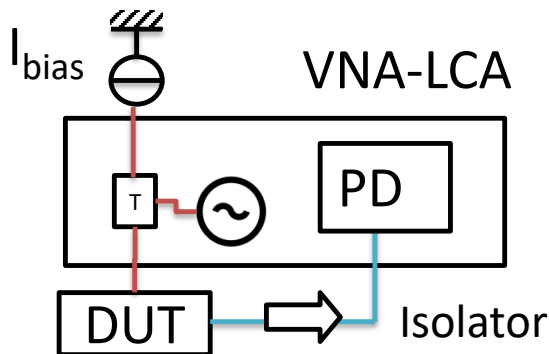
Neglecting nonlinear gain coefficients, we have  $K = 4\pi^2\tau_p$ .  $\tau_{\Delta N}$  is the differential carrier lifetime. The 3 dB frequency bandwidth is around the relaxation oscillation frequency:

$$f_{3dB} = f_r \sqrt{1 + \sqrt{2}} \quad (3.11)$$

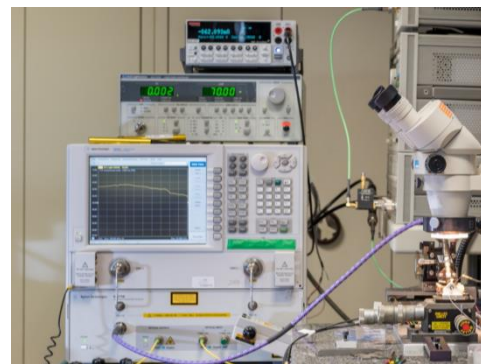
### Bandwidth measurements

I measured the electro-optical laser small signal responses with a dedicated bench sketched on fig. 3.9a and b. A small current modulation with frequency  $f = \omega/2\pi$  is added by a vector network analyser (VNA) and mixed with the bias current  $I_{bias}$ . Output optical signal is detected on a photodiode (PD) and analysed by the VNA. The modulation frequency  $f$  is swept from 0 to 20 GHz to recover the laser transfer function. Measured small signal bandwidth of a directly modulated laser has two contributions:

- Laser parasitic response due to capacitance
- Intrinsic laser response



(a)



(b)

Figure 3.9: (a) Sketch and (b) photograph of the measurement bench.

The parasitic capacitance may have several origins. In the case of our shallow ridge structure, the fact that  $p$  contact is above the  $n$  doped layer leads to a capacitance. With laser series resistor  $R_s$  it introduces a cut-off frequency  $f_C = \frac{1}{2\pi R_s C}$ . The measured response is the product of the two contributions:

$$|H(\omega)|^2 = \frac{\omega_R^4}{(\omega_R^2 - \omega^2)^2 + (\omega\gamma)^2} \times \frac{1}{1 + (\omega R_s C_{ld})^2} \quad (3.12)$$

Responses are measured for increasing bias current and are displayed in fig. 3.10a. To recover the intrinsic response, we need to separate the intrinsic opto-electronic response from the parasitic response. As the parasitic response is independent of bias current, we simply need to compare two biasing conditions to extract the parasitic response, as described in details in [20].

From those measurement we can extract  $f_C = 7$  GHz, as sketched in fig. 3.10b. With  $R_s \approx 5 \Omega$ , we have a parasitic capacitance of  $5$  pF. This value is higher than expected for the shallow ridge structure used in this thesis as typical values are around 400 fF [18]. This value can be reduced by simply etching the  $n$  doped layer which is below the  $p$  contact.

As we have subtracted the parasitic response, we can fit the resulting curve and extract the intrinsic 3 dB bandwidth and relaxation oscillation frequency (ROF).

As expected by equation 3.8, measured 3 dB bandwidth plotted in fig. 3.10c increases linearly with squared root of drive current, and achieves 13 GHz at 115 mA. I also plotted in fig. 3.10d the damping coefficient  $\gamma$  versus the square of relaxation oscillation frequency. The expected linear variation is well reproduced by experiments. As defined in eq. 3.10, we can extract from fig. 3.10d a  $K$  factor of 0.18 ns and  $\frac{1}{\tau_{\Delta N}} = 4.8$  GHz. The  $K$  factor corresponds to a photon lifetime  $\tau_p = 4.5$  ps, and  $\frac{1}{\tau_{\Delta N}}$  to a differential carrier lifetime of 0.2 ns. Those results are comparable with bandwidths of III-V on silicon lasers reported by other groups [21].

In this section I presented the direct modulation properties of III-V on silicon lasers which are compatible with high speed operation. In the next section I will discuss its chirp properties.

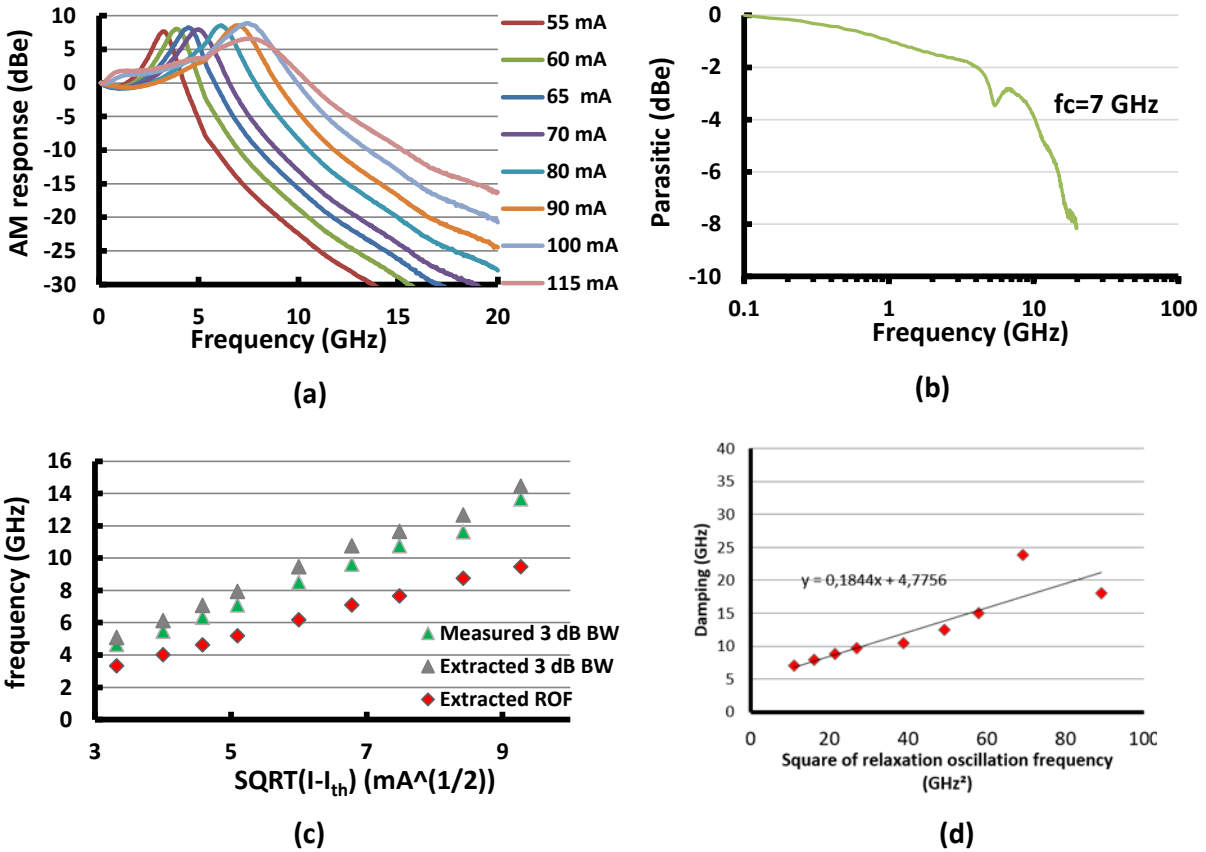


Figure 3.10: (a) III-V/Si DFB laser small signal bandwidth for increasing bias currents. (b) Extracted parasitic response. The dip around 5 GHz is caused by the VNA. (c) Measured 3 dB bandwidth (green triangles), extracted 3 dB bandwidth (grey triangles) and extracted relaxation oscillation frequency (red diamonds) versus  $\sqrt{I - I_{th}}$ . (d) Damping coefficient versus square of relaxation oscillation frequency.

### 3.2.2 DML chirp

In directly modulated lasers, we apply a current modulation  $\Delta I$  to obtain a power modulation  $\Delta P$ . In semiconductor lasers, phase and amplitude are coupled by the linewidth enhancement factor. An amplitude modulation leads to a frequency modulation. Induced frequency chirp is [17]:

$$\nu - \nu_0 = \frac{\alpha_H}{4\pi} \left( \frac{1}{P} \frac{dP}{dt} - \frac{R_{sp}}{P} + \frac{\epsilon_{NL} P}{\tau_p} \right) \quad (3.13)$$

In this equation,  $\nu_0$  is the unmodulated frequency,  $\alpha_H$  is the linewidth enhancement factor,  $P(t)$  is the modulated output power,  $R_{sp}$  is the spontaneous emission rate,  $\epsilon_{NL}$  is the gain compression factor and  $\tau_p$  is the photon lifetime.

A simple and accurate method to measure  $\alpha_H$  uses small signal amplitude and frequency response. We use the VNA to impose a small signal amplitude modulation with depth  $m$  and frequency  $f_m$ . the induced frequency modulation has an amplitude  $\beta$ . We measure intensity and frequency modulation response with a Mach-Zehnder interferometer locked on the laser wavelength with a feedback loop, as described in fig. 3.11a. A Mach-Zehnder interferometer converts frequency fluctuations into intensity fluctuations. Laser is first locked in position A of fig. 3.11b. In this position, positive frequency fluctuations are converted to positive

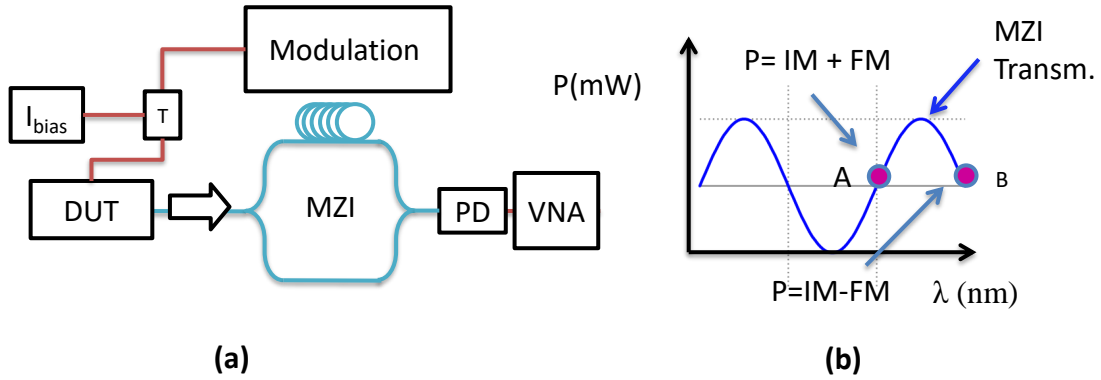


Figure 3.11: (a) Schematic of the measurement setup. (b) principle of operation

intensity fluctuations. In position B positive frequency fluctuation are converted to negative intensity fluctuations. As described in more details in [22], if  $M_+$  is the interferometer output in position A and  $M_-$  in position B we have:  $|\frac{2\beta}{m}|(f_m) \sim |\frac{M_+ - M_-}{M_+ + M_-}|$ . In [23], Schimpe et al. explained that  $|\frac{2\beta}{m}| \rightarrow \alpha_H$  when  $f_m$  is large compared to a "corner frequency"  $f_{cor}$  which is usually around 100 MHz. Measurement of  $|\frac{2\beta}{m}|$  is presented in fig. 3.12a, and evolution of  $\alpha_H$  with bias current in fig. 3.12b.  $\alpha_H \approx 2.5$  are typical values for quantum well lasers.

In equ.3.13, the first term is the transient chirp and the two other are adiabatic chirp.

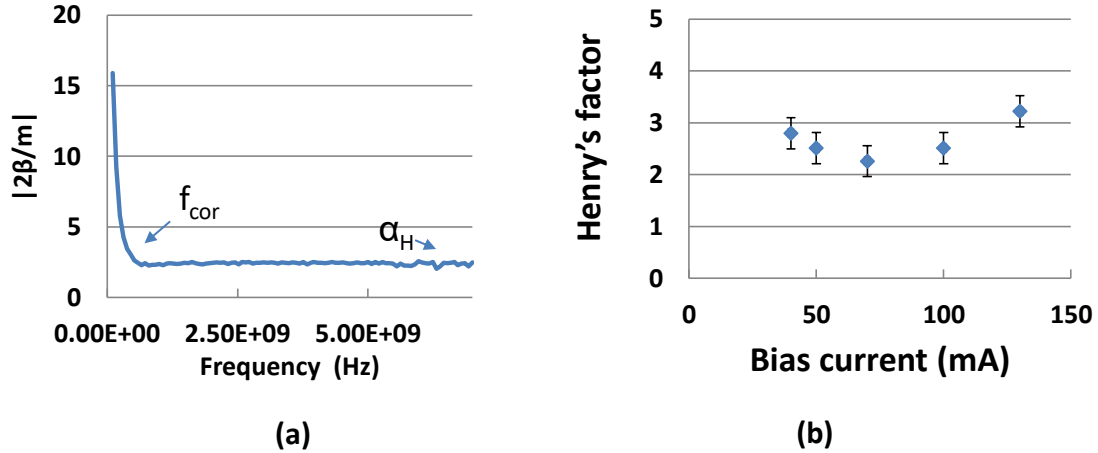


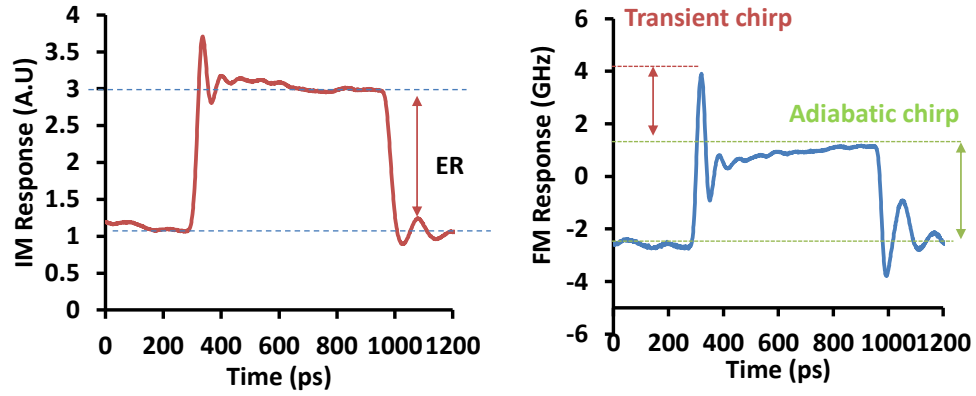
Figure 3.12: (a) modulus of  $\frac{2\beta}{m}$  showing the corner frequency  $f_{cor}$  and linewidth enhancement factor  $\alpha_H$ . (b) Measured  $\alpha_H$  for different bias current.  $\alpha_H$  is around 2.5 and slightly depends on bias current.

Adiabatic chirp is the frequency difference between "1" and "0" symbols (fig. 3.13.a). Transient chirp is associated to transitions from "0" to "1" symbols. To measure transient and adiabatic chirp, we modified the setup used for linewidth enhancement factor measurement. We replaced the small signal modulation by a large signal square signal at 1 GHz.

Both adiabatic and transient chirp depend on bias current and swing voltage. In [24] p.34, the author shows that for the same extinction ratio, adiabatic chirp increases with bias current while transient chirp stays constant.

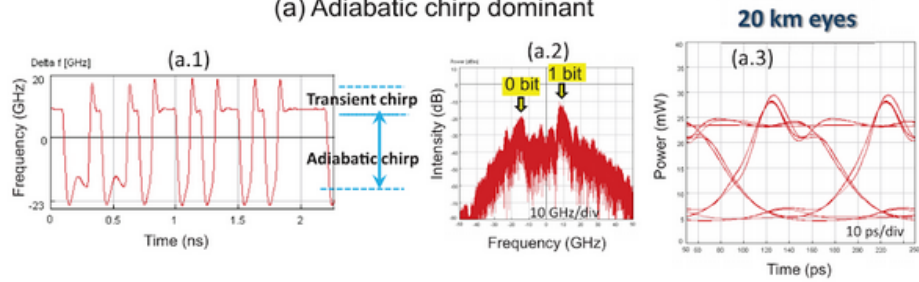
Here I show the results in the same experimental conditions to be presented in the 25 Gb/s transmission experiment. The large signal amplitude response is displayed in the left part of fig. 3.13a, with a 4.5 dB extinction ratio. The large signal frequency response is displayed in the right part of fig. 3.13a. I define transient and adiabatic chirp in this figure, as in [25]. The device shows a positive adiabatic and transient chirp of 3 GHz. Positive adiabatic chirp is expected for laser with no reflective facets (anti-reflection coated lasers or integrated lasers) as presented in [26] and [27], p139. Both adiabatic and transient chirp degrade eye diagram after transmission. However, as described in fig. 3.13b, adiabatic chirp has a much weaker influence on transmission.

In this section, I reviewed the chirp properties of hybrid III-V on silicon lasers. As we will see in the next section, chirp affects the transmission reach.

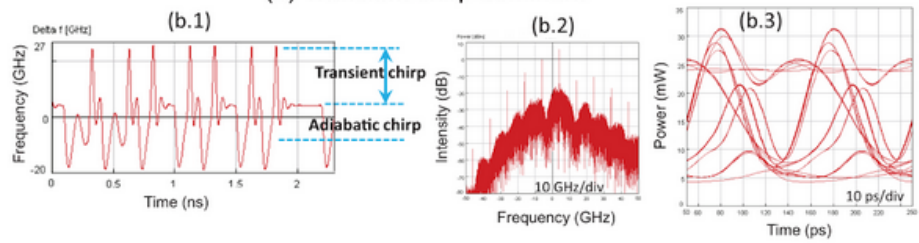


(a)

(a) Adiabatic chirp dominant



(b) Transient chirp dominant



(b)

Figure 3.13: (a) Large signal amplitude (left) and frequency response (right) with definition of extinction ratio (ER), transient and adiabatic chirp. (b) Simulated effect of adiabatic and transient chirp on transmission, from [25].

### 3.2.3 Pros and cons of DML sources

Distributed feedback directly modulated lasers (DML) have several advantages over externally modulated lasers. DFB are:

- simple to fabricate and easy to operate
- compact, low cost and low power consumption
- high power
- compatible with uncooled operation

However, DML may have limited reach and extinction ratio. As sketched in fig. 3.14, DML performances depends on bias current. If the bias current  $I_{bias}$  is close to threshold, we have a high extinction ratio  $\frac{P_2}{P_1}$  and a low adiabatic chirp. We have seen in the previous section that damping coefficient increases with bias current. If the damping coefficient is too low the eye diagram is disturbed as '0'  $\rightarrow$  '1' bit transition are affected by relaxation oscillations. If we increase the bias current to  $I'_{bias}$  and keep the same  $\Delta I$  we will have an extinction ratio  $\frac{P'_2}{P'_1}$  which can be greatly reduced compared to  $\frac{P_2}{P_1}$ . However, other parameters are improved. First, output power is proportional to  $I_{bias}$ . Secondly, 3 dB bandwidth is proportional to

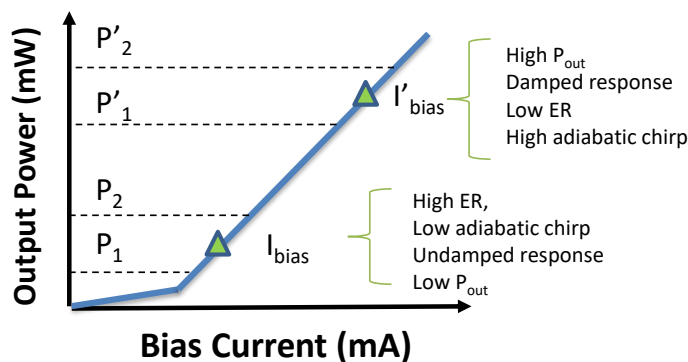


Figure 3.14: Optimisation of directly modulated laser modulation parameters. In usual directly modulated laser, there is a trade-off between output power and extinction ratio.

$\sqrt{I - I_{th}}$ . Then, damping factor  $\gamma$  increases with  $\sqrt{I - I_{th}}$ . A higher damping factor leads to cleaner eye diagrams. Nevertheless, if  $I_{bias}$  is increased,  $\Delta I$  has to be augmented to obtain the same extinction ratio. This leads to higher adiabatic chirp and a limited reach. For C band access networks a 6 dB extinction ratio with 20 km reach is needed, which is difficult

to obtain. In the next section I will discuss how to extend the reach of DMLs. In particular, I will present a filter for extinction ratio enhancement and reach extension.

### 3.2.4 Filtered DMLs and CML

Intensity modulation induces a detrimental frequency modulation. In the C band, fibre has a dispersion coefficient of 17 ps/nm/km. Hence spectral components don't propagate at the same speed and signal is distorted after a certain distance. InP DFB DML from III-V lab have a reach limited to 15 km at 10 Gb/s with 6 dB extinction ratio.

Using a low chirp material, Lelarge *et al.*[28] demonstrated a transmission distance of 65 km but extinction ratio was limited to 3 dB. As sketched in fig. 3.15a, in DML spectrum of symbol '0' is redshifted with respect to symbol '1'. The wavelength difference is the adiabatic chirp analysed in the previous section. Using an external spectral filter, we can take advantage of adiabatic chirp to enhance ER and reach. As indicated in this figure, the spectral filter has a sharp wavelength dependence. In fig. 3.15b, the filter is adjusted at its optimum position: it suppresses the '0' bit, enhancing the extinction ratio.

In 2006, Azna LLC demonstrated this behaviour [29]. They used a laser with an external

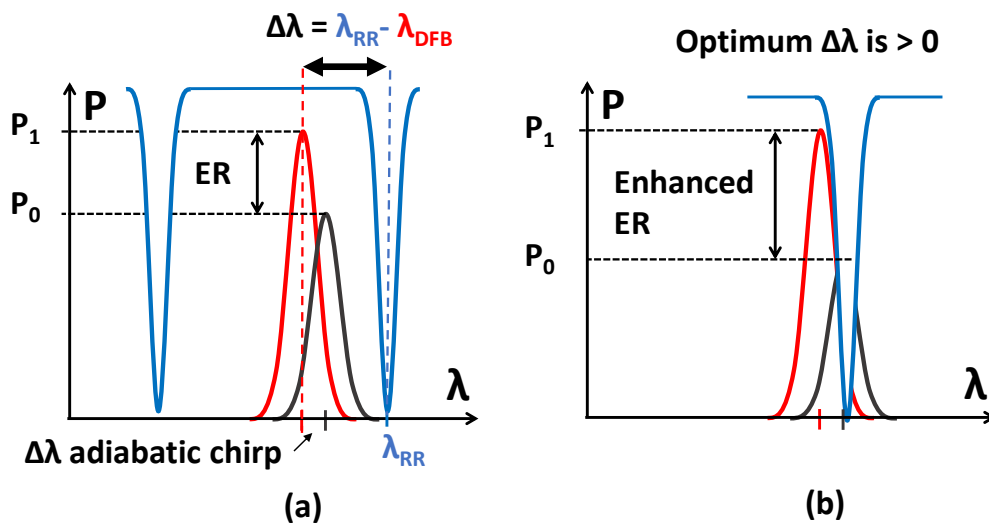


Figure 3.15: Operation principle of extinction ratio enhanced DMLs.

filter, integrated in a XFP package (fig. 3.16a).

To reduce its size, it would be interesting to integrate the filter closely with the laser. Different groups presented such a device. Each step represents an integration improvement: in fig. 3.16b (NEC), a planar lightwave circuit ring resonator (RR) is co-packaged with a laser [30].

At III-V lab, Chimot *et al.* developed a monolithically integrated laser and ring resonator on Indium phosphide in 2015 [31].

In this thesis, I present a novel integrated III-V/Si DFB laser and silicon ring resonator. silicon RRs have several advantages:

- small size and large free spectral range (FSR). A low footprint reduces manufacturing costs. In this work, RR footprint is only 5% of the total chip size. A small RR corresponds to a large FSR. A large FSR is more convenient for measurements as RR transmission dips can be easily detuned from laser wavelength.
- low internal loss. As internal losses are lower in our platform than in InP [31], RR with higher finesse is possible. Extinction ratio enhancement depends on filter slope thus on RR finesse.
- no technology complexity for the RR fabrication compared to that of standalone DFB lasers as RR are fabricated in the same technology process. In a pure III-V platform, active-passive integration is not straightforward as it requires regrowth [24].

In the next section, I will first recall the RR transmission formulae.

### 3.2.5 Add-drop ring resonator filters

Here, the extinction ratio enhancement filter is a silicon on insulator ring resonator. In this work, we use the through port noted  $b_1$  in fig. 3.17a.  $T$  is the power transmission coefficient of the directional coupler and  $\alpha_l = \exp(-\alpha_0 L/2)$  is the round trip amplitude loss. The round trip phase is  $\theta = \frac{2\pi}{\lambda} \times n_{eff} L$ , with  $L$  the ring resonator perimeter and  $n_{eff}$  the effective index of the waveguide. For the add-drop filter, we have the transmission formula:

$$\mathfrak{T}_t(\theta) = \left| \frac{b_1}{a_1} \right|^2 = \frac{T - T\alpha_l \times 2 \cos(\theta) + T\alpha_l^2}{1 - T\alpha_l \times 2 \cos(\theta) + (T\alpha_l)^2} \quad (3.14)$$

Transmission versus wavelength for different values of the directional coupler coefficient  $T$  is presented in fig. 3.17b, for a 200 GHz free spectral range. As  $T$  increases, filter transmission depth and insertion losses decreases.

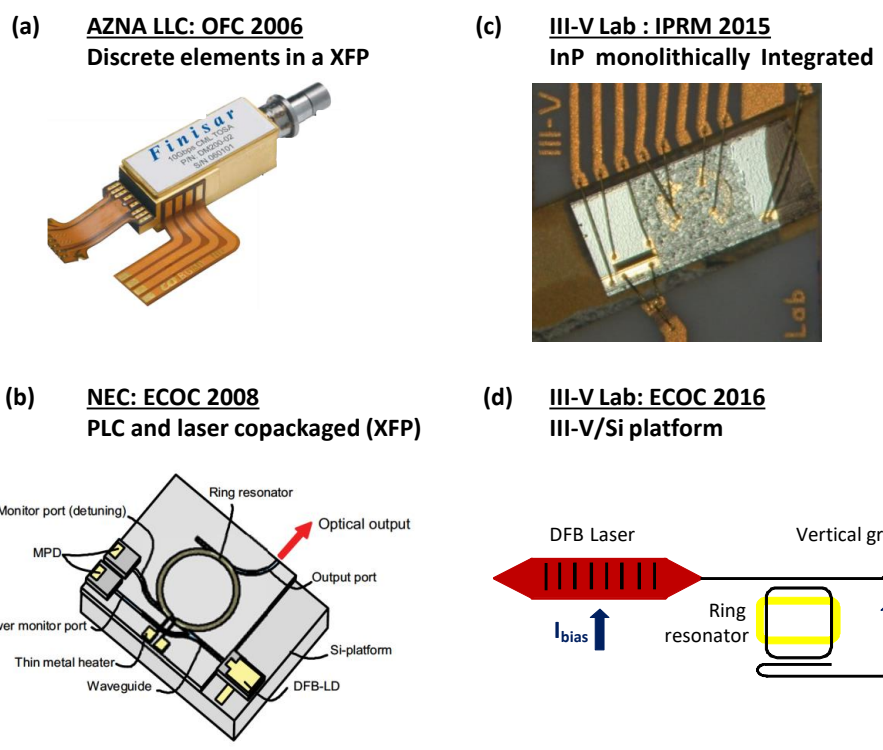


Figure 3.16: 4 implementations of the filter DML: (a) original demonstration by Azna LLc. (b) First integrated prototype with PLC. (c) III-V monolithic integration. Authors made active-passive integration by butt-joint. (d) Present work. Ring resonator footprint has been reduced by 100 compared to (c)

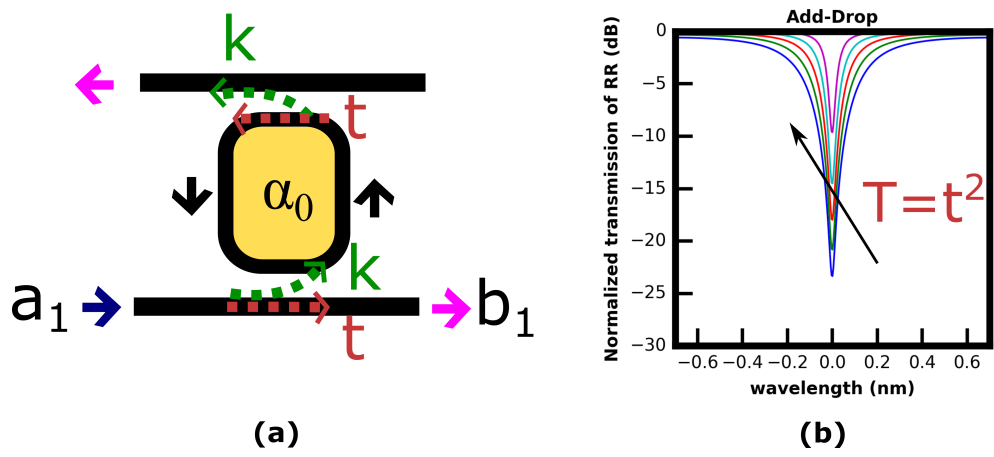


Figure 3.17: (a) Schematic of an add drop ring resonator filter. (b): through port transmission versus wavelength for a directional coupler coefficient  $T$  varying from 0.5 (blue) to 0.9 (purple) by 0.1.

### 3.3 Directly modulated III-V/Si DFB Laser integrated with extinction ratio enhancement filter

#### 3.3.1 Basic characteristics of extinction ratio enhanced DFB laser

As we use the through port of the ring resonator for filtering, we made all characterisations using this port. We first detune the ring transfer function from the laser wavelength to make it transparent and measure laser basic characterisations.

The laser L-I curve, presented in fig. 3.18b, shows threshold current of 37 mA and fiber coupled power of more than 2.5 mW. Waveguide output power is 4 times fiber coupled power as fiber grating couplers are not optimized and generate 6 dB loss. The differential efficiency is  $0.03 \times 4 = 0.12$  mW/mA.

Threshold of optimized InP DFB lasers are usually below 20 mA and maximum waveguide

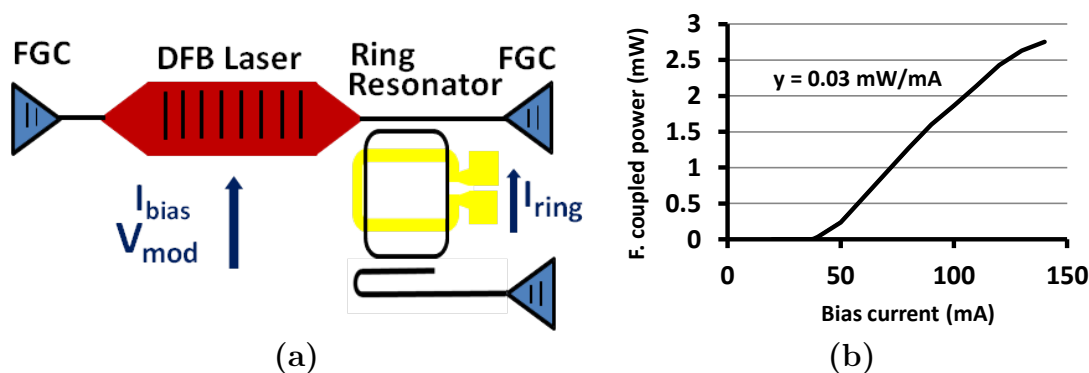


Figure 3.18: (a) Schematic of the hybrid III-V/SOI laser with RR extinction ratio enhancement filter. (b) L-I characteristics of a III-V/Si DFB laser measured after vertical grating, with 37 mA threshold and fiber coupled power greater than 2.5 mW.

output power is above 20 mW, twice the III-V/Si values. However, output power is already comparable to III-V on silicon lasers reported by other research institutions.

In fig. 3.19, we present the laser spectrum. The side mode suppression ratio is better than 40 dB, limited by a mode arising 10 nm away from the stop-band. In fig. 3.6b we noted that a mode with a slightly lower index (thus lower Bragg wavelength) than the main mode was present. This mode is mainly confined in the silicon waveguide and thus exhibits lower QW overlap but higher grating strength  $\kappa$ . In contrast with RR based tunable laser, the III-V/Si taper is outside the laser cavity. Hence the second mode threshold gain is not increased by the taper and it may compete with the dominant mode.

In the next section, I will introduce the extinction ratio enhancement filter which is after the laser.

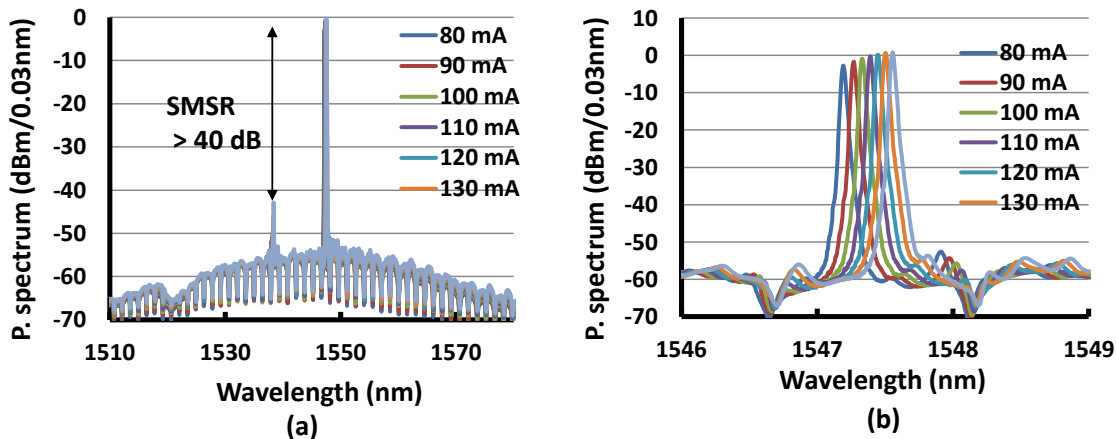


Figure 3.19: (a) Laser spectra for bias currents from 80 to 130 mA, showing SMSR greater than 40 dB. Amplified spontaneous emission is filtered by the ring resonator. (b) Close up spectra for different bias currents.

### 3.3.2 Fabricated RR filter

RR has a racetrack geometry with footprint of  $0.15 \times 0.045 = 0.007 \text{ mm}^2$ . As a first try, we chose a RR with  $FSR_R = 200 \text{ GHz}$  and  $T = 0.5$ . Measured transfer function of the fabricated RR is reproduced in fig. 3.20a, showing FSR of 187 GHz. Experimental data is fitted with equ. 3.14 with  $T\alpha_l = 0.52$ . This value is a little higher than the design value of 0.49 due to small fabrication errors.

On top of the RR, we deposited a nickel-chrome heater to finely tune the detuning  $\Delta\lambda$  between RR resonance and laser wavelength. In this fabrication run, the heater resistance is  $R = 690 \Omega$ .

As we inject current in the resistor, we dissipate a thermal power  $P_r$ . As heater temperature increases, the RR effective index increases and the RR comb shifts to longer wavelength. In fig. 3.20 we measured a wavelength shift of 2 GHz/mW. We can monitor  $\Delta\lambda$  with sub GHz accuracy with reasonable power consumption.

A small thermal crosstalk causes a laser wavelength drift of 6 GHz between the two curves. In the next section, I will review the impact of RR on laser dynamic characteristics when the filter is used as an extinction ratio enhancement filter.

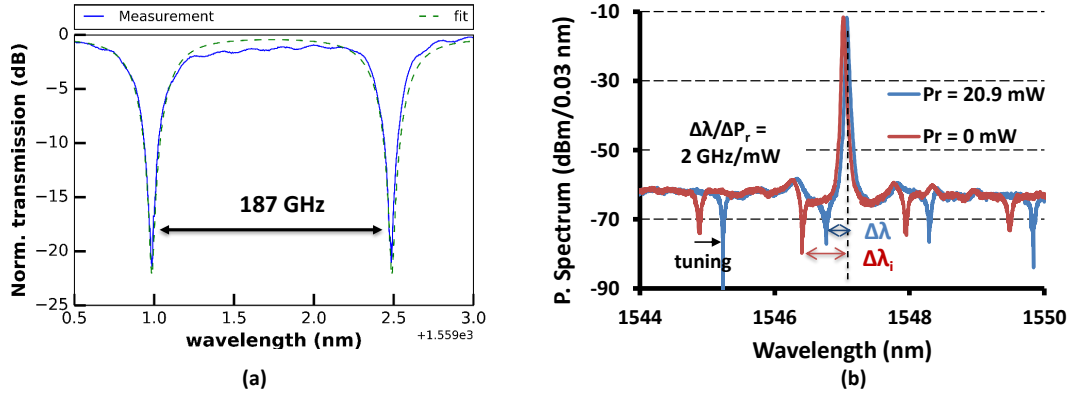


Figure 3.20: (a) Experimental (green) and fitted (blue dash) transmission of Fabricated SOI RR showing 20 dB extinction and 187 GHz FSR. (b) Spectrum of the laser + RR device, for two injected currents in the RR resistor. With the ring heater, it is possible to change the detuning  $\Delta\lambda$  between laser and RR.

### 3.3.3 RR impact on laser dynamics

As linewidth enhancement factor and nonlinear gain coefficients are positive, adiabatic chirp is positive: '1' symbols are blueshifted compared to '0' symbols. We thus work in a region of the filter where the transmission decreases with wavelength (Positive  $\Delta\lambda$ , as in fig. 3.15). We measure the large signal Intensity modulation (IM) response at 1 Gb/s in fig. 3.21a.

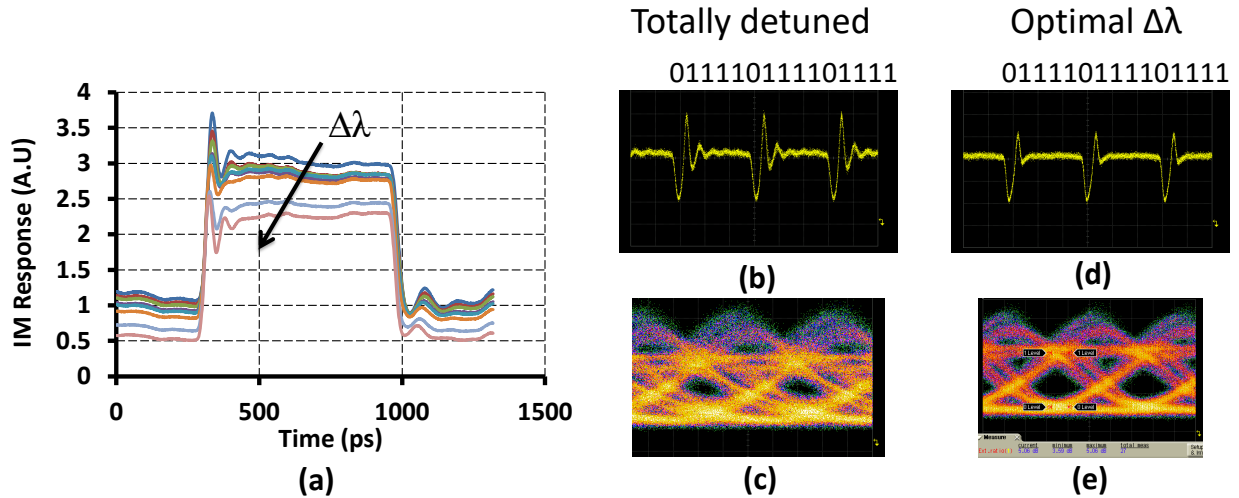


Figure 3.21: Effect of RR on IM response. (a) Measured IM response for decreasing detuning  $\Delta\lambda$  showing increase of extinction ratio. (b) Sequence of 1 bits at 25 Gb/s followed by one zero when the RR transmission is totally detuned. (c) The corresponding eye diagram at 25 Gb/s is noisy. (d) Same sequence of bit in the optimal RR tuning condition and (e) corresponding open eye diagrams.

As  $\Delta\lambda$  decreases, modulation depth increases from 4.5 to more than 6 dB using the RR filter. Moreover, the influence of relaxation oscillation frequency on IM response is greatly reduced, as sketched on the right panel. Measured intensity for a sequence of '1' symbols at 25 Gb/s followed by one '0' symbol is displayed in fig. 3.21.b when the ring transmission is totally detuned. After a  $1 \rightarrow 0$  transition, '1' symbols are distorted. As this is also seen on  $0 \rightarrow 1$  transitions, eye diagram is noisy. Those experimental conditions were chosen to have a high extinction ratio with low chirp, resulting in a response which is not sufficiently damped.

As sketched in fig. 3.21de, the picture is really different in the optimal detuning condition of laser and RR as '1'  $\rightarrow$  '0' transitions now have little impact on following symbols. This IM improvement due to filtering was highlighted in [29] (fig.2). It is due to the limited bandwidth of the filter as well as frequency modulation to intensity modulation conversion. In [25] p 126, the author points out that the main feature of CML was the flat FM response induced by  $IM \rightarrow FM$  conversion. Using the same setup as in 3.2.2, we measured the large signal chirp for decreasing  $\Delta\lambda$ . Results are reported in fig. 3.13a in the biasing conditions of 25 Gb/s transmission experiment of section 3.4.2. When  $\Delta\lambda$  decreases, the transient chirp

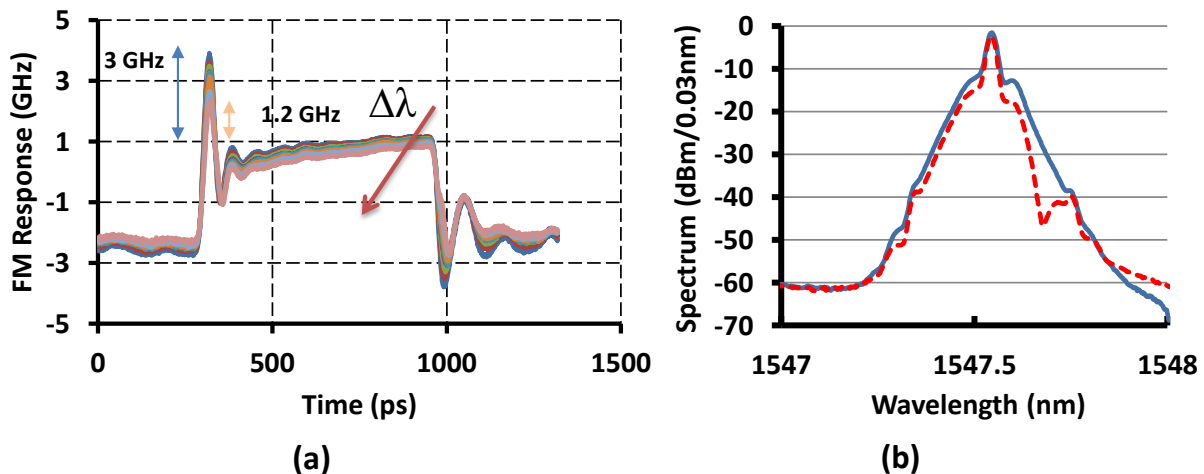


Figure 3.22: (a) Large signal frequency response for decreasing detuning  $\Delta\lambda$ . (b) Spectrum when  $\Delta\lambda$  is large (no impact on spectrum) in blue, and for the optimal  $\Delta\lambda$  used in the transmission experiment in red.

is filtered out and decreases from 3 GHz to 1.2 GHz, while adiabatic chirp is only slightly reduced from 3.3 to 3.2 GHz. The transient chirp reduction is attributed to  $IM \rightarrow FM$  conversion. The negative acquired chirp is proportional to the filter slope, as described in [25], p 125.

As indicated in fig. 3.22b, reducing transient chirp is critical to increase reach as it has a great impact on signal transmission. Transient chirp values are different from [4] as an alternative definition was used. We also plot the modulated spectrum of the laser with (red) and without (blue) RR filtering in fig. 3.22b. We can clearly see the cut-off of red-side spectral component by the RR. As already mentioned this spectral component corresponds to '0' symbol.

As both adiabatic and transient chirp parameters are very low, it will be possible to transmit data on distances standardized in access networks. In future works, we may decrease even more transient chirp to obtain a flat top FM response and achieve longer distances.

## 3.4 Transmission experiments

### 3.4.1 Modulation at 10 Gb/s

A schematic of the transmission experimental setup is shown in fig. 3.23. I already described eye diagram and bit error rate (BER) measurements in section 2.3.3. Bias and pseudo random bit sequence (PRBS) with  $2^{31} - 1$  bits are mixed with a bias T. An isolator protects the laser from reflections which affect the BER. Hybrid III-V on silicon laser sensitivity to feedback has been studied in [32]. The laser light propagates on various lengths of single-mode-fiber (SMF), and is switched to either eye diagram or BER measurements. At 10 Gb/s, the avalanche photodiode (APD) in the receiver has a sensitivity of -32 dBm at  $\text{BER} = 10^{-3}$ . This BER value is chosen as it is the forward error correction (FEC) limit in NG-PON2 access network.

To overcome fiber losses there is an erbium-doped-fiber-amplifier (EDFA) and a band

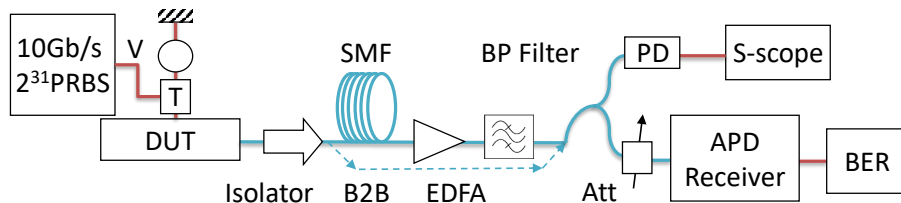


Figure 3.23: Experimental setup at 10 Gb/s.

pass filter inserted in the transmission line. Before the error counter there is a variable attenuator to measure the bit error rate as a function of received power. To determine the best configuration for a long reach transmission, the integrated DFB and RR chipset is at

first optimized in a back to back (B2B) configuration. The DFB is biased at  $I = 83 \text{ mA} \approx 2I_{th}$  with a  $V_{pp}$  of 1.6 V. The SMF-coupled output power is 1.5 dBm. Using the ring heater, we vary the detuning between laser and ring resonator dip. As the detuning decreases, the BER is improved up to an optimal value. Extinction ratio increases from 5.3 dB when the ring doesn't filter to 6.5 dB in the best case. This configuration is retained for a transmission experiment, and the results are presented in fig. 3.24. As can be seen in the red curve of fig. 3.24, the back to back BER reach below  $10^{-10}$ . The  $10^{-3}$  sensitivity is -29 dBm. The 3 dB penalty compared to APD sensitivity is attributed to imperfect eye diagram (overshoot) and non optimal extinction ratio ( $ER < 10 \text{ dB}$ ). The  $10^{-3}$  sensitivity is 1dB better after 25 km (green curve). This is consistent with an eye diagram slightly more open. The device shows no penalty compared to back to back for a 50 km transmission (purple curve). Eye diagram is widely open and BER reaches below  $10^{-10}$ . 75 and 90 km transmissions are possible with a penalty of 2 and 5 dB respectively. An error floor arises at BER =  $10^{-6}$  and  $10^{-4}$  for 75 km (black curve) and 90 km (yellow curve) respectively and eye diagrams are distorted.

The 50 km eye diagram shows long '1'  $\rightarrow$  '0' symbol transitions. As '1' bit are blue-shifted,

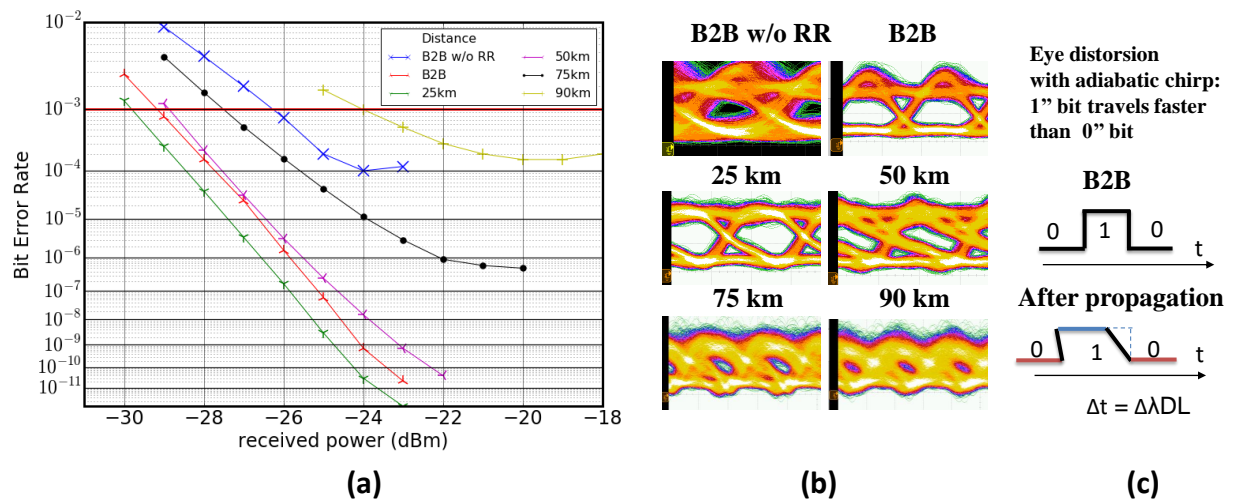


Figure 3.24: Transmission results at 10 Gb/s. (a) Bit error rate versus received power for different fibre length. (b) Corresponding eye diagrams. (c) Eye diagram distortion with adiabatic chirp. As '1' bits arrives sooner than '0' bits  $1 \rightarrow 0$  transitions are longer after propagation.

they travel faster than '0' bit, with an arrival time difference  $\Delta t = \Delta\lambda DL$ . In this formula,  $\Delta\lambda$  is the adiabatic chirp,  $D = 17 \text{ ps/nm/km}$  is the fiber dispersion and  $L$  is the fibre length. With  $\Delta\lambda = 0.025 \text{ nm}$  and  $L = 50 \text{ km}$ ,  $\Delta t = 22 \text{ ps}$ , a quarter of the bit duration at 10 Gb/s. The calculated  $\Delta t$  is consistent with the distortion of the 50 km eye diagram. This phenomenon is sketched in fig. 3.24c.

The back to back BER curve when the RR is totally detuned (blue curve) is obtained in the same biasing condition as the other curves. As biasing conditions are no longer optimised, the penalty is 3 dB compared to the optimal condition with RR filter. When the RR is detuned, the 50 km transmission is not possible for all biasing conditions, demonstrating the performance enhancement when using a RR filter.

### 3.4.2 Modulation at 25 Gb/s and beyond

After an upgrade of the measurement bench, I operated the laser + RR chipset at 25.5 Gb/s. EDFA is removed from the transmission line and placed only for eye diagram measurement as achievable distances are lower at 25 Gb/s than at 10 Gb/s. The receiver is now an integrated semiconductor optical amplifier and PIN photodiode, with a sensitivity of -27 dBm at BER of  $10^{-3}$ . Further details about this receiver can be found in [33].

DFB laser is now biased at 100 mA with a 1.8 Vpp swing, corresponding to the optimized condition for the 20 km transmission distance. The RR gives the best BER performance enhancement for a power loss of 2.2 dB, resulting in 0 dBm of fibre coupled power and an ER of 5 dB. Fig.3.25a shows the BER results of the transmission experiment. The back to back

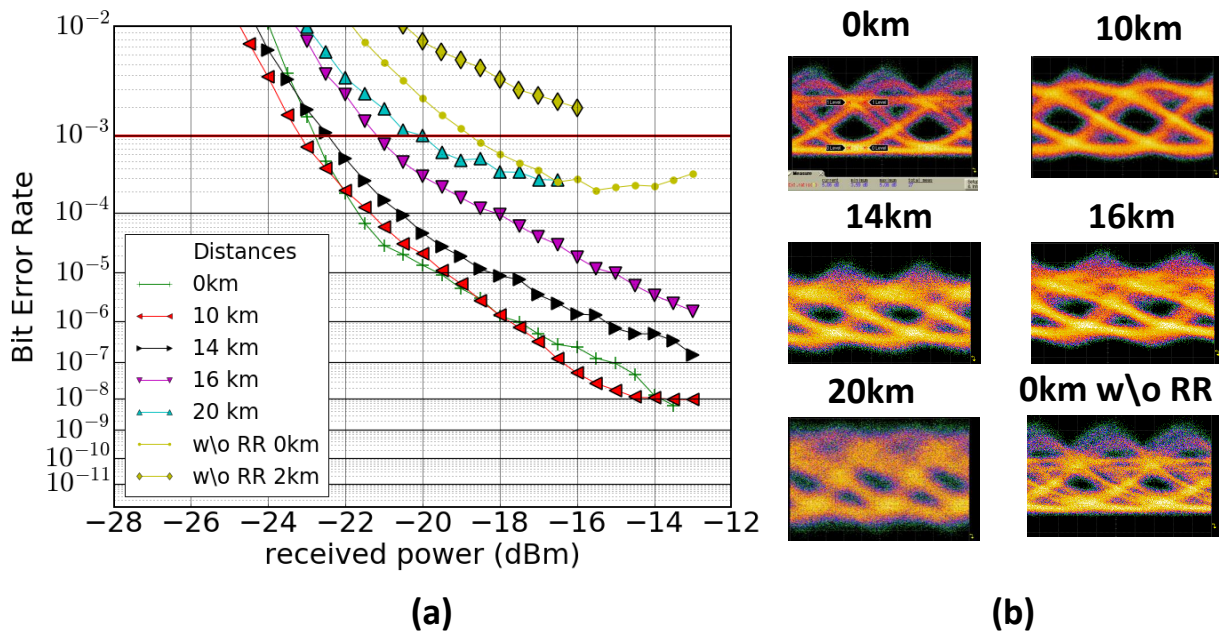


Figure 3.25: (a) Bit Error rate measurements at 25.5 Gb/s for different propagation distances (b) Corresponding Eye diagram.

(green cross) and 20 km (cyan triangle) sensitivity are -22.5 dBm and -20 dBm respectively.

As the fiber coupled power is 0 dBm, the power budget is hence 20 dB for a transmission distance of 20 km.

As the receiver decision threshold and delay are optimized only for a received power of -17 dBm for all curves, the BER curve slope changes at higher received power due to non optimal decision threshold. For this reason, back to back sensitivity at  $BER = 10^{-3}$  could be improved by at least 1.5 dB.

A very small penalty of less than 0.5 dB is observed for propagation distances up to 14 km. Transmission under  $10^{-3}$  FEC limit is possible up to 20 km with 2.5 dB penalty.

Fig.3.25 shows that eye diagrams remain open after transmission. When the RR is largely detuned (yellow dots) the sensitivity is 4 dB worse than with RR and error floor appears. The transmission penalty drastically increases with more than 4 dB after 2 km (yellow diamonds), evidencing the beneficial role of the RR filter.

Fig. 3.26 shows result in similar conditions with 28 and 32 Gb/s signals. In Back to back configuration, the BER sensitivity is -21.5 dBm and -22 dBm for 28 and 32 Gb/s respectively hence less than 1dB worse than for 25 Gb/s signals. Reach is limited to 16 km at 28 Gb/s and 10 km at 32 Gb/s.

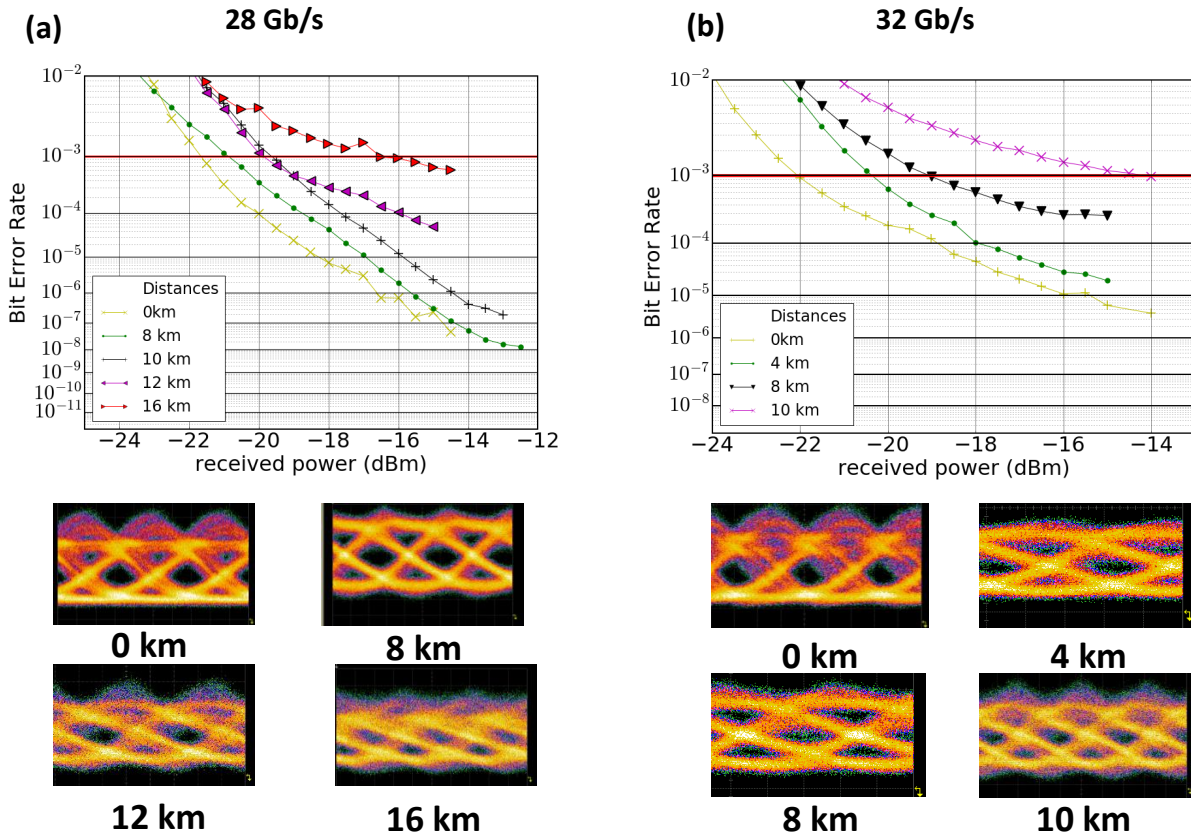


Figure 3.26: Bit Error rate measurements and eye diagrams at (a) 28 Gb/s (left) and (b) 32 Gb/s (right). Compared to 25 Gb/s, reach is limited to 16 km at 28 Gb/s and 10 km at 32 Gb/s. The bandwidth limitation can be seen on the eye diagram.

### 3.4.3 Comparison with state of the art

As described in table 3.1, the fabricated devices compete with state of the art III-V/Si DFBs demonstrated by other research institutions. Reported fiber coupled power of III-V on silicon DFBs are a few mW. There are high fibre coupling losses as it is still difficult to implement low loss grating or edge coupler in the III-V on silicon platform. This problem will be solved in a near future as those components are already available in the silicon platform [34]. Apart from the result reported by Intel, waveguide coupled power are around 10 mW. Intel proved that III-V on silicon DFBs with similar characteristics to their pure III-V counterpart are possible.

Abbasi et al. [21] reported 28 Gb/s operation with bandwidth similar to the work presented here. To go beyond 28 Gb/s, it is possible to use bandwidth enhancement with photon-photon resonance. This phenomenon is associated with a passive feedback from a reflector near the laser facet [35] or the grating coupler [36]. As this effect depends on the feedback phase, it requires an additional control. It is also possible to adapt III-V DMLs designs of [14] to III-V on silicon lasers.

	Group	Year	$\lambda$ ( $\mu\text{m}$ )	$I_{th}$ (mA)	L ( $\mu\text{m}$ )	wg P (mW)	fib. P (mW)	mod. speed
Zhang et al.[37]	UCSB	2014	1.5	9	200	3.8	/	12.5
Abbasi et al.[21]	Gent U.	2015	1.5	17	400	6	1.2	28
Duprez et al.[38]	CEA Leti	2015	1.3	36	700	11	2.8	12
Blum [39]	Intel	2017	1.3	20	/	25	/	/
This work [4]	III-V Lab	2017	1.5	37	600	/	2.8	28

Table 3.1: III-V on silicon lasers state of the art.

We now need to compare our transmission results with other filtered DMLs. As sketched in table 3.2 and fig. 3.16 several group reported 10 Gb/s results as it is an industry standard for 1.55  $\mu\text{m}$  metropolitan networks. Chirp managed lasers [29] and [30] have superior transmission characteristics as:

- Laser bandwidth and operating conditions are optimized
- Laser adiabatic chirp and filter are optimized to obtain a flat top FM response

Filtered DML show transmission distance greater than needed for access networks (20-40 km). Output power in [31] is greater than non integrated devices. This is not an intrinsic difference as non integrated device packaging can be very low loss. However, ref. [31] proves

that with monolithic integration in InP, a high output power emitter can be made in a very small form factor. Our device is also fully integrated, and features a size reduction greater than 5 compared to [31]. Performances are lower in term of output power as our device has non optimal design/fabrication, and high coupling losses. A significantly higher bias was used in [31].

Higher bitrates were first investigated in [40], already achieving 40 Gb/s operation. The filtered DML gained attention again as they may be used for future Passive optical networks. First results were obtained using non integrated laser and silicon RR filter [2], or commercial filter [41].

In this thesis, I presented the first integrated filtered DML working at 25 Gb/s. The device has a 20 km reach with BER below the usual FEC limit of access networks. Fiber coupled power is 0 dBm and the receiver sensitivity after transmission is -20 dBm. Filter power penalty has not been taken into account in [40] and [41] in contrast with the work presented here.

10 Gb/s	Group	size $mm^2$	Distances (km)	ER (dB)	P (dBm)
Maghrefteh et al. [29]	Azna LLC	42.25	200	11.5	0
Yokoyama et al. [30]	NEC	5.8	300	7.4	-1
Chimot et al. [31]	III-V Lab	0.76	65	9	5.8
This work [3]	III-V Lab	<b>0.12</b>	90	6.5	-3

higher bitrate	Group	size $mm^2$	Distance (km)	ER (dB)	P (dBm)
Yu et al. [40]	NEC	non int.	15.8 km @ 40 Gb/s	5	9
Abbasi et al. [41]	Gent. U	non int.	20 km @ 28 Gb/s	4.8	-2
This work [4]	III-V Lab	<b>0.12</b>	20 km @ 25 Gb/s	5	0

Table 3.2: Filtered DML state of the art at 10 Gb/s and for higher bitrate

### 3.5 Design improvements

In the result presented above, we obtained a reach of 90 km at 10 Gb/s and 20 km at 25 Gb/s, with BER below access network FEC limit. To obtain those results, we work with a 6.5 dB ER at 10 Gb/s and 5 dB extinction ratio (ER) at 25 Gb/s. In those operation conditions, the extinction ratio improvement is limited by the designed RR. Future emitters should have fiber coupled power greater than 5 dBm and ER greater than 10 dB.

The later condition is important for operation in four level amplitude format PAM4. With

PAM4, we can double the bit rate with the same symbol rate (expressed in Baud units). However, in PAM4  $ER$  has to be increased to obtain the same performances as On-Off keying. Preliminary PAM4 results of the laser + RR chipset at 25 Gb/s (12.5 Gbaud) are shown in fig. 3.27. Optical eye diagrams are not sufficiently open to obtain good transmission results.

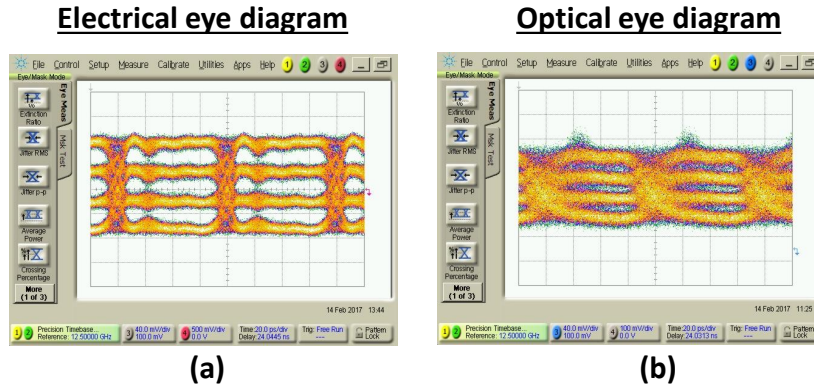


Figure 3.27: PAM4 modulation at 25 Gb/s (12.5 Gbaud). (a) Electrical eyes and (b) optical eye diagram back to back. The eye opening is reduced because of a low achievable extinction ratio.

To obtain  $ER \approx 10$  dB there are two options:

- Increase voltage swing
- Increase filter slope

Extinction ratio and adiabatic chirp increases with voltage swing. A greater adiabatic chirp lead to a more efficient filtering. However, as both transient and adiabatic chirp increases, it may be impossible to obtain long transmission distances. If we increases the filter slope, it could be possible to keep a low chirp and achieve  $ER > 10$  dB.

For 25 Gbaud PAM4, laser bandwidth should be higher than 20 GHz. We tried to increase laser bandwidth in a fabrication run completed in 2017. In this fabrication run, laser length was decreased to 400  $\mu\text{m}$ . Fibre coupled power reached 4 mW at 200 mA, slightly higher than the first generation. Laser bandwidth is also improved, as sketched in fig. 3.28, with measured 3 dB bandwidth greater than 14 GHz. In the modulation response, there is a small low frequency cut-off in the 0-2 GHz region. This phenomenon may be due to carrier transport effects [42] [25].

### New filter design

In the previous section, I showed that filtering enhances the amplitude modulation response, with lower influence of relaxation oscillation frequency, and the frequency modulation re-

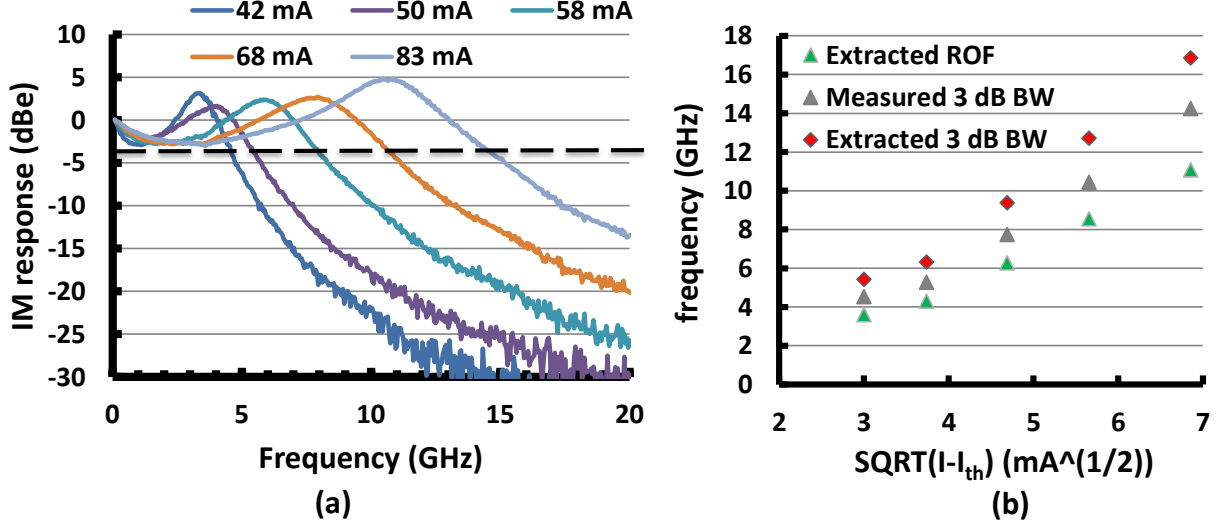


Figure 3.28: (a) DFB laser small signal bandwidth. Feedback from vertical coupler affects bandwidth at higher bias current.(b) Measured frequency parameters versus  $\sqrt{I - I_{th}}$ .

sponse, with lower transient chirp. However, the extinction ratio enhancement was limited. New filters designs are needed to have larger extinction ratio enhancement.

In this work, the RR filter has directional coupler coefficient  $T = 0.5$  and a free spectral range of 187 GHz. The extinction ratio enhancement is proportional to the derivative of the RR transmission (filter slope). As described in fig. 3.29a, increasing the coefficient  $T$  increases the filter slope coefficient. As the filter is operated with 3 dB insertion losses or less, I plotted the slope at -3 dB in fig. 3.29b to better compare the impact of the coefficient  $T$  on filtering properties. A filter with  $T= 0.9$  should be integrated with a DFB laser. It would be interesting to compare the insertion losses and extinction ratio enhancement of such device with the work presented here. Another solution is to use an alternative filter architecture. A ring resonator in a "notch" configuration with only one directional coupler (fig. 3.30b) is particularly suited for extinction ration enhancement as it may have a high filter slope. The notch filter intensity transfer function is:

$$\mathfrak{T}_n = \frac{T + \alpha_l^2 - 2t\alpha_l \cos(\theta)}{1 + T\alpha_l^2 - 2t\alpha_l \cos(\theta)} \quad (3.15)$$

Fig. 3.30b shows the transmission versus wavelength of the notch filter for different directional coupler values. It has a very different spectral shape when compared to the add drop filter. If the coupling coefficient of the directional coupler is very different from the loss coefficient  $\alpha_l$ , the filter has a flat response. If it is close to this value, it is a very sharp filter

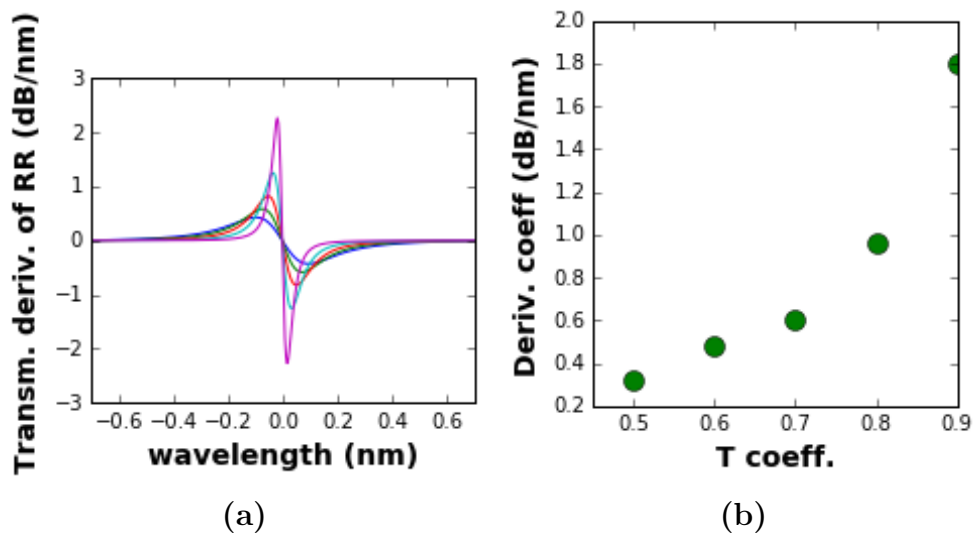


Figure 3.29: (a) Derivative of the RR transfer function versus wavelength for  $T=0.5$  (blue) to  $T=0.9$  (purple) by 0.1. (b) Extracted filter slope at -3 dB insertion loss.

(critical coupling).

This feature makes it more dependant of the fabrication process than add-drop rings:  $\alpha_l$  depends on waveguide losses which can vary with a factor 4 depending on fabrication conditions. In the Add-Drop configuration, coupling losses of the second directional coupler help to have a transmission quasi independent of internal losses. A notch filter should be integrated with a DFB laser in a new fabrication run.

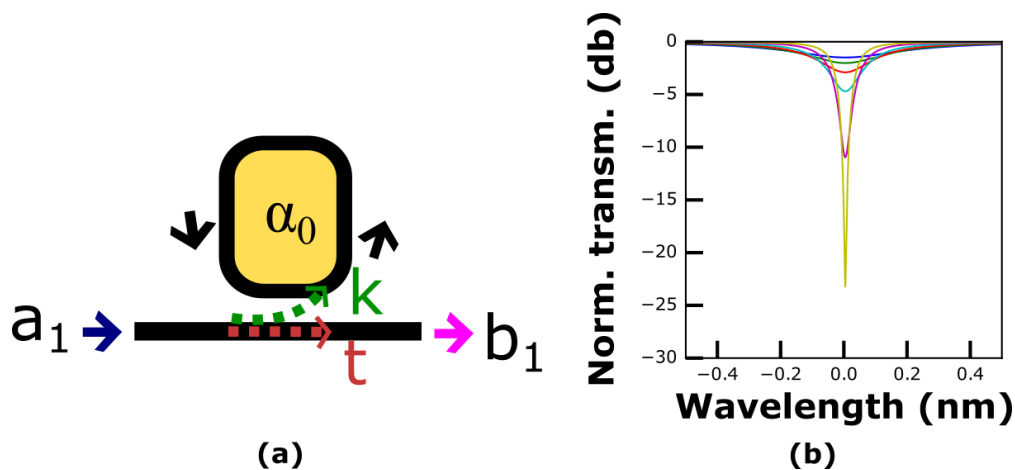


Figure 3.30: (a) Schematic of an add drop ring resonator filter. (b): transmission versus wavelength for a directional coupler coefficient  $T$  varying from 0.5 (blue) to 0.9 (purple) by 0.1 and 0.95 (yellow).

### 3.6 DFB laser with tapered grating

As explained in introduction, it is easier to use  $\lambda/4$  phase-shifted lasers rather than HR-AR laser: cleaving the laser and making a coating on an integrated laser facet is not convenient. However,  $\lambda/4$  phase shifted lasers suffer from lower external efficiencies as the power is emitted equally at both ends of the cavity. In this section, I report on a hybrid III-V on SOI DFB laser without phase-shift or coatings.

The grating structure is similar to a dual-pitch laser proposed in [1] and realized in [43]. In this design the effective refractive index is constant in a first section and varied in a second short section. It is sketched in fig. 3.31: To qualitatively understand how this design works,

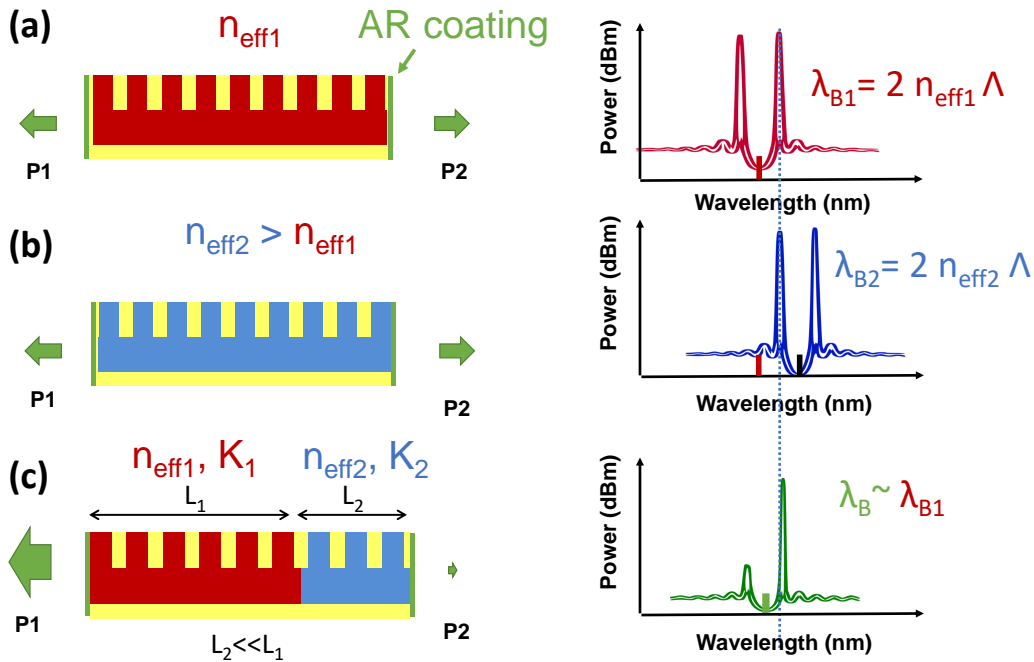


Figure 3.31: Phase shift free DFB principle. Spectrum depends on the effective index of the waveguide (a). In (b), effective index is slightly increased compared to (a). (c) proposed structure.

we can consider each section independently, as presented in fig. 3.31ab. If an AR-AR coated DFB laser is made of each section, each laser is dual mode. The two DFB sections have a Bragg wavelength  $\lambda_{B1,2}$  which is slightly different. In the second section the effective index  $n_{eff2}$  is greater than in the first section, leading to stop-band shifted to higher wavelength. The proposed structure, sketched in fig. 3.31c is composed of a section of index  $n_{eff1}$  and length  $L_1$  and a section of index  $n_{eff2}$  and length  $L_2$ . With this design, the threshold gain of the mode with higher wavelength is lowered as there is a greater feedback for this mode.

As  $L_2 \gg L_1$  the cavity modes are only a little perturbation of the homogeneous DFB presented in fig. 3.31a. TMM simulations indicate that the grating strength ratio controls the output power ratio  $\frac{P_1}{P_2}$  leading to higher per facet efficiency than  $\lambda/4$  phase shifted lasers.

### device presentation

The hybrid III-V on silicon structure is recalled in fig. 3.32, with the longitudinal and transverse cross section. The tapered grating device structure top view is presented in

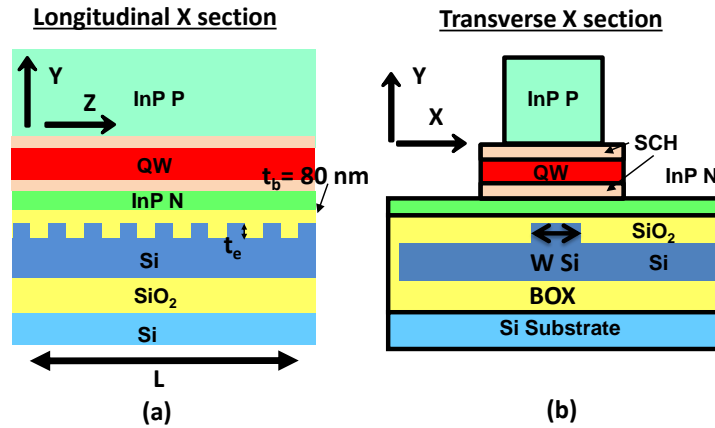


Figure 3.32: Hybrid III-V on silicon longitudinal (a) and transverse (b) structure. Device Parameters depend on  $W$   $Si$ .

fig. 3.33a. The laser silicon waveguide, represented in orange, is under the III-V stack pictured in red. The passive silicon waveguide, in blue, leads to a fibre grating coupler (FGC) at the left side.

The device has a  $370 \mu\text{m}$  long first section with a grating strength  $\kappa_1 = 47 \text{ cm}^{-1}$ . In the  $30 \mu\text{m}$  second section, the silicon waveguide is gradually enlarged, leading to two effects:

- The grating strength is increased
- The effective index is increased

The grating strength  $\kappa$  increase with waveguide width  $W$   $Si$  is depicted in fig. 3.33b in blue. As already presented in section 3.2, it comes from a higher confinement in the grating with increasing  $W$   $Si$ . The mean value of  $\kappa_2$  is twice the value of the first section, resulting in a total  $\kappa L$  product of 2.

As silicon has a higher effective index than III-V material the hybrid mode effective index increases with  $W$   $Si$ , as presented in fig. 3.33.b in red. The refractive index in the second

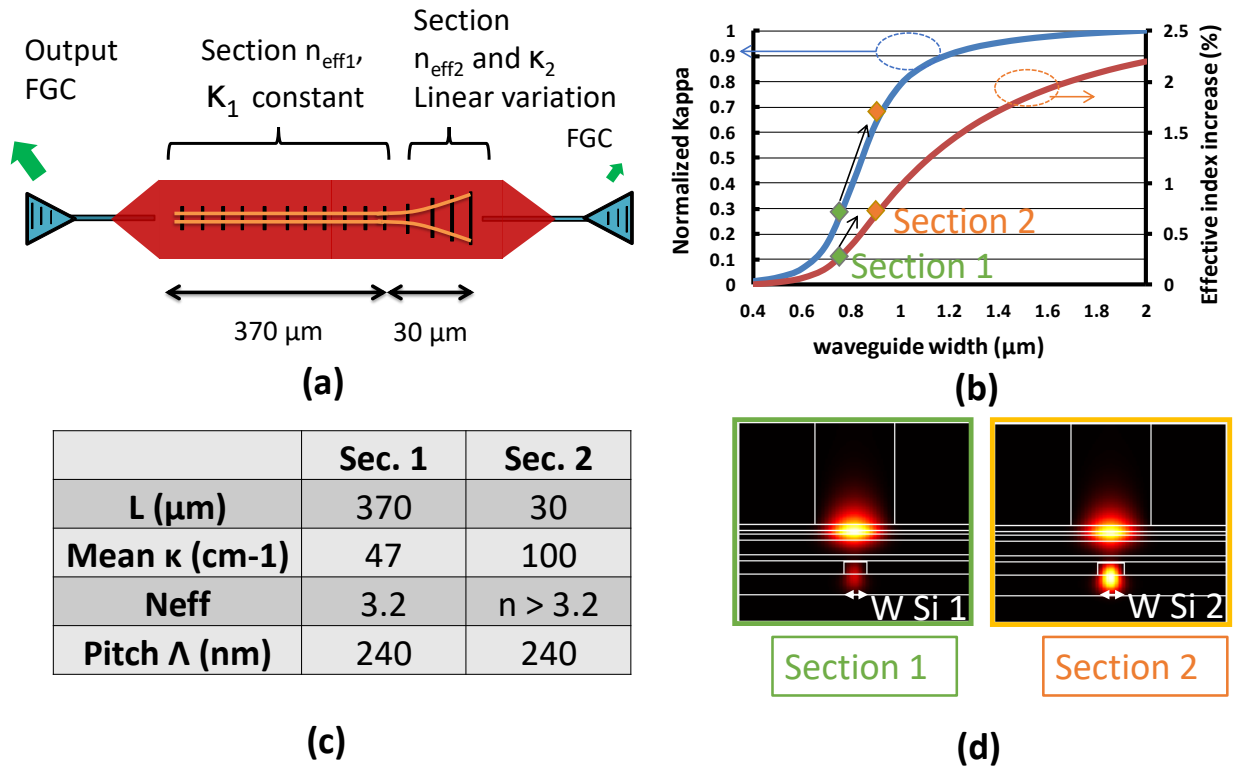


Figure 3.33: Tapered grating design. (a) Sketch of the device. (b) The effective index and grating strength of the uniform grating is represented by a green dot. In the tapered region, both effective index and grating strength evolve up to the yellow dot. (c) Table of grating design (d) mode profile for the two dots in (b).

section is 0.5 % higher than in the first section. As explained in the previous section, it favours the mode with the longer wavelength.

Values of effective index and grating strength are sketched by green and orange dots in fig. 3.33b. For the values considered here, both effective index and  $\kappa$  evolve linearly with  $W$ . It means that the linear silicon waveguide width enlargement create a linear increase of  $n_{eff2}$  and  $\kappa_2$  in the second section. Parameters of the two sections are summarized in fig. 3.33c, and mode profiles in the straight and at the end of the varying section are presented in fig. 3.33d. In the previous section I considered a step index variation between the two sections. As I will present in the next section, the linear index variation presented here have the same effect on cavity modes.

### Transfer matrix method simulations and static characteristics

To validate the design, I performed simulation based on transfer matrix method. Cavity modes are displayed in fig. 3.34. They show the breaking of the symmetry with a preferred long wavelength mode. The calculated threshold gain difference is  $2.1 \text{ cm}^{-1}$ , enabling single mode emission with sufficient SMSR [9]. Simulations indicate that the symmetry breaking

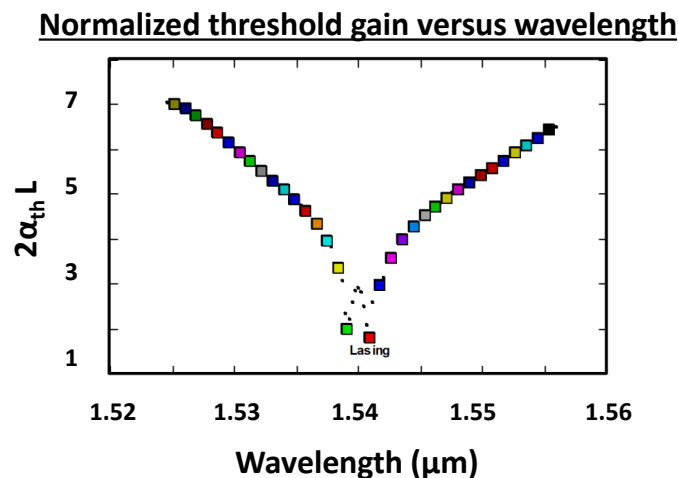


Figure 3.34: Normalized threshold gain calculated by transfer matrix method

comes from the index difference between the two sections and not from the grating strength difference. The calculated spectrum (fig. 3.35a) has a 50 dB SMSR. The experimental SMSR (fig. 3.35b) is always better than 40 dB when the bias current is varied from 100 to 150 mA. The difference between experimental and simulated stopband widths is below 5 % indicating a good agreement between experiments and modelling.

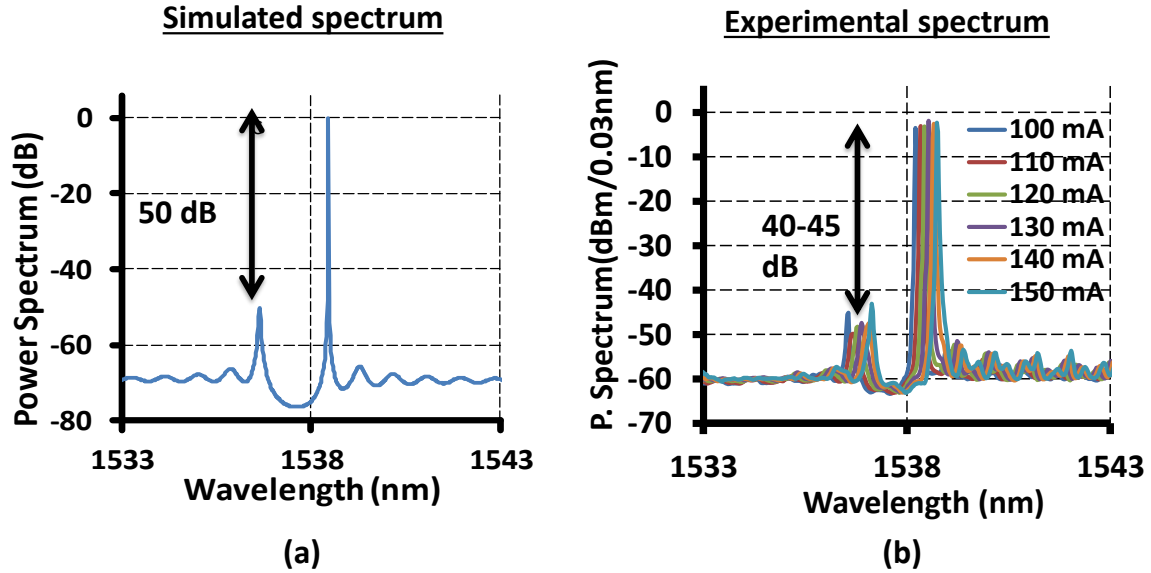


Figure 3.35: (a) Simulated spectrum at  $2 I_{th}$  and (b) experimental spectrum for increasing bias current.

The higher grating strength  $\kappa_2$  in the second section makes the intensity distribution in the cavity asymmetric and localized in the front facet of the laser. The collected power is thus enhanced. Fig. 3.36a shows the calculated intensity distribution in the cavity for the proposed device. For comparison, the intensity of a phase-shifted laser is depicted, presenting 1.8x less facet power. Simulations indicate that the increase in facet power comes from the grating strength ratio between the two sections. In future designs we may increase the power asymmetry enlarging more the waveguide width to have a larger grating strength. However, threshold gain margin may decrease if a too large silicon waveguide is used as indices would be very different in the two sections.

During this thesis, I designed devices with higher threshold gain margin and higher cavity asymmetry that will be tested in the following years. Fig. 3.36b shows experimental L-I curve of the laser and of a  $\lambda/4$  phase shifted laser from the same bar. If the threshold is the same we can see that the two-section laser has 1.5 more power than the conventional  $\lambda/4$  phase-shifted laser, confirming the great advantage of the proposed design.

In the 160-180 mA bias current range, there is a mode hop: the lasing mode is on the other side of the stop-band. This mode hop is due to a residual feedback from the vertical coupler which introduces a typical facet reflectivity of 1%. As in coated DFB, the impact of facet reflectivity on threshold gain is phase sensitive [11]. The feedback phase depends on injected current as it slightly changes the effective index due to thermal effects. The mode

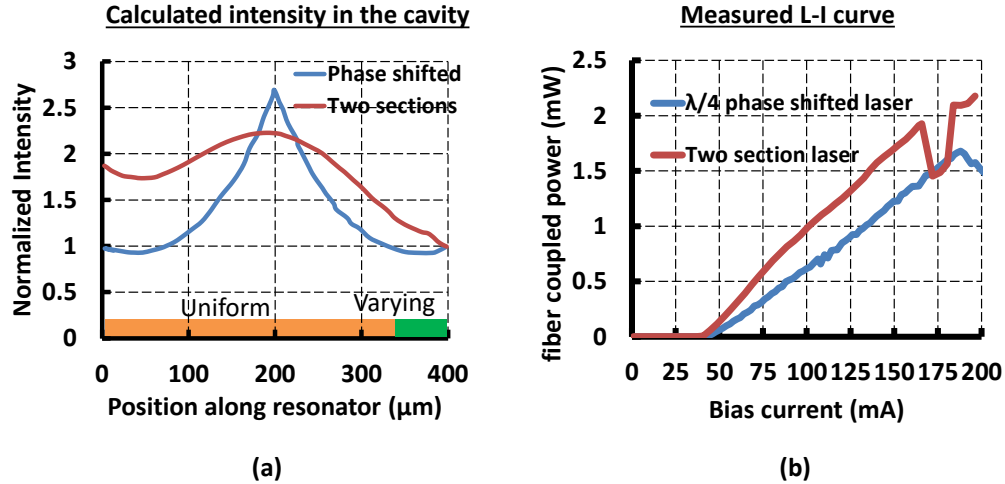


Figure 3.36: (a) Normalized intensity versus position along resonator for a  $\lambda/4$  phase shifted laser (blue) and DFB with tapered grating (red). Section with uniform and varying parameters are indicated in orange and green respectively. (b) Measured L-I curve for the two cases.

hop is thus present only for a specific bias current range. Mode hops will be suppressed with lower feedback grating couplers [44]. An increase of threshold gain margin may also lead to a lower feedback sensitivity.

In [45] and [15] a Bragg reflector at the cavity end is used to have a single mode laser and increase output power asymmetry (DFB-DR). However, the design is fundamentally different as the Bragg reflector is passive. Although both papers presented stable single mode operation, the fact that refractive index in the passive section does not follow the temperature or bias current induced refractive index changes in the active section might be a problem for DFB-DR designs.

### 3.6.1 Direct modulation at 25 Gb/s

In order to validate the component in system conditions, direct modulation experiment is performed at 25 Gb/s. Bit error rates curves and eye diagrams are displayed on fig. 3.37. The laser is biased at 140 mA and a 1.7 V<sub>pp</sub> is applied, resulting in 3 dB extinction ratio. The extinction ratio is limited by the maximum voltage swing available. The pseudo-random-bit-sequence length was  $2^{31} - 1$ . Error free performance is obtained for back to back and after 2 km transmission over standard single mode fiber. The penalty after 2 km is less than 0.5 dB.

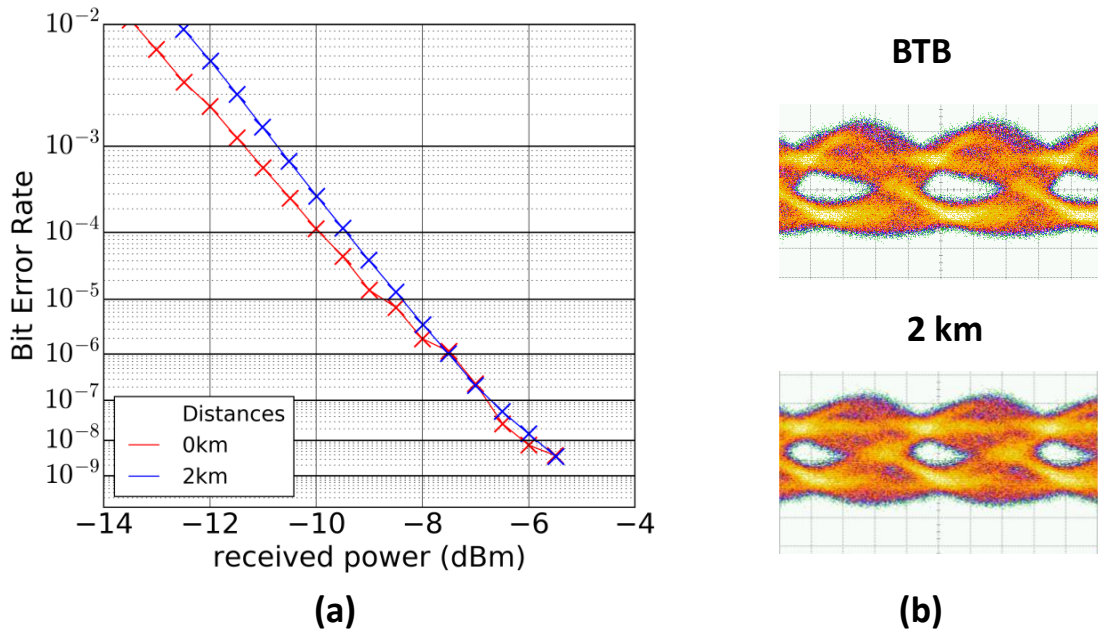


Figure 3.37: (a) BER Results at 25 Gb/s for back to back and after 2 km. (b) Corresponding eye diagrams with 3 dB extinction ratio. PRBS length is  $2^{31} - 1$ .

### 3.7 Chapter conclusion

We designed and fabricated two types of C band DFB lasers. First, we investigated usual  $\lambda/4$  phase shifted DFBs. Integrated with extinction ratio enhancement filter, those directly modulated lasers are promising devices as we obtained:

- open eye diagram with 5 dB extinction ratio at 25 Gb/s
- 20 km reach with limited penalty
- 20 dB power budget when used with a SOA-PIN receiver

Then I demonstrated a novel design that takes advantage of the hybrid platform. This laser has a little section with effective index and grating strength variation. The index variation ensures the single mode behavior and the grating strength variation lead to a power asymmetry in the cavity. As the taper is done in the silicon process it doesn't increase the technology complexity. We validated the design by transfer matrix method based simulations. Numerical results greatly reproduce experiments. The structure has:

- 1.5x better efficiency than  $\lambda/4$  phase shifted lasers

- Direct modulation at 25 Gb/s shows error free operation after 2 km

Further work will now consider new designs to increase the cavity power asymmetry and improve modulation bandwidth.

## Outlook

This chapter was dedicated to high speed DFB lasers. In the future, 1.3  $\mu\text{m}$  very high speed DFB arrays should also be considered, for intra-datacenter application or 100-400 Gb/s Ethernet. For CWDM4-CWDM8 applications, selective area growth can be implemented to meet the 20 nm channel spacing. For both applications, integration with passive multiplexers is of great interest to have a cost-effective transceiver [46]. The hybrid III-V on silicon platform is highly versatile as quantum well overlap and grating strength are precisely controlled by changing the width of the silicon waveguide  $W_{Si}$ . As we have seen in the last section, DFB with axially varying parameters which take advantage of this feature can be designed and fabricated. In the next chapter, I will introduce another axially varying DFB design, the high Q hybrid laser.

## References

- [1] G. P. Agrawal and A. H. Bobeck. “Modeling of distributed feedback semiconductor lasers with axially-varying parameters”. In: *IEEE Journal of Quantum Electronics* 24.12 (Dec. 1988), pp. 2407–2414.
- [2] V. Cristofori et al. “25-Gb/s Transmission Over 2.5-km SSMF by Silicon MRR Enhanced 1.55- $\mu\text{m}$  III-V/SOI DML”. In: *IEEE Photonics Technology Letters* 29.12 (June 2017), pp. 960–963.
- [3] A. Gallet et al. “Integrated Hybrid III-V/SOI Directly Modulated DFB Laser and Ring Resonator at 10 Gbit/s”. In: *IEEE Photonics Technology Letters* 29.17 (Sept. 2017), pp. 1424–1426.
- [4] A. Gallet et al. “Hybrid III-V on Silicon Integrated Distributed Feedback Laser and Ring Resonator for 25 Gb/s Future Access Networks”. In: *Journal of Lightwave Technology* 36.8 (Apr. 2018), pp. 1498–1502.
- [5] A. Gallet et al. “Design, Fabrication and Characterization of Hybrid III-V/SOI Phase-Shift Free DFB Laser with Tapered Silicon Waveguide”. In: *2018 European Conference on Optical Communication (ECOC)*. Aug. 2018, pp. 1–3.

- [6] H. Kogelnik and C. V. Shank. “Coupled-Wave Theory of Distributed Feedback Lasers”. In: *Journal of Applied Physics* 43.5 (1972), pp. 2327–2335. eprint: <https://doi.org/10.1063/1.1661499>.
- [7] M. Nakamura et al. “GaAs Ga<sub>1-x</sub>Al<sub>x</sub>As double-heterostructure distributed-feedback diode lasers”. In: *Applied Physics Letters* 25.9 (1974), pp. 487–488. eprint: <https://doi.org/10.1063/1.1655559>.
- [8] G. Morthier and P. Vankwikelberge. *Handbook of distributed feedback laser diodes*. 1997.
- [9] J. Buus, M.-C. Amann, and D. J. Blumenthal. “Single Mode Laser Diodes”. In: *Tunable Laser Diodes and Related Optical Sources*. IEEE, 2005.
- [10] G. Bjork and O. Nilsson. “A new exact and efficient numerical matrix theory of complicated laser structures: properties of asymmetric phase-shifted DFB lasers”. In: *Journal of Lightwave Technology* 5.1 (Jan. 1987), pp. 140–146.
- [11] W. Streifer, R. Burnham, and D. Scifres. “Effect of external reflectors on longitudinal modes of distributed feedback lasers”. In: *IEEE Journal of Quantum Electronics* 11.4 (Apr. 1975), pp. 154–161.
- [12] T. Nakajima et al. “Wide temperature range Operation (20–80 C) of 53.2 Gbit/s NRZ directly modulated 1.3  $\mu$ m DFB Lasers transmitted over 2 km”. In: *2018 ISLC Conference, mC4*. Sept. 2018, pp. 1–3.
- [13] K. Nakahara et al. “Direct Modulation at 56 and 50 Gb/s of 1.3- $\mu$ m InGaAlAs Ridge-Shaped-BH DFB Lasers”. In: *IEEE Photonics Technology Letters* 27.5 (Mar. 2015), pp. 534–536.
- [14] Y. Matsui et al. “28-Gbaud PAM4 and 56-Gb/s NRZ Performance Comparison Using 1310-nm Al-BH DFB Laser”. In: *Journal of Lightwave Technology* 34.11 (June 2016), pp. 2677–2683.
- [15] Y. Matsui et al. “55 GHz Bandwidth Distributed Reflector Laser”. In: *Journal of Lightwave Technology* 35.3 (Feb. 2017), pp. 397–403.
- [16] *Bilt Itest current sources*. URL: <https://www.uni-kassel.de/projekte/sequoia/home.html>.
- [17] Coldren, Corzine, and Masanovic. *Diode Lasers and Photonic Integrated Circuits*. John Wiley & Sons, 2012.

- [18] M. M. Norbert Grote and M. Ortsiefer. *Laser components, in Fibre Optic Communication: Key Devices Springer Series in Optical Science*.
- [19] Y. Matsui et al. “Transceiver for NG-PON2: Wavelength tunability for burst mode TWDM and point-to-point WDM”. In: *2016 Optical Fiber Communications Conference and Exhibition (OFC)*. Mar. 2016, pp. 1–3.
- [20] P. A. Morton et al. “Frequency response subtraction for simple measurement of intrinsic laser dynamic properties”. In: *IEEE Photonics Technology Letters* 4.2 (Feb. 1992), pp. 133–136.
- [21] A. Abbasi et al. “28 Gb/s direct modulation heterogeneously integrated C-band InP/SOI DFB laser”. In: *Opt. Express* 23.20 (Oct. 2015), pp. 26479–26485.
- [22] J.-G. Provost and F. Grillot. “Measuring the Chirp and the Linewidth Enhancement Factor of Optoelectronic Devices with a Mach–Zehnder Interferometer”. In: *IEEE Photonics Journal* 3.3 (Apr. 2011), pp. 476–488.
- [23] R. Schimpe, J. Bowers, and T. Koch. “Characterisation of frequency response of 1.5  $\mu\text{m}$  InGaAsP DFB Laser diode and InGaAs PIN photodiode by heterodyne measurement technique.” English (US). In: *Electronics Letters* 22.9 (Jan. 1986), pp. 453–454.
- [24] S. Joshi. “Quantum dash based photonic integrated circuits for optical telecommunications”. 2014TELE0031. PhD thesis. 2014.
- [25] Y. Matsui. “Directly Modulated Laser Technology: Past, Present, and Future”. In: *Datacentre Connectivity Technologies: Principle and Practice*. 2018.
- [26] B. Thedrez et al. “Power and facet phase dependence of chirp for index and gain-coupled DFB lasers”. In: *Conference Digest. ISLC 1998 NARA. 1998 IEEE 16th International Semiconductor Laser Conference (Cat. No. 98CH361130)*. Oct. 1998, pp. 175–176.
- [27] F. Grillot. “Lasers monomodes à faible sensibilité à la rétroaction optique pour les transmissions à 2,5 GBit/s sans isolateur”. 2003BESA2005. PhD thesis. 2003.
- [28] F. Lelarge et al. “Chirp optimization of 1550nm InAs/InP Quantum Dash based directly modulated lasers for 10Gb/s SMF transmission up to 65Km”. In: *2010 22nd International Conference on Indium Phosphide and Related Materials (IPRM)*. May 2010, pp. 1–3.
- [29] D. Mahgerefteh et al. “Chirp Managed Laser and Applications”. In: *IEEE Journal of Selected Topics in Quantum Electronics* 16.5 (2010), pp. 1126–1139.

- [30] Y. Yokoyama et al. “10.709-Gb/s-300-km transmission of PLC-based chirp-managed laser packaged in pluggable transceiver without any optical or electrical dispersion compensation”. In: *2008 34th European Conference on Optical Communication*. Sept. 2008, pp. 1–2.
- [31] N. Chimot et al. “Monolithic Integration on InP of a DML and a Ring Resonator for Future Access Networks”. In: *IEEE Photonics Technology Letters* 28.19 (Oct. 2016), pp. 2039–2042.
- [32] A. Gallet et al. “Long delay optical feedback sensitivity of hybrid III-V/SOI directly modulated DFB lasers”. In: *2017 IEEE 14th International Conference on Group IV Photonics (GFP)*. 2017, pp. 115–116.
- [33] C. Caillaud et al. “Integrated SOA-PIN Detector for High-Speed Short Reach Applications”. In: *Journal of Lightwave Technology* 33.8 (Apr. 2015), pp. 1596–1601.
- [34] R. Marchetti et al. “High-efficiency grating-couplers: Demonstration of a new design strategy”. In: *Scientific Reports* 7 (Nov. 2017).
- [35] J. Kreissl et al. “40 Gbit/s Directly Modulated Passive Feedback Laser with Complex-Coupled DFB Section”. In: *33rd European Conference and Exhibition of Optical Communication*. Sept. 2007, pp. 1–2.
- [36] A. Abbasi et al. “Direct and Electroabsorption Modulation of a III–V-on-Silicon DFB Laser at 56 Gb/s”. In: *IEEE Journal of Selected Topics in Quantum Electronics* 23.6 (Nov. 2017), pp. 1–7.
- [37] C. Zhang et al. “Low threshold and high speed short cavity distributed feedback hybrid silicon lasers”. In: *Opt. Express* 22.9 (May 2014), pp. 10202–10209.
- [38] H. Duprez. “From design to characterization of III-V on silicon lasers for photonic integrated circuits”. 2016LYSEC005. PhD thesis. 2016.
- [39] R. Blum. “Scaling the compute and high speed networking needs of the datacenter with silicon photonics”. In: *2017 European Conference on Optical Communication (ECOC) Market Focus*. Sept. 2017, pp. 1–2. eprint: <https://www.intel.com/content/www/us/en/architecture-and-technology/silicon-photonics/market-focus-article.html>.
- [40] J. Yu et al. “Applications of 40-Gb/s Chirp-Managed Laser in Access and Metro Networks”. In: *Journal of Lightwave Technology* 27.3 (Feb. 2009), pp. 253–265.

- [41] A. Abbasi et al. “10-/28-Gb Chirp Managed 20-km Links Based on Silicon Photonics Transceivers”. In: *IEEE Photonics Technology Letters* 29.16 (Aug. 2017), pp. 1324–1327.
- [42] R. Nagarajan et al. “Effects of carrier transport on high-speed quantum well lasers”. In: *Applied Physics Letters* 59.15 (1991), pp. 1835–1837. eprint: <https://doi.org/10.1063/1.106213>.
- [43] F. Grillot et al. “Analysis, fabrication, and characterization of 1.55-  $\mu\text{m}$  selection-free tapered stripe DFB lasers”. In: *IEEE Photonics Technology Letters* 14.8 (Aug. 2002), pp. 1040–1042.
- [44] J. H. Song et al. “Grating Coupler Design for Reduced Back-Reflections”. In: *IEEE Photonics Technology Letters* 30.2 (Jan. 2018), pp. 217–220.
- [45] T. Fujii et al. “Heterogeneously Integrated Membrane Lasers on Si Substrate for Low Operating Energy Optical Links”. In: *IEEE Journal of Selected Topics in Quantum Electronics* 24.1 (Jan. 2018), pp. 1–8.
- [46] X. Pommarede. “Hybrid III-V/Si photonics integrated circuits for optical communication applications”. PhD thesis.

# Chapter 4

## High Q hybrid lasers

Single wavelength narrow linewidth sources are attractive for several applications. For example, low cost and low power consumption lasers may be used for IEEE 400G ZR data centers interconnects. Sensors like frequency modulated continuous wave (FMCW) LIDAR also need a low noise single wavelength source [1].

In this chapter, I will present a narrow linewidth distributed feedback laser based on a high quality factor grating.

In the first section, I will introduce the linewidth and describe the different ways to decrease it: high power laser, low linewidth enhancement factor laser and high Q laser. The latter is a low internal and mirror loss DFB laser.

In the second section, I will describe the design of high Q lasers. I will first introduce quality factors and explain why a low linewidth is expected. I will then describe the grating structure in more details, following A. Yariv [2] and C.T. Santis's work [3]. In high Q lasers, the grating doesn't have a phase shift but a parabolic tapered structure to obtain single mode operation and a Gaussian intensity distribution along the cavity.

In section 3 and 4, I will describe the static and dynamic characteristics of such lasers. In particular, I will show that the  $K$  parameter is as high as 4.1 ns. This is more than 20 times greater than in high speed lasers presented in the precedent chapter.

To finish I will describe linewidth measurements using the self-heterodyne and the frequency noise methods. I will show that High Q hybrid laser best linewidth is 27 kHz. Preliminary results on high Q hybrid lasers have been published in [4].

## 4.1 Introduction to narrow linewidth DFB lasers

In 1982, Henry modified the Schawlow-Townes formula to account for phase-amplitude coupling [5]. The full width at half maximum linewidth is:

$$\Delta\nu = \frac{R_{sp}}{4\pi I}(1 + \alpha_H^2) \quad (4.1)$$

$R_{sp}$  is the spontaneous emission rate,  $I$  is the average intensity in the cavity and  $\alpha_H$  the linewidth enhancement factor. Using Einstein's relations, we can link the spontaneous rate with the gain:  $R_{sp} = v_g g n_{sp}$ , where  $n_{sp}$  is the inversion factor,  $g$  the gain and  $v_g$  the group velocity [6]. As in [5], the average intensity in the cavity  $I$  can be expressed with the facet power  $P_0$ :  $I = \frac{2P_0}{h\nu v_g \alpha_m}$ , where  $h\nu$  is the photon energy.

Henry's linewidth formula is thus:

$$\Delta\nu = \frac{v_g^2 h\nu n_{sp} g \alpha_m}{8\pi P_0} \times (1 + \alpha_H^2) \quad (4.2)$$

As described by [7], this formula derived for Fabry-Perot lasers is also valid for DFBs if we use the DFB mirror loss coefficient  $\alpha_m$  evaluated by coupled mode theory.

In chapter 3, I indicated that achievable modulation speed is inversely proportional to  $g = \alpha_0 + \alpha_m$ . High speed lasers are thus usually short and have low  $\kappa L$  to increase mirror loss coefficient  $\alpha_m$ . The quantum well overlap is high to have a low threshold, leading to high internal losses. This design is therefore not suitable for low linewidth operation, with III-V/SOI high speed DFB lasers linewidth of about 1 MHz [8].

To obtain a narrow linewidth, the first simple idea is to increase  $\kappa L$ , as it quickly decreases mirror losses  $\alpha_m$ . As we will see this may not be sufficient to obtain a narrow linewidth.

### $\lambda/4$ phase shifted DFB with high $\kappa L$

We fabricated hybrid III-V on silicon  $\lambda/4$  phase shifted DFBs lasers with high  $\kappa L$ . Compared to the designed presented in chapter 3 we increased the laser length from 400 to 800  $\mu\text{m}$  and increased  $\kappa$ . Measured laser spectrum for simulated  $\kappa L = 3.9, 6.7$  and  $9.8$  at threshold and at  $I_b = 3I_{th}$  are presented in fig. 4.1. Spectra are highly multimode in the second case.

As  $\kappa L$  increases, intensity is more and more confined in the center of the cavity, as sketched in fig. 4.1c. Longitudinal spatial hole burning (LSHB) occurs: carrier density is no longer constant in the cavity as stimulated recombinations strongly deplete carrier population in the center of the cavity [9]. As refractive index depends on carrier density, the index profile

and the phase shift value are disturbed.

As the threshold gain margin of phase shifted lasers depends on the phase shift value, it is affected by LSHB, leading to multimode spectrum when threshold gain margin is too low. As only increasing  $\kappa L$  is not an efficient way to reduce the linewidth, other ways should be investigated, as presented in the next section.

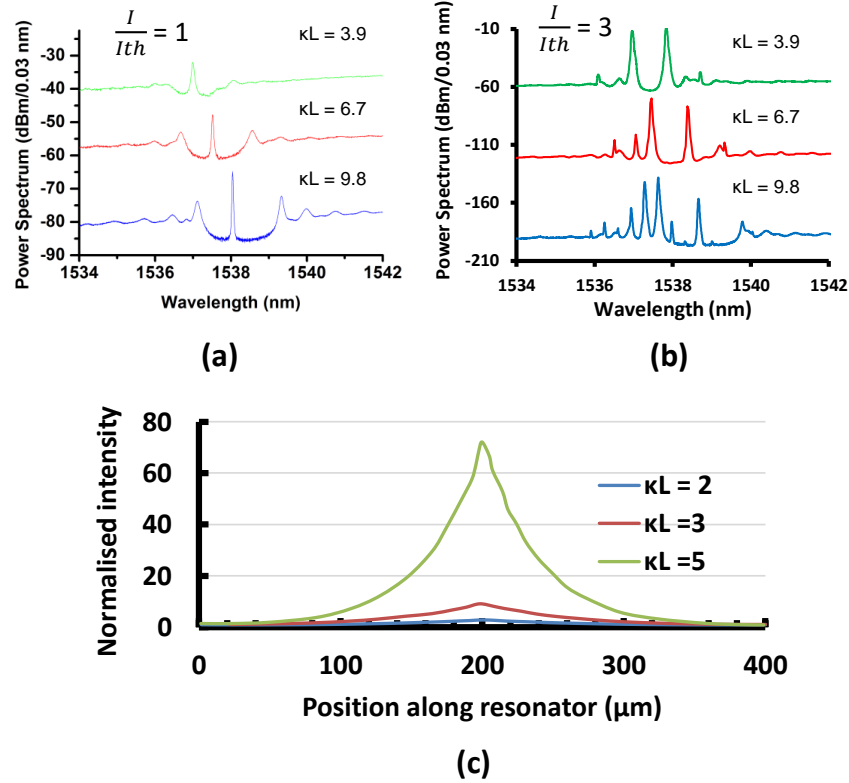


Figure 4.1: Measured spectrum of fabricated hybrid III-V/SOI phase shifted DFB lasers with high  $\kappa L$  (a) at threshold (b) at  $I_b = 3I_{th}$ . The y axis is shifted for easier comparison. (c) Normalized intensity for  $\kappa L = 2, 3$  and  $5$ .

## Low linewidth DFB designs

To reduce the DFB laser linewidth, three main ways have been proposed:

- Output power increase
- Linewidth enhancement factor reduction
- High reduction of both internal and mirror losses

As linewidth is proportional to  $\frac{1}{P_0}$ , high power lasers have a narrow linewidth. To achieve high output power, thermal roll-off that arises far above threshold has to be mitigated. For this reason, high power DFBs are usually longer ( $L \approx 1\text{mm}$ ) and have lower quantum well confinement than high speed DFB [10].

In such structures, longitudinal spatial hole burning may introduce a linewidth re-broadening at high power [11]. Corrugation pitch modulated lasers are designed to mitigate such effect, achieving a linewidth as low as 3.5 kHz for 55 mW output power [12]. Another way to reduce spatial hole burning is to set  $\kappa L \approx 1$  to obtain a flat intensity distribution. In [10] the fabricated high power laser has a linewidth better than 300 kHz.

As the linewidth is proportional to  $1 + \alpha_H^2$  decreasing  $\alpha_H$  is also a way to reduce the linewidth. For this purpose, quantum dots active region is promising as reported linewidth enhancement factor are near zero [13]. According to Henry's formula, if  $\alpha_H$  diminishes from 2.5 to 0, the linewidth is reduced by  $1 + 2.5^2 \approx 10$ . With such material, researchers from Kassel University reported a DFB laser with a linewidth as low as 110 kHz [14]. However, dot size is not easily controllable and laser performances may vary on the same wafer or for lasers of two different wafers.

In the following, I will now describe a third way to obtain a narrow linewidth: the high Q hybrid laser. Such lasers have very low internal and mirror losses. As both loss coefficients are divided by more than 10 compared to high speed designs, the linewidth improvement according to equ. 4.2 should be around 100. Such structures have been realised in [3], with a best linewidth of 18 kHz. More recently, a 1 kHz linewidth has been reported [15]. In this chapter, I will describe similar devices realised in III-V Lab-Leti platform.

## 4.2 High Q hybrid laser design

### 4.2.1 Introduction to Q factors

Q factor is an alternative description of laser losses: high Q lasers are simply low loss lasers. If  $\nu$  is the laser frequency, the total, internal and external quality factors are:

$$Q = 2\pi\nu\tau_p = \frac{2\pi\nu}{v_g(\alpha_0 + \alpha_m)} \quad (4.3)$$

$$Q_{ext} = \frac{2\pi\nu}{v_g\alpha_m} \quad (4.4)$$

$$Q_i = \frac{2\pi\nu}{v_g\alpha_0} \quad (4.5)$$

They are linked by:

$$\frac{1}{Q} = \frac{1}{Q_{ext}} + \frac{1}{Q_i} \quad (4.6)$$

The photon lifetime  $\tau_p$  is defined as  $\frac{1}{\tau_p} = v_g(\alpha_0 + \alpha_m) = v_g g$ , with the group velocity  $v_g = \frac{c}{n_g}$ . The waveguide Group index  $n_g$  is calculated without taking into account the grating.

As in chapter 3,  $\alpha_m$  is calculated by transfer matrix method. As we will see in section 4.2.4, in high Q laser the grating strength is only twice the value of high speed lasers. As indicated in [16], coupled mode theory equations are valid as the grating strength is still way lower than the Bragg wavenumber.

Generally, optical resonator external quality factor is not defined with the mirror loss coefficient but as ([17], or [18] equ.26):

$$\frac{1}{Q_{ext}} = \frac{2P_1}{2\pi\nu W} \quad (4.7)$$

where  $W$  is the stored energy in the cavity and  $P_1$  is the power escaping one side of the cavity. I link the two descriptions for a phase shifted laser in annex A, following [18] and [19]. In the next section I will link Q factors with laser linewidth and introduce high Q lasers.

## 4.2.2 Design introduction

As described by Henry's formula, losses govern the noise properties of semiconductor lasers. With quality factor expression, the linewidth formula becomes

$$\Delta\nu = \frac{\pi h\nu^3 n_{sp}}{2QQ_{ext}\eta_d(I - I_{th})} \times (1 + \alpha_H^2) \quad (4.8)$$

In this equation, total loss  $g$  is replaced with its expression in terms of total quality factor  $\frac{2\pi\nu}{v_g Q}$  and mirror losses  $\alpha_m$  by  $\frac{2\pi\nu}{v_g Q_{ext}}$ . The facet power  $P_0$  is the differential efficiency  $\eta_d$  times the bias current relative to threshold  $(I - I_{th})$ . With this formulation, the role of  $Q$ ,  $Q_{ext}$  and  $\eta_d$  is clearly outlined.

To reduce the linewidth, we will significantly increase  $Q$ . As total quality factor is limited by  $Q_i$ , it should be considered first. As described in [20], Indium phosphide p-doped regions have a high loss coefficient due to intervalence band absorption (IVBA). n-doped regions

have a smaller absorption coefficient:

$$\alpha_{InPp} = 20 \times \Gamma_{InPp} \frac{d_p}{10^{18}} \text{ cm}^{-1} \quad (4.9)$$

$$\alpha_{InPn} = 2.5 \times \Gamma_{InPn} \frac{d_n}{10^{18}} \text{ cm}^{-1} \quad (4.10)$$

In those formulae,  $\Gamma$  is the optical confinement and  $d$  is the doping concentration. In our structure  $d_p = 10^{18} \text{ cm}^{-3}$  and  $d_n = 1.5 \cdot 10^{18} \text{ cm}^{-3}$ . To make high Q lasers, we will use the same hybrid III-V on silicon platform used for tunable and high speed DFB lasers, recalled in fig. 4.2. In particular, the III-V epitaxy is not changed. The hybrid III-V on silicon

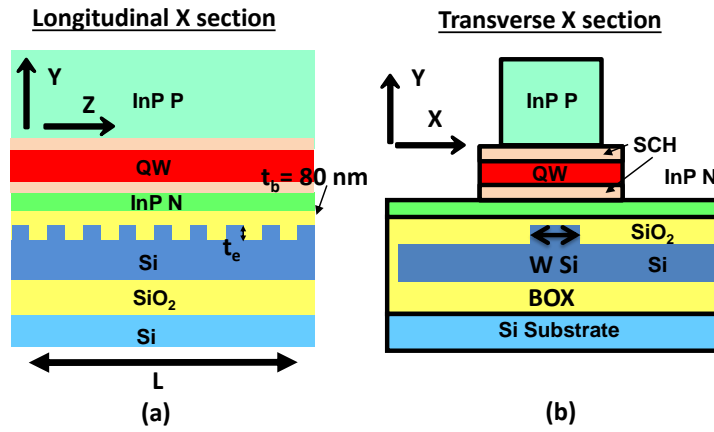


Figure 4.2: Hybrid III-V on silicon longitudinal (a) and transverse (b) structure. Device Parameters depend on  $W Si$ .

platform has a specific feature: the optical mode overlap with the III-V material is set by design. Depending on the silicon waveguide width  $W Si$ , which definition is recalled in fig. 4.2, light can be either quasi totally confined in the III-V or in the silicon waveguide. With the commercial software Fimmwave, the total III-V overlap and the  $p$ - and  $n$ -doped InP overlap is calculated. As seen in fig. 4.3a in purple, when  $W Si$  increases from  $0.7$  to  $2 \mu\text{m}$ , the total III-V overlap decreases from  $90\%$  to  $5\%$ .

$p$  and  $n$  doped region induced loss coefficients are described by an internal quality factor  $Q_i^{III-V}$ . As sketched in fig. 4.3a in blue, it increases from  $17\ 000$  to more than  $410\ 000$  when  $W Si$  evolve from  $0.7$  to  $2 \mu\text{m}$ , resulting in a  $24x$  improvement. As indicated in [21], the silicon internal Q factor is greater than  $1$  million, hence  $Q_i^{III-V}$  limits the internal Q factor.

To increase the total quality factor, the external Q factor is also augmented. In fig. 4.3a, I showed that III-V overlap decreases with  $W Si$ , meaning that silicon overlap augments.

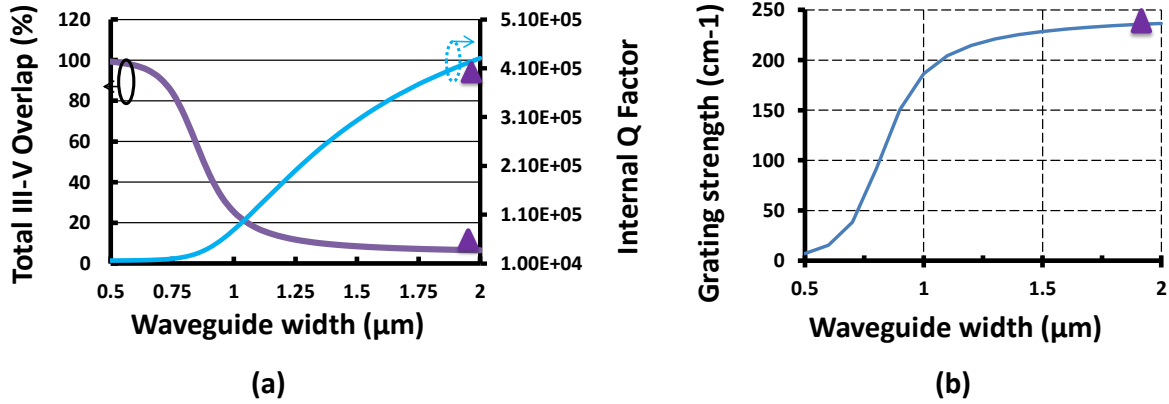


Figure 4.3: (a) Total III-V Overlap (purple curve) and internal quality factor (blue curve) versus waveguide width  $W_{Si}$ . (b) Grating strength versus waveguide width  $W_{Si}$  evaluated in chapter 3. The high Q design is represented by a purple triangle.

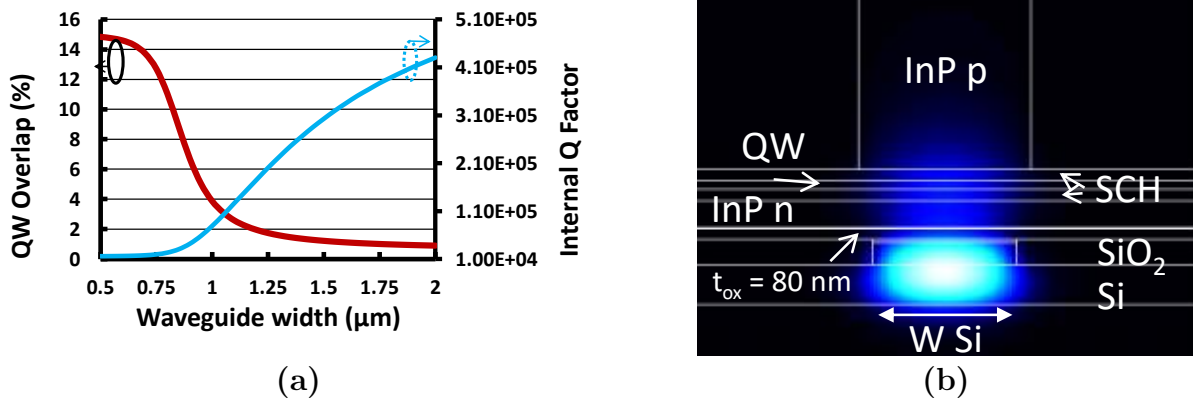


Figure 4.4: (a) Quantum well overlap (red) and internal Q factor (blue) versus waveguide width  $W_{Si}$ . (b) High Q hybrid laser calculated intensity cross section. 95 % of light is in the silicon waveguide.

Since the grating is in the silicon waveguide, a larger  $W$   $Si$  increases the grating strength as it is proportional to the grating overlap.

In section 3.1.2, I estimated the DFB grating strength evolution with  $W$   $Si$ , as reproduced in fig. 4.3b. As the grating strength is high for  $W$   $Si = 2 \mu\text{m}$ , we have a high  $Q_{ext}$  (ie high  $\kappa L$ ) with limited length. Fabricated high Q hybrid laser have  $\kappa L$  as high as 11.

In equation 4.8, linewidth also depends on threshold current and differential efficiency.

### Threshold current and differential efficiency of high Q lasers

As depicted in fig. 4.3a, in high Q lasers the quantum well overlap is reduced below 1% (barriers are not taken into account). However, it doesn't imply a high threshold current as the low quantum well overlap is balanced by low losses. More precisely, laser threshold is obtained when the gain  $G(N_{th})$  equals the losses:

$$G(N_{th}) = \Gamma_{QW} a \times (N_{th} - N_{tr}) = g = \frac{2\pi\nu}{v_g Q} \quad (4.11)$$

$\Gamma_{QW}$  is the quantum well overlap,  $a$  is the differential gain,  $N_{th}$  and  $N_{tr}$  are the carrier density at threshold and at transparency respectively. When  $W$   $Si$  evolves from 0.7 to 2  $\mu\text{m}$ , the internal Q factor is multiplied by 24. As presented in red in fig. 4.4a, in the same time  $\Gamma_{QW}$  is only divided by 15. Interestingly, in our platform, carrier density at threshold  $N_{th}$  (or threshold current) can be reduced by decreasing  $\Gamma_{QW}$ .

To obtain a high output power, we need to balance internal and external Q factor to obtain a sufficient differential efficiency  $\eta_d$ . It is given by [22]:

$$\eta_d = \frac{h\nu}{e} \times \frac{1}{2} \frac{\alpha_m}{\alpha_0 + \alpha_m} = \frac{h\nu}{e} \times \frac{1}{2} \frac{Q}{Q_{ext}} = \frac{h\nu}{e} \times \frac{1}{2} \times \frac{1}{1 + \frac{Q_{ext}}{Q_i}} \quad (4.12)$$

In this equation,  $h\nu$  is the photon energy and  $e$  is the elementary charge. This equation indicates that it is not useful to increase  $Q_{ext}$  above  $Q_i$ . To see the dependence of threshold and differential efficiency with  $Q_{ext}$ , we fabricated samples with different external Q factor (see section 4.2.4). The intensity distribution cross section is presented in fig. 4.4. We can clearly see that with such a structure, the mode is highly confined in the silicon waveguide. Balancing internal and external Q factor for DFB laser linewidth was already outlined in 1985 in [7]. As silicon is low loss, hybrid III-V/Si waveguides have significantly smaller internal losses than InP waveguides. For example, internal loss coefficient reported in [23] was  $6.4 \text{ cm}^{-1}$ , corresponding to a Q factor of  $2.2 \times 10^4$ . This is one order of magnitude larger

than losses calculated in fig. 4.3. As sketched in fig. 4.5, the III-V region overlap depends on the bonding oxide thickness. In [3], the bonding oxide thickness was only 5 nm, leading

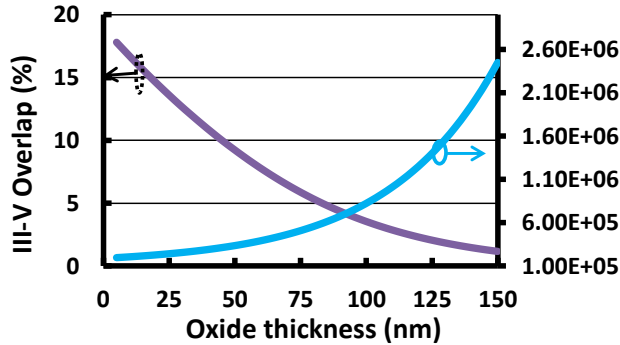


Figure 4.5: III-V overlap and Q factor versus bonding oxide thickness.

to a total III-V overlap of 15 %. As III-V/lab-Leti platform has a 80 nm bonding oxide, the total III-V region overlap is 5%. The internal Q factor is thus increased compared to [3]. High Q hybrid laser with higher bonding oxide has been reported very recently [15].

The bonding oxide thickness is not easily controllable: the tolerance range can be +/- 30 nm on a wafer, impacting the internal quality factor of high Q laser.

In this section, I showed that internal quality factor is increased with a low InP overlap. The external quality factor is also augmented with a high  $\kappa L$  product. In the following section, I will introduce the grating structure. The grating has high  $Q_{ext}$ , relatively high threshold gain margin and produces a Gaussian intensity distribution along the cavity.

### 4.2.3 Grating parameters

To describe the grating we will follow the derivation presented in [2]. The grating introduces a little permittivity variation  $\Delta\epsilon = \epsilon_0\Delta n^2$ , with the convention of  $\Delta n^2 = n_u^2 - n_e^2$  in the grating region.  $n_u$  and  $n_e$  are respectively the effective index in the un-etched and etched regions. Grating strength  $\kappa$  is evaluated by:

$$\kappa = \frac{-\omega\epsilon_0}{4\pi} \int_{-\infty}^{\infty} \Delta n^2(x) |\mathcal{E}_y^s(x)|^2 dx \quad (4.13)$$

where  $\mathcal{E}_y^s$  has a propagation constant close to the Bragg wavenumber. The mode, the perturbation  $\Delta n^2$  and the grating strength  $\kappa$  are evaluated with matlab. In this work, the grating structure is similar to [3]. We can describe this structure with the photonic crystal formalism [2]. In solids, the periodic crystal structure is associated with an electronic bandgap.

A grating can be seen as a material with a periodic variation of dielectric constant, thus having a "photonic bandgap". Photons with frequency in the bandgap are reflected by the structure. Valence and conduction band edges, respectively  $f_v$  and  $f_c$  are defined as:

$$f_c - f_v = \frac{\kappa c}{\pi n_{eff}} \quad (4.14)$$

$f_c - f_v$  is the reflection bandwidth of fig. 4.6 if  $\kappa L \gg 1$ . As sketched in fig. 4.6b, the grating is etched on top of the silicon laser rib waveguide. Grating properties depend on the etched tooth width  $w_t$ .

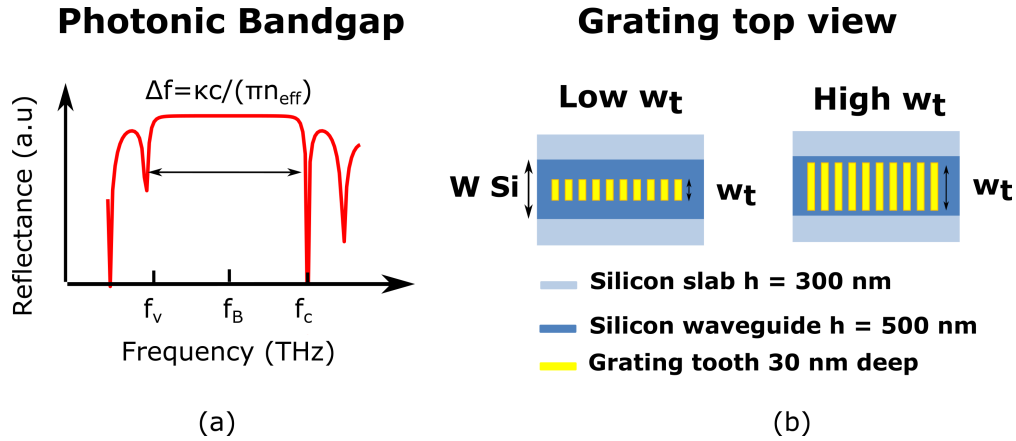


Figure 4.6: (a) reflectance spectrum and band edges definitions. (b) Grating parameters depend on tooth width  $w_t$

To describe the structure, we can use either the grating strength-Bragg frequency variables or the conduction and valence band edge variables, as they are linked by the following equations [2]:

$$\begin{cases} |\kappa| = \frac{n_{eff} \times 2\pi(f_c - f_v)}{2c} \\ f_B = \frac{f_c + f_v}{2} \end{cases} \iff \begin{cases} f_c = f_B + \frac{|\kappa|c}{2\pi n_{eff}} \\ f_v = f_B - \frac{|\kappa|c}{2\pi n_{eff}} \end{cases} \quad (4.15)$$

The two descriptions are equivalent. As sketched in fig. 4.7a, when the tooth width  $w_t$  is enlarged from 400 to 1200 nm, the grating strength  $|\kappa|$  increases from 90 to 220  $cm^{-1}$ . The high grating strength comes from a high index difference between silicon and silica and a high mode confinement in the grating.

Silica index is half the index of silicon. When  $w_t$  increases, the mode is more confined in the silica, leading to a lower etched tooth refractive index  $n_e$ . Evolution of the relative refractive index  $n_u - n_e$  with  $w_t$  is sketched in fig. 4.7a, where  $n_u$  is the un-etched refractive index.

The Bragg frequency is  $f_B = \frac{c}{2\bar{n}\Lambda}$ , with  $\bar{n} = (n_u + n_e)/2$ . As  $n_e$  decreases with  $w_t$ , the Bragg frequency  $f_B$  augments with  $w_t$ . If  $f_0 = \frac{c}{2n_u\Lambda}$  is the Bragg frequency when  $w_t \rightarrow 0$ , offset frequencies are defined as  $f_c - f_0$  and  $f_v - f_0$ . The evolution of  $f_c - f_0$  and  $f_v - f_0$  are displayed in fig. 4.7b. As there is a plus/minus sign in the equation of  $f_c/f_v$ , conduction and valence band edges evolve very differently with grating width.

In those calculations the III-V material is not included. It is a reasonable assumption as silicon overlap is 95%. In this section, I described the evolution of grating parameters with tooth width  $w_t$ , defined in fig. 4.6b. In high Q hybrid lasers, the grating tooth width  $w_t$  evolves along resonator position. I will introduce such structure in the next section.

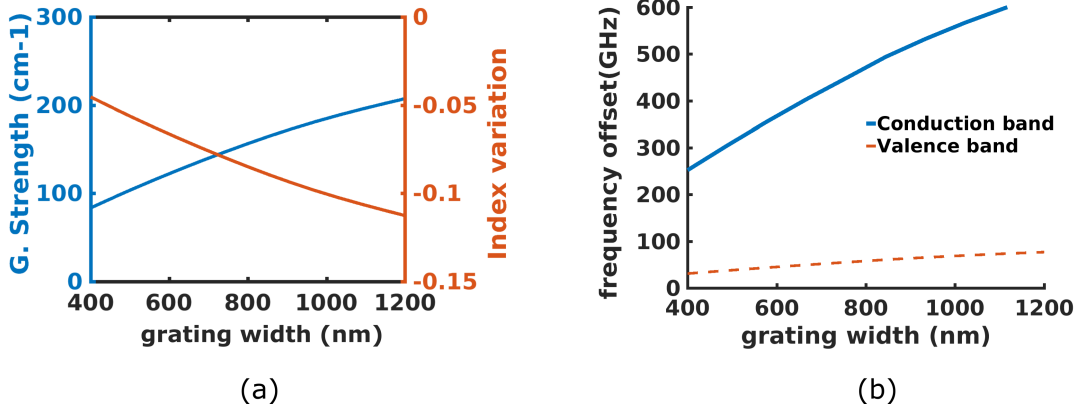


Figure 4.7: (a) Evolution of grating strength (blue) and effective index difference  $n_u - n_e$  (orange) with tooth width. (b) Evolution of valence and conduction band edges with tooth width.

## Design presentation

High Q lasers are DFB lasers with axially varying parameters, as presented in [24]. As in chapter 3, if  $\beta_0 = \frac{2\pi}{\lambda_B}$  is the Bragg wavenumber, the field  $E(z)$  is the sum of a propagating wave  $R$  and a contra-propagating wave  $S$ :

$$E(z) = R(z) \exp(-j\beta_0 z) + S(z) \exp(j\beta_0 z) \quad (4.16)$$

If  $\Delta\beta = \beta - \beta_0$  is the detuning, coupled wave equations for a uniform distributed feedback structure with no reflecting facets link  $R$  and  $S$  [16]:

$$\begin{cases} \frac{dR}{dz} + (\alpha_{th} - j\Delta\beta)R = j\kappa S \\ \frac{dS}{dz} + (\alpha_{th} - j\Delta\beta)S = j\kappa R \end{cases} \quad (4.17)$$

deriving the first equation and injecting the result in the other yields:

$$\frac{d^2 R}{dz^2} = -(-|\kappa|^2 - (\alpha_{th} - j\Delta\beta))R(z) \quad (4.18)$$

In [3] and [25], p110 Caltech researchers interpreted equ.4.18 as a time-independent Schrödinger equation. They identified  $|\kappa|$  as the potential and  $\Delta\beta$  as the particle energy.

In physics, a harmonic potential has a parabolic spatial dependence. In Schrödinger's equation, if the potential is harmonic, the fundamental mode wave-function spatial distribution is a Gaussian. In analogy with quantum mechanics, if  $|\kappa|$  is a parabolic function of  $z$  then  $R$  will have a Gaussian evolution with  $z$ . This yields only if  $\lambda_B$  varies slowly with resonator position  $z$ . This assumption will be discussed in section 4.2.4.

In our devices the spatial variation of  $|\kappa|$  and  $n_{eff}$  is made by varying the etched tooth width  $w_t$  with resonator position ( $z$  axis). As in [3], the grating has two sections: one parabolic tapered grating with length  $L_C$  and two uniform sections at each side with length  $L_B$ .

As shown in fig. 4.7b, both grating strength and indices evolve linearly with tooth width. The grating parabolic tooth width profile (fig. 4.8a) is hence transferred to a parabolic grating strength and index profile.

When  $w_t$  increases, the etched index  $n_e$  decreases, as already presented in fig.4.8a in orange. As only  $w_t$  varies, the un-etched tooth index doesn't change. As a consequence the mean index  $\bar{n}$  decreases in  $L_C$  with a parabolic profile, as presented in fig. 4.8b in blue. Grating strength profile is also parabolic (fig. 4.8c).

Those two variations are captured in fig. 4.8d in the band structure formalism. As Bragg frequency is the mean of conduction and valence band edges, it increases in  $L_C$ . As  $\kappa$  is proportional to the band difference, it also increases in  $L_C$ .

In this section, I introduced the high Q design which have a grating width variation along resonator position. To obtain the Gaussian intensity profile, this variation has to be carefully designed, as analysed in the next section.

## Design rules

In high Q hybrid lasers, grating strength and effective index have a parabolic variation along resonator position. The two key parameters are the length  $L_C$  and the valence band edge difference  $\Delta f_v$ .  $\Delta f_v$  depends on the minimal and maximal grating width  $w_{t,min}$  and  $w_{t,max}$ . Exact conditions to have a Gaussian profile can be found solving equ.4.18, as presented in [21], p 59.

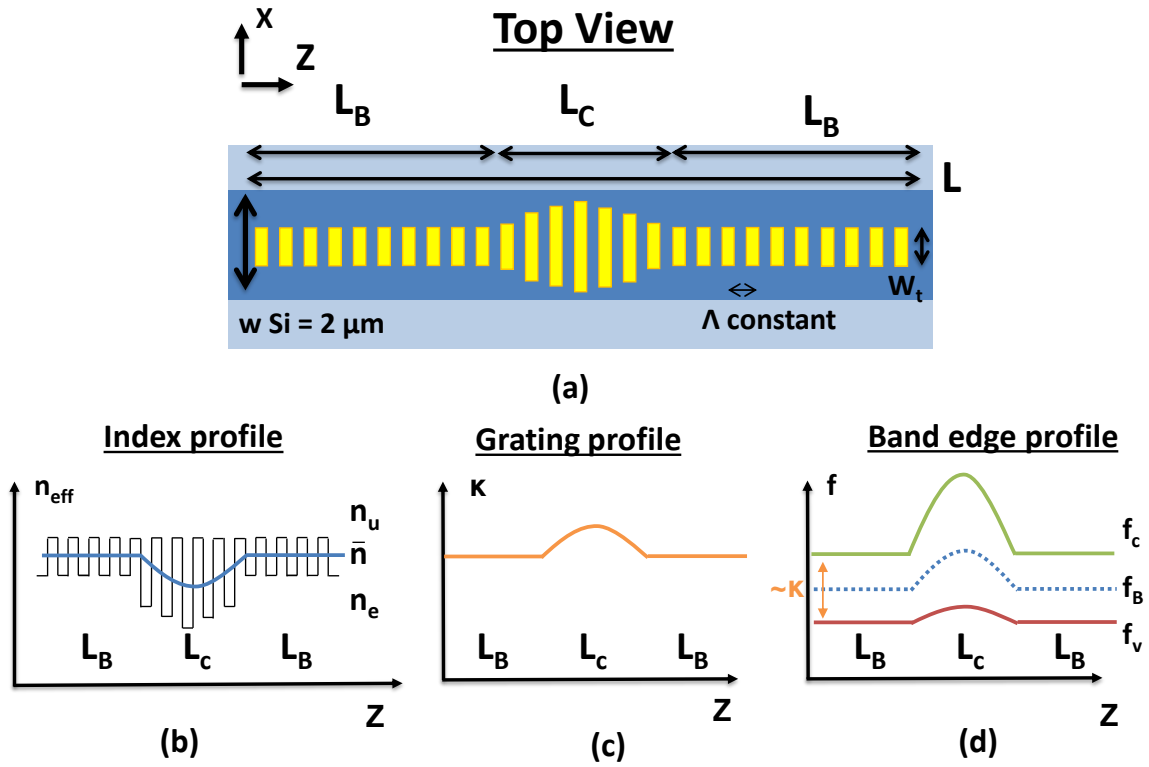


Figure 4.8: (a) Top view of the silicon waveguide. The 300 nm silicon slab is in light blue, the 500 nm laser silicon waveguide in blue and the 30 nm tooth etched regions in yellow. The grating has two regions: a parabolic tapered grating in the centre and a uniform grating at each side. Schematics of the corresponding (b) index profile, (c) grating profile and (d) band edges profile.

Here, we will only explain the design choices. First,  $w_{t,max}$  should not be too high to keep a linear index and grating strength variation with  $w_t$ . Simulations show that to have a long  $L_C$ , a high  $\Delta f_v$  is needed. Long  $L_C$  is preferable as it increases the mode spreading in the cavity. However, a high  $\Delta f_v$  means a low  $w_{t,min}$ , thus a low grating strength  $\kappa$  in  $L_B$ . Then a higher length is needed to have the same  $\kappa L$ . Simulations indicate that the high Q mode frequency  $f_{HQ}$  is always between  $f_v(\omega_{t,min})$  and  $f_v(\omega_{t,max})$ . For the parameters investigated here, the length  $L_B$  doesn't impact the Gaussian intensity profile.

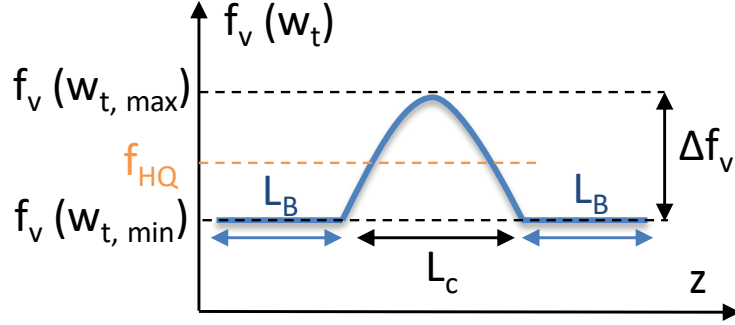


Figure 4.9: Key design parameters are  $L_c$  and  $\Delta f_v$ .

#### 4.2.4 Actual design

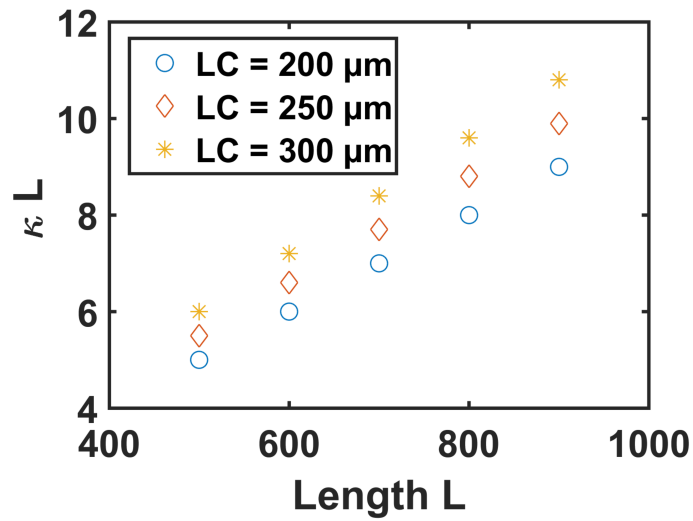
The fabricated design parameters are presented in table 4.10. We chose  $L_C = 200, 250$  and  $300 \mu m$ .  $L_B$  is adjusted to have total lengths  $L = 2L_B + L_C$  of 500, 600, 700, 800 and 900  $\mu m$ . The grating pitch  $\Lambda = 240$  nm is set to have  $\lambda_B \approx 1550$  nm. The mean  $\kappa L$  product is presented in fig. 4.10b.  $\kappa L$  ranges from 5 to 11, depending on total length  $L$ . Such values are significantly higher than in high speed or high power DFB designs, which values typically range from 1 to 2.5. As  $\kappa$  is greater in  $L_C$  than in  $L_B$ ,  $\kappa L$  values increases with increasing  $L_C$  for a given  $L$ . High  $\kappa L$  values correspond to high external Q factors.

I used equ. A.2 to compute the external quality factor, presented in fig. 4.10c, reaching several hundred thousand. As described in introduction,  $Q_{ext}$  should not be above  $Q_i$  to keep reasonable efficiency. In the following, I will only describe devices with  $L_C = 250 \mu m$  as performances were similar for the two other values.

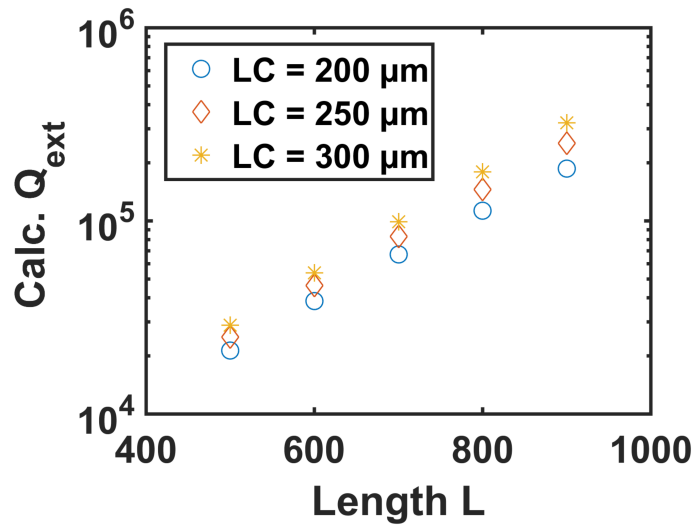
Design parameter

Lc ( $\mu\text{m}$ )	2Lb+Lc ( $\mu\text{m}$ )	$\Lambda$ (nm)	Tooth variation in Lc (nm)
200	500	240	400-1200
250	600		
300	700		
	800		
	900		

(a)



(b)



(c)

Figure 4.10: High Q laser design parameters. (a) Design values. (b) Corresponding calculated  $\kappa L$  product for the 15 fabricated designs. (c) Corresponding external Q factor.

## High Q mode

In fig. 4.8, the grating strength and effective index parabolic profiles were sketched. In this section, the actual parameters are described. In  $L_B$ ,  $w_t$  is 400 nm, leading to a grating strength of  $90 \text{ cm}^{-1}$ . In  $L_C$ , the tooth width evolves from 400 to 1200 nm. The corresponding grating strength evolves from  $90 \text{ cm}^{-1}$  in  $L_B$  up to  $220 \text{ cm}^{-1}$  in the center of  $L_C$ . This evolution is presented in fig. 4.11 in blue. Grating strengths are about half the values presented in [21], p52. Here grating teeth are 30 nm deep, a lower value than the 50 nm value reported in [21]. Longer devices are designed to have similar external quality factors. In the design presented here, the etched index decreases in  $L_C$  but the un-etched index stays constant. This is featured in fig. 4.11a in orange where we can see that the effective index variation is parabolic in the center of the cavity. The maximal variation is around 0.02 in  $L_C$ . If we consider that  $L_C/2 = 125 \mu\text{m}$  corresponds to 525 grating periods we can conclude that the index change is very small at the scale of one grating period. This was the main assumption to have a varying Bragg wavenumber in equ. 4.18. The actual band structure is presented in fig. 4.11b. In  $L_C$ , offset frequency evolves from 31 to 77 GHz. As

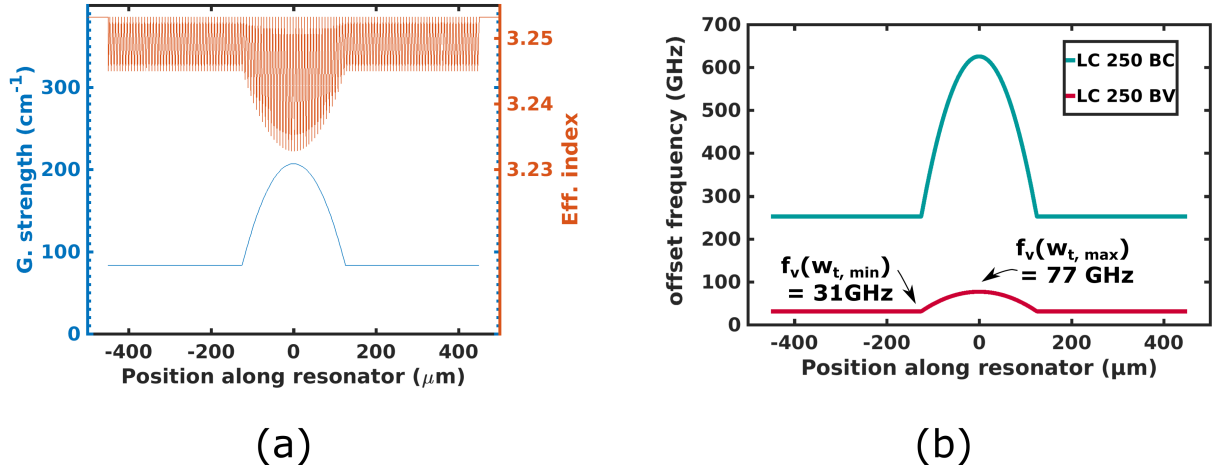


Figure 4.11: Actual design parameters for  $L_C = 250 \mu\text{m}$  and  $L = 900 \mu\text{m}$ . (a) Evolution of grating strength (blue) and index (orange) in a fabricated design with  $L_C = 250 \mu\text{m}$  and  $L = 900 \mu\text{m}$ . (b) Corresponding band structure.

shown in fig. 4.12a the grating reflection spectrum is chirped. The high Q mode is on the low frequency side of the stopband and has an offset frequency of 42 GHz. High Q mode frequency is between  $f_v(w_t, \min)$  and  $f_v(w_t, \max)$ , as explained in the previous section. The normalized intensity along laser cavity is presented in fig. 4.12b. As in [3], the profile is close to a Gaussian in the centre of the cavity. This intensity profile decreases the grating

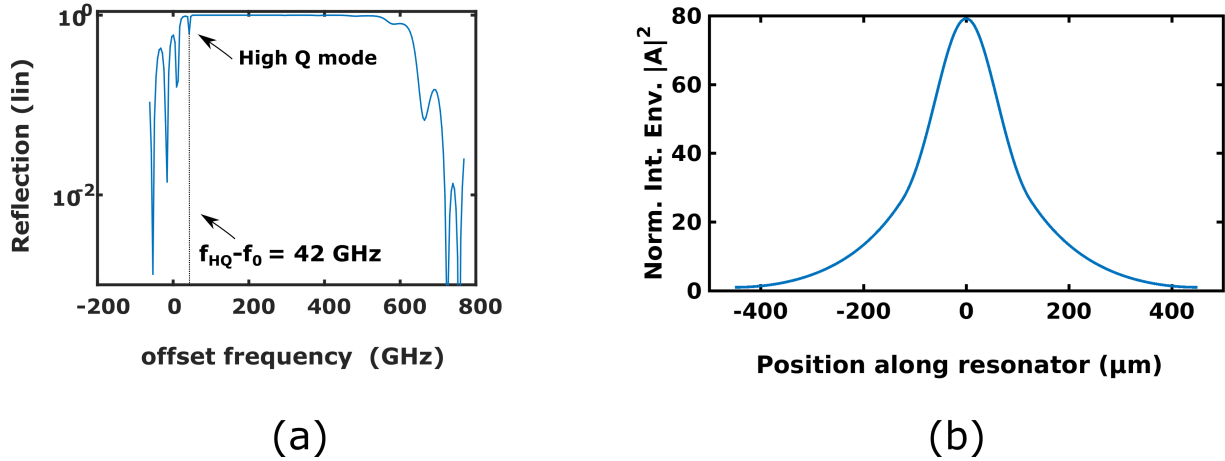


Figure 4.12: Actual design parameters for  $L_C = 250 \mu\text{m}$  and  $L = 900 \mu\text{m}$ . (a) Reflection spectrum. (b) Normalized intensity envelope.

radiation loss due to gentle confinement properties ([21], p56). Preliminary passive quality factor measurements obtained with an "optical coherence tomography setup" [26] indicate that intrinsic quality factor associated with silicon losses is above  $10^6$ , meaning that internal losses in the silicon cavity are negligible.

As the intensity is less confined in the center of the cavity than for phase shifted laser, longitudinal spatial hole burning (LSHB) should be lower. Moreover, as the length where  $w_t$  varies is large compared to the phase shift of  $\lambda/4$  phase shifted laser, LSHB may have less impact on threshold gain margin. In the next section, I will present threshold gain calculations with transfer matrix method.

#### 4.2.5 Threshold gain calculations

As we have seen in the introduction of chapter 3, phase shifted DFB lasers have high threshold gain margin, leading to high SMSR [22]. It is thus interesting to calculate cavity modes and corresponding threshold gain margin for high Q hybrid lasers. As in chapter 3, the calculation is made with transfer matrix method.

The results are displayed in fig. 4.13 for a  $900 \mu\text{m}$  long high Q laser with  $L_C = 250 \mu\text{m}$  and compared with a  $\lambda/4$  phase shifted laser of same length and same  $\kappa$ . To be consistent with chapter 3,  $\alpha_m L = 2\alpha_{th} L$  is plotted versus wavelength. As outlined in the previous section, the mode with lowest threshold gain is at the right side of the stop-band. The chirped stop-band is also reproduced: the mode spacing is different at each sides. High Q hybrid

laser threshold gain margin is approximately half the  $\lambda/4$  phase shifted case. It may be sufficient to have high side mode suppression ratio, as we will see in section 4.3.2.

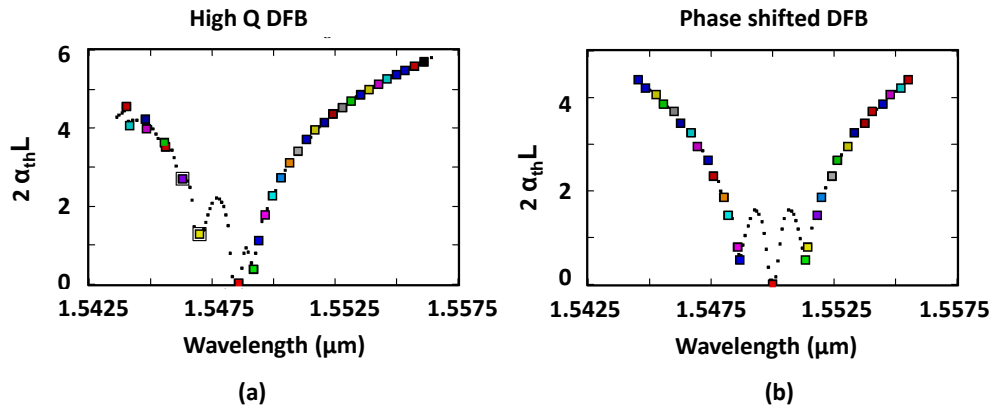


Figure 4.13: Cavity modes and threshold gain margin for (a) a high Q hybrid laser and (b) a phase shifted laser of same length and  $\kappa$ .

## 4.3 Laser static characteristics

The high Q hybrid laser top view is sketched in fig. 4.14. As discussed in previous sections, the grating is etched on the laser rib waveguide, represented in blue. The waveguide is 2  $\mu\text{m}$  wide and the grating width  $w_t$  varies along the resonator. The etched region is represented in yellow. On top of the silicon waveguide is the III-V region, in red. After the grating, light is coupled to a passive silicon waveguide which lead to a fiber grating coupler (light blue). After fabrication, lasers are tested on wafer on a thermally controlled stage at 20°C. In this section I will show L-I curves, spectra and linewidth enhancement factor of high Q lasers. I will compare the results with hybrid III-V on silicon DFB lasers of chapter 3. In the following "high speed DFB" refers to those devices.

### 4.3.1 Light-Intensity characteristics

In fig. 4.15a, the light-intensity of high Q lasers for  $L_C = 250 \mu\text{m}$  and L varying from 500 to 900  $\mu\text{m}$  is presented. Maximal single facet fibre coupled power is greater than 2.5 mW at 200 mA. The slope of L-I curves is 0.02 mW/mA for all lasers. Taking into account the 6 dB loss of the fibre grating coupler, the single facet output power is 10 mW and the differential



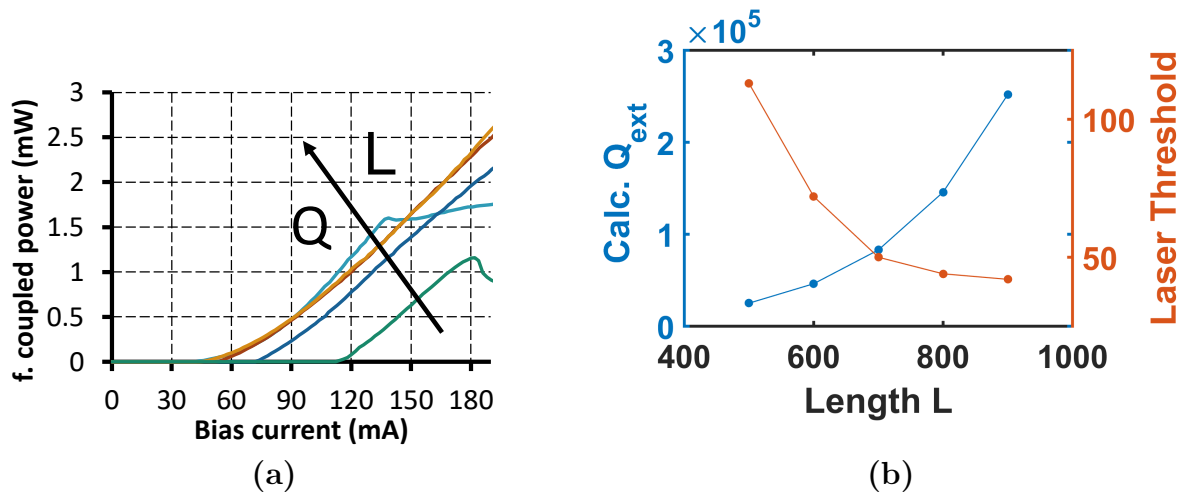


Figure 4.15: (a) Light-intensity curves for  $L_C = 250 \mu\text{m}$  and total length ranging from 500 to 900  $\mu\text{m}$ . The kink in the L-I curve for  $L = 900 \mu\text{m}$  was not observed for other samples with the same design. (b) Evolution of threshold with length  $L$ , and calculated external Q factor. Threshold drops when external quality factor increases, as in equ. 4.11.

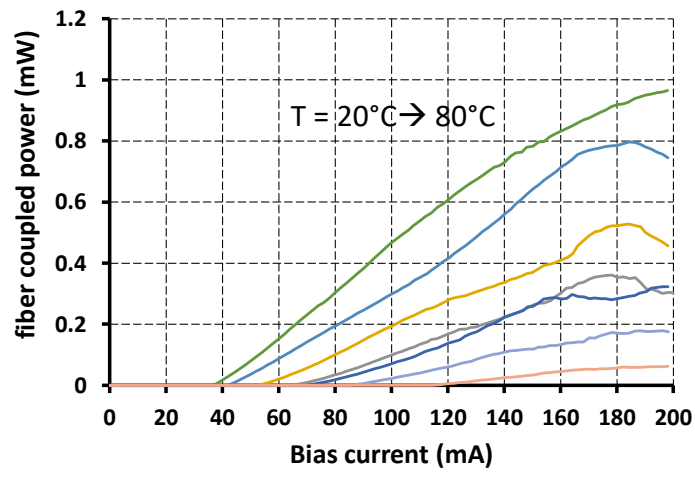


Figure 4.16: L-I dependence on temperature, from 20 to 80°C by 10 °C.

### 4.3.2 Spectra

Spectrum of a 800  $\mu\text{m}$  long high Q hybrid laser is presented in fig. 4.17a for a 100 mA bias current. It shows SMSR greater than 55 dB limited by a higher order spatial mode, as in high speed DFBs. Fig. 4.17b is a close up spectrum in the same operating condition. The high Q mode is on the right side of the stop band, in agreement with fig. 4.12a. Modes on the sides of the stop-band are highly suppressed, confirming the sufficient threshold gain margin.

On fig. 4.17c, we reported the SMSR for different bias conditions for device lengths ranging from 500 to 900  $\mu\text{m}$ : SMSR is always better than 40 dB. It slightly decreases at high bias current, as a side mode 10 nm away from the stop band arises.

Fig. 4.17d shows the high Q hybrid laser spectrum near threshold. It confirms that laser stop band is chirped : mode spacing at the right side of the stopband is approximatively twice the value at the left side. This is in good agreement with threshold gain calculations presented in 4.13, and reflection spectra of fig. 4.12a. In fig. 4.17e, we plotted the experimental stop-band width defined in fig. 4.17d for the different cavity length. The designed values represented in blue are very close to the experimental data in red, validating our simulation tool.

### 4.3.3 Linewidth enhancement factor

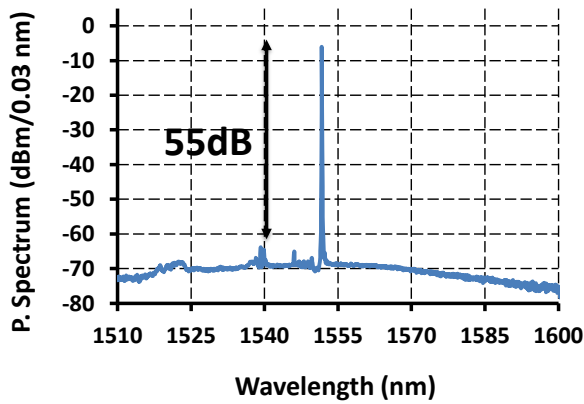
Linewidth enhancement factor is determined by InP material parameters. As described in [28], it yields even if the confinement in III-V is low : the device  $\alpha$  factor is  $1 + \eta$  times the material  $\alpha$  factor, with  $\eta \ll 1$ .  $\eta$  is given by [28]:

$$\eta \approx \frac{\mathcal{G} \times 2\pi}{\lambda n_{mat}} \ll 1 \quad (4.20)$$

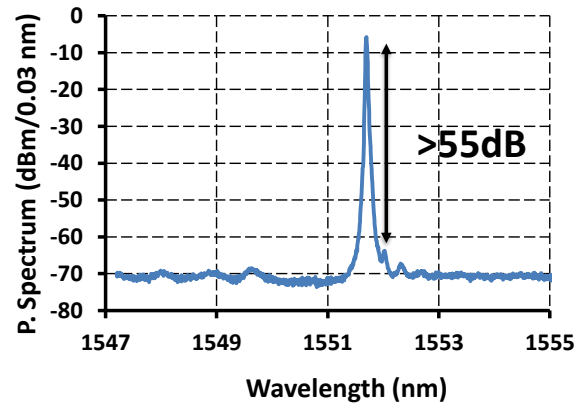
$\mathcal{G} = a(N_{th} - N_{tr})$  is the material gain per unit length. In high Q lasers the modal gain  $\Gamma_{QW}\mathcal{G}$  is greatly reduced. As losses drop in the same proportion, the material gain  $\mathcal{G}$  is similar to high speed lasers.  $\eta$  parameter is thus not significantly changed in high Q lasers.

Measured linewidth enhancement factors  $\alpha_H$  are presented in fig. 4.18. We used the same measurement setup described in section 3.2.2. For a specific device, the chirp parameter doesn't significantly change with bias current. Nevertheless,  $\alpha_H$  is as high as 3.7 for short devices and as low as 2.4 for long devices.

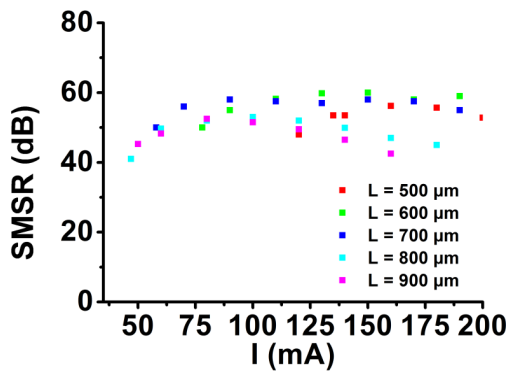
Linewidth enhancement factor  $\alpha_H$  increases with carrier density  $N$  [28]. In fig. 4.15b we showed that longer devices have lower threshold. Hence linewidth enhancement factor dif-



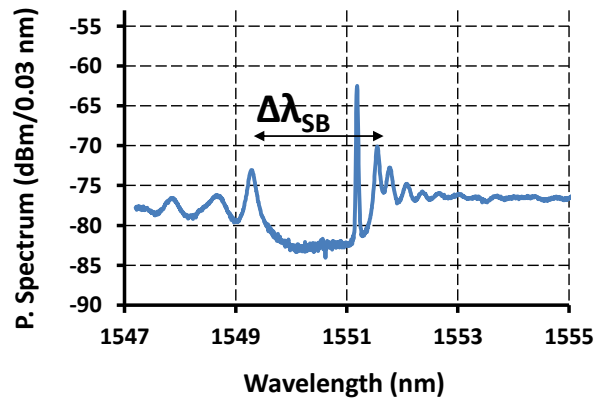
(a)



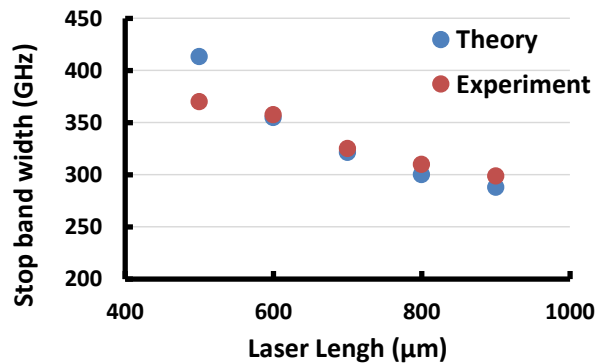
(b)



(c)



(d)



(e)

Figure 4.17: Spectrum of high Q hybrid laser with  $L = 800 \mu\text{m}$ . (a) A SMSR better than 55 dB is obtained. (b) Close up spectrum. (c) Evolution of SMSR for different bias conditions and total length. (d) spectrum at threshold showing the chirped stop-band. (e) Experimental and theoretical stop band width for the different cavity lengths.

ferences are due to carrier density changes. Evolution of linewidth enhancement factor with device threshold current is presented in fig. 4.18b.

We measured a linewidth enhancement factor of 2.5 for high speed lasers of similar threshold current, which is close to measured values for high Q lasers.

In the next section we will present the dynamics and noise properties of high Q hybrid lasers. We will show that they are really different from high speed lasers.

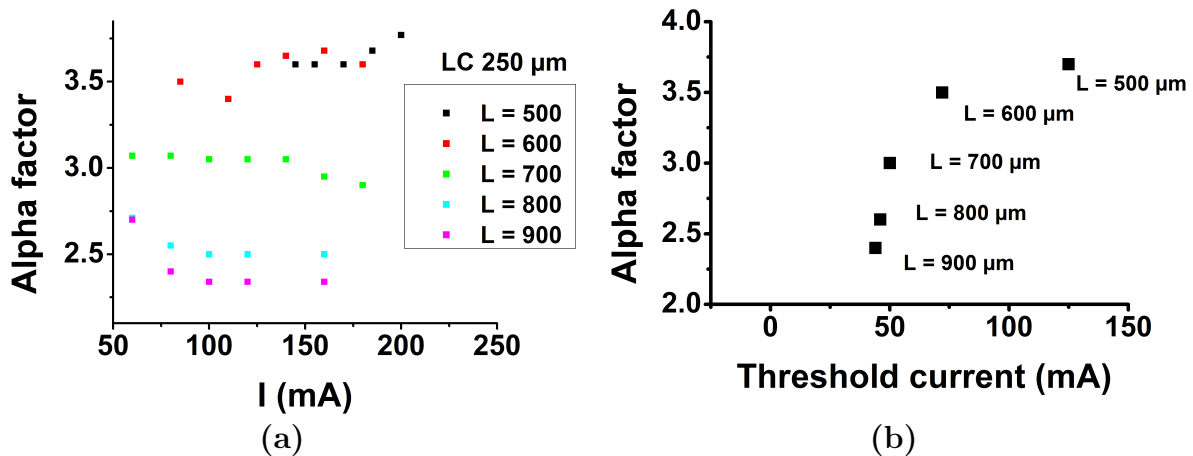


Figure 4.18: (a) High Q hybrid laser linewidth enhancement factor evolution with bias current for  $LC = 250 \mu\text{m}$  and different length  $L$ . (b) Evolution of linewidth enhancement factor with threshold current of the corresponding lasers.

## 4.4 High Q laser dynamics and noise properties

In this section we will present small signal bandwidth, relative intensity noise and linewidth measurements. We will review the impact of a high quality factor on those properties.

### 4.4.1 Small signal bandwidth

The small signal bandwidth of high Q hybrid lasers are measured using a vector network analyser, as in chapter 3. The measured AM transfer function for increasing bias current is displayed in fig. 4.19. Relaxation oscillation frequencies are significantly lower than for high speed DFB. It increases from 500 MHz to 2 GHz when bias current evolves from 50 to 110 mA. For 115 mA, high speed DFB relaxation oscillation frequency was greater than 9 GHz. If  $v_g$  is the group velocity,  $a$  the differential gain,  $N_p$  the photon density and  $\tau_p$  the photon

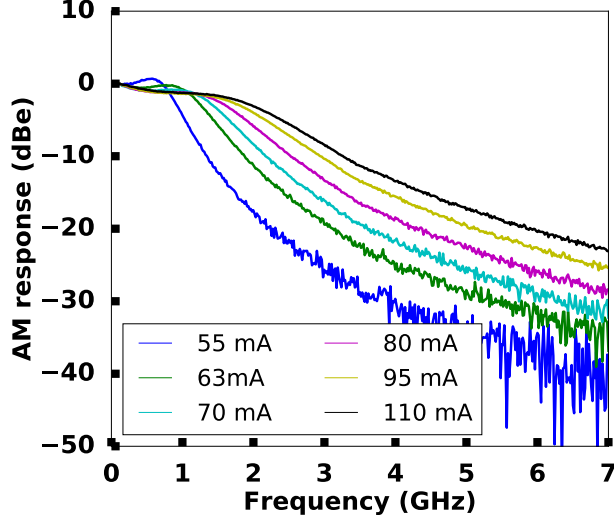


Figure 4.19: Small signal bandwidth of High Q hybrid laser with  $L_C = 250$  and  $L = 800 \mu\text{m}$  for increasing bias current. Laser threshold was 45 mA.

lifetime, the relaxation oscillation frequency  $f_r$  is:

$$\omega_r^2 = (2\pi f_r)^2 \approx \frac{v_g a N_p}{\tau_p} \quad (4.21)$$

This equation indicates that the low  $f_r$  comes from the high photon lifetime. As above threshold, photon density  $N_p$  is proportional to  $I - I_{th}$ , relaxation oscillation frequency  $f_r$  is proportional to  $\sqrt{I - I_{th}}$ . This is experimentally demonstrated in fig. 4.20a, as  $f_r$  increases very linearly with  $\sqrt{I - I_{th}}$ .

In contrast with high speed DFB, the modulation response is highly damped: it is not peaked around  $f_r$ . Again, this is a signature of a high photon lifetime. If  $\gamma$  is the damping coefficient,  $\frac{1}{\tau_e}$  the inverse of carrier lifetime and  $f_r$  the relaxation oscillation frequency, we have [29]:

$$\gamma = K \times f_r^2 + \frac{1}{\tau_e} = 4\pi\tau_p f_r^2 + \frac{1}{\tau_e} \quad (4.22)$$

The damping rate is proportional to the photon lifetime. In fig. 4.20b, we plotted the fitted damping coefficient  $\gamma$  versus  $f_r^2$ . As expected,  $\gamma$  evolves linearly with  $f_r^2$ . The fitted  $K$  factor is  $K = 4.1$  ns. The interception with the y-axis gives an inverse differential carrier lifetime of  $\frac{1}{\tau_e} = 2.5$  GHz. Neglecting nonlinear coefficients,  $K = 4\pi\tau_p$  where  $\tau_p$  is the photon lifetime. We can extract a photon lifetime as high as 103 ps. This high photon lifetime is simply due to the high quality factor. In fig. 4.20c, the  $K$  factor is extracted for different total length  $L$ .

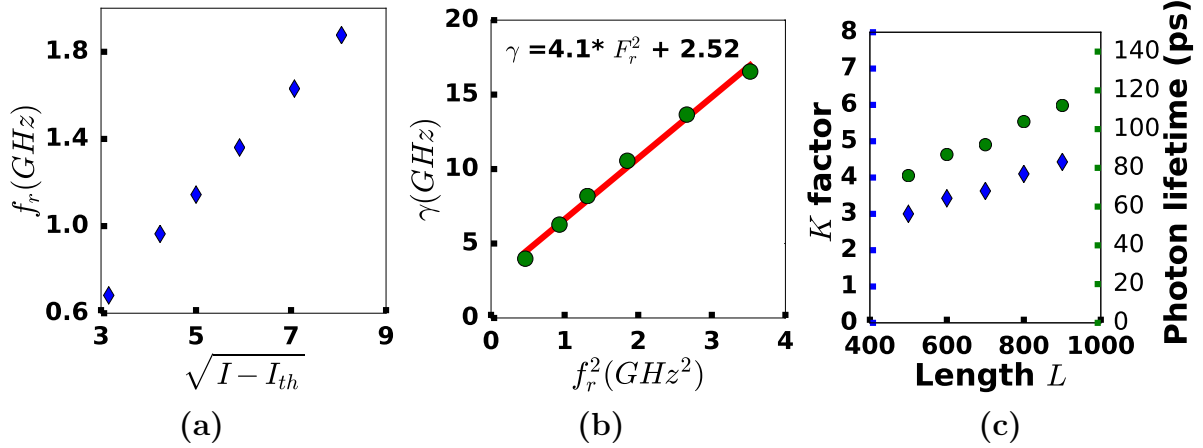


Figure 4.20: (a) Evolution of relaxation oscillation frequency with  $\sqrt{I - I_{th}}$  for high Q hybrid laser with  $L_C = 250$  and  $L = 800 \mu\text{m}$ . (b) Evolution of Damping coefficient with  $f_r^2$  for the same laser. (c) Evolution of  $K$  factor for  $L_C = 250 \mu\text{m}$  and different total length  $L$ .

Although the exponential dependence is not reproduced, the quality factor increases with the total length as expected. The measured response of fig. 4.19 is a typical second order transfer function, as in high speed DFBs. After the relaxation oscillation frequency, the response drops with a 40 dB/decade slope, a typical feature of class B lasers [30]. Future designs with a higher photon lifetime may lead to class A dynamics.

#### 4.4.2 Relative intensity noise measurements

The relative intensity noise is [30]:

$$RIN(f) = \frac{4R_{sp}}{\langle N_{ph} \rangle} \times \frac{(\gamma_e^2) + (2\pi f)^2 + \frac{(2\pi f_r)^2 \gamma_e}{R_{sp}}}{((2\pi f_r + 2\pi f)^2 + \Gamma_r^2) ((2\pi f_r - 2\pi f)^2 + \Gamma_r^2)} \quad (4.23)$$

$\langle N_{ph} \rangle = \frac{P_0}{h\nu}$  is the mean photon density,  $R_{sp}$  is the spontaneous emission rate,  $\gamma_e$  the inverse of carrier lifetime,  $f$  the frequency of interest,  $f_r$  the relaxation oscillation frequency,  $\gamma$  the damping factor and  $\Gamma_r$  defined as :

$$\Gamma_r = \frac{\pi f_r^2}{\gamma} \quad (4.24)$$

Calculated RIN curves for increasing bias current is presented on fig. 4.21, for typical values of  $f_r$  and  $\gamma$ . RIN is low for frequency below  $f_r$ , is peaked at  $f \approx f_r$  and decays after  $f_r$ . As bias current increases, RIN value decreases as output power and damping coefficient increase.

With high power designs, RIN below -160 dB/Hz for output power of 167 mW have recently been obtained [10]. We measure the RIN with a dedicated test bench, presented in fig. 4.22a.

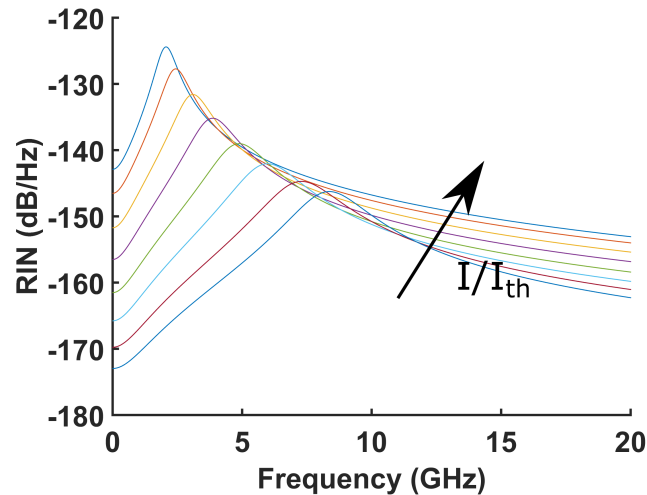


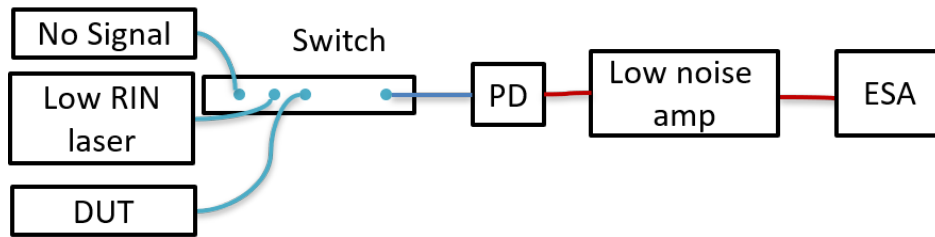
Figure 4.21: Calculated RIN values for increasing bias current. RIN strongly depends on  $f_r$  and  $\gamma$ .

Three measurements are needed to obtain laser relative intensity noise [31]:

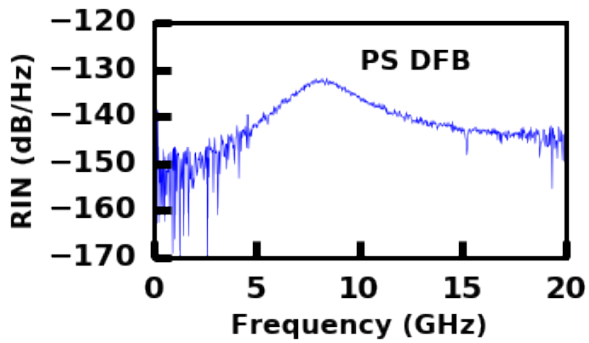
- A measurement without light to calibrate the bench noise.
- A measurement with a very low RIN laser (a YAG laser) to calibrate the shot noise contribution.
- A measurement of laser itself.

The RIN is extracted from those three measurements. The measured relative intensity noise of a high speed DFB is presented in fig. 4.22b for  $I/I_{th} = 2.7$ . The RIN is as low as -150 dB/ Hz for frequency below  $f_r$  but as high as -135 dB/ Hz for  $f \approx f_r$ .

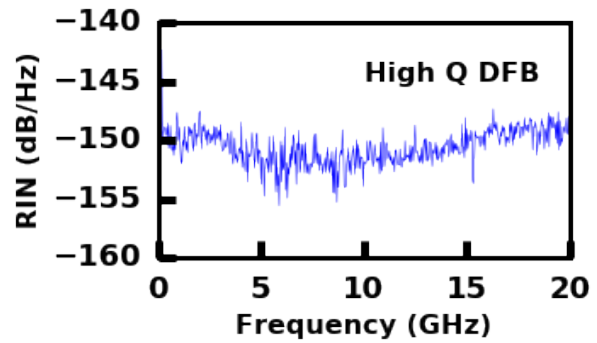
Relative intensity noise (RIN) of a high Q DFB is measured for  $I/I_{th} = 2.8$  and displayed on fig. 4.22c. The RIN is very different from the high speed laser, with a flat RIN characteristic and level below -147 dB/Hz. A very little increase of the RIN due to  $f_r$  can be seen around 2 GHz, in agreement with the small signal bandwidths presented in fig. 4.19. RIN increases again from 10 to 20 GHz due to the limited side mode suppression ratio. From equ. 4.23 and fig. 4.21, the RIN strongly depends on the relaxation oscillation frequency  $f_r$  and the damping coefficient  $\gamma$ . As we have seen for small signal bandwidth measurements, a high photon lifetime gives low  $f_r$  and  $\gamma$ , leading to low and flat RIN. In the next section, I will present the linewidth of high Q hybrid lasers.



(a)



(b)



(c)

Figure 4.22: (a) Relative intensity noise measurement setup. (b) RIN of high speed phase shifted DFB, for  $I/I_{th} = 2.7$  (c) RIN of high Q DFB for  $I/I_{th} = 2.8$

### 4.4.3 Linewidth measurements

#### Linewidth measurements with classical self heterodyne method

Laser linewidth can be evaluated with the classical delayed self-heterodyne method [32] sketched in fig. 4.25. In one arm of the interferometer, the signal frequency is shifted with an acousto-optic modulator. In the other arm, the signal is delayed with a 20 km fiber coil. The signal is recombined, detected with a photodiode and displayed on a spectrum analyser. The interferogram depends on the ratio of delay time  $\tau$  given by the fiber length and laser

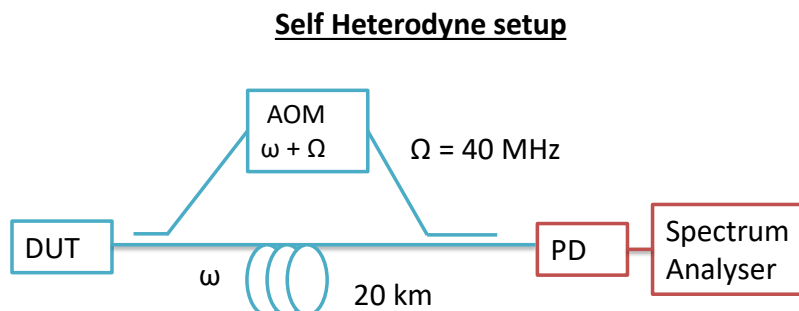


Figure 4.23: Classical self heterodyne measurement

coherence time  $\tau_c$  given by the source linewidth. Effect of fiber length on interferogram is explained in details in [33]. Usually, people choose a delay  $\tau$  such that  $\frac{\tau}{\tau_c} \approx 10$ . With such a delay, the interferogram is a lorentzian curve if the laser intrinsic linewidth is the dominant source of noise. Its -3 dB width equals twice the laser linewidth.

Laser spectral linewidth is fundamentally limited by the Schawlow-Townes formula. However, the spectral profile can be broadened by thermal or drive current induced fluctuations. Those perturbations are frequency dependant, and generally decrease with an  $\frac{1}{f^\alpha}$  law. As fluctuations induced by drive current are important, very low noise sources need to be used [34].

I measured a high Q hybrid lasers with this method. Lasers were mounted on alumina bases and driven with very low noise current sources [35]. Interferogram is presented in fig. ??a for a 70 mA bias current ( $1.8 I_{th}$ ). The data doesn't fit with a lorentzian distribution. As in [36], the interferogram is broadened by technical noise. Data is thus fitted with a pseudo Voigt profile. In self-heterodyne measurements, the optical linewidth is half the 3 dB bandwidth of the measured interferogram. The extracted 3 dB Voigt fit is 365 kHz for a 70 mA bias current ( $1.6 I_{th}$ ), confirming that high Q lasers have low linewidth. The Voigt linewidth takes into account the lorentzian linewidth and  $\frac{1}{f^\alpha}$  technical noise. Effect of technical noise may be

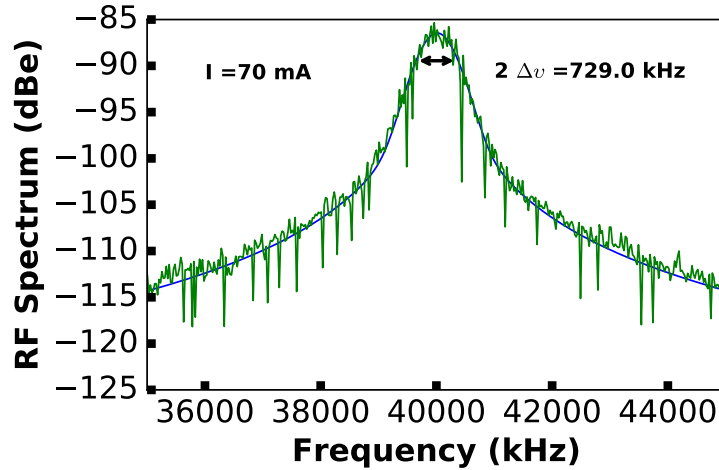


Figure 4.24: Linewidth measurement of a high Q DFB with the self heterodyne method.

important for some applications [37], but it can't be easily linked with the Voigt linewidth. To characterise the laser noise properties, it is necessary to retrieve the Lorentzian linewidth. As here profile is very broad, extracting the Lorentzian linewidth doesn't give precise values. As in [36], one solution is to use an interferometer with a short delay, as the Gaussian part of the interferogram depends on the delay length. Indeed, the interferometer acts as a high pass frequency filter which cut-off frequency decreases with delay [36]. However, with a short delay the curve fitting is more complex.

In the next section I will present frequency noise measurements. With this method we can properly separate Schawlow-Townes-Henry linewidth from technical noise.

### Frequency noise measurements with self heterodyne method

To measure the frequency noise we can use a frequency discriminator [3] [38]. As described in fig. 4.25, here the frequency noise measurement is a modified self-heterodyne method. After the interferometer, the signal is detected on a photodiode and recorded on a sampling scope. Phase and frequency noise power spectral density (PSD) is then calculated by FFT in matlab. With this method, the frequency noise doesn't depend on the interferometer delay length. Acquisition time gives the lower frequency bound measurement (Shannon sampling theorem). For the data presented here, I used a 100 ms long sequence. The upper frequency limit is  $\frac{f_{AOM}}{4} = 20$  MHz. At a certain frequency, technical noise no longer dominates and frequency noise reaches a plateau  $S_0$ . Schawlow-Townes-Henry linewidth is linked to  $S_0$  by

([37], p185):

$$\Delta\nu = 2\pi S_0 \quad (4.25)$$

The factor 2 comes from our definition of  $S_0$ . More details on frequency noise measurements

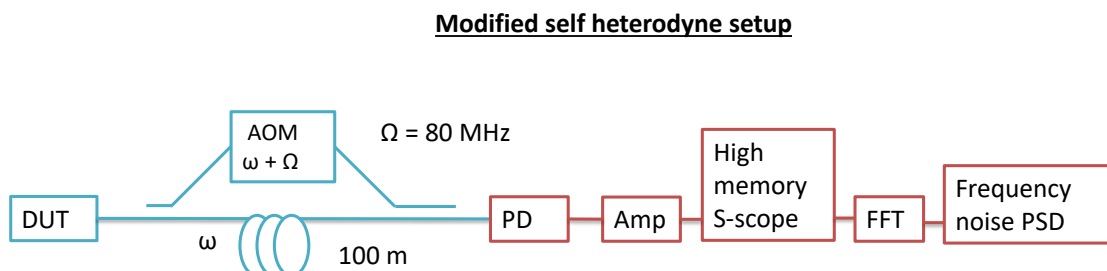


Figure 4.25: Self heterodyne setup. Laser output is split to an acousto-optic modulator and delay and recombined in a photodiode. The signal is acquired with a high memory sampling scope and analysed offline with matlab.

can be found in [39] and [37]. I measured the linewidth of a high speed DFB with this set-up. The frequency noise curves are presented in fig. 4.26a, for different bias current injected in the laser. Frequency noise floor is obtained for frequencies above 2 MHz. The two spikes at high frequency come from non-ideal delay calibration. The extracted Schawlow-Townes-

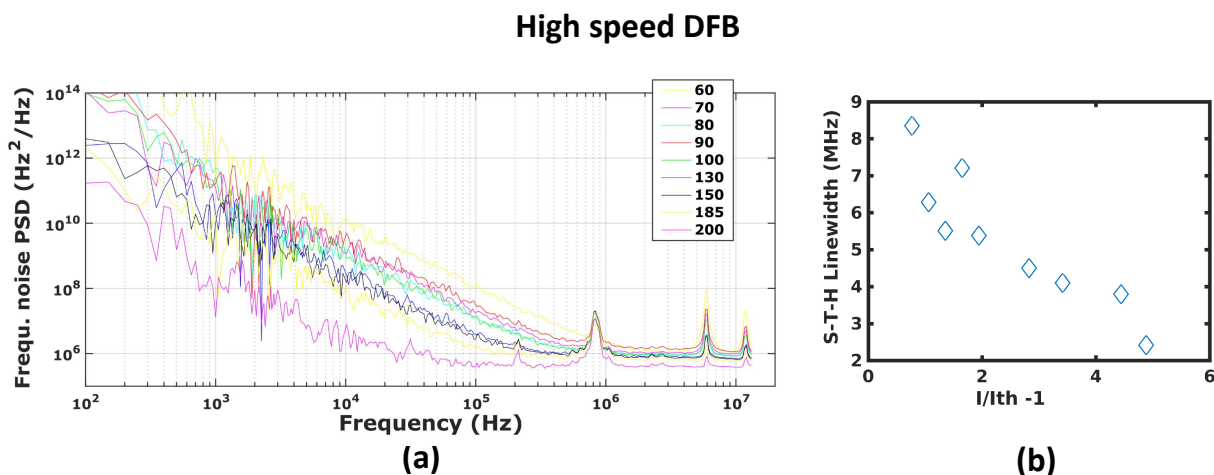


Figure 4.26: High speed DFB linewidth measurements. (a) Frequency noises curves for increasing bias current, showing technical noise and plateau  $S_0$ . (b) Corresponding linewidths are between 9 and 2 MHz.

Henry linewidth are displayed on fig. 4.26b. Linewidth decreases with bias current, with minimal values of 2.2 MHz at 200 mA. Those values are comparable with recently reported

III-V/Si DFB lasers [8]. I measured the frequency noise of a high Q hybrid laser with  $L = 800 \mu\text{m}$  for increasing bias current. Results are presented in fig. 4.27ab for bias currents from 55 to 100 mA, and fig. 4.27cd for bias currents from 80 to 160 mA. Fig. 4.27 b and d are close up of fig. 4.27 a and c respectively. Spikes at  $f = 200 \text{ kHz}$ ,  $1 \text{ MHz}$  or  $4.5 \text{ MHz}$  comes from the current source as using another current source slightly increase or decrease the peak values. The ripple at high frequency comes from non-ideal delay calibration. As in the case of phase shifted laser, we can see in fig. 4.27 that frequency noise decreases with frequency up to a plateau, obtained for  $f = 1 \text{ MHz}$ . However, it is clear from fig. 4.27c that it is only true for bias current up to 65 mA. This means that above this value, technical noise dominates.

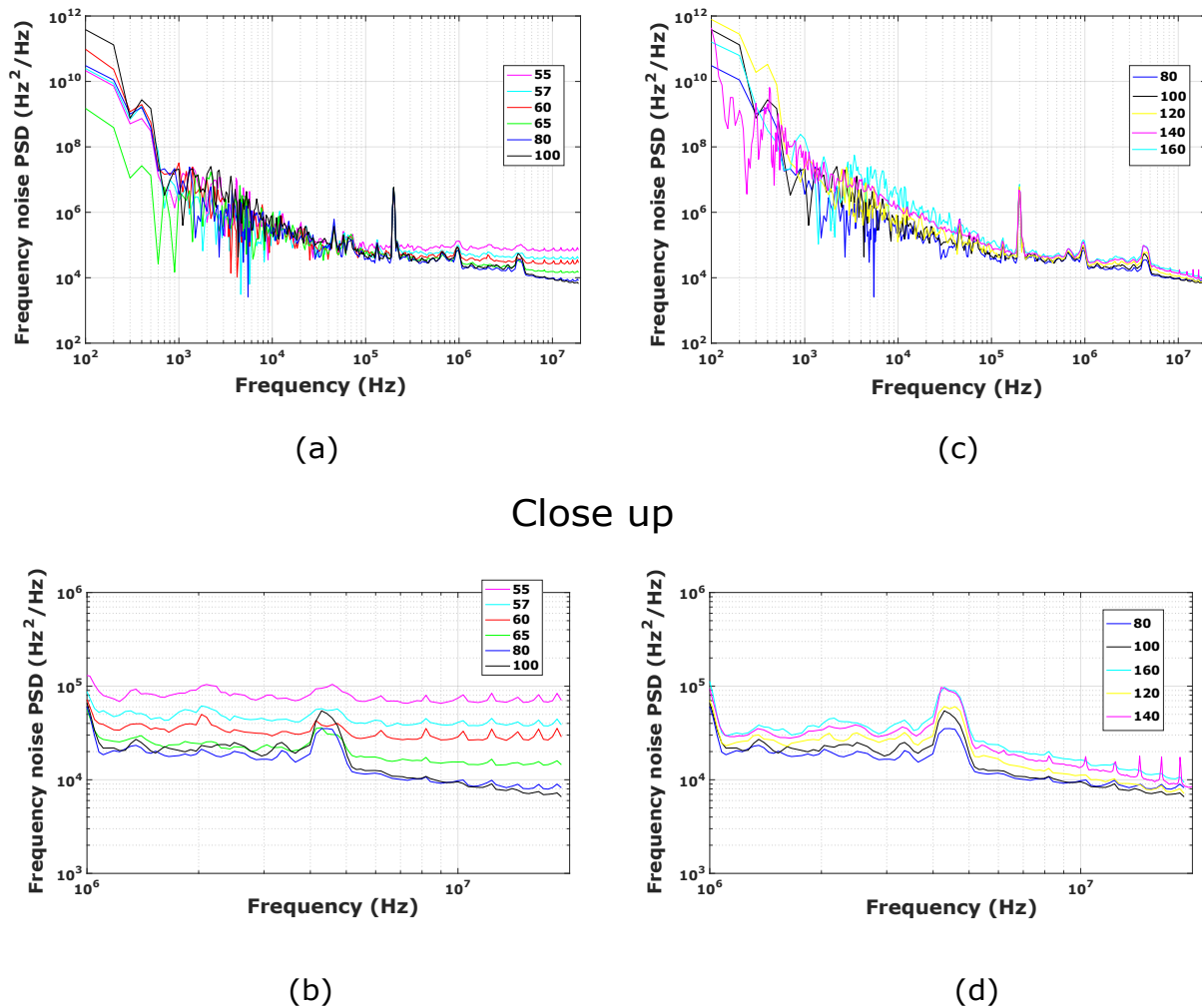


Figure 4.27: Frequency noise power spectral density for a high Q laser with  $L_C = 250 \mu\text{m}$  and  $L = 800 \mu\text{m}$  for (a)  $I_b = 55$  to  $100 \text{ mA}$  and (b)  $80$  to  $160 \text{ mA}$ . (c) and (d) are close up of (a) and (b) in the  $1\text{-}20 \text{ MHz}$  range.

The minimal frequency noise is  $6.5 \cdot 10^3 \text{ Hz}^2/\text{Hz}$ , corresponding to a linewidth better than 41 kHz. It is obtained for a bias current of 100 mA ( $\frac{I}{I_{th}} = 2.2$ ). As can be seen in fig. 4.27b and d, frequency noise increases for bias currents higher than 100 mA. It increases in a wide frequency band ranging from 10 kHz to 20 MHz. As this band is wide, we can conclude that the frequency noise increase comes from a greater technical noise. We can also conclude that technical noise is not independent of bias current.

The extracted minimal linewidth is plotted in fig. 4.28 for the high Q laser in orange and the high speed laser in blue. High Q hybrid laser linewidth is 50 times below the high speed laser case, demonstrating the interest of such design. In the next section, I will compare the linewidth of the different designs presented in section 4.2.4.

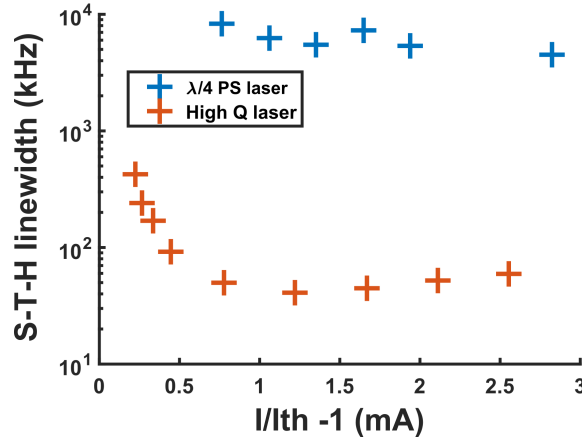


Figure 4.28: Extracted Schawlow-Townes-Henry linewidth of High Q hybrid laser (orange) and classical phase shifted laser (blue). High Q laser linewidth is 50x times narrower than high speed phase shifted laser. The best linewidth is 41 kHz.

## Laser cavity comparison

Expressed with quality factor variables, the Schawlow-Townes-Henry linewidth formula is:

$$\Delta\nu = \frac{\pi h\nu^3 n_{sp}}{2QQ_{ext}\eta_d(I - I_{th})} \times (1 + \alpha_H^2) \quad (4.26)$$

As described in fig. 4.10, lasers with five different lengths with increasing external quality factor were fabricated. Q factor has an impact on the other laser parameters. In section 4.3 I showed that threshold current decreases with Q factor, as expected by the threshold condition. Interestingly, the differential efficiency  $\eta_d$  didn't depend on Q. As indicated by

measurements of section 4.18, linewidth enhancement factor  $\alpha_H$  decreases with  $Q$  as it depends on carrier density at threshold  $N_{th}$ , which decreases with  $Q$ . I measured lasers of the same bar with  $L_C = 250 \mu\text{m}$  and total length ranging from 500 to 900  $\mu\text{m}$ .

As in the precedent section, linewidth is extracted by frequency noise measurements. Schawlow-Townes-Henry (S-T-H) linewidths versus normalised bias current  $I/I_{th} - 1$  is presented in fig. 4.29a. Linewidth of every laser decreases with  $I/I_{th} - 1$  down to the same linewidth floor of 40 kHz, meaning that technical noise affects similarly all lasers.

As expected, linewidth decreases with increasing  $Q$ , as blue, orange, yellow, purple and green curve values stay in this order for linewidth above the noise floor. Above the noise floor, linewidths fit well with a  $1/P$  dependence, as presented in fig. 4.29b. Residual linewidth is the y axis intercept of the  $1/P$  fit [12]. From fig. 4.29 we can extract a residual linewidth of 13 kHz for laser with  $L = 900 \mu\text{m}$ , which is 3 times above the noise floor.

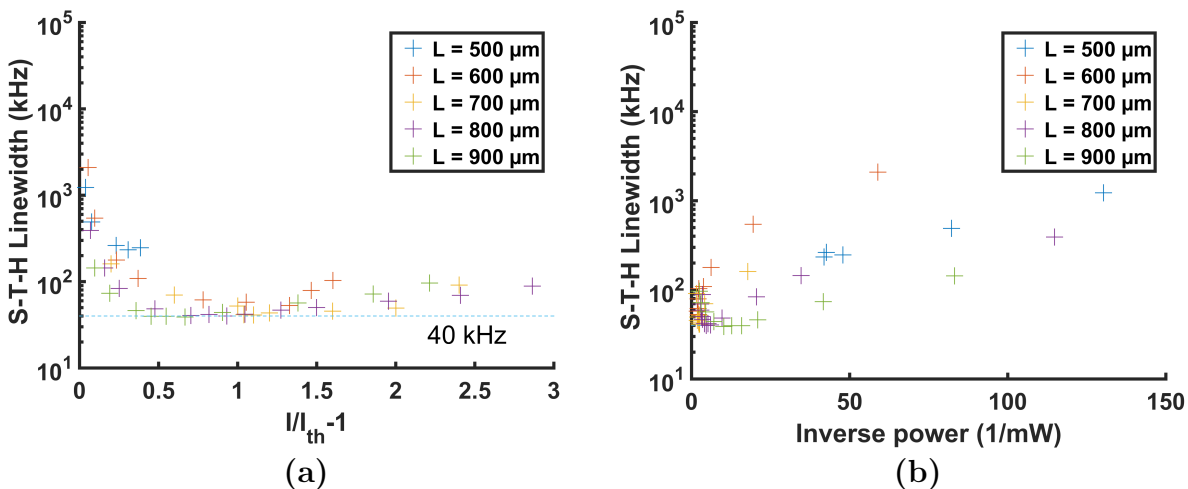


Figure 4.29: High Q hybrid laser linewidth versus (a)  $I/I_{th} - 1$  and (b) versus inverse fiber coupled power for the different fabricated cavities.

To overcome the noise floor, frequency noise measurements should be measured at higher frequencies. The frequency noise measurement range had been lastly improved up to 40 MHz compared to the 20 MHz presented above. With such setup, I measured a linewidth floor of  $\Delta\nu = 4.2 \times 2\pi = 27 \text{ kHz}$ , presented on fig. 4.30. In a near future, developing a setup presented in [3], or [40], may lead to lower measured linewidth.

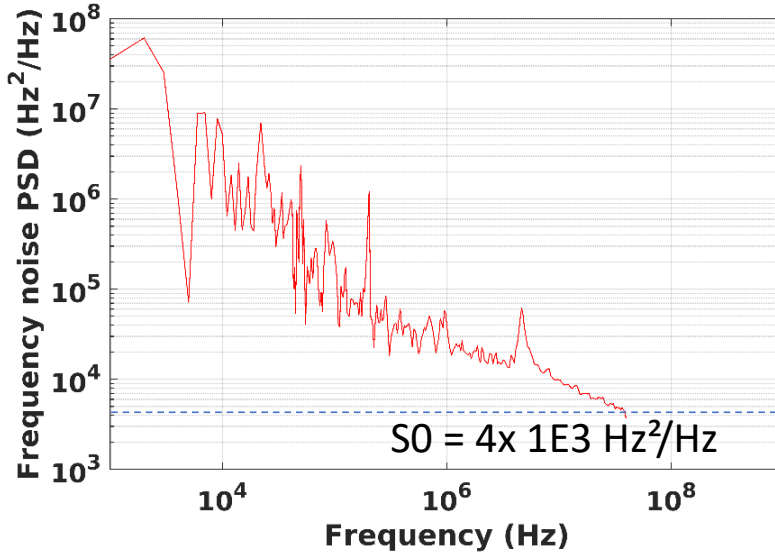


Figure 4.30: High Q hybrid laser best linewidth is 27 kHz.

## 4.5 Chapter conclusion

In this chapter, I investigated high Q hybrid lasers. They are described by the same formalism as phase shifted or tapered grating described in chapter 3. The basic idea of this design is to reduce total losses by a factor greater than 10. As in all semiconductor lasers, p- and n-doped regions are necessary to inject carriers in the active region.

As described in the beginning of this chapter, those regions induce losses that may limit the noise properties. In III-V Lab-Leti hybrid III-V on silicon platform, I showed how to bury the mode in a very low loss silicon waveguide, limiting the overlap with p- and n-doped regions.

As the quantum well confinement is below 1%, mirror losses need also to be reduced to obtain low threshold. This means that  $\kappa L$  product (or equivalently external quality factor) is very high. The high photon lifetime affects the dynamic characteristics.

First, relaxation oscillation frequency  $f_r$  is significantly lower than in high speed DFB, with values from 0.5 to 2 GHz depending on bias current. Secondly, relative intensity noise is as low as -147 dB/Hz with flat level on a 20 GHz range.

This is both a consequence of low spontaneous emission rate, low  $f_r$  and a high damping coefficient. Those three characteristics are directly linked with the high photon lifetime. The last consequence of high photon lifetime is the laser linewidth. Linewidths of high Q DFB are reduced by a factor 50 compared to high speed designs. Linewidth floor due to technical

noise is 40 kHz, comparable with the 50 kHz reported in [3].

### Future work and outlook

In a near future, it would be interesting to measure the linewidth with a frequency discriminator, as it is possible to measure the frequency noise up to the GHz range. With such setup developed in [3], a lower noise floor may be achieved. Using the same setup as in [3] and [15] would result in a clearer device comparison. It is also possible to measure the linewidth with a coherent receiver [40]. In [38], it is shown that noise floor has no effects on heterodyne DPSK coherent detection. It would be interesting to demonstrate such a result experimentally with a high Q hybrid laser.

It is also important to understand how spatial hole burning affects those lasers, both theoretically using transfer matrix method and experimentally using a setup developed in [41]. Now that first high Q laser are demonstrated in III-V lab/Leti platform, new devices can be designed, with cavities optimized for lower threshold current or higher power.

In this thesis, I showed that a 40 mA threshold is achievable even if the III-V region overlap is reduced to 5%. As sketched in fig. 4.31, III-V overlap is reduced by a factor 4 compared to the first high Q hybrid laser [3] as a higher oxide thickness is used, and it is similar to the devices reported lastly in [15]. High Q hybrid lasers performances depend on internal losses,

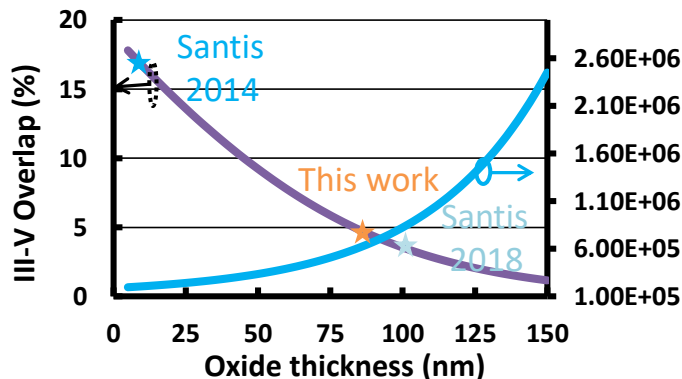


Figure 4.31: Reported High Q III-V/Si hybrid lasers with different bonding thickness. As lasers from Caltech use a different structure, the quantum well overlap value is only a rough estimate. Data is from [3] and [15]

limited here by III-V region absorption coefficients. To reduce those losses, we can further increase the oxide thickness up to values where silicon losses dominate.

Moreover, better performances will be obtained if III-V doping concentration, III-V active region design and silica bonding thickness are optimized.

## References

- [1] A. Martin et al. “Photonic Integrated Circuit-Based FMCW Coherent LiDAR”. In: *J. Lightwave Technol.* 36.19 (Oct. 2018), pp. 4640–4645.
- [2] A. Yariv. *Quantum Electronics, 3rd Edition*. 1987.
- [3] C. T. Santis et al. “High-coherence semiconductor lasers based on integral high-Q resonators in hybrid Si/III-V platforms”. In: *Proceedings of the National Academy of Sciences* 111.8 (2014), pp. 2879–2884. eprint: <http://www.pnas.org/content/111/8/2879.full.pdf>.
- [4] A. Gallet et al. “Dynamic and Noise Properties of High-Q Hybrid Laser”. In: *2018 IEEE International Semiconductor Laser Conference (ISLC)*. Sept. 2018, pp. 1–2.
- [5] C. Henry. “Theory of the linewidth of semiconductor lasers”. In: *IEEE Journal of Quantum Electronics* 18.2 (Feb. 1982), pp. 259–264.
- [6] K. Petermann. “Basic Laser Characteristics”. In: *Laser Diode Modulation and Noise*. Dordrecht: Springer Netherlands, 1988, pp. 5–58.
- [7] K. Kojima, K. Kyuma, and T. Nakayama. “Analysis of the spectral linewidth of distributed feedback laser diodes”. In: *Journal of Lightwave Technology* 3.5 (Oct. 1985), pp. 1048–1055.
- [8] S. Keyvaninia et al. “Heterogeneously integrated III-V/silicon distributed feedback lasers”. In: *Opt. Lett.* 38.24 (Dec. 2013), pp. 5434–5437.
- [9] H. Soda et al. “Stability in single longitudinal mode operation in GaInAsP/InP phase-adjusted DFB lasers”. In: *IEEE Journal of Quantum Electronics* 23.6 (June 1987), pp. 804–814.
- [10] M. Faugeron et al. “High-Power Tunable Dilute Mode DFB Laser With Low RIN and Narrow Linewidth”. In: *IEEE Photonics Technology Letters* 25.1 (Jan. 2013), pp. 7–10.
- [11] W. Ming-Chiang, L. Yu-hwa, and W. Shyh. “Linewidth broadening due to longitudinal spatial hole burning in a long distributed feedback laser”. In: *Applied Physics Letters* 52.14 (1988), pp. 1119–1121. eprint: <https://doi.org/10.1063/1.99180>.
- [12] M. Okai et al. “Corrugation-Pitch-Modulated Distributed Feedback Lasers with Ultranarrow Spectral Linewidth”. In: *Japanese Journal of Applied Physics* 33.5R (1994), p. 2563.

- [13] D. J. et al. “Semiconductor quantum dot lasers epitaxially grown on silicon with low linewidth enhancement factor”. In: *Applied Physics Letters* 112.25 (2018), p. 251111. eprint: <https://doi.org/10.1063/1.5025879>.
- [14] B. A. et al. “Widely tunable narrow-linewidth 1.5  $\mu\text{m}$  light source based on a monolithically integrated quantum dot laser array”. In: *Applied Physics Letters* 110.18 (2017), p. 181103. eprint: <https://doi.org/10.1063/1.4982716>.
- [15] C. T. Santis et al. “Quantum control of phase fluctuations in semiconductor lasers”. In: *Proceedings of the National Academy of Sciences* 115.34 (2018), E7896–E7904. eprint: <https://www.pnas.org/content/115/34/E7896.full.pdf>.
- [16] H. Kogelnik and C. V. Shank. “Coupled-Wave Theory of Distributed Feedback Lasers”. In: *Journal of Applied Physics* 43.5 (1972), pp. 2327–2335. eprint: <https://doi.org/10.1063/1.1661499>.
- [17] J. D. Jackson. *Classical electrodynamics*. 3rd ed. New York, NY: Wiley, 1999.
- [18] H. Haus and C. Shank. “Antisymmetric taper of distributed feedback lasers”. In: *IEEE Journal of Quantum Electronics* 12.9 (Sept. 1976), pp. 532–539.
- [19] H. Haus and C. Shank. “Antisymmetric taper of distributed feedback lasers”. In: *IEEE Journal of Quantum Electronics* 12.9 (Sept. 1976), pp. 532–539.
- [20] H. C. Casey and P. L. Carter. “Variation of intervalence band absorption with hole concentration in p-type InP”. In: *Applied Physics Letters* 44.1 (1984), pp. 82–83. eprint: <https://doi.org/10.1063/1.94561>.
- [21] C. T. Santis. “High-coherence hybrid Si/III-V semiconductor lasers”. PhD thesis. 2013.
- [22] J. Buus, M.-C. Amann, and D. J. Blumenthal. “Single Mode Laser Diodes”. In: *Tunable Laser Diodes and Related Optical Sources*. IEEE, 2005.
- [23] M. Faugeron. “Diode laser 1.5 micron de puissance et faible bruit pour l’optique hyperfréquence.” 2012SUPL0018. PhD thesis. 2012.
- [24] G. P. Agrawal and A. H. Bobeck. “Modeling of distributed feedback semiconductor lasers with axially-varying parameters”. In: *IEEE Journal of Quantum Electronics* 24.12 (Dec. 1988), pp. 2407–2414.
- [25] S. T. Steger. “A fundamental approach to phase noise reduction in hybrid Si/III-V lasers”. PhD thesis. 2014.

- [26] S. Combrié et al. “Comb of high-Q Resonances in a Compact Photonic Cavity”. In: *Laser & Photonics Reviews* 11.6 (), p. 1700099. eprint: <https://onlinelibrary.wiley.com/doi/pdf/10.1002/lpor.201700099>.
- [27] G. Levaufre. “Circuits photoniques intégrés incluant des lasers hybrides III-V sur silicium pour applications en télécommunication très haut débit”. PhD thesis. 2016.
- [28] M. Osinski and J. Buus. “Linewidth broadening factor in semiconductor lasers—An overview”. In: *IEEE Journal of Quantum Electronics* 23.1 (Jan. 1987), pp. 9–29.
- [29] Coldren, Corzine, and Masanovic. *Diode Lasers and Photonic Integrated Circuits*. John Wiley & Sons, 2012.
- [30] G. Baili. “Contribution à la réduction du bruit d’intensité relatif des lasers à semiconducteurs pour des applications aux radars”. PhD thesis. 2008, 1 vol. (209 p.)
- [31] M. C. Cox, N. J. Copner, and B. Williams. “High sensitivity precision relative intensity noise calibration standard using low noise reference laser source”. In: *IEE Proceedings - Science, Measurement and Technology* 145.4 (July 1998), pp. 163–165.
- [32] T. Okoshi, K. Kikuchi, and A. Nakayama. “Novel method for high resolution measurement of laser output spectrum”. In: *Electronics Letters* 16.16 (July 1980), pp. 630–631.
- [33] L. Richter et al. “Linewidth determination from self-heterodyne measurements with subcoherence delay times”. In: *IEEE Journal of Quantum Electronics* 22.11 (Nov. 1986), pp. 2070–2074.
- [34] G. H. Duan and P. Gallion. “Drive current noise induced linewidth in tunable multielectrode lasers”. In: *IEEE Photonics Technology Letters* 3.4 (Apr. 1991), pp. 302–304.
- [35] *Bilt Itest current sources*. URL: <http://www.itest.fr/BE2100/>.
- [36] H. Ludvigsen, M. Tossavainen, and M. Kaivola. “Laser linewidth measurements using self-homodyne detection with short delay”. In: *Optics Communications* 155.1 (1998), pp. 180–186.
- [37] N. Von Bandel. “Development and study of low noise laser diodes emitting at 894 nm for compact cesium atomic clocks”. 2017MONTs003. PhD thesis. 2017.
- [38] K. Kikuchi. “Effect of 1/f-type FM noise on semiconductor-laser linewidth residual in high-power limit”. In: *IEEE Journal of Quantum Electronics* 25.4 (Apr. 1989), pp. 684–688.

- [39] J.-P. Tourrenc. “Caractérisation et modélisation du bruit d’amplitude optique, du bruit de fréquence et de la largeur de raie de VCSELS monomodes émettant autour de 850 nm”. PhD thesis. 2005, 1 vol. (204 p.)
- [40] H. Debregeas et al. “2kHz Linewidth C-Band Tunable Laser by Hybrid Integration of Reflective SOA and SiO<sub>2</sub> PLC External Cavity”. In: *2014 International Semiconductor Laser Conference*. Sept. 2014, pp. 50–51.
- [41] F. Girardin et al. “Determination of nonlinear gain coefficient of semiconductor lasers from above threshold spontaneous emission measurement”. In: *IEEE Photonics Technology Letters* 6.8 (Aug. 1994), pp. 894–896.

# Chapter 5

## General Conclusion

**I**NTEGRATED optics was initiated exactly 50 years ago, in a Bell System Technical Journal paper by S. E. Miller [1]. It has been a commercial technology for 15 years [2] and has attracted great interest recently with the development of silicon photonics.

In introduction, I showed that photonic integration is an established technology as it offers reduction in size and power consumption compared to discrete optics. Silicon photonics challenges pure Indium phosphide integration platform as high performances components can be made in large silicon foundries. To develop lasers in the silicon photonics platform, the heterogeneous integration has several advantages. First, III-V wafer growth is made in a standard III-V cleanroom. Then, after bonding the laser lithography and etching methods are similar to pure III-V process. To finish, coupling to SOI waveguides is possible as a thin bonding oxide separates III-V and silicon.

In this thesis, I investigated the properties of hybrid III-V on silicon tunable lasers based on ring resonators, high speed distributed feedback lasers and low noise high Q hybrid lasers. I focused on modelling, designs, mask layout and measurements of those devices.

## Results and future work

### Chapter 2

In the second chapter, I investigated ring resonator based tunable lasers. Silicon ring resonator systems are efficient filters as a high finesse can be designed with reasonable insertion losses. The results are summarized in the following:

- Comparison of tunable laser with different filter systems. Laser with Ring and Mach

Zehnder interferometer filter has 30 nm tuning range and 40 dB SMSR. Double ring resonator laser can reach 40 nm tuning range and 45 dB SMSR.

- Optimisation of output reflectivity. Differential efficiency is doubled, reaching 0.12 mW/mA and maximum output power gets greater than 21 mW.
- Fast switching widely tunable laser with 45 nm tuning range, 50 mA threshold and fibre coupled power greater than 1.5 mW. A 1.5 ns switching time between two channels has been measured.
- Tunable laser for NG-PON2. The tunable laser demonstrates excellent direct modulation performances compatible with NGPON2 thanks to its low chirp. Besides, the integration of an SOA as an optical gate allows to reach an excellent wavelength stability in burst mode operation.

Future work includes new developments on ring and Mach Zehnder interferometer laser with greater SMSR. As it has simpler tuning range, it is particularly suited for access network. In [3], a preliminary result on tunable laser with large tuning range has been obtained. Increasing the tuning range is important as ultra-wide systems are more and more needed. Those devices can benefit from output power optimizations realized in this thesis. As the differential efficiency  $\eta_d$  is proportional to  $\frac{\alpha_m}{\alpha_0 + \alpha_m}$ , greater values can be achieved by reducing internal losses. In section 2.2, I obtained preliminary results on fast tunable lasers. Those lasers will be validated in system experiments in a near future. The last section was dedicated to NG-PON2 access networks. I used an integrated SOA as a burst switch. Further work is needed to prove the compliance with NG-PON2 standard, in particular bit error rate measurements in burst mode operation. Recently, a silicon photonics tunable receiver has been reported [4]. If both emitter and receiver are compliant with the standard, fabricating an integrated transceiver can be interesting as it may be cost-effective.

## Chapter 3

In the third chapter, I demonstrated the potential of distributed feedback directly modulated lasers (DML) operating in the C band. The tested DFB laser has 37 mA threshold, fiber coupled power greater than 2.5 mW at 140 mA and SMSR greater than 40 dB. It is integrated with a low loss silicon ring resonator to increase transmission reach. The results are:

- Modulation at 10 Gb/s: Error free operation up to 50 km (BER < 1E-10) with no penalty. The transmission is possible up to 90 km with BER under  $10^{-3}$  FEC limit.

- Modulation at 25 Gb/s: Transmission under 1E-3 FEC limit up to 14 km with no penalty and 20 km with 2.5 dB penalty.
- I tested innovative DFB designs with a two section grating, in order to modify photons distribution in the cavity. In the tapered section, both effective index and grating strength increase. Transfer Matrix Method analysis gives a good agreement with experiments. A 1.5x efficiency improvement compared to standard shifted DFB of same bar is obtained.

In a near future, two section lasers may also be integrated with ring resonator filter. In a long term view, 1.3  $\mu\text{m}$  very high speed DML arrays is important for intradatacenter application or 100-400 Gb/s Ethernet.

## Chapter 4

This chapter was dedicated to high Q hybrid lasers, originally introduced by Caltech researchers [5]. Those devices take advantage of very low loss silicon waveguides to obtain a narrow linewidth. In introduction, I showed that high loss reduction can be realised without threshold current increase nor significantly lower differential efficiency. I then demonstrated that although structure parameter were different from [5], a high Q design was possible in our platform. The results are summarized in the following:

- Fabricated devices demonstrated fiber coupled power greater than 2.5 mW, and lower threshold is 40 mA. Lasers are highly single mode, with typical SMSR greater than 55 dB. I measured a linewidth enhancement factor of 2.5 for the longer device.
- Small signal electro-optical bandwidths features low relaxation oscillation frequency and high damping factor.
- Relative intensity noise below -147 dB/Hz have been measured, with flat profile over the 0-20 GHz frequency range.
- The measured best linewidth of high Q laser is 27 kHz. It is limited by technical noise.

In a near future, it would be interesting to measure the frequency noise with a frequency discriminator as in [5]. With such setup, it would be simpler to compare the results. New designs have been implemented in a fabrication run but couldn't be fabricated yet. Such devices have even higher  $\kappa L$  product to push the high Q concept to its limit. In a long term

perspective, the bonding thickness may be further increased to reduce the III-V overlap, down to values where silicon losses dominate. Moreover, the III-V structure can be optimized for high Q lasers via doping concentration and III-V active region design optimizations.

## Performance summary

In this thesis I investigated tunable lasers based on ring resonators, high speed distributed feedback lasers and high Q hybrid lasers. In the following table, I compare my results with state of the art III-V on silicon components. Main results of the second chapter are the increase in output power and tuning speed of widely tunable lasers. Preliminary results are reported on burst mode operation with integrated tunable laser and SOA. In the third chapter I described high speed DFB lasers. I obtained modulation speed comparable with state of the art results. I notably increased the reach using a silicon ring resonator filter. As the reach is already 20 km with 5 dB extinction ratio, those first results are promising for future access networks.

In the last chapter, I investigated High Q hybrid lasers, designed for low linewidth operation. Lasers had 40 mA minimal threshold and 2.5 mW fiber coupled power. Measured linewidth were comparable to results presented in [5]. The RIN shows a flat dependence with frequency, with level below -147 dB/Hz.

State of the art	wg P (mW)	$\Delta\nu$ (kHz)	Tun. speed	Mod.	Reach
RR Tun. laser	15 [6]	18 [6]	$\mu$ s [7]	10 Gb/s [8]	25 km [8]
DFB laser	25 [9]	1000 [10]	ns [11]	28 Gb/s [12]	2 km [12]
High Q DFB	8 [5]	18 [5] 1[13]	/	/	/

This work	wg P (mW)	$\Delta\nu$ (kHz)	Tun. speed	Mod.	Reach
RR Tun. laser	<b>21</b> [14]	/	<b>1.5 ns</b> [15]	10 Gb/s	25 km
DFB laser	/	2000	/	25 Gb/s	<b>20 km</b> [16]
High Q DFB	10	27	/	/	/

Table 5.1: Comparison of III-V/Si lasers developed in this thesis and state of the art components presented in chapter 1. Principal achievements are highlighted in bold.

## Outlook

In this thesis, I demonstrated that hybrid III-V on silicon lasers are promising for optical communications. The silicon photonics platform offers high performances modulators and photodiodes. In a near future, it would be interesting to integrate such components with lasers in photonic integrated circuits (PIC). Narrow linewidth lasers developed in this thesis can be integrated with optical phased array and photodiode to make a Lidar prototype. For optical communications, tunable lasers integrated with I-Q silicon modulators and coherent receiver are necessary [17]. Integrated silicon coherent transceiver can operate in a very large bandwidth, from 1260 to 1630 nm [18]. This is eight time the bandwidth of typical III-V active region. Development of regrowth steps and selective area growth in the III-V on silicon platform can be interesting to combine ultra wide modulators and coherent receivers with ultra wide band lasers. Very recently, a modulator with record efficiency and insertion losses that take advantage of the hybrid III-V on silicon platform has been demonstrated [19]. Laser integration with such modulator is of great interest [20].

## References

- [1] S. E. Miller. “Integrated optics: An introduction”. In: *The Bell System Technical Journal* 48.7 (Sept. 1969), pp. 2059–2069.
- [2] R. Nagarajan et al. “Large-scale photonic integrated circuits”. In: *IEEE Journal of Selected Topics in Quantum Electronics* 11.1 (Jan. 2005), pp. 50–65.
- [3] H. Elfaiki et al. “Ultra Wide Hybrid III-V On Silicon Tunable Laser”. In: *2018 ECOC Conference*. Sept. 2018, pp. 50–51.
- [4] P. Dong, Y. Chen, and L. L. Buhl. “Reconfigurable four-channel polarization diversity silicon photonic WDM receiver”. In: *2015 Optical Fiber Communications Conference and Exhibition (OFC)*. Mar. 2015, pp. 1–3.
- [5] C. T. Santis et al. “High-coherence semiconductor lasers based on integral high-Q resonators in hybrid Si/III-V platforms”. In: *Proceedings of the National Academy of Sciences* 111.8 (2014), pp. 2879–2884. eprint: <http://www.pnas.org/content/111/8/2879.full.pdf>.
- [6] M. Tran Anh et al. “Multi-Ring Mirror-Based Narrow-Linewidth Widely-Tunable Lasers in Heterogeneous Silicon Photonics”. In: *2018 European Conference on Optical Communication (ECOC)*. Sept. 2018, pp. 1–3.
- [7] G. Duan et al. “Hybrid III-V Silicon Photonic Integrated Circuits for Optical Communication Applications”. In: *IEEE Journal of Selected Topics in Quantum Electronics* 22.6 (Nov. 2016), pp. 379–389.
- [8] G. Levaufre. “Circuits photoniques intégrés incluant des lasers hybrides III-V sur silicium pour applications en télécommunication très haut débit”. PhD thesis. 2016.
- [9] R. Blum. “Scaling the compute and high speed networking needs of the datacenter with silicon photonics”. In: *2017 European Conference on Optical Communication (ECOC) Market Focus*. Sept. 2017, pp. 1–2. eprint: <https://www.intel.com/content/www/us/en/architecture-and-technology/silicon-photonics/market-focus-article.html>.
- [10] S. Keyvaninia et al. “Heterogeneously integrated III-V/silicon distributed feedback lasers”. In: *Opt. Lett.* 38.24 (Dec. 2013), pp. 5434–5437.
- [11] S. Dhoore et al. “Electronically Tunable DFB Laser on Silicon”. In: *2018 International Semiconductor Laser Conference*. Sept. 2018, pp. 1–2.

- [12] A. Abbasi et al. “28 Gb/s direct modulation heterogeneously integrated C-band InP/SOI DFB laser”. In: *Opt. Express* 23.20 (Oct. 2015), pp. 26479–26485.
- [13] C. T. Santis et al. “Quantum control of phase fluctuations in semiconductor lasers”. In: *Proceedings of the National Academy of Sciences* 115.34 (2018), E7896–E7904. eprint: <https://www.pnas.org/content/115/34/E7896.full.pdf>.
- [14] A. Gallet et al. “Nouveaux lasers hybrides iii/v sur silicium Largement accordables pour les reseaux d’accès NG-PON2.” In: *JNOG 2018*. Aug. 2018, pp. 1–3.
- [15] T. Verolet et al. “Hybrid III-V on Silicon Fast and Widely Tunable Laser Based on Rings Resonators with PIN Junctions”. In: *2018 Asia Communications and Photonics Conference (ACP)*. Oct. 2018, pp. 1–3.
- [16] A. Gallet et al. “Hybrid III-V on Silicon Integrated Distributed Feedback Laser and Ring Resonator for 25 Gb/s Future Access Networks”. In: *Journal of Lightwave Technology* 36.8 (Apr. 2018), pp. 1498–1502.
- [17] X. Pommarede. “Hybrid III-V/Si photonics integrated circuits for optical communication applications”. PhD thesis.
- [18] C. Doerr et al. “O, E, S, C, and L Band Silicon Photonics Coherent Modulator/Receiver”. In: *Optical Fiber Communication Conference Postdeadline Papers*. Optical Society of America, 2016, Th5C.4.
- [19] T. Hiraki et al. “Heterogeneously integrated III–V/Si MOS capacitor Mach–Zehnder modulator”. In: *Nature Photonics* (2017).
- [20] *H2020 Picture project*. URL: <http://picture-h2020.eu/>.

# Publication list

## Journal papers

- [1] A. Gallet et al. “Hybrid III-V on Silicon Integrated Distributed Feedback Laser and Ring Resonator for 25 Gb/s Future Access Networks”. In: *J. Lightwave Technol.* 36.8 (Apr. 2018), pp. 1498–1502.
- [2] A. Gallet et al. “Integrated Hybrid III-V/SOI Directly Modulated DFB Laser and Ring Resonator at 10 Gbit/s”. In: *IEEE Photonics Technology Letters* 29.17 (Sept. 2017), pp. 1424–1426.
- [3] V. Cristofori et al. “25-Gb/s Transmission Over 2.5-km SSMF by Silicon MRR Enhanced 1.55- $\mu\text{m}$  III-V/SOI DML”. In: *IEEE Photonics Technology Letters* 29.12 (June 2017), pp. 960–963.
- [4] K. Schires et al. “Passive Chaos Bandwidth Enhancement Under Dual-Optical Feedback with Hybrid III-V/Si DFB Laser”. In: *IEEE Journal of Selected Topics in Quantum Electronics* 23.6 (Nov. 2017), pp. 1–9.

## First author conference proceedings

I also included conference proceedings where students under my supervision are first author and where I am second author. ECOC 2017 paper was top scored and ACP 2018 paper received the best student paper award.

- [1] T. Verolet et al. “Hybrid III-V on Silicon Fast and Widely Tunable Laser Based on Rings Resonators with PIN Junctions”. In: *2018 Asia Communications and Photonics Conference (ACP)*. Oct. 2018, pp. 1–3.
- [2] A. Gallet et al. “Design, Fabrication and Characterization of Hybrid III-V/SOI Phase-Shift Free DFB Laser with Tapered Silicon Waveguide”. In: *2018 European Conference on Optical Communication (ECOC)*. Aug. 2018, pp. 1–3.
- [3] A. Gallet et al. “Dynamic and Noise Properties of High-Q Hybrid Laser”. In: *2018 IEEE International Semiconductor Laser Conference (ISLC)*. Sept. 2018, pp. 1–2.
- [4] A. Gallet et al. “Nouveaux lasers hybrides iii/v sur silicium Largement accordables pour les reseaux d’accès NG-PON2.” In: *JNOG 2018*. Aug. 2018, pp. 1–3.

- [5] A. Gallet et al. “Hybrid III-V on Silicon Integrated Distributed Feedback Laser and Ring Resonator for 25 Gb/s Future Access Networks”. In: *2017 European Conference on Optical Communication (ECOC)*. Sept. 2017, pp. 1–3.
- [6] I. Ghorbel et al. “25Gb/s Error-free transmission with a packaged chipset integrating a III-V/SOI DFB laser an electro-absorption modulator and a semiconductor optical amplifier”. In: *2017 IEEE 14th International Conference on Group IV Photonics (GFP)*. Aug. 2017, pp. 99–100.
- [7] A. Gallet et al. “Long delay optical feedback sensitivity of hybrid III-V/SOI directly modulated DFB lasers”. In: *2017 IEEE 14th International Conference on Group IV Photonics (GFP)*. 2017, pp. 115–116.
- [8] A. Gallet et al. “50km Error Free Transmission at 10Gb/s with an Integrated Hybrid III-V on Silicon Directly Modulated DFB Laser and Ring Resonator”. In: *ECOC 2016; 42nd European Conference on Optical Communication*. Sept. 2016, pp. 1–3.

## Other conference proceedings

- [1] V. Cristofori et al. “Direct Modulation of a Hybrid III-V/Si DFB Laser with MRR Filtering for 22.5-Gb/s Error-Free Dispersion-Uncompensated Transmission over 2.5-km SSMF”. In: *ECOC 2016; 42nd European Conference on Optical Communication*. Sept. 2016, pp. 1–3.
- [2] V. Cristofori et al. “25-Gb/s transmission over 2.5-km SSMF by silicon MRR enhanced 1.55- $\mu\text{m}$  III-V/SOI DML”. In: *2017 IEEE Photonics Conference (IPC)*. Oct. 2017, pp. 357–360.
- [3] V. Cristofori et al. “Directly modulated and ER enhanced hybrid IH-V/SOI DFB laser operating up to 20 Gb/s for extended reach applications in PONs”. In: *2017 Optical Fiber Communications Conference and Exhibition (OFC)*. Mar. 2017, pp. 1–3.
- [4] R. N. Sheehan et al. “1310 nm Data transmission using silicon photonic integrated circuit comprising directly modulated DFB laser and SOA”. In: *2017 SBMO/IEEE MTT-S International Microwave and Optoelectronics Conference (IMOC)*. Aug. 2017, pp. 1–4.
- [5] S. Gomez et al. “Wideband chaos in hybrid III-V/silicon distributed feedback semiconductor lasers under optical feedback”. In: *2017 SPIE Photonics west conference*. Vol. 10098. 2017, pp. 10098 - 10098 - 7.

- [6] V. Cristofori et al. “1.5-  $\mu\text{m}$  Directly modulated transmission over 66 km of SSMF with an integrated hybrid III-V/SOI DFB laser”. In: *2017 IEEE 14th International Conference on Group IV Photonics (GFP)*. Aug. 2017, pp. 103–104.
- [7] H. Elfaiki et al. “Ultra Wide Hybrid III-V on Silicon Tunable Laser”. In: *2018 European Conference on Optical Communication (ECOC)*. Sept. 2018, pp. 1–3.
- [8] A. Shen et al. “A Packaged Silicon Photonic Circuit Integrating a Hybrid Tunable Laser, a Modulator and an Amplifier”. In: *2018 IEEE 15th International Conference on Group IV Photonics (GFP)*. Aug. 2018, pp. 1–2.
- [9] R. Sheehan et al. “Repeaterless data transmission at 1310 nm using silicon photonic integrated circuit”. In: *2018 SPIE Photonics europe conference*. Vol. 10686. 2018, pp. 10686 - 10686 - 6.

# Chapter 6

## Résumé en Français

LES débits des réseaux optiques augmentent exponentiellement mais les prix des composants sont stables. Ce paradigme, appelé "loi de Moore photonique" impose de développer de nouveaux composants. L'intégration photonique répond à cette problématique car elle permet de réduire la taille et la consommation d'énergie par rapport aux systèmes assemblés à partir de composants unitaires.

L'intégration photonique a débuté il y a 50 ans, avec un papier de S. E. Miller dans le Bell System Technical Journal [1]. C'est une technologie commerciale depuis 15 ans [2] et a récemment suscité un grand intérêt avec le développement de la photonique sur silicium.

La photonique sur silicium challenge la plate-forme d'intégration sur InP car des composants à hautes performances peuvent être fabriqués dans une fonderie silicium. Ceux-ci sont de plus petite taille et produits sur de plus grandes plaques. En photonique sur silicium, les composants sont fabriqués sur des plaques de 200 ou 300 mm, à comparer avec les plaques de 76 mm de la plateforme InP. Une photo de plaques silicium est présentée sur la figure 6.1. Comme les rendements par plaques sont aussi améliorés du fait d'une plus grande automatisation, les coûts des composants photoniques sur silicium sont abaissés par rapport aux composants sur InP. Les modulateurs Mach-Zehnder en silicium sont déjà implémentés dans des produits pour les liaisons courtes ou longues distances [3] [4].

Pour développer les lasers sur cette plateforme, l'intégration hétérogène présente plusieurs avantages. Tout d'abord, la croissance des wafers III-V se fait dans une salle blanche III-V standard. Ensuite, après le collage, la lithographie et les méthodes de gravure sont similaires aux procédés de réalisation des lasers III-V. Pour finir, le couplage aux guides d'ondes silicium est possible car un mince oxyde de collage sépare les deux wafers.

Récemment, une nouvelle approche a été proposée qui repose sur l'épitaxie directe de boîtes

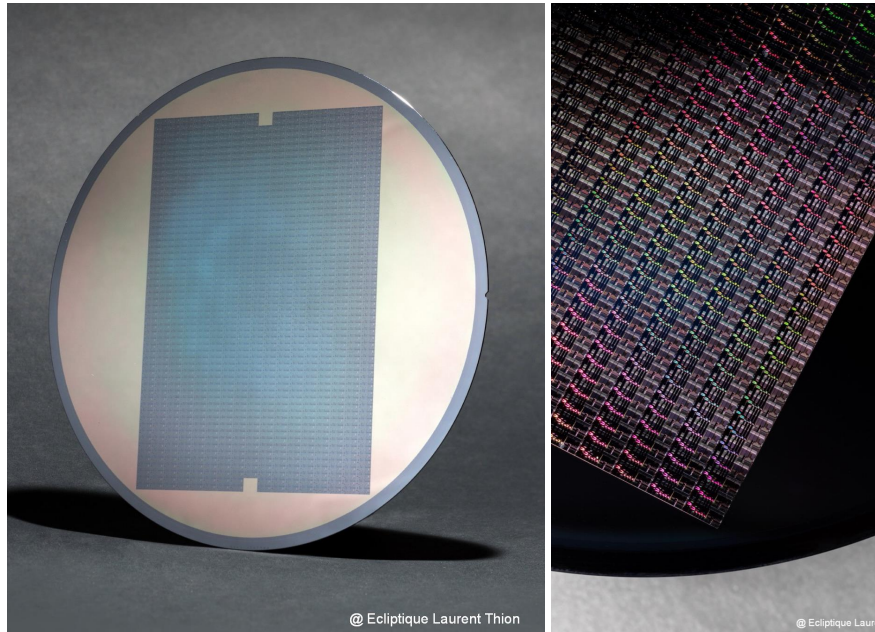


Figure 6.1: Photos de plaques silicium.

quantiques sur silicium. Si cette plateforme permet de supprimer l'étape de collage, elle ne propose pas d'intégration avec les composants silicium pour le moment. Les avantages et inconvénients des différentes plateformes d'intégration sont résumés dans le tableau suivant:

Platform	Laser	Ø comp	Maturité	D. plaque (mm)	rendement	Fabless
InP	yes	++	+++	76	++	Oui
Silicon Photonics	Non	+++	+++	200-300	+++	Yes
III-V/Si bonding	Oui	+++	++	200-300	/	No
III-V/Si dir. growth	Oui	++	+	200-300	/	Non

Table 6.1: Avantages et inconvénients des différentes plateformes d'intégration photonique. Ø comp correspond à la taille des composants.

Dans cette thèse, je présente la réalisation de nouveaux composants hybrides III-V sur silicium pour les communications optiques. J'ai étudié les propriétés des lasers accordables basés sur des résonateurs en anneau en silicium, des lasers à rétroaction distribuée modulés directement à grande vitesse et des lasers à haut facteur de qualité à faible bruit. Je me suis concentré sur la modélisation, la conception, le dessin des masques de fabrication et les mesures de ces dispositifs.

## Chapitre 2

Dans le deuxième chapitre, j'ai étudié les lasers accordables avec des résonateurs en anneau. Les systèmes de résonateurs en anneau en silicium sont des filtres efficaces pour les lasers accordables: une grande finesse peut être conçue avec des pertes d'insertion raisonnables. Le laser accordable est composé d'un miroir de Bragg à l'arrière, du système de filtrage, d'une transition III-V/Si, d'une section de gain de  $400 \mu\text{m}$ , d'une autre transition III-V/Si et d'un miroir de Bragg de sortie. Dans la zone de gain, le confinement dans les puits quantiques est de 10% (hors barrières). Après le miroir de sortie, la lumière est extraite par un coupleur vertical (FGC). Le laser peut également être clivé dans la région III-V pour minimiser les pertes de couplage. La lumière est ensuite couplée à une fibre optique. Dans un premier temps, j'ai étudié différentes architectures de lasers accordables. J'ai comparé les systèmes de filtrage: le laser avec anneau et filtre interféromètre Mach Zehnder a une plage d'accord de 30 nm et un SMSR de 40 dB. Le laser à double résonateur en anneau peut atteindre une plage d'accord de 40 nm et un SMSR de 45 dB. Pour obtenir le maximum de puissance, les lasers sont clivés dans la région de gain, ce qui donne un coefficient de réflexion de 30% à la facette. La puissance de sortie peut être augmentée en optimisant la réflectivité de cette facette. Pour un laser à anneau et Mach-Zehnder, un traitement anti-reflet de 2% permet d'obtenir les meilleures performances. Comme le graphique P-I présenté dans la figure suivante le montre, le rendement différentiel d'un laser à anneau et Mach-Zehnder est doublé à 0.12 mW/mA et la puissance de sortie maximale est supérieure à 21 mW. Dans un second temps,

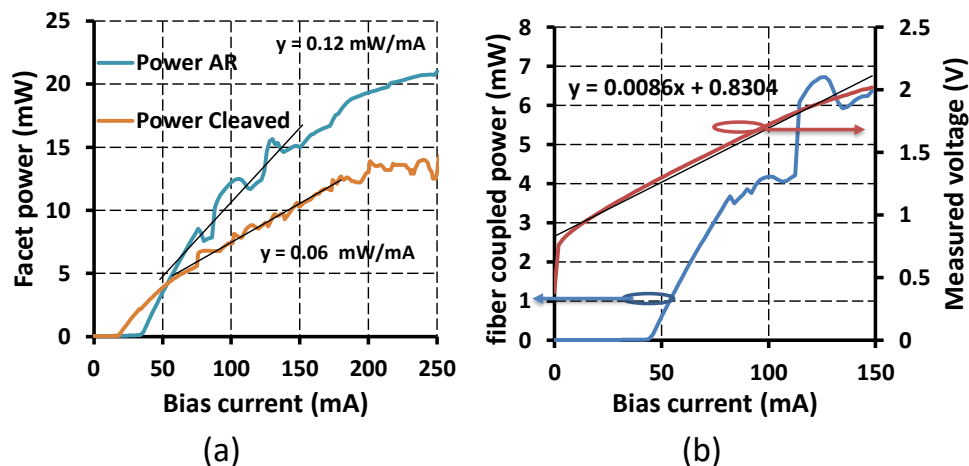


Figure 6.2: (a) Courbe P-I pour un laser clivé et un laser avec traitement anti-reflet AR de 2%. La puissance à 200 mA est multipliée par 1.5. (b) Puissance couplée dans la fibre avec plus de 6 mW à 120 mA. L'efficacité est proche des valeurs des lasers DBR de III-V lab [5], p218.

j'ai étudié un laser à commutation de longueur d'onde rapide. Le laser a une large plage d'accord de 45 nm, un seuil de 50 mA et une puissance couplée dans la fibre supérieure à 1,5 mW. Un temps de commutation de 1,5 ns entre deux canaux a été mesuré. Enfin, j'ai montré que le laser accordable démontre d'excellentes performances de modulation directe compatible avec le NGPON2 grâce à son faible chirp. De plus, l'intégration d'un SOA comme porte optique permet d'atteindre une excellente stabilité de longueur d'onde en mode paquet.

### Chapitre 3

Dans le troisième chapitre, je démontre le potentiel des lasers à rétroaction distribuée directement modulés (DML) fonctionnant dans la bande C. Comme le montre la figure 6.3, le laser DFB testé a un seuil de 37 mA, une puissance couplée à la fibre optique supérieure à 2,5 mW à 140 mA. Le taux de réjection des modes secondaire est supérieur à 40 dB. Il est intégré à un résonateur en anneau de silicium à faible perte pour augmenter la portée de transmission. J'ai aussi obtenu les résultats résumés dans la suite.

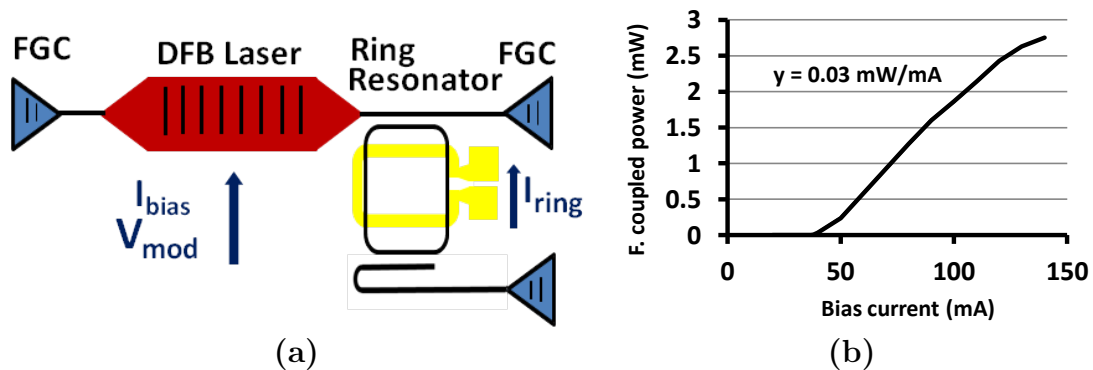


Figure 6.3: a) Schéma du laser hybride III-V/SOI avec filtre d'amélioration du taux d'extinction. b) Caractéristique L-I d'un laser III-V/Si DFB mesuré après un coupleur vertical, avec un seuil de 37 mA et une puissance couplée dans la fibre supérieure à 2,5 mW.

- Le laser a un faible chirp adiabatique de 3,2 GHz. Le chirp transitoire est réduit par l'anneau jusqu'à 1.2 GHz.
- Modulation à 10 Gb/s : Fonctionnement sans erreur jusqu'à 50 km (Taux d'erreur binaire (TEB)  $< 1E-10$ ) sans pénalité. La transmission est possible jusqu'à 90 km avec un TEB inférieur à la limite FEC de  $10^{-3}$ .



avec des SMSR typiques supérieurs à 55 dB. J'ai mesuré un facteur de Henry de 2,5 pour l'échantillon le plus long.

- Les bandes passantes électro-optiques petit signal se caractérisent par une faible fréquence d'oscillation de relaxation et un facteur d'amortissement élevé. Le facteur K peut atteindre 4.1 ns, ce qui donne une durée de vie des photons de 103 ps.
- Le bruit d'intensité relatif est inférieur à -147 dB/Hz. Il a un profil plat dans la gamme de fréquences de 0-20 GHz.
- La meilleure largeur de raie obtenue pour un laser à Q élevé est de 27 kHz. Elle est limitée par le bruit technique.

Dans un futur proche, la structure III-V pourra être optimisée pour les lasers à Q élevé grâce à un choix de concentration de dopage du matériaux III-V, à l'optimisation de la conception de la région active III-V et à l'optimisation de l'épaisseur de collage.

## Résumé des performances

Dans cette thèse, j'ai étudié les lasers accordables basés sur des résonateurs en anneau, des lasers à rétroaction distribuée à grande vitesse et des lasers hybrides à Q élevé. Dans le tableau suivant, je compare mes résultats avec l'état de l'art III-V sur silicium. Les principaux résultats du deuxième chapitre sont l'augmentation de la puissance de sortie et de la vitesse d'accord des lasers largement accordables. Les résultats préliminaires sont rapportés sur le fonctionnement en mode burst avec laser accordable et SOA intégrés. Dans le troisième chapitre, j'ai décrit les lasers DFB à grande vitesse. J'ai obtenu une vitesse de modulation comparable aux résultats de l'état de l'art. J'ai augmenté la portée en utilisant un résonateur en anneau en silicium. Comme la portée est déjà de 20 km avec un taux d'extinction de 5 dB, ces premiers résultats sont prometteurs pour les futurs réseaux d'accès. Dans le dernier chapitre, j'ai étudié les lasers hybrides à fort facteur de qualité, conçus pour avoir une faible largeur de raie. Les lasers avaient un seuil minimal de 40 mA et une puissance couplée à la fibre de 2,5 mW. La largeur de raie mesurée était comparable aux résultats présentés dans [6].

State of the art	wg P (mW)	$\Delta\nu$ (kHz)	Tun. speed	Mod.	Reach
RR Tun. laser	15 [7]	18 [7]	$\mu$ s [8]	10 Gb/s [9]	25 km [9]
DFB laser	25 [10]	1000 [11]	ns [12]	28 Gb/s [13]	2 km [13]
High Q DFB	8 [6]	18 [6] 1[14]	/	/	/

This work	wg P (mW)	$\Delta\nu$ (kHz)	Tun. speed	Mod.	Reach
RR Tun. laser	<b>21</b> [15]	/	<b>1.5 ns</b> [16]	10 Gb/s	25 km
DFB laser	/	2000	/	25 Gb/s	<b>20 km</b> [17]
High Q DFB	10	27	/	/	/

Table 6.2: Comparaison des lasers III-V/Si développés dans cette thèse avec l'état de l'art présenté dans le chapitre 1. Les principaux résultats sont indiqués en caractères gras.

## Perspectives

Dans cette thèse, j'ai démontré que les lasers hybrides III-V sur silicium sont prometteurs pour les communications optiques. La plate-forme photonique silicium offre des modulateurs et des photodiodes hautes performances. Dans un avenir proche, il serait intéressant d'intégrer de tels composants avec des lasers dans des circuits intégrés photoniques (PIC). Les lasers à largeur de raie étroite développés dans le cadre de cette thèse peuvent être intégrés à une photodiode pour réaliser un prototype Lidar. Pour les communications optiques, des lasers accordables intégrés avec des modulateurs silicium I-Q et un récepteur cohérent sont nécessaires [18]. L'émetteur-récepteur intégré cohérent en silicium peut fonctionner sur une très large bande passante, de 1260 à 1630 nm [4]. C'est 8 fois la bande de gain typique des régions de gain III-V. Le développement d'étapes de reprise d'épitaxie et de croissance sélective de III-V sur la plate-forme silicium peut être intéressant pour combiner des modulateurs, récepteurs cohérents et lasers ultra-large bande. Très récemment, un modulateur avec une efficacité et des pertes d'insertion record qui tire profit de la plateforme hybride III-V sur silicium a été démontré [19]. L'intégration de lasers avec un tel modulateur est d'un grand intérêt [20].

## References

- [1] S. E. Miller. “Integrated optics: An introduction”. In: *The Bell System Technical Journal* 48.7 (Sept. 1969), pp. 2059–2069.
- [2] R. Nagarajan et al. “Large-scale photonic integrated circuits”. In: *IEEE Journal of Selected Topics in Quantum Electronics* 11.1 (Jan. 2005), pp. 50–65.
- [3] A. Narasimha et al. “A Fully Integrated 4×10-Gb/s DWDM Optoelectronic Transceiver Implemented in a Standard 0.13μm CMOS SOI Technology”. In: *IEEE Journal of Solid-State Circuits* 42.12 (Dec. 2007), pp. 2736–2744.
- [4] C. Doerr et al. “O, E, S, C, and L Band Silicon Photonics Coherent Modulator/Receiver”. In: *Optical Fiber Communication Conference Postdeadline Papers*. Optical Society of America, 2016, Th5C.4.
- [5] H. Debrégeas. *Widely Tunable Laser Diodes, in Fibre Optic Communication: Key Devices Springer Series in Optical Science*.
- [6] C. T. Santis et al. “High-coherence semiconductor lasers based on integral high-Q resonators in hybrid Si/III-V platforms”. In: *Proceedings of the National Academy of Sciences* 111.8 (2014), pp. 2879–2884. eprint: <http://www.pnas.org/content/111/8/2879.full.pdf>.
- [7] M. Tran Anh et al. “Multi-Ring Mirror-Based Narrow-Linewidth Widely-Tunable Lasers in Heterogeneous Silicon Photonics”. In: *2018 European Conference on Optical Communication (ECOC)*. Sept. 2018, pp. 1–3.
- [8] G. Duan et al. “Hybrid III-V Silicon Photonic Integrated Circuits for Optical Communication Applications”. In: *IEEE Journal of Selected Topics in Quantum Electronics* 22.6 (Nov. 2016), pp. 379–389.
- [9] G. Levaufre. “Circuits photoniques intégrés incluant des lasers hybrides III-V sur silicium pour applications en télécommunication très haut débit”. PhD thesis. 2016.
- [10] R. Blum. “Scaling the compute and high speed networking needs of the datacenter with silicon photonics”. In: *2017 European Conference on Optical Communication (ECOC) Market Focus*. Sept. 2017, pp. 1–2. eprint: <https://www.intel.com/content/www/us/en/architecture-and-technology/silicon-photonics/market-focus-article.html>.

- [11] S. Keyvaninia et al. “Heterogeneously integrated III-V/silicon distributed feedback lasers”. In: *Opt. Lett.* 38.24 (Dec. 2013), pp. 5434–5437.
  - [12] S. Dhoore et al. “Electronically Tunable DFB Laser on Silicon”. In: *2018 International Semiconductor Laser Conference*. Sept. 2018, pp. 1–2.
  - [13] A. Abbasi et al. “28 Gb/s direct modulation heterogeneously integrated C-band InP/SOI DFB laser”. In: *Opt. Express* 23.20 (Oct. 2015), pp. 26479–26485.
  - [14] C. T. Santis et al. “Quantum control of phase fluctuations in semiconductor lasers”. In: *Proceedings of the National Academy of Sciences* 115.34 (2018), E7896–E7904. eprint: <https://www.pnas.org/content/115/34/E7896.full.pdf>.
  - [15] A. Gallet et al. “Nouveaux lasers hybrides iii/v sur silicium Largement accordables pour les reseaux d’accès NG-PON2.” In: *JNOG 2018*. Aug. 2018, pp. 1–3.
  - [16] T. Verolet et al. “Hybrid III-V on Silicon Fast and Widely Tunable Laser Based on Rings Resonators with PIN Junctions”. In: *2018 Asia Communications and Photonics Conference (ACP)*. Oct. 2018, pp. 1–3.
  - [17] A. Gallet et al. “Hybrid III-V on Silicon Integrated Distributed Feedback Laser and Ring Resonator for 25 Gb/s Future Access Networks”. In: *Journal of Lightwave Technology* 36.8 (Apr. 2018), pp. 1498–1502.
  - [18] X. Pommarede. “Hybrid III-V/Si photonics integrated circuits for optical communication applications”. PhD thesis.
  - [19] T. Hiraki et al. “Heterogeneously integrated III-V/Si MOS capacitor Mach-Zehnder modulator”. In: *Nature Photonics* (2017).
  - [20] *H2020 Picture project*. URL: <http://picture-h2020.eu/>.
- 
- [1] S. E. Miller. “Integrated optics: An introduction”. In: *The Bell System Technical Journal* 48.7 (Sept. 1969), pp. 2059–2069.
  - [2] R. Nagarajan et al. “Large-scale photonic integrated circuits”. In: *IEEE Journal of Selected Topics in Quantum Electronics* 11.1 (Jan. 2005), pp. 50–65.
  - [3] A. Narasimha et al. “A Fully Integrated 4×10-Gb/s DWDM Optoelectronic Transceiver Implemented in a Standard 0.13μm CMOS SOI Technology”. In: *IEEE Journal of Solid-State Circuits* 42.12 (Dec. 2007), pp. 2736–2744.

- [4] C. Doerr et al. “O, E, S, C, and L Band Silicon Photonics Coherent Modulator/Receiver”. In: *Optical Fiber Communication Conference Postdeadline Papers*. Optical Society of America, 2016, Th5C.4.
- [5] H. Debrégeas. *Widely Tunable Laser Diodes, in Fibre Optic Communication: Key Devices Springer Series in Optical Science*.
- [6] C. T. Santis et al. “High-coherence semiconductor lasers based on integral high-Q resonators in hybrid Si/III-V platforms”. In: *Proceedings of the National Academy of Sciences* 111.8 (2014), pp. 2879–2884. eprint: <http://www.pnas.org/content/111/8/2879.full.pdf>.
- [7] M. Tran Anh et al. “Multi-Ring Mirror-Based Narrow-Linewidth Widely-Tunable Lasers in Heterogeneous Silicon Photonics”. In: *2018 European Conference on Optical Communication (ECOC)*. Sept. 2018, pp. 1–3.
- [8] G. Duan et al. “Hybrid III-V Silicon Photonic Integrated Circuits for Optical Communication Applications”. In: *IEEE Journal of Selected Topics in Quantum Electronics* 22.6 (Nov. 2016), pp. 379–389.
- [9] G. Levaufre. “Circuits photoniques intégrés incluant des lasers hybrides III-V sur silicium pour applications en télécommunication très haut débit”. PhD thesis. 2016.
- [10] R. Blum. “Scaling the compute and high speed networking needs of the datacenter with silicon photonics”. In: *2017 European Conference on Optical Communication (ECOC) Market Focus*. Sept. 2017, pp. 1–2. eprint: <https://www.intel.com/content/www/us/en/architecture-and-technology/silicon-photonics/market-focus-article.html>.
- [11] S. Keyvaninia et al. “Heterogeneously integrated III-V/silicon distributed feedback lasers”. In: *Opt. Lett.* 38.24 (Dec. 2013), pp. 5434–5437.
- [12] S. Dhoore et al. “Electronically Tunable DFB Laser on Silicon”. In: *2018 International Semiconductor Laser Conference*. Sept. 2018, pp. 1–2.
- [13] A. Abbasi et al. “28 Gb/s direct modulation heterogeneously integrated C-band InP/SOI DFB laser”. In: *Opt. Express* 23.20 (Oct. 2015), pp. 26479–26485.
- [14] C. T. Santis et al. “Quantum control of phase fluctuations in semiconductor lasers”. In: *Proceedings of the National Academy of Sciences* 115.34 (2018), E7896–E7904. eprint: <https://www.pnas.org/content/115/34/E7896.full.pdf>.

- [15] A. Gallet et al. “Nouveaux lasers hybrides iii/v sur silicium Largement accordables pour les reseaux d’accès NG-PON2.” In: *JNOG 2018*. Aug. 2018, pp. 1–3.
- [16] T. Verolet et al. “Hybrid III-V on Silicon Fast and Widely Tunable Laser Based on Rings Resonators with PIN Junctions”. In: *2018 Asia Communications and Photonics Conference (ACP)*. Oct. 2018, pp. 1–3.
- [17] A. Gallet et al. “Hybrid III-V on Silicon Integrated Distributed Feedback Laser and Ring Resonator for 25 Gb/s Future Access Networks”. In: *Journal of Lightwave Technology* 36.8 (Apr. 2018), pp. 1498–1502.
- [18] X. Pommarede. “Hybrid III-V/Si photonics integrated circuits for optical communication applications”. PhD thesis.
- [19] T. Hiraki et al. “Heterogeneously integrated III–V/Si MOS capacitor Mach–Zehnder modulator”. In: *Nature Photonics* (2017).
- [20] *H2020 Picture project*. URL: <http://picture-h2020.eu/>.

# Appendices

# Appendix A

## $Q_{ext}$ calculations for phase shifted lasers

In introduction of chapter 4, I defined the external quality factor with the threshold gain coefficient  $\alpha_{th}$ :

$$\frac{1}{Q_{ext}} = \frac{\lambda v_g}{\pi c} \times \alpha_{th} \quad (\text{A.1})$$

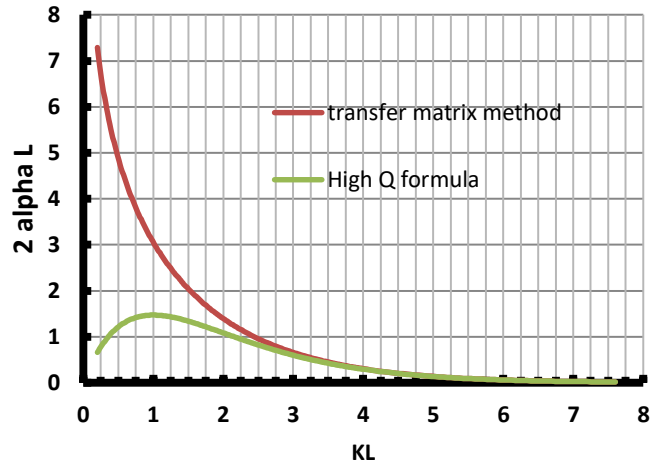
In section 4.2.4, I indicated that the following equation can be used to calculate the quality factor:

$$\frac{1}{Q_{ext}} = \frac{2P_1}{\omega W} \quad (\text{A.2})$$

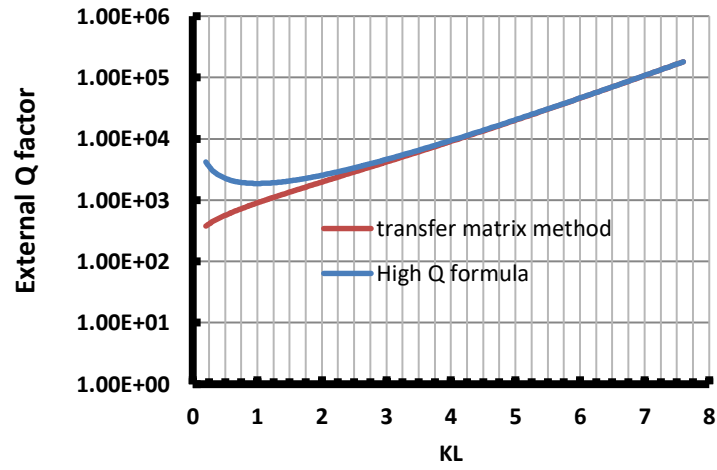
The quality factor is the stored energy  $W$  divided by the escaping energy  $\frac{2P_1}{\omega}$ . Haus gives a formula for equ.A.2 for a  $\lambda/4$  phase shifted laser if  $\kappa L \gg 1$  [1], p246:

$$\frac{1}{Q_{ext}} = \frac{\lambda v_g}{\pi c} \times \left( \frac{2\kappa L}{L} \times \exp(-\kappa L) \right) = \frac{\lambda v_g}{\pi c} \times \mathfrak{U} \quad (\text{A.3})$$

Comparing A.1 and A.2 we remark that  $\mathfrak{U}$  should be equal to  $\alpha_{th}$ . In order to be independent of the structure and to be consistent with chapter 3, I plot  $2\alpha_{th}L$  calculated with Transfer matrix method and  $2\mathfrak{U}L$  as a function of  $\kappa L$  in fig. A.1.a. As  $\kappa L$  increases, the difference between the two values exponentially decreases. It reaches below 1% as soon as  $\kappa L$  is greater than 4. Q factor versus  $\kappa L$  from equation A.1 and A.2 is also plotted in fig. A.1b. This calculations indicate that both method give the same result.



(a)



(b)

Figure A.1: (a) Normalized threshold gain calculated with TMM (red) and equation A.2. (b) Corresponding external Q factor.

# List of Acronyms

**BER** Bit Error Rate.

**CMP** Chemical Mechanical Planarisation.

**DC** Directionnal Coupler.

**DFB** Distributed feedback.

**DSP** Digital Signal Processing.

**EDFA** Erbium Doped Fiber Amplifier.

**FEC** Forward Error Correction.

**FGC** Fiber Grating Coupler.

**FP** Fabry-Perot.

**FSR** Free Spectral Range.

**I/Q modulator** In phase/Quadrature modulator.

**InP** Indium Phosphide.

**laser** Light Amplification by Stimulated Emission of Radiation.

**MZM** Mach-Zehnder modulator.

**ONU** Optical Network Unit.

**OOK** On-Off Keying.

**OSA** Optical Spectrum Analyser.

**PIC** Photonic Integrated Circuit.

**Q** Quality factor.

**RIE** Reactive Ion Etching.

**RR** Ring Resonator.

**SEM** Scanning Electron Microscope.

**SMF** Single Mode Fiber.

**SMSR** Side Mode Suppression Ratio.

**SOA** Semi-Conductor Amplifier.

**SOI** Silicon on Insulator.

**TUL** Tunable Laser.

**WDM** Wavelength Division Multiplexing.

**Titre:** Sources lasers hybrides III-V sur silicium pour les communications optiques

**Mots clés:** Telecommunications, Lasers Hybrides, Photonique sur Silicium

**Résumé:**

L'intégration photonique permet de réduire la taille et la consommation d'énergie des systèmes de communication par fibre optique par rapport aux systèmes assemblés à partir de composants unitaires. Cette technologie a récemment suscité un grand intérêt avec les progrès de l'intégration sur InP et le développement de la photonique sur silicium. Cette dernière challenge la plate-forme d'intégration sur InP car des composants à hautes performances et faibles coûts peuvent être fabriqués dans des fonderies originellement développées pour la microélectronique. Les lasers sont l'une des pièces maîtresses des émetteurs-récepteurs pour les communications optiques. Leur intégration sur la

plateforme silicium permet de développer des émetteurs-récepteurs comprenant les fonctions critiques d'émission de lumière, de modulation et de détection sur une même puce. L'intégration de matériaux III-V par collage moléculaire sur plaque silicium permet de produire de grands volumes : plusieurs dizaines voire centaines de composants sont réalisés par wafer. Dans cette thèse, j'ai étudié théoriquement et expérimentalement les propriétés des lasers accordables basés sur des résonateurs en anneau en silicium, des lasers à rétroaction distribuée modulés directement et des lasers à haut facteur de qualité qui présentent un faible bruit de phase et d'intensité.

**Title:** Hybrid III-V/Si lasers for optical communications

**Keywords:** Telecommunications, Hybrid Lasers, Silicon Photonics

**Abstract:**

Photonic integration reduces the size and energy consumption of fiber optic communication systems compared to systems assembled from discrete components. This technology has recently attracted a great interest with the progress of integration on InP and the development of silicon photonics. The latter challenges the integration platform on InP as high-performance and low-cost components can be manufactured in foundries originally developed for microelectronics. Lasers are one of the main parts of transceivers for op-

tical communications. With their integration on the silicon platform, transceivers that include the critical functions of light emission, modulation and detection on the same chip can be made. In the heterogeneous integration platform, components are manufactured in high volumes: several tens or even hundreds of components are produced per wafer. In this thesis, I studied theoretically and experimentally the properties of tunable lasers based on silicon ring resonators, directly modulated distributed feedback lasers and low noise high-quality factor lasers.

